UNIVERSIDADE DE LISBOA

INSTITUTO SUPERIOR TÉCNICO

DNA recognition system on bioactive paper using fusions of carbohydrate-binding modules and IgG-binding Z domains

Ana Margarida de Mendonça Rosa

Supervisor: Doctor Duarte Miguel de França Teixeira dos Prazeres
Co-Supervisor: Doctor Pedro Miguel Neves Ribeiro Paulo

Thesis approved in public session to obtain the PhD Degree in
Biotechnology and Biosciences

Jury final classification: Pass with Distinction

2020

UNIVERSIDADE DE LISBOA

INSTITUTO SUPERIOR TÉCNICO

DNA recognition system on bioactive paper using fusions of carbohydrate-binding modules and IgG-binding Z domains

Ana Margarida de Mendonça Rosa

Supervisor: Doctor Duarte Miguel de França Teixeira dos Prazeres
Co-Supervisor: Doctor Pedro Miguel Neves Ribeiro Paulo

Thesis approved in public session to obtain the PhD Degree in
Biotechnology and Biosciences

Jury final classification: Pass with Distinction

Jury

Chairperson: Doctor Isabel Maria de Sá Correia Leite de Almeida, Instituto Superior Técnico, Universidade de Lisboa

Members of the Committee:

Doctor Pedro Miguel Ribeiro Viana Baptista, Faculdade de Ciências e Tecnologia, Universidade NOVA de Lisboa

Doctor Carlos Mendes Godinho de Andrade Fontes, Faculdade de Medicina Veterinária, Universidade de Lisboa

Doctor Duarte Miguel de França Teixeira dos Prazeres, Instituto Superior Técnico, Universidade de Lisboa

Doctor Gabriel António Amaro Monteiro, Instituto Superior Técnico, Universidade de Lisboa

Doctor Pedro Ricardo Martins Lopes da Fonte, Escola de Ciências e Tecnologias da Saúde, Universidade Lusófona de Humanidades e Tecnologia

Funding Institution

Fundação para a Ciência e a Tecnologia

2020

Resumo

O papel bioativo tem potencial para ser utilizado no desenvolvimento de bioensaios de baixo custo, requerendo a imobilização de biossensores na celulose e um processo conveniente de produção de sinal de captura do analito-alvo. Este trabalho foca-se no desenvolvimento de um sistema de reconhecimento molecular em matrizes de celulose para a deteção colorimétrica de ácidos nucleicos. A estratégia é baseada no reconhecimento de híbridos de ADN biotinilado por anticorpos anti-biotina imobilizados em celulose através de uma proteína quimérica ZZ-CBM. Esta fusão combina um modulo de ligação a hidratos de carbono (CBM) com afinidade para a celulose e um domínio Z duplo (ZZ) que se liga a anticorpos do tipo IgG. Nanopartículas de ouro (AuNPs) conjugadas com ADN complementar são usadas como sonda colorimétrica para hibridar com o ADN-alvo biotinilado.

As fusões ZZ-CBM produzidas e purificadas foram caracterizadas por dicroísmo circular. Além disso, foi demonstrada a capacidade de ZZ-CBM em ancorar anticorpos IgG na celulose sem alteração da sua capacidade de ligação ao alvo.

As interações moleculares entre todos os componentes do sistema de reconhecimento de ADN foram estudadas por espectroscopia de correlação de fluorescência e calorimetria de titulação isotérmica. Estimaram-se as constantes de dissociação para a hibridação de uma sonda de ADN fluorescente com o seu ADN alvo complementar marcado com biotina, para a ligação dos híbridos biotinilados ADN:ADN com anticorpo IgG anti-biotina e para a captura de anticorpo IgG com ZZ-CBM em solução.

Nanopartículas de ouro com um diâmetro médio de ~14 nm foram sintetizadas e conjugadas com oligonucleótidos tiolados para serem utilizadas como sondas colorimétricas. A capacidade de ADN-AuNPs hibridarem especificamente com ADN alvo biotinilado e, consequentemente, de se ligarem a IgG anti-biotina, foi confirmada pela sua mobilidade electroforética diferencial em gel e através do método de non-cross-linking.

Finalmente, o sistema de reconhecimento de ADN foi implementado em matrizes de celulose em três formatos: micropartículas de celulose em suspensão, poços e microcanais impressos a cera em papel. A IgG anti-biotina imobilizada em celulose através de ZZ-CBM capturou ADN biotinilado hibridado com a sonda de ADN-AuNPs, originando um sinal vermelho com uma intensidade directamente proporcional à quantidade de alvo. O sistema de bio-reconhecimento foi capaz de discriminar alvos com um elevado grau de homologia (~53%),

exceto nos poços de papel.
A prova de conceito experimental deste sistema de bio-reconhecimento baseado em celulose, bem como o conhecimento obtido sobre as interações moleculares envolvidas, contribui para o desenvolvimento de dispositivos analíticos simples.

Palavras-chave: *Módulos de ligação a hidratos de carbono; celulose; interações moleculares; reconhecimento de ADN; nanopartículas de ouro.*

Abstract

Bioactive paper constitutes a promising approach for the development of cost-effective bioassays, requiring an effective immobilization of biosensors onto cellulose and a convenient process to report the capture of a specific target. This work focuses on the development of a cellulose-based molecular recognition system for the colorimetric detection of nucleic acids. The strategy is based on the recognition of biotin-labeled DNA hybrids by anti-biotin antibodies immobilized on cellulose through a ZZ-CBM chimeric protein. This fusion combines a carbohydrate-binding module (CBM) with affinity to cellulose and a double Z domain (ZZ) that binds to IgG antibodies. Gold nanoparticles (AuNPs) conjugated with complementary DNA are used as a colorimetric probe which hybridizes with the biotinylated DNA target.

After production and purification, ZZ-CBM fusions were characterized by circular dichroism. In addition, the ability of ZZ-CBM to anchor IgG antibodies on cellulose with preserved antibody target binding activity was demonstrated.

Fluorescence correlation spectroscopy and isothermal titration calorimetry were employed to study the molecular interactions between all components of the DNA recognition system. Dissociation constants were estimated for the hybridization of a fluorescent DNA probe with its complementary biotin-labeled DNA target, for the binding of biotinylated DNA:DNA hybrids with anti-biotin IgG antibody and for the capture of IgG antibody with ZZ-CBM in solution.

Spherical ~14 nm citrate-capped AuNPs were synthesized and conjugated with thiolated oligonucleotides to be used as colorimetric probes. The ability of DNA-AuNPs to specifically hybridize with biotin-labeled DNA targets and subsequently bind to anti-biotin IgG was confirmed by the differential electrophoretic mobility in gel and through the non-cross-linking method.

Finally, the DNA recognition system was implemented in three bioactive paper formats: wax-printed cellulose paper wells or microchannels, and cellulose microparticles in suspension. Anti-biotin IgG attached to cellulose via ZZ-CBM was able to capture biotin-labeled DNA hybridized with DNA-AuNPs probe, generating a red capture signal with an intensity that increased with the increasing amount of target. This bio-recognition system was able to discriminate targets with a high degree of homology (~53%), except in the paper wells

format.

The experimental proof of concept of this cellulose-based biorecognition system, as well as the insight gained into the molecular interactions involved, contributes to the development of simple analytical devices based on “reader-free” testing.

Keywords: *Carbohydrate-binding modules; cellulose; molecular interactions; DNA recognition; gold nanoparticles.*

Acknowledgments

The first thing that pops up to my mind to describe this journey is a "roller coaster". Ups and downs. Loops. High speed. Low speed. Too slow at some point. What a roller coaster of a ride this has been. It is getting close to the end and, looking back, I am glad to have met a few people during this process. They helped me somehow to keep following the track, and I am very thankful for that.

Professor Miguel, for the opportunity, ingenuity, guidance, persistence, support, positive mindset. It is hard to express in words the invaluable contribution in helping me achieve this stage. Thank you, thank you, and thank you.

Pedro Paulo, for welcoming me in Centro de Química Estrutural, for the teaching, valuable help, readiness. Certainly one of the most pedagogical persons I have met as a student.

It was a great privilege to be mentored by these two people.

Prof. Pedro Baptista's research group at the Department of Life Sciences, Faculty of Sciences and Technology (FCT NOVA). The training provided by Fábio Carlos and Bruno Veigas helped me dealing with gold nanoparticles and their functionalization.

Prof. Carlos Fontes' research group at the Centre for Interdisciplinary Research in Animal Health (CIISA), Faculty of Veterinary Medicine. Namely the help of Pedro Bule and Virgínia Pires for assistance in ITC measurements.

The Institute for Bioengineering and Biosciences for hosting me during this work. The day-to-day support and good mood of iBB colleagues was much appreciated. The great help of João Trabuco and Salomé during the initial stage of the work with gold nanoparticles. The assistance of António, Rosarinho and Sónia with my research. The fruitful discussions with Rui Silva. The valuable help of Ana Pfluck in circular dichroism measurements. The knowledge sharing and insightful discussions within my research group about my experiments.

The Portuguese Foundation for Science and Technology, for the funding (grant UID/BIO/04565/2013, PhD grant SFRH/BD/87792/2012).

Mariana, for cheering me up throughout this journey.

Henrique, for the wake-up calls and constant support.

My parents, for the support and the no-questions-asked.

Thank you all.

Abbreviations and Symbols

aa	Amino acid
AKD	Alkyl ketene dimer
AP	Alkaline phosphatase
APTES	3-aminopropyltriethoxysilane
AuNPs	Gold nanoparticles
BCA	Bicinchoninic acid
BeStSel	Beta structure selection
BP	Band pass
BSA	Bovine serum albumin
CAZy	Carbohydrate-Active enZYmes Database
CBM	Carbohydrate-binding module
CBM3	Family-3 CBM from *Clostridium thermocellum*
CBM64	Family-64 CBM from *Spirochaeta thermophila*
CCD	Charge coupled device
CD	Circular dichroism
C-DNA	Complementary target DNA
CipA	Cellulosome-integrating protein A
C-TbDNA	DNA target from *Trypanosoma brucei*
CV	Column volume
DLS	Dynamic light scattering
DNA	Deoxyribonucleic acid
dsDNA	Double stranded DNA
DTT	Dithiothreitol
ELP	Elastin-like-protein
FCS	Fluorescence correlation spectroscopy
FITC	Fluorescein isothiocyanate
GFP	Green fluorescent protein
HAT	Human African Trypanosomiasis
HIV	Human immunodeficiency virus
IgG	Immunoglobulin G
IMAC	Immobilized metal affinity chromatography
IPTG	Isopropyl β-D-1-thiogalactopyranoside
ITC	Isothermal titration calorimetry
LAMP	Loop-mediated isothermal amplification
LB	Luria-Bertani
LP	Long pass
LSPR	Localized surface plasmon resonance
NC-DNA	Non-complementary target DNA
NC-TbDNA	Non-complementary sequences for TbDNA
NIH	National Institutes of Health
NRMSD	Normalized root mean squared deviation
*o*PAD	Origami-based paper analytical devices

PBS	Phosphate buffered saline
PDB	Protein data bank
PDITC	1,4-phenylenediisothiocyanate
PDL	Pulsed diode laser
PDMS	Polydimethylsiloxane
PNIPAM	Poly(N-isopropylacrylamide)
PSIPRED	Position Specific Iterative-blast based secondary structure PREDiction
RGB	Red, Blue, Green
RMSD	Root mean squared deviation
RNA	Ribonucleic acid
RT	Room temperature
SDS	Sodium dodecyl sulfate
SDS-PAGE	Sodium dodecyl sulfate polyacrylamide gel electrophoresis
SEM	Scanning electron microscopy
SRA	Serum resistance-associated
ssDNA	Single stranded DNA
T.b.	*Trypanosoma brucei*
T.b.g.	*Trypanosoma brucei gambiense*
T.b.r.	*Trypanosoma brucei rhodesiense*
TBE	Tris, borate, EDTA
TbgDNA	DNA targets from *Trypanosoma brucei gambiense*
TbrDNA	DNA target *Trypanosoma brucei rhodesiense*
TEM	Transmission electron microscopy
TgsGP	*T.b. gambiense* surface glycoprotein
TST	Tris, saline, Tween
TT	Tris, Tween
UV	Ultraviolet light
µPADs	Microfluidic paper-based analytical devices
2D	Two-dimensional
3D	Three-dimensional
$[\theta]$	Mean molar ellipticity per residue
$\langle \boldsymbol{I} \rangle$	Average intensity
A	Absorbance
A_{R}	Amplitude of the reaction term
A_{SPR}	Absorbance at the surface plasmon resonance peak
b	Monomer size
C	Concentration
C_{t}	End-effect term
D	Diameter
D	Diffusion coefficient
$\bar{D}$	Average diffusion coefficient
D_{B}	Diffusion coefficient of bound species
D_{F}	Diffusion coefficient of free species
D_{h}	Hydrodynamic diameter
$G_{\mathrm{D}}(\tau)$	Correlation function for the diffusion process

$G_R(\tau)$	Correlation function for the reaction process
k	Boltzmann constant
k_-	Dissociation rate constant
k_+	Association rate constant
K_a	Association constant
K_d	Dissociation constant
L	Penetration distance of a liquid
l	Optical path length
L	Total contour length of a molecule
M_W	Molecular weight
N	Number of molecules
n	Stoichiometry
N_A	Avogadro's number
N_b	Number of bound molecules
N_f	Number of free molecules
n_H	Hill coefficient
p	Aspect ratio
θ	Observed ellipticity
Q_b	Brightness of bound species
Q_f	Brightness of free species
R	Gas constant
R	Collision radius
R_h	Hydrodynamic radius
t	Time
T	Temperature
W_B	Width of the barrier
W_C	Width of the hydrophilic channels
W_G	Gap between the edges of the wax-printed lines before melting
W_P	Width of the printed line
z_0	Axial dimension of a 3D Gaussian
γ	Surface tension
$\Delta\mathcal{E}$	Molar differential extinction coefficient
ΔG	Gibbs free energy change
ΔH	Enthalpy
ΔS	Entropy change
η	Viscosity
κ	Geometric factor describing the focal volume shape
λ	Wavelength
ρ_{paper}	Density of paper
τ_b	Diffusion time of bound molecules
τ_D	Diffusion time
τ_f	Diffusion time of free molecules

τ_R	Relaxation time
χ_B	Fraction of bound fluorescent species
χ_F	Fraction of free fluorescent species
ω_0	Radial dimension of a 3D Gaussian
$\boldsymbol{\delta I}$	Intensity variance

Table of Contents

List of Figures

List of Tables

Chapter 1

Introduction

1.1 Diagnostic tests

Diagnostic tests are essential tools for the appropriate prevention and treatment of diseases. These tools allow the identification of the presence and etiology of a disease, the monitoring of the effects of interventions (whether preventive or therapeutic) and the determination of drug resistance.[1] The usefulness of diagnostic tests relates to their ability to detect an individual with disease or exclude an individual without disease.[2] A positive test result can indicate the presence of a target analyte related to an abnormal or undesirable condition, whereas a negative test result indicates the absence of a target analyte, i.e. a normal or desirable condition – or vice versa. Accordingly, the ideal test would return a positive result for all patients with the disease (sensitivity) and a negative result for all disease-free cases (specificity).[2,3]

Molecular diagnostic tests are used to identify a health condition through the analysis of DNA or RNA of an organism. Advances in molecular biology techniques such as in nucleic acids amplification and sequencing have allowed high sensitivity and specificity, therefore empowering molecular diagnostics in clinical laboratories, namely for infectious diseases.[4–6] Molecular diagnostics has been reported to be the fastest growing segment in the *in vitro* diagnostics market, expecting to register a compound annual growth rate of 9.1% between 2017 and 2023.[7,8]

Diagnostic testing is a crucial part of today's medical practice. As a result, diagnostic technologies have become increasingly automated with improved reliability and reduced operator time. Despite these advances, most modern diagnostic technologies require highly trained personnel and centralized laboratory infrastructures with expensive equipment. This limits the access to people living in remote areas or in settings with sub-optimal to virtually inexistent technological infrastructures.[9] In particular, settings with limited laboratory infrastructures and cost constraints offer technical challenges for the development of diagnostic tests, such as the lack of clean water, no electricity for equipment and/or lack of cold storage facilities.[10]

The World Health Organization has recognized this inequality of access to healthcare, and established that an appropriate diagnostic test for resource-limited sites should have a set of characteristics that are abbreviated by the acronym ASSURED: Affordable; Sensitive (few false negatives); Specific (few false positives); User-

friendly (simple to perform with minimal training); Rapid and Robust; Equipment-free; and Deliverable to those who need it.[11] In fact, there are multiple initiatives fostering innovation for the development of more simple and accessible diagnostics, including from non-profit companies (e.g. Diagnostics for All), philanthropic foundations (e.g. Bill and Melinda Gates Foundation) and non-profit organizations (e.g. Foundation for Innovative New Diagnostics).[12–15]

Hence the importance of developing sensitive and specific diagnostic tests that are robust, reliable (the ability of the test to produce consistent results when performed under similar circumstances), affordable and rapid.[3,16] The ultimate goal is to design simple tests that are cheap to produce, simple to perform and able to produce visual readouts with no equipment required.[11]

1.2 Paper-based analytical devices

Cellulose paper or paper-based materials (cardboards, fabrics) are considered bioactive materials when displaying active recognition and/or functional capabilities.[17] Bioactive paper can be explored for the development of applications in a number of fields, such as biosensing, textiles, biomedical materials and smart packaging.[18–21] In the case of paper-based sensors, their development has been aimed at applications in medical diagnostics, food safety and environmental control.[18,22–25]

Paper is one of the most promising materials for producing low-cost and technically simple bioassays because of characteristics like affordability, wide availability, lightness, biodegradability and hydrophilicity of a porous structure that allows for solutions to flow through capillarity. In addition, paper is compatible with several biological and chemical assays and provides a good platform for colorimetric testing because it is usually white and provides strong contrast with a colored substrate.[17,26,27]

Paper-based assays have long been used for testing the presence of biomarkers in a biological fluid, such as for testing glucose in urine.[28] However, it was only in 2007 that patterned paper was introduced as an inexpensive platform that could become the basis for portable and technically simple bioassays.[29] Since then, patterned paper tools, which allows one to create well-defined channels and reaction zones, has been considered a game-changing technology well suited for point-of-care diagnostics in low-resource settings.[30]

Paper structure and properties

Many paper types are composed primarily of cellulose fibers derived from wood. Cellulose is the main structural component of plant cell walls, making it the most abundant natural polymer in the biosphere. This biopolymer is by definition a biocompatible material.[31] Cellulose is a linear polysaccharide homopolymer composed of β(1-4) linked D-glucose residues (see Figure 1-1). It is an organic compound represented by the formula $(C_6H_{10}O_5)_n$ where the chain length depends on

the cellulose source material and on the extraction treatments.[32] The parallel stacking of multiple cellulose chains form fibrils with regions where the cellulose chains are arranged in a highly ordered (crystalline) or disordered (amorphous-like) structure. The crystalline regions are insoluble in most solvents and are less susceptible to chemical reactions than amorphous regions, which readily uptake water.[33] The degree of crystallinity, which depends on the origin of cellulose, is usually ~50%, thus making cellulose swell but not dissolve in water.[17,32]

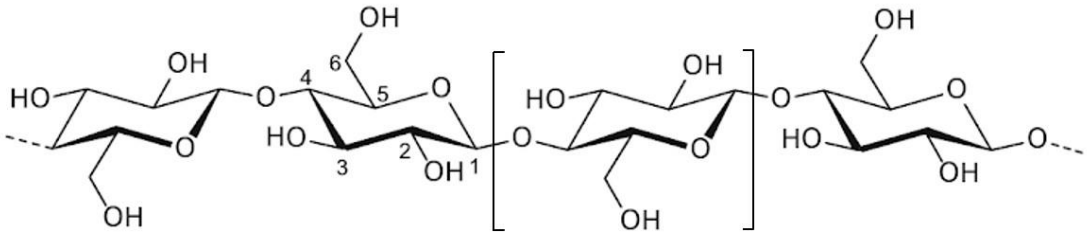

Figure 1-1 The molecular structure of cellulose (adapted from [34]).

Cellulose fibers are typically hollow tubes approximately 1.5 mm long, 20 µm wide, with a wall thickness of ~2 µm. The fibers are mainly arranged as layers in the XY-plane of paper. As a consequence, the spreading of fluids in paper is usually faster laterally than it is vertically.[17,35] The speed of liquid wicking through paper is an important parameter for assay performance, because it not only influences the contact time between target analytes and reagents but also the distribution of reagents deposited in the paper reaction zone. This affects the intensity and homogeneity of the detection signal's development.[36]

Paper is described by its thickness (or caliper, m) and basis weight (g/m^2), *i.e.* the mass of dry paper per unit of area. These macroscopic properties are correlated and are used to determine the bulk density of paper, ρ_{paper}, which is given by:

$$\rho_{paper} = \frac{basis\ weight}{thickness} \quad (1\text{-}1)$$

For example, Whatman grade 1 cellulose chromatography paper, a widely used filter paper for laboratory applications, has a thickness of 180 µm and a basis weight of 87 g/m^2, which translates into a density of ρ_{paper} ~483 kg/m^3. On its turn, the density of the solid component cellulose of wood fiber is ρ_{fiber} ~1540 kg/m^3. Based on these ρ_{paper} and ρ_{fiber} values, the corresponding pore-volume fraction of Whatman grade 1 chromatography paper is ~0.69.[17,36] The porosity of paper, which is related to the spaces between fibers, un-collapsed fiber lumens and the intrinsic porosity of the fiber walls, is a structural characteristic that is determined by the packing of fibers and pigments in the sheet during the papermaking process. This is illustrated in the scanning electron microscope images of chromatographic paper Whatman No. 1 in Figure 1-2, which show the tangle of multiscale fibers and network of pores characteristic of cellulose. Porosity influences some of the paper's final properties like opacity, strength and absorptivity, which in turn influences the capillary flow. Porosity also affects the deposition of reagents on paper.[17,37]

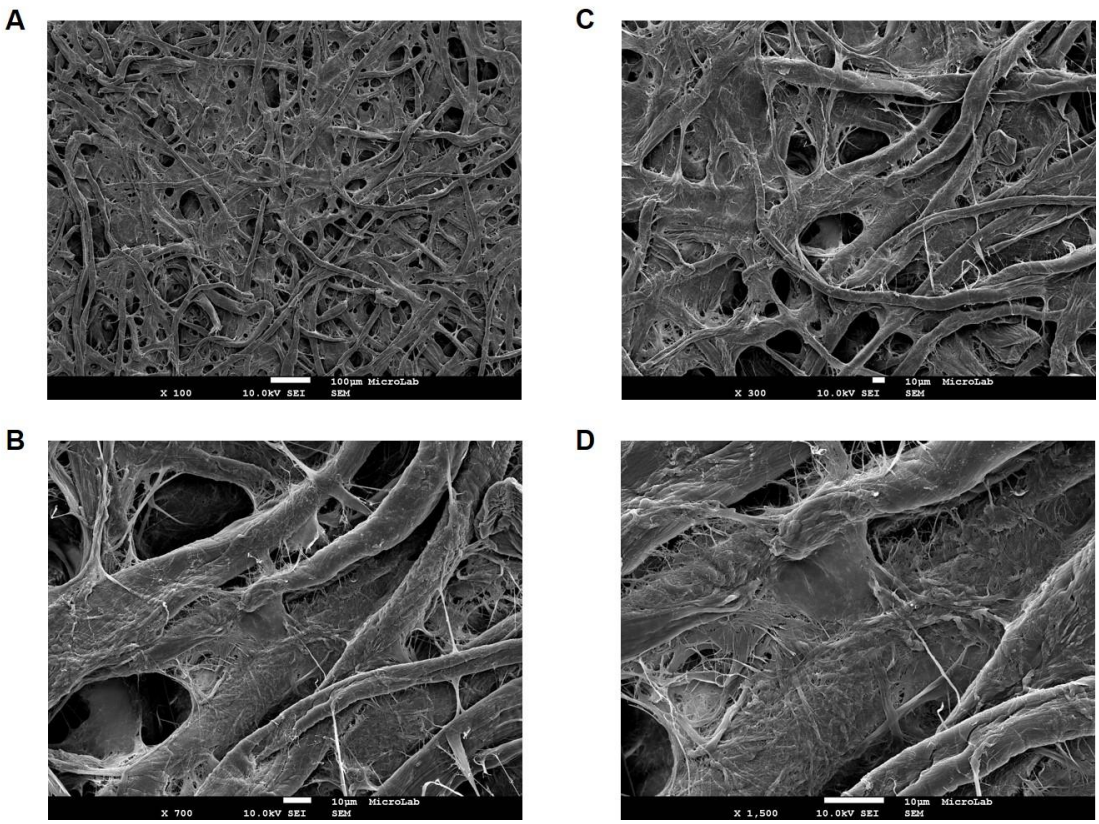

Figure 1-2 Microscopic structure of Whatman No. 1 chromatographic paper at different magnifications: (A) 100x; (B) 300x; (C) 700x; (D) 1500x. The paper sample was covered with a conductive layer of gold-palladium particles and observed on a Hitachi S2400 SEM microscope in low vacuum mode. Scale bars represent 100 µm in (A) and 10 µm in (B), (C) and (D).[38–41]

Paper is an anisotropic material in which mass distribution is usually not constant in the Z dimension (thickness) of a paper sheet. The density is usually maximal at the center and decreases near the surfaces. Another artifact of the papermaking process is fiber orientation, with a slightly preferred orientation along the direction on which the paper was made on the paper machine. As such, the angle at which the paper is cut may influence liquid transport along a strip of paper in a lateral-flow assay.[17,37]

All these paper structure parameters influence the maximum amount of biosensing molecules that can be immobilized on the surface of cellulose. This can be estimated by multiplying the maximum density of the immobilized sensor molecules by the specific surface area of the paper structure accessible to the biosensor. Most polymers and proteins attached to paper display a maximum density ranging between 0.1 and 1 mg/m^2. Paper structures present a wide range of surface area accessible to the biosensor, depending also on the size of the biomolecules (smaller biomolecules will access smaller pores, resulting in a higher surface area accessible to the biomolecules, and vice versa).[17] Hong *et al.* reported that the accessible surface area of Whatman No. 1 filter paper, a conventional paper substrate, is ~9.8 m^2/g of cellulose for a recombinant fusion protein.[42] Accordingly, and assuming a more compact biosensor with a maximum density of 1 mg/m^2, Whatman No. 1 filter paper can take up ~9.8 mg

of biosensor per g of paper (i.e. ~1%).

Bioactive paper

Bioactive paper for analytical bioassays might be functional in several formats. In the direct-contact format, the bioactive paper would report the presence of a specific analyte coming into contact with its cellulose (or modified cellulose) matrix.[17] This spot-test analysis method is carried out by mixing drops of a sample with specific reagents on a piece of paper, cellulose-coated glass slides or cellulose particles.[43–45] Paper-based plates with microwells, which are functionally related to conventional 96- and 384-well plates fabricated in plastic, represent an alternative platform for bioassays. These paper-based plates are compatible with microplate readers, scanners and mobile device cameras for quantitative assays measurements of absorbance, fluorescence or color (RGB intensity).[43,46]

Paper can also be a component of lateral flow tests, in which fluids are introduced onto one end of a paper strip and flow through capillarity to reach reaction zones. Numerous bioanalytical assays employ lateral-flow devices, e.g. over-the-counter pregnancy test kits.[47,48] Lateral flow systems that explore paper and capillary forces provide advantages that are unique to paper and similar porous substrates. One of the advantages is that a form of sample filtration occurs when the liquid flows, with larger particles or microorganisms being trapped on the paper pore network. This allows the separation of particulates (dust, dirt) from a biological fluid that is assayed in the field under non-sterile conditions, thus preventing contaminants from interfering with the assay.[29] As a filter, bioactive paper can also allow the concentration of pathogens, e.g. bacteria are easily trapped in the paper matrix.[17]

Bioactive papers with lateral flow format can additionally serve to expose a sample consecutively to a series of binding sites along the paper surface. Unbound components can then be removed through the application of a washing solution.[17] In this context, paper can be either cut or patterned to define reaction zones or to create channel networks that can transport fluids to different regions of the paper surface without the need for external pumps.[17,29,49]

1.3 Fabrication of paper devices

The first paper-based tests used paper that was manually cut into sections or strips and treated with the relevant reagents for analyte detection. Although these are easy to fabricate, efforts have been made to produce more complex paper devices with enhanced functionality.[50,51]

The patterning of paper makes it possible to create analytical devices with distinct reactions zones connected by networks of microfluidic channels. In lateral flow formats, the patterning process defines the width and length of the microfluidic channels, whereas the height is defined by the thickness of the paper substrate.[26]

Paper devices can be fabricated by using two-dimensional and three-dimensional methods, to direct flow in both horizontal and vertical dimensions depending on the complexity of the biosensor application.[52]

Several strategies have been reported to fabricate paper devices that differ in terms of cost, convenience and resolution.[26] Common strategies rely on either creating barriers within the paper itself or on the selective cutting of paper to create paper devices with multiple formats and functionalities.[50] The fundamental principle underlying many fabrication techniques is to pattern hydrophilic-hydrophobic contrast on a sheet of paper in order to create hydrophilic channels, reaction zones and reservoirs (paper) delimited by hydrophobic barriers. In order for these barriers to be water impermeable, the patterning agent is required to extend across the entire thickness of the paper. It is also important to take into account that the capillary flow of fluids across a paper channel depends on its dimension, the characteristics of the paper substrate and of the environment (temperature, relative humidity).[26,29]

Table 1-1 summarizes the characteristics, advantages and limitations of some of the methods used for patterning paper. To choose the most suitable fabrication technique of paper devices for an intended application, factors such as equipment availability, cost of materials and swiftness and simplicity of the fabrication process should be considered.[53]

Table 1-1 Advantages and limitations of various fabrication techniques of paper devices (adapted from[27,51,52]).

Fabrication technique	Patterning agents	Equipment	Advantages	Limitations
Photolithography[29]	Photoresist	Lithography equipment; hot plate; UV lamp (or sunlight)	High resolution of channels with sharp barriers	Hydrophilic areas exposed to polymers and solvents; vulnerable to bending
Plotting[54]	Polydimethylsiloxane (PDMS)	Desktop plotter	No exposure to polymers or solvents; Inexpensive	Low resolution; requires a customized plotter
Plasma treatment[55]	Alkyl ketene dimer (AKD)	Photomask; vacuum plasma reactor; hot plate	Inexpensive	Hydrophilic areas exposed to polymers and solvents; each pattern requires a customized mask
Flexography printing[56]	Polystyrene	Commercial flexographic printer	Allows direct roll-to-roll production in existing printing houses	Multi-step process that requires frequent cleaning to avoid contamination
Laser treatment[57]	Surface treated hydrophobic papers	CO_2 laser cutting and engraving system	High resolution; inexpensive	Requires extra coating for liquid flow
Paper cutting[58,59]	-	Computer-controlled X-Y knife plotter or a home cutter printer	No exposure to polymers or solvents	Devices must be encased in tape to provide structural support and facilitate

				manipulation
Inkjet printing[60]	AKD	Desktop printer; hot plate	Inexpensive; reagents can also be inkjet into the patterned paper	Requires modified inkjet printers
Inkjet etching[61]	Polystyrene	Desktop printer	Reagents can also be inkjet into the patterned paper	Hydrophilic areas exposed to polymers or solvents; requires modified inkjet printers
Wax screen-printing[62]	Wax	Hot plate; laser printer to create screens	Simple; no exposure to polymers or solvents	Low resolution; requires different screens for different patterns
Wax printing[63,64]	Wax	Printer; Hot plate or oven	Simple; no exposure to polymers or solvents	Low resolution

Photolithography was one of the first successful approaches to pattern paper for bioassays comprising hydrophilic paper bounded by a hydrophobic polymer. Photolithography involves i) impregnation of paper with a photoresist, ii) selective polymerization of the photoresist by exposure to UV light through a transparency mask, and iii) removal of the unexposed photoresist from the paper with organic solvents.[29] Other methods were described that use modified desktop plotters to define patterns of PDMS, or roll-to-roll flexography units to print polystyrene to form liquid guiding boundaries and layers on paper substrates.[54,56] Inkjet printing with a modified equipment also allows the selective hydrophobization of paper using cellulose reactive hydrophobic agents, which are printed onto paper and then polymerized with heat to create hydrophilic-hydrophobic contrast.[60]

Surface treated hydrophobic papers can be patterned via inkjet etching or via plasma oxidation through a metal mask to locally remove the pre-deposited hydrophobic coating.[55,61] Another subtractive approach that can selectively convert hydrophobic areas to hydrophilic ones uses a CO_2 laser to alter the wettability of the paper hydrophobic surface coating; the hydrophilic patterns are then coated with silica microparticles to allow lateral diffusion.[57]

Paper can be precisely cut into patterns of channels and test zones by using a computer-controlled knife or a home cutter printer.[58,59] The patterned paper can then be sealed, thereby allowing ease handling of the paper devices.

Both wax printing and wax screen-printing methods consist of printing patterns of solid wax on the surface of paper and melting the wax so that it penetrates the full thickness of the paper to form complete hydrophobic barriers. In the direct wax printing method, wax channels and test zones are printed on paper either using a wax

pen or printers.[63,64] On its turn, wax screen-printing makes use of a transparency (mask) to create the screen through which the solid wax is rubbed onto the paper.[62]

In the pursuit of simplification, other fabrication techniques were described, including a handheld stamping process and paper patterning using permanent marker inks. The former involves the stamping of the desired pattern on paper: a paraffinized paper, which was previously immersed into liquid paraffin, is placed over plain paper; a preheated metal stamp with the desired pattern is put in contact with the layered paper pieces to allow the thermal transfer of the paraffin from the paraffinized paper to the plain paper.[65] The latter makes use of commercially available Sharpie ink permanent markers to create hydrophobic barriers on paper drawn using an X-Y plotter.[66]

Patterning paper via wax printing

Wax printing was first described by Lin's group. Patterning paper by this method is very convenient, easy and fast. Furthermore, associated costs and toxicity are low and it is easy to dispose of patterned paper devices once they have been used.[27,53,63] The method requires only two steps: the printing of pre-designed patterns of wax on the surface of paper, and the subsequent melting of the wax into paper to form complete hydrophobic barriers.[63,64] The process for patterning paper with wax can either be done using a wax pen to draw the desired pattern on paper, or with a solid wax printer to rapidly form well-defined patterns on paper.[63] The print head of these inkjet printers dispenses a wax-based ink (melted wax) as liquid droplets on the surface of the paper, where they cool and solidify immediately without further spreading.[64] After printing, the printed wax is melted (e.g. in an oven or with a hot plate) so that it penetrates the full thickness of the paper. These wax-printed barriers contain aqueous solutions solely due to the fact that the hydrophilic cellulose fibers are rendered hydrophobic by the wax coating and not to the blocking of pores (Figure 1-3).[63,64]

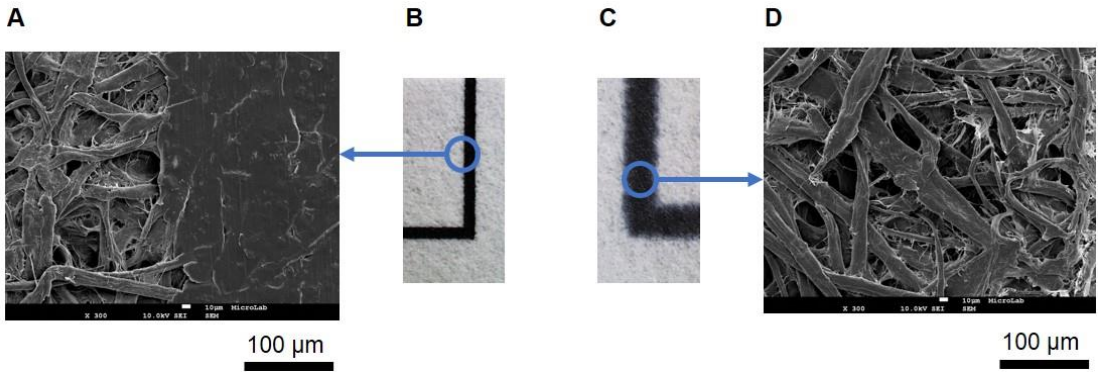

Figure 1-3 Wax-printed hydrophobic barriers designed as black lines on a white paper background, (A,B) before and (C, D) after melting on a hot plate. Scanning electron microscopy images show that the tangle of fibers characteristic of cellulose is kept after the film of (A) printed wax is (D) melted. Adapted from [67].

This method has several advantages that render it promising for the development of low-cost devices for the monitoring of health in low-resource settings. After designing patterns of hydrophobic barriers using drawing software, it takes only a few minutes to pattern a sheet of paper through the printing and heating steps. The

hydrophilic reaction areas are never exposed to polymers that could contaminate them and printing of different colors is possible, a feature that may be useful in some circumstances. The production costs are low and the patterning process is simple and non-toxic, exempting the use of a clean room, UV lamp, mask or any organic solvent.[26,63,64] Furthermore, the same wax-printing method can be alternatively used to control flow rates in paper channels by varying the permeability of paper.[68]

Because paper fibers tend to be more horizontal than vertical, lateral spreading of fluids in paper is generally faster than vertical spreading. This effect results in hydrophobic barriers that are wider on the printed face of the paper sheet. The spreading of molten wax in paper is a process of capillary flow in porous materials described by Washburn's equation:[69]

$$L = \gamma D t / 4\eta^{1/2} \quad (1\text{-}2)$$

where L corresponds to the distance that a liquid of viscosity η and surface tension γ penetrates in porous materials with an average pore diameter D in time t.

Assuming the heating temperature is constant, since the viscosity of the wax is dependent on the temperature, all the other parameters are fixed and the distance of wax penetration into paper from the edge of the printed line will be constant, regardless of the width of the printed line. Therefore, the width of the hydrophobic barrier is related to the width of the printed line by the following equation[64]:

$$W_B = W_P + 2L \quad (1\text{-}3)$$

where W_B represents the width of the barrier, W_P the width of the printed line, and L is the distance that the wax spreads perpendicularly from the edge of the printed line (see Figure 1-4). Carrilho *et al.* studied the spreading of molten wax in Whatman No. 1 chromatography paper in order to calculate the dimensions of a printed pattern required to produce a given paper-based device. They demonstrated that the width of the hydrophobic barrier of molten wax is linearly dependent on the width of the printed line, as predicted by the equation above.[64]

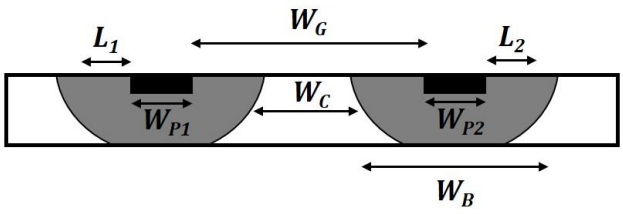

Figure 1-4 Schematic representation of the spreading of molten wax in paper. The black rectangles and the gray area represent the wax before and after the heating step, respectively. W_P – printed width of the line; W_G - gap between the edges of the lines before melting; W_B – thickness of the hydrophobic barrier defined as the middle point between the front and back width values; L – spreading of the wax in relation to the original edge of the line (adapted from [64]).

The width of a hydrophilic channel defined by two parallel hydrophobic barriers can be estimated by:[64]

$$W_C = W_G - 2L \quad (1\text{-}4)$$

where W_C represents the width of the hydrophilic channels and W_G the space (or gap) between the two printed lines, measured on the edges of the lines. In the absence of reference designs, these equations are useful to aid the initial design of wax-printed microchannels. Small changes could then be performed within minutes after testing prototypes for adjustments.[64]

The smallest functional paper-based microfluidic channels fabricated using wax-printing have an average barrier width of 850±50 µm and a hydrophilic channel of 561±45 µm. This lower resolution of microfluidic channels when compared with other methods is the main drawback of the wax printing technique to fabricate paper devices.[27,64]

Nevertheless, given its simplicity and rapidity, wax printing has been used to fabricate paper-based analytical devices in multiple formats for different purposes.[50] For example, wax-printed circles with a simple well-plate design were used for localized paper functionalization with gold nanoparticles or detection of pathogenic bacteria in food.[70,71] In another application, wax-printed microplate paper platforms equivalent to the conventional 384-well microplate were designed with standard microplate dimensions. The resulting "paper microplate", which is compatible with a microplate reader, was then used in multiple assays targeting DNA detection.[46] Microfluidic paper-based analytical devices (µPADs) comprising a single channel where samples flow by capillarity have also been set up to sequentially perform test and control reactions.[72] This simple concept has been extended by using wax-printed µPADs with two or more hydrophilic channels. This design makes it possible to split and direct sample volumes into independent reaction zones, allowing for the simultaneous detection of different analytes ("multiplexing").[63,64] Crooks' group reported the fabrication of three-dimensional origami-based paper analytical devices (*o*PAD) by wax printing and paper folding, which allows the deposition of reagents on different layers of the *o*PAD before DNA detection assays are initiated.[73] Other three-dimensional channel architectures can be fabricated by using wax-printed hemi-channels (or half-closed channels) or fully enclosed-channels, rather than ordinary open channels which extend through the entire thickness of the paper substrate, thus offering additional design flexibility.[74]

1.4 Biosensors immobilization

Paper-based assays designed for the detection of analytes or pathogens must perform some kind of biorecognition function. This biorecognition refers to the ability of the paper device to recognize and capture the target pathogen or analyte (a bio or

chemical marker). For this purpose, the paper surface is functionalized with biorecognition agents (also called biosensors) such as antibodies, bacteriophages, DNA aptamers and enzymes.

The structure and surface chemistry of paper affect the ability to attach biomolecules to the cellulose paper matrix and the maximum quantity of biosensors that can be immobilized.[17,75] For example, the porosity of paper together with its surface chemistry affect its properties when wet, which are important for bioactive paper fabrication by printing of coating.[17] For bioanalytical usage, the structure and surface chemistry of the chosen paper matrix must facilitate biomolecule immobilization and minimize non-specific adsorption.[75] Immobilization strategies to attach biorecognition agents to paper can be classified into physical methods (including direct adsorption and through carrier particles), chemical immobilization and biochemical coupling.[17,32]

Direct physical adsorption relies on the adherence of biosensors onto wet or dry paper surfaces via van der Waals/hydrophobic and electrostatic forces. While this method constitutes the simplest attachment pathway, it is difficult to control and may result in heterogeneous surfaces with biomolecules attached in a randomly oriented manner, which can lead to reduced activity. Furthermore, the physisorbed molecules are weakly bound to paper fibers and tend to slowly leach from the surface, which affects the surface density and consequently the sensitivity of the paper assay.[17,75,76] Huang *et al.* immobilized antibodies on paper via physical adsorption to study the effect of relative humidity and bovine serum albumin (BSA) on the paper-immobilized antibody bioactivity. They verified that antibody stability decreased with increasing relative humidity. On its turn, the pretreatment of paper with BSA increased antibody longevity, regardless of humidity.[77] Costa *et al.* also used the physical adsorption strategy to immobilize glucose oxidase and peroxidase onto paper. They spotted and allowed enzyme solutions to dry on two formats of wax-printed paper devices: 2D lateral flow sensor in which the sample flows from a single inlet into multiple reaction/detection zones; 3D sensor with stacked layers of paper using double-sided adhesive tape with holes, filled with cellulose powder to allow the contact between the adjacent layers. Solutions with increasing concentrations of glucose were tested and color changes were observed corresponding in intensity to the amount of glucose. A high color uniformity was obtained in the reaction zones of the 3D sensor, whereas there was evidence of some color carryover in the reaction zones of the 2D lateral flow sensor.[78]

A variant of the direct adsorption methodology consists in coupling sensing biomolecules to colloidal particles that serve as carriers for biosensor immobilization on paper. These so-called bioactive inks (i.e. carrier particles loaded with biomolecules) can then be printed, coated or even added during the paper-making process in order to penetrate the fiber network.[17,32] For example, Pelton's group used carboxylated poly(N-isopropylacrylamide) (PNIPAM) microgels as carriers for DNA aptamer and antibody immobilization on paper. After coupling streptavidin to the microgels, biotin-terminated DNA aptamers or biotin-terminated antibodies were

coupled to the streptavidin-labeled PNIPAM microgels by affinity interactions. The modified microgels were then dispensed and immobilized on filter paper through spotting and air-drying. The experiments revealed that both the DNA aptamer and antibody retained their recognition capabilities and that the microgels did not come off when the dried paper was successively immersed in buffer or eluted in buffer.[79] Evans *et al.* prepared silica nanoparticles coated with 3-aminopropyltriethoxysilane (APTES) and loaded on paper to facilitate the adsorption of a number of analytical enzymes. With trapped silica nanoparticles within the structure of cellulose, they observed an improved color uniformity and intensity in colorimetric bioassays for the detection of lactate, glucose and glutamate in artificial urine.[80]

In the chemical immobilization approach, (bio)molecules are attached to paper fibers by strong and chemically stable covalent bonds. The surface chemistry of most cellulose substrates is not suitable for the direct functionalization of the hydroxyl groups (see Figure 1-1) with biomolecules in water at low temperature.[17] Because of the lack of surface reactivity, cellulose substrates need to be activated by reaction with small molecules or polymers to introduce the surface functional groups adequate for the bioconjugation reactions required for anchoring biosensors.[17] As an example, Araújo *et al.* activated the cellulose surface of filter paper with an amine-reactive linking agent, 1,4-phenylenediisothiocyanate (PDITC), which allows the subsequent coupling of amine-labeled single stranded DNA (ssDNA)probes. Such functionalized paper bearing ssDNA probe was able to detect target DNA hybridization via capillary transport.[81] Böhm *et al.* developed a method for the covalent attachment of enzymes onto paper fibers with preserved functional activity. Paper is modified by photo-crosslinking with benzophenone-containing copolymers bearing ester groups, and enzymes are subsequently immobilized onto the polymer-modified paper through a transamidation reaction. This method enabled the immobilization of glucose oxidase and peroxidase for glucose sensing.[82]

In biochemical coupling, or bioaffinity attachment, biosensors are bound to the paper substrate through biochemical binding agents. This strategy ensures controlled orientation of the active molecule, which results in enhanced activity, and can be reversible despite the immobilized biomolecule being strongly bound.[32] The usual biochemical coupling approach requires modifications of both biomolecules and substrates with interacting components such as protein/ligand couples.[32] For example, Orelma *et al.* developed a method to immobilize biotinylated antibodies with retained activity on cellulosic substrate. The method is based on the attachment of avidin (a tetrameric biotin-binding protein) to cellulose by physical adsorption or chemical conjugation and on the strong avidin-biotin interaction.[83] Another biochemical coupling method is specific to cellulose, which assumes the role of one of the binding partners. This is the case of carbohydrate-binding modules (CBMs), which are able to selectively and spontaneously adhere to cellulose. CBMs have been used as affinity tags for the targeted immobilization of biosensors onto cellulose by resorting to CBM-biosensor fusions prepared by genetic and protein engineering

approaches.[17,75,84] For example, CBMs have been coupled to bioactive peptides for improved cell adhesion to bacterial cellulose,[85] to antibody-binding proteins for antibody purification on cellulose resins,[86] and to enzymes for enhanced cellulolytic enzyme reactivity or development of colorimetric detection reporters.[87,88] The use of CBMs to bind biomolecules on paper will be analyzed in more detail in the next section.

Irrespective of the chosen method for the immobilization of biorecognition molecules onto cellulose matrices, it is important to retain the original functionality of the biomolecules as far as possible for the biosensor to work. Moreover, the immobilization strategy should be compatible with automated coating and/or printing methods to facilitate potential large-scale applications.[75]

Carbohydrate binding modules

The molecular recognition of carbohydrates by proteins is essential in several biological processes, namely the enzymatic degradation of insoluble polysaccharides by glycoside hydrolases. Since the target glycosidic bonds are often inaccessible to the active site of these carbohydrate-active enzymes, many glycoside hydrolases are modular and contain catalytic modules attached to non-catalytic carbohydrate-binding modules (CBMs). CBMs comprise a contiguous amino acid sequence of ~30-200 residues with a discrete fold having carbohydrate-binding activity. The CBMs' structure enables them to bring the associated catalytic modules into close and prolonged association with their substrates, thus potentiating the enzyme's activity.[89,90]

Structural and functional studies reveal that the topology of CBM ligand-binding sites complements the conformation of the target polysaccharide. As such, CBMs can be classified into three major types based on their different ligand specificities and topology of the binding site: type A ("surface binding"), type B ("glycan chain binding") and type C module ("small sugar binding"). The binding site of type A CBMs comprises a planar hydrophobic platform containing aromatic amino acid residues. The planar architecture of the binding sites is thought to be complementary to the flat surfaces of insoluble crystalline polysaccharides like cellulose or chitin. In type B CBMs, the binding site architecture displays clefts of varying depths and comprises subsites able to accommodate the individual sugar units of the polysaccharide. As in type A CBMs, aromatic residues are important in ligand binding, and the orientation of these amino acids influences their binding specificity. Finally, type C CBMs bind optimally to mono-, di- or tri-saccharides, thus lacking the extended binding site grooves of type B modules. In general, it is more frequent to identify and characterize CBM types A and B due to the limited presence of type C CBMs in plant cell wall active glycoside hydrolases.[84,89]

CBMs can also be classified into families depending on specific characteristics such as the amino acid sequence, binding specificity and structure. Currently, 191823

CBMs have been divided into 86 different families in the Carbohydrate-Active enZYmes Database (CAZy), and 647 modules still remain non-classified.[84,91,92]

Carbohydrate-binding module family 3 (CBM3), in particular, comprises 1632 modules of ~150 amino acid residues, which have been found mostly in bacteria (1625 modules).[92] The family 3 CBMs have been identified in numerous bacterial enzymes and in non-hydrolytic proteins, including the scaffolding protein A from the cellulosome of *Clostridium thermocellum*.[93] This anaerobic and moderately thermophilic bacterium (55-56ºC) exhibits one of the most efficient enzymatic degradation of the recalcitrant substrate crystalline cellulose.[94,95]

C. thermocellum produces extracellular multienzymatic complexes termed cellulosomes, which are firmly bound to the bacterial cell wall, but are also flexible enough to bind strongly to cellulose substrate. The cellulossome comprises catalytic subunits (cellulases and related enzymes subunits) and a multiple-domain polypeptide subunit CipA (cellulosome-integrating protein A), which is responsible for the structural organization of the cellulosome. The non-hydrolytic protein CipA acts both as a scaffolding component and as a cellulose-binding factor. The organization of the catalytic subunits into a multifunctional enzyme complex is considered responsible for the efficient synergy of the cellulosome components in the high-rate cellulose utilization.[93,96]

Protein CipA (~197 kDa molecular weight, 1854 amino acid residues) consists of different domains with specific functions, as illustrated in Figure 1-5. CipA contains nine cohesin domains, which interact with complementary dockerin domains present in enzymatic subunits, in order to integrate the hydrolytic enzymes into the cellulosome complex. In addition, a dockerin domain is also present, which associates the cellulosome to the surface of the bacterial cell envelope. The enzyme complex is anchored to the substrate via a family 3 CBM with affinity to cellulose, which is located between the second and third cohesins. The CBM3 from CipA is flanked by linker regions with sufficient length and flexibility to allow the efficient orientation and operation of the catalytic subunits.[94,97–99]

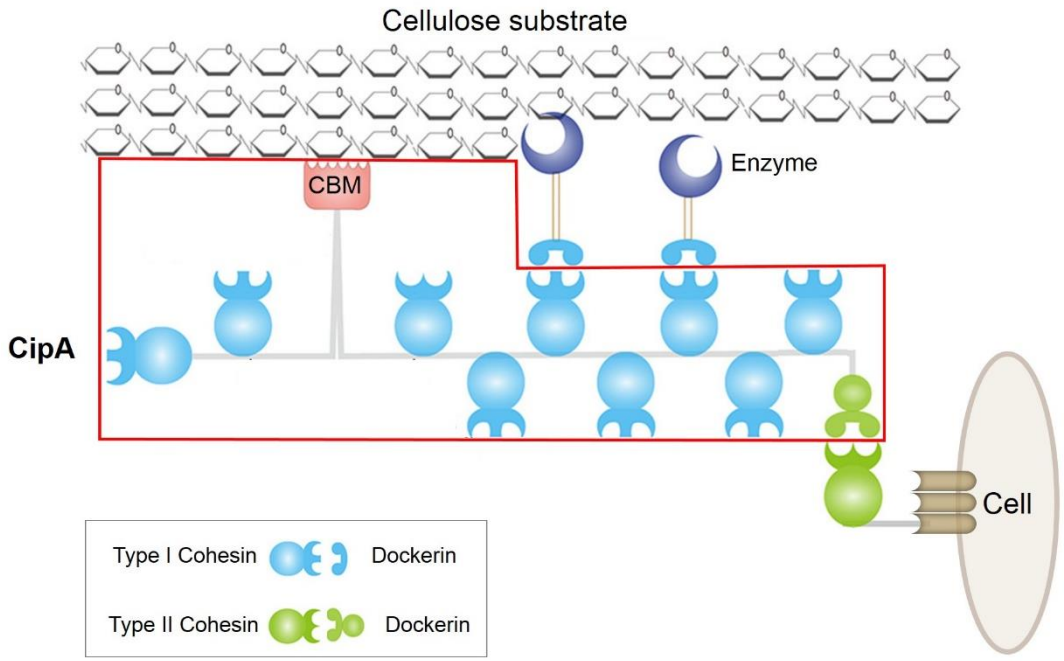

Figure 1-5 Simplified schematic representation of the *C. thermocellum* cellulosome. The scaffoldin protein CipA (bordered in red) comprises nine cohesion, a dockerin and a carbohydrate binding module, which mediates the attachment of the whole complex to cellulose. Adapted from [100,101].

CBM3 is classified as a type A CBM, having a planar surface that interacts firmly with crystalline cellulose. It was reported to have a binding constant of the order of 10^6 M^{-1} (K_d value of 0.4 µM). CBM3 is responsible for the primary recognition and binding of the scaffolding subunit, along with its attached catalytic subunits, to the cellulose substrate.[93,102]

The crystal structure of CBM3 from the *C. thermocellum* CipA was first proposed by Tormo *et al.*.[93] CBM3 displays a nine-stranded jellyroll topology arranged in two antiparallel β sheets with a Ca^{2+} ion to stabilize the folding (see Figure 1-6A). The structure of this module forms a flat planar surface with a series of surface-exposed amino acids, which potentially interact with three successive chains of the crystalline cellulose lattice. It is proposed that the amino acid residues in the planar strip and the anchoring residues play essential roles in cellulose binding. The CBM3 structure thus forms a flat binding surface that complements the flat surface of its cellulose substrate.[93,103]

CBM3 can be combined with other biomolecules using recombinant protein fusion technology. Such CBM-based constructs, specifically composed of modules having affinity for cellulose, can be used as affinity tags for the attachment of biomolecules onto a cellulose matrix.[84] This strategy has been used to characterize CBM3 and to produce fusions with application in different biotechnological areas. For example, Lehtiö *et al.* probed the location of the binding site of CBM3 on crystalline cellulose using a CBM3 fused to a modified staphylococcal protein A (ZZ-domain), which has high affinity to the Fc portion of IgG.[104] These ZZ-CBM fusions were labeled with gold-conjugated antibodies for visualization of binding to cellulose crystals by

transmission electron microscopy (TEM). The authors suggested that CBM3 from *C. thermocellum* CipA preferably binds to the hydrophobic 110 face of cellulose. In order to better understand the enzymatic cellulose hydrolysis mechanism, Hong *et al.* used a fusion protein containing CBM3 and a green fluorescent protein (GFP) to determine the cellulose accessibility to cellulase. They reported a value of ~9.8 m^2/g of cellulose for the accessibility of cellulose filter paper to the recombinant fusion protein.[42]

Other fusion proteins comprising CBM3 have been used to modify cellulose substrates and immobilize biorecognition agents for biosensor applications. For example, Morag's group prepared various non-DNA microarrays on cellulose-coated glass slides, in which CBM3-containing fusion proteins mediate ligand immobilization. The binding determinants fused to the CBM molecule retained their activity after immobilization onto cellulose, such that HIV-related peptides fused to CBM were able to detect HIV-related antibodies and multiple antibodies were exactly anchored to the microarrays spots *via* a ZZ-CBM fusion.[44] A similar approach, based on ZZ-CBM fusion protein for antibody immobilization, was used to prepare μPADs for fluorescent DNA detection. The immobilized antibodies were able to recognize and capture labeled-DNA hybrids on the paper device during the course of capillary migration.[67] This recombinant fusion protein was also employed to functionalize both paper and cellulose microparticles with gold nanoparticles. Biotin-coated gold nanoparticles were bridged *via* ZZ-CBM:anti-biotin antibody complex on the cellulose matrices, yielding a rich red color.[71]

More recently, a structural and functional study of the *Spirochaeta thermophila* CBM64C revealed its versatile capacity to bind both crystalline and soluble carbohydrates under a wide range of extreme physicochemical conditions.[105] The structure of this module exhibits nine β-strands arranged in a β-sandwich jelly-roll fold, and a small helix (see Figure 1-6B). Similarly to other type A CBMs, both β-sheets of CBM64C form a flat, untwisted surface. The flat surface identified in the protein structure constitutes a large carbohydrate interacting platform. It was reported to bind very tightly to regenerated cellulose, with a binding constant of the order of ~1.9×10^6 M^{-1}. The compact structure of CBM64C, increased biochemical stability and tenacious capacity to bind cellulose firmly provide valuable properties for the binding of functional molecules to cellulose matrices.

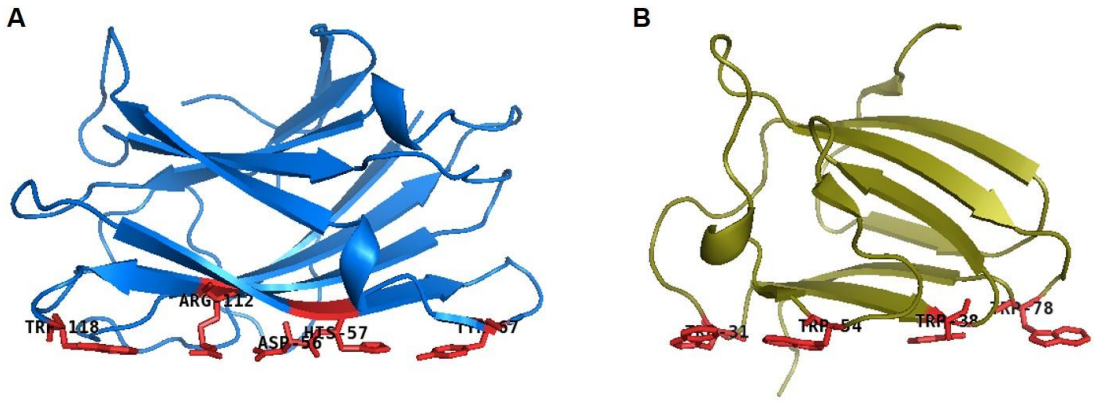

Figure 1-6 Structure of (A) CBM3 from *C. thermocellum* with PDB code 1NBC and (B) CBM64 from *S. thermophila* with PDB code 5LU3. The structure of these modules forms a flat binding surface that complements the topology of the carbohydrate substrate. The proposed cellulose-binding residues are highlighted in red.[93,105] Figure were generated using the PyMOL program (http:// pymol.org).[106]

The possibility of employing recombinant CBM-fusion technology, comprising a module with high affinity to cellulose like CBM3 or CBM64, without interfering significantly with the biological activity of the fusion partner, can be useful for the site-directed immobilization of biomolecules to cellulose for bioactive paper fabrication.

1.5 Reporting mechanisms

The capture of a target analyte or pathogen by a recognition agent immobilized on a paper device must be followed by some type of reporting of the biorecognition event. The reporting function of a paper-based device is based on the production of a signal by the device that is transmitted to the user.[17,29] It serves to inform the occurrence of target capture events and possibly to quantify the amount captured, since the signal intensity is generally proportional to analyte concentration. Several strategies can be adopted to signal the capture of a specific target, such as those based on chemiluminescent, fluorescent, electrochemical or colorimetric readouts.[50,107]

Chemiluminescence reporting is based on the detection of light generated by a chemical reaction, in which one of the formed products is in an excited state and emits light upon decaying to a lower energy state.[107] This reporting strategy has been previously applied to paper devices for uric acid determination, which were based on oxidase reactions coupled with chemiluminescence reactions of a rhodamine derivative with the generated hydrogen peroxide. The concentration of uric acid in the sample was proportional to the chemiluminescence intensity as measured by the detector.[108]

The production of a fluorescence signal is considered to be a very sensitive reporting strategy. However, it requires relatively sophisticated instrumentation to read the fluorescence emission. Furthermore, due to the addition of optical brightening agents in the papermaking process, the interference from background signal of the paper

substrate can pose a challenge in fluorescence detection.[17,50] Despite all this, fluorescence reporting has been used in paper-based sensors and efforts have been made to develop handheld portable fluorescence readers, for example, by integrating a fluorescence imaging device with commercial smartphone technology and a paper-based analytical tool.[109] Ali *et al.* recently reported a wax-printed paper-based sensor for the fluorescence detection of bacteria using a composite ink made of fluorogenic DNAzyme probe. The paper microzones were ink-jet printed with a DNAzyme-loaded ink that is capable of cleaving the fluorogenic substrate to produce a fluorescent signal in the presence of the target. This sensor was capable of detecting increased fluorescence intensity in liquid samples (diluted milk, diluted apple juice and drinking water) spiked with *Escherichia coli*.[110]

Electrochemical sensing generally requires three electrodes (working, reference and counter electrode) and a potentiostat. These electrodes can be screen printed or pen/pencil drawn using carbon ink or silver/silver chloride ink.[107] This reporting strategy, while less prone to variations that are caused by fluctuations in the ambient light or by the auto-fluorescence from paper matrices, still requires the use of a reading equipment. As an example, Whitesides' group developed an electrochemical paper-based analytical device by using a commercially available assay kit to measure β-hydroxybutyrate, a biomarker for diabetic ketoacidosis. The wax-printed paper device was combined with a commercial glucometer as the electrochemical reader.[111]

Colorimetric testing is particularly suitable for paper-based devices because the white background of paper highlights color changes. This reporting strategy has been widely implemented on paper-based sensors due to the possibility of visually assessing some target detection with the naked eye, which is sufficient for a yes/no answer or semi-quantitative detection with the aid of a calibration chart.[26,51] Limitations of colorimetric detection include the non-uniform color distribution across the detection zone and variations in visual perception of the color development/change between different users.[51] To overcome this biased signal reading, commercial scanners or camera-equipped smartphones with intensity-correction software can be used for consistent image acquisition and analysis.[26,50]

Colorimetric detection typically relies on an enzymatic or a chemical color-change reaction. For example, as described previously to illustrate the use of physical adsorption to immobilize molecules on paper, Costa *et al.* performed a colorimetric assay on paper for glucose detection based on enzymatic reactions. Glucose oxidase was applied to decompose glucose into hydrogen peroxide, which is then used by peroxidase for the oxidation of colorimetric indicators (4-aminoantipyrine + 3,5-dichloro-2-hydroxybenzenesulfonic acid, or potassium iodide). The intensity of the resulting color change from colorless to pink/brown was proportional to the initial amount of glucose in the sample.[78] Noble metal nanoparticles, such as silver and gold nanoparticles, have been widely used as colorimetric labels because of their high extinction coefficients and the strongly size-, shape- and distance-dependent optical properties. In addition, their surface is receptive to functionalization with

biomolecules that can bind to specific targets.[51,112,113] Tsai *et al.* developed a method for the molecular diagnosis of tuberculosis by employing gold nanoparticles (AuNPs) and a paper-based platform. The detection strategy was based on color change of AuNPs under different aggregation states upon hybridization between ssDNA probe and target *Mycobacterium tuberculosis* double stranded DNA (dsDNA) sequences. The change in color from red to blue in the presence of increased concentration of target dsDNA was monitored through RGB analysis (blue/red ratio) of smartphone images of the paper testing spots.[114] The optical properties of AuNPs and their use as colorimetric reporters will be explored in more detail in the next section.

Gold nanoparticles

Colloidal AuNPs have been widely employed as reporting agents for colorimetric bioassays due to their optical properties, surface-to volume ratio, stability, ease of synthesis and surface functionalization.[115] Dispersed, small-sized spherical nanoparticles with ~5-50 nm in diameter exhibit an intense red color in aqueous solution, and generally have a size-relative absorption peak at ~520-530 nm.[112,116] Their extinction coefficients are proportional to their size and are significantly higher, by around three orders of magnitude, than those of common organic dye molecules. As a result, colloidal dispersions of AuNPs at nanomolar concentration are colorful enough to be detected by naked eye. In addition, their relatively small size allows the distribution of AuNPs in high density onto reaction zones leading to a more intense colorimetric result.[112,117,118] These properties allow for sensitive detection of target analytes with minimal consumption of materials and without the need for reading equipment for qualitative interpretation.[51]

The intense red color of AuNPs is due to the localized surface plasmon resonance (LSPR) phenomenon, which can be described as the collective oscillation of the conduction electrons of gold atoms due to the resonant excitation by the incident photons (Figure 1-7). This electron oscillation is confined by the particle surface inducing a polarization that for small particles can be accurately described as a dipole oscillation along the direction of the electric field of the light. The frequency at which the oscillation amplitude reaches its maximum is known as the LSPR, and for spherical AuNPs it induces strong absorption and scattering of the incident light in the visible region. The efficiency of light absorption and scattering scales with the particle's volume and squared-volume, respectively. For this reason, light absorption is favored in smaller AuNPs (e.g. with 20-40 nm in diameter), while scattering is more pronounced for larger size particles (e.g. ~80 nm). For such large particle sizes, the LSPR absorption band also shifts to longer wavelength due to the increasing contribution of multipolar modes, yielding a bluish/purple solution.[115,119] The LSPR phenomenon is also influenced by the proximity of other nanoparticles. When AuNPs come into close proximity, reaching interparticle distances smaller than ~2.5 times their individual diameter, or even aggregate, the individual LSPR modes are perturbed by interparticle plasmon coupling, which has been described through a plasmon hybridization model. This phenomenon may result in a color change from red to blue

due to the significant red-shifting of the LSPR frequency and broadening of surface plasmon band. The red-to-blue color shift induced by aggregation events has been explored as an output signal for colorimetric biodetection.[112,115,118,120]

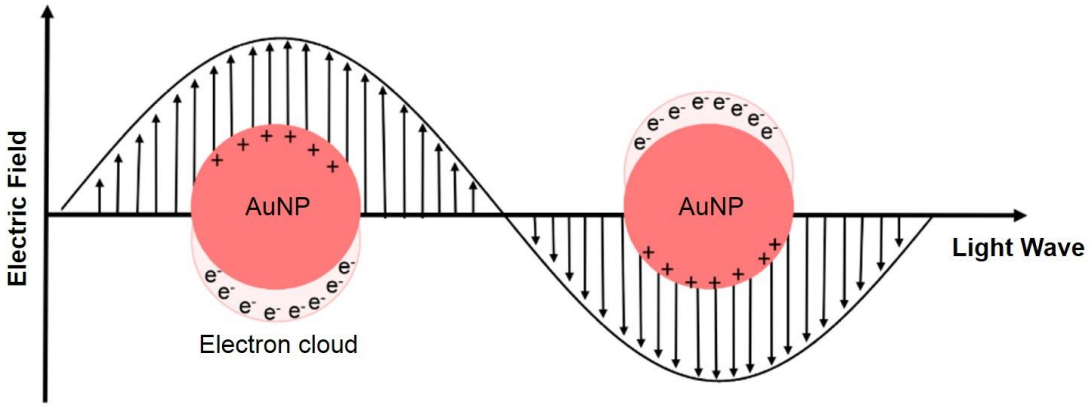

Figure 1-7 Schematic illustration of localized surface plasmon resonance in metal (gold) nanoparticles. The electric field of incident light induces coherent collective oscillation of surface electrons. Adapted from Cordeiro *et al.*. [115]

The surface chemistry of AuNPs has allowed their conjugation with numerous recognition biomolecules such as antibodies and oligonucleotides. The surface functionalization/modification can be based on electrostatic interactions, hydrophobic interactions, specific binding affinity and covalent conjugation.[115,118] For example, Zhao *et al.*[112] prepared a paper-based bioassay using AuNPs functionalized with a thiol-modified DNA or its thiol-labeled complementary sequence, which aggregated upon hybridization (interparticle DNA hybridization). These blue colored DNA-cross-linked AuNPs aggregates were used as colorimetric probes for the detection of an endonuclease (DNase I), which cleaves dsDNA cross-linkers and therefore dissociates AuNPs aggregates to yield a well-dispersed, red-colored nanoparticle suspension. Veigas *et al.*[46] also took advantage of the distance-dependent optical properties of AuNPs to develop a colorimetric bioassay on a wax-printed paper microplate impregnated with a concentration of salt capable of inducing AuNPs' aggregation. The red colored probe was prepared with AuNPs modified with thiol-labeled oligonucleotides specific for the detection of DNA from *M. tuberculosis*. The presence of complementary DNA targets prevents aggregation of the DNA-modified AuNPs, while a visible color change from red to blue occurs in the absence of complementary target. The color change associated with the AuNPs aggregation state was monitored through Red, Blue, Green (RGB) analysis of images captured with a smartphone device.

In the context of developing bioactive paper for bioassays free of specialized reading equipment, functionalized AuNPs would be suitable as colorimetric reporters for diagnostic testing in low tech, remote settings.

Chapter 2

Work plan and Objectives

The general objective of this work is to develop a biomolecular recognition system to be combined with cellulose-based platforms for the colorimetric detection of nucleic acids using gold nanoparticles (AuNPs). Specifically, the study focuses on the implementation of a detection system based on the recognition of a hybrid of a DNA target with a DNA probe by IgG antibodies immobilized on cellulose matrices (e.g. paper, microparticles) through a chimeric protein of ZZ domains fused with a carbohydrate-binding module (CBM) - see Figure 2-1. The CBM part of the fusion protein comprises either a family 3 CBM derived from *Clostridium thermocellum* or a family 64 CBM from *Spirochaeta thermophila*, both with high binding capacity to cellulose substrates.[93,105] The double Z domain is a synthetic derivative of the staphylococcal protein A that is able to capture IgG antibodies *via* their Fc fragment.[121] The ZZ-CBM fusion mediates the anchoring of a mouse monoclonal anti-biotin antibody (isotype IgG2a) onto cellulose. This antibody is subsequently used to capture a biotin-labeled DNA target that is pre-hybridized with a complementary DNA probe immobilized onto AuNPs, giving rise to a red colored signal due to the accumulation of particles at the surface of the modified cellulose.

DNA sequences associated with *Trypanosoma brucei* species, the causative agent of Human African Trypanosomiasis (HAT, or sleeping sickness) will be used as model targets. HAT is a protozoan parasitic infection caused by *T.b. rhodesiense* or *T.b. gambiense*, and it is cyclically transmitted through the bite of infected tsetse flies (*Glossina* genus). This neglected tropical disease is restricted to sub-Saharan Africa with focal distribution, whose transmission occurs mainly in rural areas, located at long distance from the formal health system.[122] HAT is fatal without prompt diagnosis and treatment to prevent parasites from crossing the blood–brain barrier and invading the central nervous system. The treatment of HAT is subspecies- and state-specific, hence the interest in designing DNA tests to identify the infecting subspecies.[123,124] Given this background, three probe sequences will be used in this study for the detection of DNA oligonucleotide targets related to *T. brucei* and its subspecies: one DNA probe that is complementary to a *T. brucei*-specific sequence and two other DNA probes designed for the discrimination of target sequences related to *T.b. gambiense* and *T.b. rhodesiense*, respectively.

In order to fulfill the primary aim of this work and to better understand the working mechanism of the recognition system, the following specific objectives were determined:

- Production and purification of fusion proteins comprising ZZ domains and a CBM3 or CBM64, and assessment of their ability to anchor IgG antibodies onto cellulose using pull-down capture assays;
- Study of the intermolecular interactions involved in the DNA detection system, from the DNA probe hybridization with its labeled target sequence, to the capture of the resultant DNA hybrids by IgG antibodies bound to ZZ-CBM fusions;
- Synthesis and characterization of AuNPs functionalized with distinct DNA sequences for the differential hybridization with DNA targets;
- Implementation of the recognition system in different cellulose-based platforms (paper, microparticles) for the colorimetric detection of DNA hybrids.

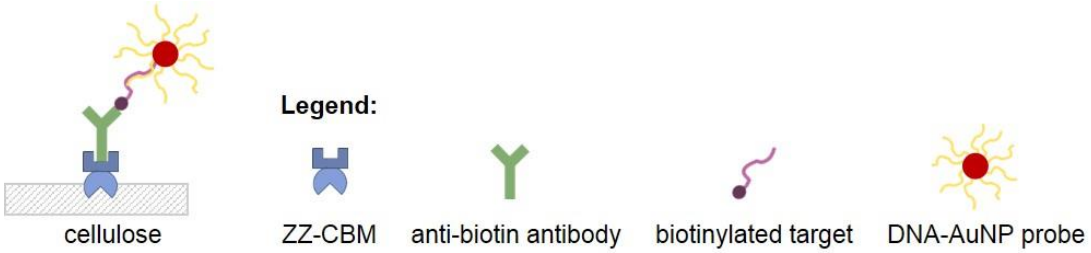

Figure 2-1 Schematic representation of the DNA biomolecular recognition system explored in this thesis. On cellulose (e.g. paper, microparticles), a ZZ-CBM fusion (CBM is depicted in blue and ZZ in dark blue) is used to anchor an anti-biotin antibody to cellulose, which then captures hybrids formed by biotin-labeled targets and AuNPs functionalized with DNA probes.

Chapter 3

Attachment of antibodies onto cellulose using ZZ-CBM fusions

3.1 Introduction

The designation "bioactive paper" comprises a range of cellulose-based paper-like materials with functional capabilities, which can be explored for the development of applications in a range of fields, e.g. biosensing, textiles, biomedical materials, smart packaging.[18–21] The functionalization of paper to enable recognition of a desired target in the context of bioanalytical assays requires its impregnation with recognition agents (biosensors). As these biosensing molecules are expensive, their attachment to cellulose is recommended to prevent leaching when the bioactive paper is exposed to aqueous solutions.[17] Therefore, an important step in creating bioactive paper is to develop a procedure for the immobilization of biomolecules such as antibodies, enzymes, cells, proteins and DNA, on a paper matrix.[75]

The attachment of biomolecules onto cellulose is not the only requirement to develop an effective paper-supported assay. Namely, the control of the location of the biomolecules in the paper structure and their orientation will also influence their availability to capture analytes of interest. In the case of antibodies, a site-directed orientation is essential to maximize complementary binding to antigens through their antigen-binding Fab sites.[76] In this context, an affinity strategy based on CBMs with high affinity to cellulose can be applied for an effective immobilization of antibodies on paper. CBMs are non-catalytic domains involved in the anchorage of polysaccharide-degrading enzymes to their substrates, thus enhancing their activity.[89] Type A CBMs, in particular, display a planar binding site that interacts with the flat surface of crystalline polysaccharides, namely cellulose.[89]

CBMs have been used as affinity tags and then fused with other molecules to mediate the immobilization of antibodies on cellulose.[44,125–127] For example, a family-3 CBM from *Clostridium thermocellum* (CBM3) was already fused to IgG-binding ZZ domains for cellulose-based biosensor applications.[44,67] The Z domain is a synthetic fragment derived from the B domain of the staphylococcal protein A.[121] Its divalent (ZZ) form exhibits higher affinity for the Fc fragment of IgG antibodies when compared to the monovalent form (Z).[128] The fusion of CBM with ZZ is one of the key components of the DNA biomolecular recognition system envisaged in this work (Figure 2-1 of Chapter 2), providing the biomolecular interface between the cellulose

microfibrils of the support and the antibody that will be used to capture pre-formed hybrids of DNA target and DNA probe.

In the first part of this chapter, the ability of the CBM3 from *C. thermocellum* to recognize cellulose is first demonstrated by studying the binding of a fusion of CBM with a green fluorescent protein (GFP) to cellulose microparticles (Figure 3-1A). CBM3 is used as a benchmark CBM, whereas GFP is included as a reporter to expedite the detection of binding. Then, fusions of two type A modules, the family-3 CBM from *C. thermocellum* (CBM3) and a family-64 CBM from *Spirochaeta thermophila* (CBM64), with ZZ domains are designed to enable an effective attachment of antibodies onto cellulose paper. CBM64 is selected as a potential alternative to CBM3, since recent studies describe that it is exceptionally stable and presents a high binding capacity to cellulose.[105] The results shown describe the production, purification and structural characterization by circular dichroism (CD) spectroscopy of the fusions of CBM3 and CBM64 with ZZ domains. The ability of the ZZ-CBM fusions to anchor antibodies onto cellulose in a reversible and site-specific manner is further studied and explored using pull-down assays (Figure 3-1B). Finally, the ability of cellulose-immobilized antibodies *via* ZZ-CBM to capture their specific target molecules is assessed through the exposure of modified paper to an antigen-containing solution (Figure 3-1C).

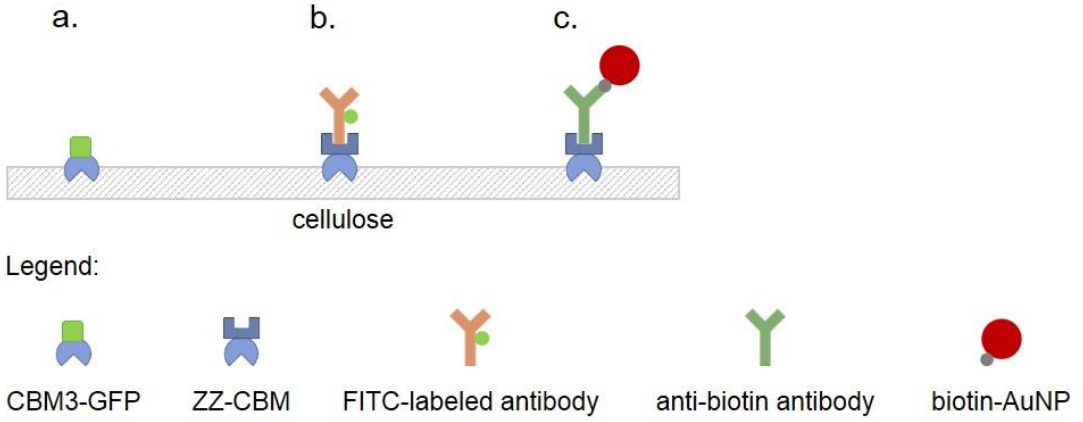

Figure 3-1 Schematic representation of the assays designed to study the CBM-based functionalization of cellulose for the immobilization of antibodies. Experiments were designed to study: (a.) the capacity of CBM3 fused with GFP to bind to cellulose; (b.) the ability of ZZ-CBM fusion to anchor FITC-labeled IgG antibodies and (c.) the ability of anti-biotin antibody immobilized on cellulose *via* ZZ-CBM to capture biotin-coated AuNPs. FITC indicates fluorescein isothiocyanate.

3.2 Experimental

Materials

Purified GFP and CBM3-GFP fusion were provided by NZYTech, Lda.. This fusion was expressed in *Escherichia coli* and contains an N-terminal Green Fluorescence

Protein (GFP), an internal hexa-His tag for purification through immobilized metal affinity chromatography (IMAC), and a C-terminal CBM3 from *C. thermocellum* ATCC 27405 (accession number ABN54273.1).

Sigmacell cellulose type 20 microparticles (S3504) and microcrystalline cellulose powder (product number 435236) were purchased from Sigma-Aldrich (St. Louis, Missouri). Whatman no. 1 chromatography paper (180 μm thick, 25 × 25 cm sheets) was purchased from VWR (catalog number: 3001-878).

FITC-labeled human total IgG was purchased from Sigma-Aldrich (St. Louis, MO). AuNPs conjugated with biotin - InnovaCoat Gold Biotin, 40 nm - were obtained from Innova Biosciences (Cambridge, UK).

Binding efficacy of CBM3-GFP to cellulose

The cellulose binding ability of CBM3-GFP was tested on Sigmacell cellulose type 20 and microcrystalline cellulose powder, following a procedure designed to visualize the fluorescence of GFP. First, 1 mg of the cellulose substrate was suspended in 98 µl of TST buffer (50 mM Tris buffer, pH 7.6, 150 mM NaCl, 0.05% Tween 20). Then, 20 pmol of CBM-GFP (2 µl) was added to the particle suspensions to a final concentration of 0.4 µM. After a 20-minute incubation at room temperature (RT), particles were washed three times with TST buffer with intercalating 2-minute centrifugation steps at 10,000 g. The binding of the CBM3-GFP fusion was analyzed qualitatively by examining the cellulose substrates by fluorescence microscopy. Images were obtained with a CCD color camera (Olympus XC30) mounted on a Leica DMLB fluorescence microscope. The Leica I3 filter cube provided a band pass (BP) excitation of 450-490 nm and a long pass (LP) emission of 515 nm. Control experiments were performed by incubating particles with GFP or buffer alone. Each assay was done in triplicate.

Design, production and purification of ZZ-CBM64, ZZ-CBM3 and CBM3

The bi-modular recombinant fusions ZZ-CBM3 (31.742 kDa) and ZZ-CBM64 (24.025 kDa) were designed with the following features. Each ZZ-CBM fusion protein combines an N-terminal double Z domain derived from the staphylococcal protein A,[121] a 10 amino acid (aa) long linker and a C-terminal CBM – CBM3 from *C. thermocellum* ATCC 27405 (accession number ABN54273.1) or CBM64 from *Spirochaeta thermophila* DSM 6192 (accession number ADN02703.1). A C-terminal modified CBM3 (20.025 kDa) was used as a control. The cloning was outsourced to NZYTech. Briefly, the genes were cloned into the Ndel/Xhol sites of a pET21a expression vector (Novagen). On its turn, the gene encoding CBM3, containing an N-terminal hexa-histidine tag and a C-terminal cysteine residue separated by a 2 aa linker, was cloned into a pET28a expression vector. The resultant pET_ZZCBM3, pET_ZZCBM64 and pET_CBM3-C-28a plasmids were used to transform the *E. coli* DE3 strain BL21 (Novagen). The amino acid sequence of each resulting protein is displayed in Figure 3-2. The molecular weights of constructs indicated above were

calculated with the ExPASy ProtParam tool.[129]

ZZ-CBM64 (N -> C)
2 x 58 + 10 + 84=210 aa

MDNKFNKEQQNAFYEILHLPNLNEEQRNAFIQSLKDDPSQSANLLAEAKKLNDAQAPKV
DNKFNKEQQNAFYEILHLPNLNEEQRNAFIQSLKDDPSQSANLLAEAKKLNDAQAPKV
SSGLVPRGSTGEYTEIALPFSYDGAGEYYWKTDDFSTTTNWGRYVNSWNLDLLEING
TDYANTWVPQHAIPPASDGYWYIHYKGSYPWSHVEMN

ZZ-CBM3 (N -> C)
2 x 58 + 10 + 159 =285 aa

MDNKFNKEQQNAFYEILHLPNLNEEQRNAFIQSLKDDPSQSANLLAEAKKLNDAQAPKV
DNKFNKEQQNAFYEILHLPNLNEEQRNAFIQSLKDDPSQSANLLAEAKKLNDAQAPKV
SSGLVPRGSTPVSGNLKVEFYNSNPSDTTNSINPQFKVTNTGSSAIDLSKLTLRYYYTVD
GQKDQTFWCDHAAIIGSNGSYNGITSNVKGTFVKMSSSTNNADTYLEISFTGGTLEPG
AHVQIQGRFAKNDWSNYTQSNDYSFKSASQFVEWDQVTAYLNGVLVWGKEP

CBM3 (N -> C)
159 + 24 =183 aa

MGSSHHHHHHSSGPQQGLRANTPVSGNLKVEFYNSNPSDTTNSINPQFKVTNTGSSAID
LSKLTLRYYYTVDGQKDQTFWCDHAAIIGSNGSYNGITSNVKGTFVKMSSSTNNADTYL
EISFTGGTLEPGAHVQIQGRFAKNDWSNYTQSNDYSFKSASQFVEWDQVTAYLNGVL
VWGKEPGGC

Figure 3-2 Amino acid sequence of the proteins ZZ-CBM64 (top), ZZ-CBM3 (middle) and CBM3 (bottom). Green – ZZ domain; orange – linker; blue – CBM3 or CBM64; bold – His tag. The underlined amino acids are thought to be involved in the interactions with IgG or cellulose.[93,105,128]

For the production of the ZZ-CBM fusions and CBM3, recombinant *E. coli* cells were grown in Luria-Bertani (LB) medium supplemented with 100 µg/ml ampicillin (30 µg/ml kanamycin for CBM3 protein) at 37 ºC with a shaking rate of 250 rpm. Expression was induced at an OD550 of 0.5 with 1 mM of isopropyl β-D-1-thiogalactopyranoside (IPTG, Fisher Scientific). Cells were harvested 16 h after induction by centrifugation at 1,912 g, 4 ºC, for 10 minutes (Sorvall® RC-6 Plus superspeed centrifuge with SS34 rotor). The supernatant was discarded and the pellet was resuspended in a minimal volume of TST buffer (or 10 mM imidazole, 50 mM NaHEPES, pH7.5, 1 M NaCl, 5 mM $CaCl_2$ buffer solution for CBM3). Cells were then disrupted by sonication (Branson Sonifier 250) for 6 x 30 seconds on ice with 30 seconds intervals between pulses (50% duty cycle, microtip limit 6). The resulting cell solution was centrifuged at 12,000 g, 4 ºC, for 20 minutes in order to separate the supernatant containing the fusion protein from cell debris (Eppendorf centrifuge 5810R).

The two ZZ-CBM fusions were purified by affinity chromatography using a 0.5 cm diameter, 0.73 mL column packed with IgG Sepharose 6 Fast Flow (GE Healthcare)

in an ÄKTA 10 Purifier system. The purification protocol was adapted from the resin manufacturer's instructions and is described elsewhere.[67] For each purification run, the column was equilibrated with 5 column volumes (CV) of TST buffer and then loaded with ~2 mL of the supernatant containing ZZ-CBM3 or ZZ-CBM64 by washing the 2 mL sample loop with 4 mL of TST. Unbound proteins were washed away in a single step using 10 CV of TST. Finally, the bound ZZ-CBM protein was eluted with 0.5 M acetic acid, pH 2.8. The pH of the collected fractions of the purified protein was immediately neutralized with 3.2 M Tris buffer, pH 11. The purified proteins were stored in a -20 ºC freezer before use.

The CBM3 protein was purified through IMAC using a 1 mL His Trapp FF column (GE Healthcare) containing nickel. The column was equilibrated with 5 CV of buffer (10 mM imidazole, 50 mM NaHEPES pH 7.5, 1 M NaCl, 5 mM $CaCl_2$) and ~2 mL of sample was loaded. Unbound proteins were washed away with 15 CV of the equilibration buffer and then with 10 CV of a similar buffer containing 35 mM imidazole. The CBM3 was finally eluted using a buffer containing 300 mM imidazole and stored at -20 ºC until required.

Purity and molecular weight of the eluted proteins was evaluated by sodium dodecyl sulfate polyacrylamide gel electrophoresis (SDS-PAGE). The SDS-PAGE analysis was performed in polyacrylamide gels with 12% T (total concentration of both acrylamide and bis-acrylamide) and 3.3% C (concentration of the crosslinker relative to the total concentration in the resolving gel), and 4% T and 3.3% C in the stacking gel. Samples were denatured prior to loading into the wells of the gel by dilution with 0.1 M dithiothreitol (DTT, Sigma-Aldrich) and 1x Laemmli Sample Buffer (Bio-rad), prepared according to manufacturer's instructions, and incubated at 100 ºC in a water bath for 10 minutes. Gels ran at 90 V submerged in 25 mM Tris-HCl, 192 mM glycine, 0.1% SDS, pH 8.3 buffer solution and were stained with Coomassie Brilliant Blue. A 10-250 kDa protein ladder (Bio-Rad) was used as a molecular mass marker. Images were acquired with a GS-800™ Calibrated Densitometer from Bio-Rad (Hercules, CA, USA).

The concentration of the purified proteins was determined by the Bicinchoninic Acid (BCA) Protein Assay using the Pierce® BCA Protein Assay kit (microplate procedure) following the manufacturer's instructions.

Circular Dichroism

The secondary structure of CBM3, ZZ-CBM3 and ZZ-CBM64 proteins was studied by circular dichroism (CD) spectroscopy. This spectroscopic technique measures the difference in absorbance of right- and left-circularly polarized light by molecules over a range of wavelengths.[130]

Prior to spectral analysis, protein samples were dialyzed against Milli Q water using 12-14 kDa cutoff dialysis membranes (Orange Scientific, Braine-l'Alleud, Belgium) at 4ºC overnight to remove buffer constituents. CBM3, ZZ-CBM3 and ZZ-CBM64

were prepared in Phosphate Buffered Saline (PBS - pH 7.4, 0.01 M phosphate buffer, 0.027 M KCl and 0.137 M NaCl) through the addition of 10x PBS and adjusting the final protein concentration to 10 µM.

Far-ultraviolet (250-200 nm) CD spectra were recorded in an Applied Photophysics π* CD instrument under nitrogen flow at RT. A rectangular Suprasil Quartz cell from Hellma with a 0.1 cm optical path length was used. Instrumental settings were 5-nm bandwidth, 1-nm step size, time constant of 1 second and a scan rate of 20 nm/min. Each sample spectrum was averaged from eight scans and corrected by subtracting the baseline spectrum from the PBS solvent. The corrected ellipticity was converted to mean molar ellipticity per residue at wavelength λ, $[\theta]$, in units of deg cm^2 $dmol^{-1}$, using the following relationship:[131]

$$[\boldsymbol{\theta}] = \frac{\boldsymbol{\theta}}{\boldsymbol{C}\times\boldsymbol{l}\times\boldsymbol{N}} \tag{3-1}$$

where θ is the observed ellipticity at wavelength λ, C is the molar concentration of the protein in the solution, l is the optical path length, and N is the number of amino acid residues in the protein. The mean residue ellipticity is related to the molar differential extinction coefficient, $\Delta\mathcal{E}$, by $[\theta] = 3298 \times \Delta\varepsilon$.[131]

To determine the secondary structure composition of each protein, experimental CD spectra were analyzed using the BeStSel (Beta Structure Selection) software available at http://bestsel.elte.hu/.[132] The PSIPRED protein structure prediction server (bioinf.cs.ucl.ac.uk/psipred/) was used to estimate the secondary structure content based on the amino acid sequence.[133]

Consecutive anchoring of antibodies to cellulose

The ability of ZZ-CBM fusions to attach fluorescein-labeled antibodies to paper was investigated using fluorescence microscopy. In preparation for the docking experiments, small aliquots (40 nl) of 5 µM solutions of ZZ-CBM3, ZZ-CBM64, CBM3 and TST buffer (blank) were applied in triplicate onto a strip of cellulose paper (Whatman #1 chromatography paper) using a manual spotter MicroCaster (Schleicher & Schuell). Once dried, the paper was washed three times with TST buffer (2 minutes each time) to remove unbound molecules, immersed in a 0.01 µM FITC-labeled IgG solution (4 mL) and incubated at RT in the dark for 20 minutes at 300 rpm in a microplate shaker (Heidolph Instruments Titramax 1000). The paper was then washed three times and subsequently analyzed using a Leica DMLB fluorescence microscope with a Leica I3 filter set (BP 450–490 nm, LP 515 nm) coupled to an Olympus XC30 camera.

After this first analysis, paper strips were incubated with 0.5 M acetic acid, pH 2.8 at RT for 20 minutes at 300 rpm to elute bound FITC-IgG. Paper was then washed three times with TST buffer and visualized under the fluorescence microscope. After a second incubation with the FITC-IgG solution (procedure as described above) and subsequent washing (3x 2minutes in TST buffer), the paper strip was analyzed again

by fluorescence microscopy. Finally, a second low pH elution and washing with TST buffer was performed, followed by a fourth analysis under the microscope.

For signal analysis, the images were converted to 8-bit grayscale using the free software ImageJ (NIH, National Institutes of Health).[134] The fluorescent spots were selected individually by using the macro Circle Tool with a fixed radius. The mean grey intensity, which is proportional to the fluorescence intensity of each spot, was then measured and the blank value of unmodified paper was subtracted.

Capture of biotinylated gold nanoparticles by antibodies immobilized on cellulose paper *via* ZZ-CBM fusions

The ability of anti-biotin antibodies attached to paper through ZZ-CBM fusions to capture biotin-coated AuNPs was visually assessed with the naked eye as described next. In preparation for the functionalization of cellulose paper with ZZ-CBM:antibody complexes, mixtures of anti-biotin IgG (5 pmol) with different amounts of ZZ-CBM64 (0-10 pmol) were prepared in triplicate in TST buffer, and incubated at RT for 20 minutes. Each mixture (2 µL total volume) was applied onto their respective application area in the same paper strip (Whatman #1 chromatography paper) by pipetting 0.5 µL at a time and air-drying at RT between applications. The paper was washed three times with TST buffer to remove unbound molecules. The functionalized paper strip was then immersed in a 2 mL-solution of 12 pM biotin-coated, 40 nm AuNPs (biotin-AuNPs) diluted in TST and incubated at RT for 1 hour. After washing three times with TST buffer and drying at RT, the paper strip was scanned using an HP Scanjet 4400c series scanner, with settings set to a medium level of contrast and a dpi of 600. The colored image was converted to grayscale and the mean grey intensity of each spotted area with ZZ-CBM:antibody complexes was measured using ImageJ, as explained previously.

3.3 Results and discussion

Binding capacity of CBM-GFP fusion to cellulose

The ability of a CBM3-GFP fusion to bind to cellulose was qualitatively evaluated by exposing microcrystalline cellulose and Sigmacell cellulose type 20 particles to the fusion protein, followed by visualization by fluorescence microscopy. Figure 3-3 shows that the CBM3-GFP fusion is functional and binds to both substrates, as attested by the visualization of the fluorescence emitted by GFP. When cellulose was exposed to GFP alone, no GFP-related fluorescence was detected. This clearly indicates that the binding of the fusion protein to cellulose substrates was due to the cellulose-binding properties of the CBM3, and not to non-specific adsorption of GFP. A control experiment performed with buffer confirmed also that contribution from the intrinsic fluorescence of paper is negligible. Equivalent results were obtained by Pires *et al.* when testing the carbohydrate-binding efficacy of a set of type A CBMs, including CBM3 and CBM64, by exposing carbohydrate substrates like cellulose to

CBM-GFP fusions.[105]

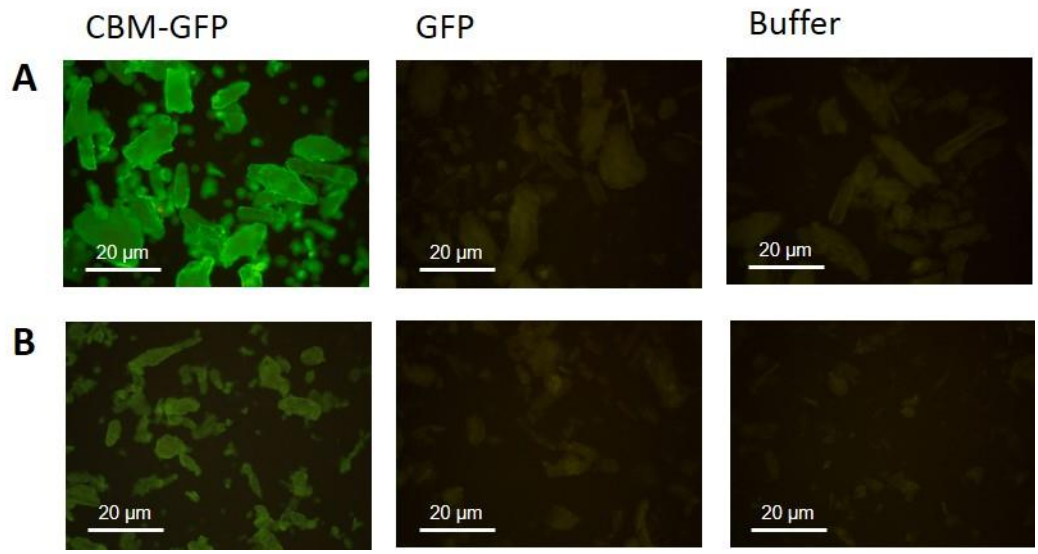

Figure 3-3 Evaluation of the ability of a recombinant CBM3-GFP fusion to bind to (A) microcrystalline cellulose and (B) Sigmacell cellulose type 20. GFP and buffer alone were used as negative controls. Images were taken with an Olympus XC30 camera mounted on a Leica DMLB fluorescence microscope (20x magnification, 2s exposure time).

This result provides an excellent demonstration of the possibility of specifically anchoring molecules of interest to cellulose through CBMs. Such approach enables an effective means of modifying cellulose substrates with biomolecules.

Production of CBM and ZZ-CBM fusions

All fusion proteins produced for this work were expressed in *E. coli*. After extracting proteins through cell disruption by sonication, ZZ-CBM3 and ZZ-CBM64 fusions were purified using an IgG column (Figure 3-4A and B). This purification step explores the high affinity of the fusion proteins towards the Fc portion of the IgG antibodies in the chromatographic matrix through the double-Z domain.[121] CBM3, on the other hand, was purified through IMAC as it possesses a poly-histidine affinity tag (Figure 3-4C).[135] The proteins flow-through/elution profile was monitored by measuring the absorbance at 280 nm at the columns outlet. The corresponding chromatograms, shown in Figure 3-4, are characterized by the presence of two peaks. The first peak is obtained during the flow-through/washing step and contains all unbound species. The second peak corresponds to the elution of ZZ-CBM3 (Figure 3-4A), ZZ-CBM64 (Figure 3-4B) and CBM3 (Figure 3-4C), which is brought about by changing to 100% of elution buffer.

The purity of collected pool fractions was qualitatively assessed through SDS PAGE. The protein gel shown in Figure 3-4D confirms that fusion proteins and CBM3 were effectively expressed and purified (lanes 2-4 relate to ZZ-CBM3, lanes 5-7 to ZZ-CBM64 and lanes 8-10 to CBM3. Lanes 2, 5 and 8 correspond to the cell lysate

supernatants (i.e. feed samples) and exhibit intense bands with molecular weights that correspond to the predicted weight of the fusion proteins, mixed with many other bands of *E. coli* proteins with different molecular weights. Lanes 3, 6 and 9 correspond to the first absorbance peak displayed in the chromatograms and correspond to unbound proteins that were washed away from the columns by the equilibration/washing buffers. Since the fusion proteins have affinity to either IgG or nickel, they remained bound to the columns during the washing step. Therefore, bands corresponding to the proteins of interest are hardly observed in these lanes. Lanes 4, 7 and 10 correspond to fractions containing the eluted fusion proteins and display essentially a single intense band. As expected, the band corresponding to ZZ-CBM3 (~32 kDa, lane 4) is located above the ZZ-CBM64 band (~24 kDa, lane 7). On its turn, CBM3 (~20 kDa, lane 10) migrated faster due to its smaller size and resulted in a band below the other two fusions.

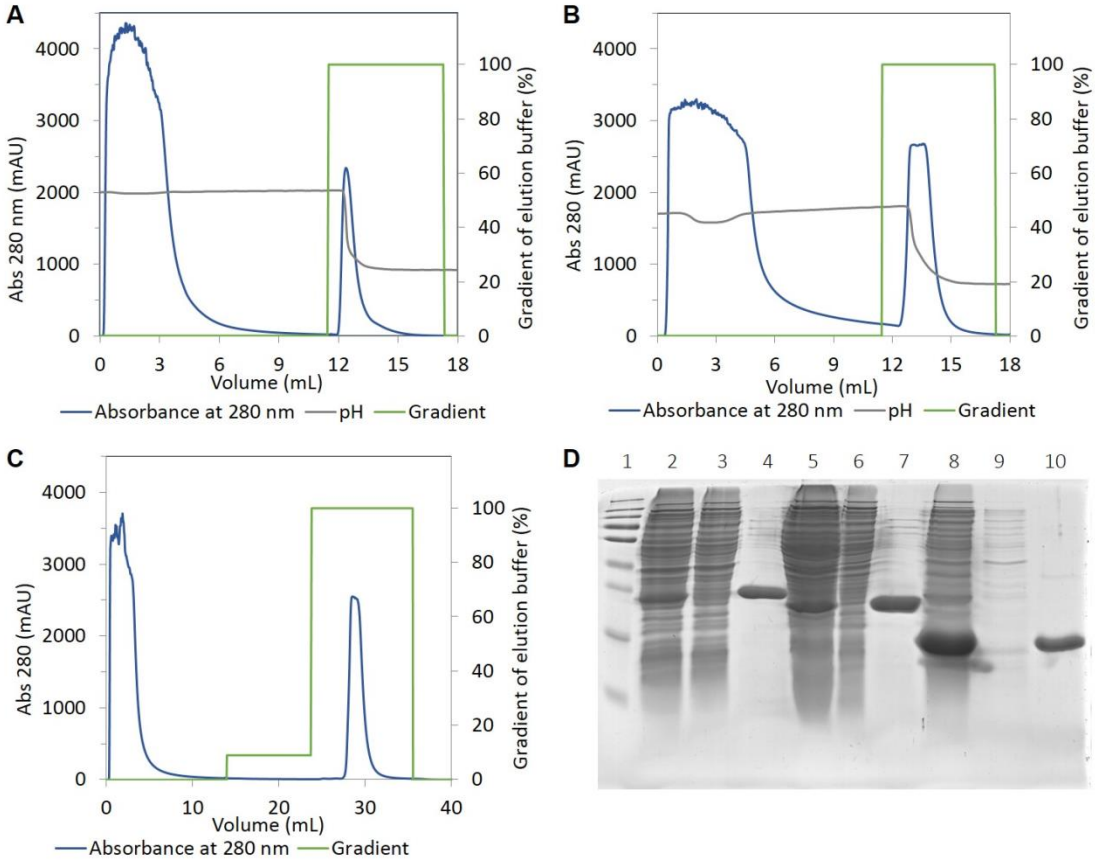

Figure 3-4 Purification of (A) ZZ-CBM3, (B) ZZ-CBM64 and (C) CBM3 by affinity chromatography. (A, B) Clarified *E. coli* lysates containing ZZ-CBM fusions were loaded onto a 0.73 mL IgG Sepharose 6 Fast Flow column equilibrated with 50 mM Tris buffer, pH 7.6, 150 mM NaCl and 0.05% Tween 20 (TST buffer). Unbound proteins were removed with 10 CV of TST buffer. ZZ-CBM fusion protein was eluted using 5 column volumes of 0.5 M acetic acid, pH 2.8. (C) Clarified *E. coli* lysates containing CBM3 were loaded onto a 1 mL HisTrap FF column equilibrated with 10 mM Imidazol, 50 mM NaHEPES pH 7.5, 1 M NaCl, 5 mM $CaCl_2$. Unbound proteins were washed away in two steps: 14 CV of equilibration buffer followed by 10 CV of a similar buffer containing 35 mM imidazole. CBM3 was finally eluted using a buffer containing 300 mM imidazole. (D) Coomassie Blue stained SDS-PAGE gel of the feed samples and the fractions collected during the chromatographic purification. Lanes ID: 1- Precision Plus Protein™ Dual Color Standards molecular weight standards (from top to bottom: 250, 150, 100, 75, 50, 37, 25, 20, 15 kDa); 2-feed sample, 3-flow through, and 4-eluted fractions of ZZ-

CBM3; 5-feed sample, 6-flow through and 7-eluted fractions of ZZ-CBM64; 8-feed sample, 9-flow through and 10-eluted fractions of CBM3.

Structural characterization of the fusion proteins

Information about the structure of the purified proteins was obtained experimentally by performing CD measurements in the far-UV region, where the peptide bond absorption band is included. The content of secondary structures of proteins can be estimated from the CD spectra. For example, α-helical proteins have double minima at 208 and 222 nm and a positive band at 193 nm, whereas all-β-structure proteins have a single negative band at 217-218 nm and a positive band at 195 nm.[131,136] The CD spectra for CBM3, ZZ-CBM3 and ZZ-CBM64 were collected over the range 250-200 nm. Data collection at lower wavelengths was hindered by the high protein concentration used to yield a sufficient CD signal.

The CD spectra of the purified proteins are shown in Figure 3-5. The CD spectrum profile of CBM3, with a single negative band at 218 nm, is indicative of a protein primarily composed of β-strands. The spectrum of ZZ-CBM3 shows the most pronounced negative peak at 218 nm, whereas the spectral profile obtained for ZZ-CBM64 shows two well-defined troughs with minima at 218 nm and near 210 nm. These results suggest the presence of a significant content of α-helices in the structure of both ZZ-CBM fusions.

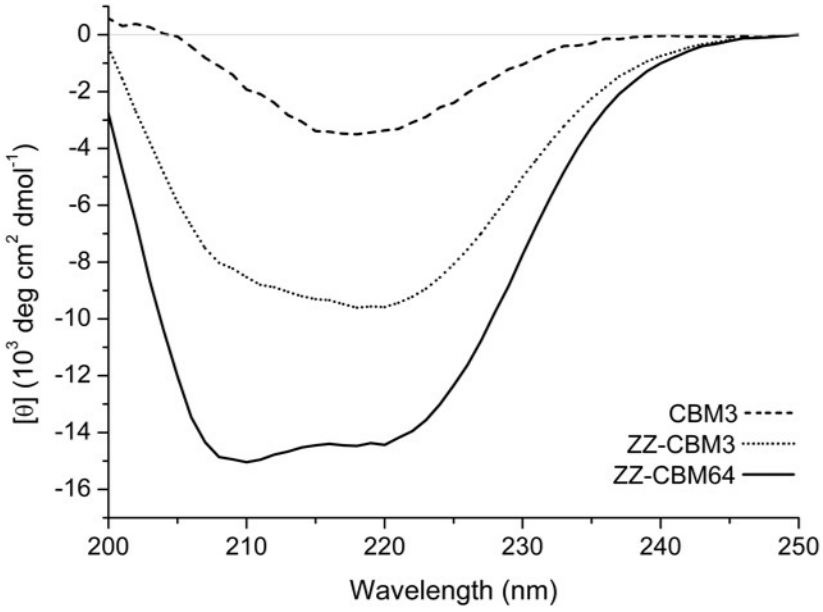

Figure 3-5 Far-UV CD spectra of CBM3 (dashed line), ZZ-CBM3 (dotted line) and ZZ-CBM64 (solid line) in PBS buffer. The vertical axis describes intensity as the mean residue molar ellipticity, *[θ]*.

A quantitative analysis of the CD spectra was performed using the BeStSel server for the determination of the secondary structure content for each protein (Table 3-1). The estimated secondary structure content obtained from BeStSel for CBM3 includes a minimal fraction of α-helices (1.4%), 42.6% β-sheets, and 56% random coils and turns. The predicted secondary structure composition of ZZ-CBM3 is of 16.4% α-

helices and 35.8% β-sheets. As for ZZ-CBM64, results revealed that 31.7% of the content correspond to α-helices, with 25.8% being β-sheets. For all three proteins, the relative secondary structure contents calculated from the CD spectra agree well with the predicted composition based on their respective amino acid sequences (see Figure 3-A1 of the section 3.5 "Appendix: Protein secondary structure prediction based on amino acid sequence").

Table 3-1 Secondary structure content (%) of CBM3, ZZ-CBM3 and ZZ-CBM64. Comparison of the secondary structure contents estimated from CD spectra using the BeStSel server (no shading) and sequence-based prediction by PSIPRED (gray shading).

	CBM3		**ZZ-CBM3**		**ZZ-CBM64**	
Alpha helices	1.4	0	16.4	11.9	31.7	30.5
Beta sheet	42.6	37.7	35.8	27.7	25.8	12.4
Others[a]	56.0	62.3	47.9	60.4	42.4	57.1
RMSD[b]	0.0451		0.0174		0.025	
NRMSD[c]	0.03649		0.00597		0.00548	

[a] Others: turns and random coils

[b] Root mean squared deviation (M^{-1} cm^{-1}), calculated after automatic conversion to $\Delta\varepsilon$ by BeStSel

[c] Normalized root mean squared deviation

All these results are in agreement with the expected secondary structure of these proteins, since the dominant fold among CBMs is the β-sandwich (including CBM families 3 and 64), whereas the staphylococcal Z domain folds into a three-helix bundle (Figure 3-6).[89,105,137] The lower fraction of β-strands predicted for the ZZ-CBM64 fusion, as well as the higher percent of α-helices, is related to the smaller size of CBM64 in comparison to CBM3 (see amino acid sequences in Figure 3-2).

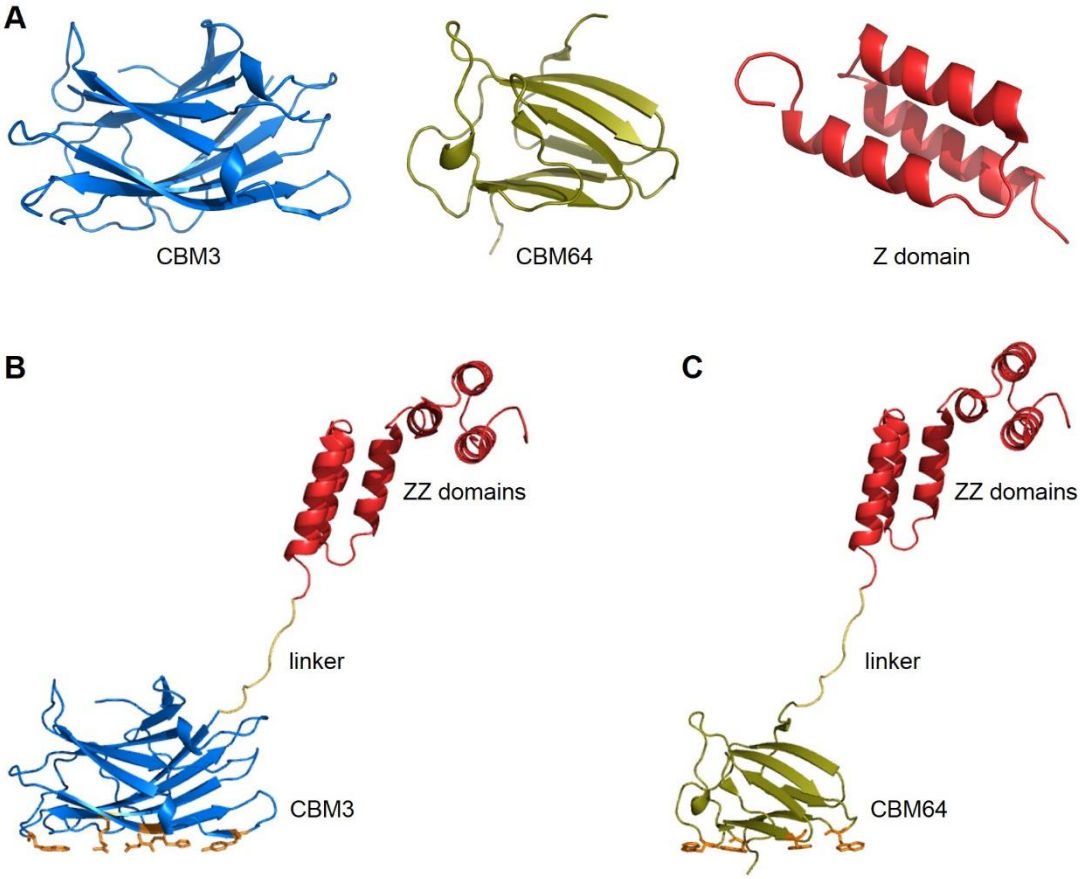

Figure 3-6 Schematic illustration of the ZZ-CBM fusion proteins and their individual components. (A) Structure of the CBM3 from *C. thermocellum* CipA (PDB 1NBC),[93] of the *S. thermophila* CBM64 (PDB 5LU3)[105] and of the Z domain of Staphylococcal protein A (PDB 1Q2N).[137] 3D structural models of (B) ZZ-CBM3 and (C) ZZ-CBM64 fusions. CBMs are linked to the double Z domain through a 10-amino acid peptide sequence (yellow), which is shown as unstructured. The proposed cellulose-binding residues are highlighted in orange.[93,105] Figures were generated using the PyMOL software.[138]

The correct folding of the individual components of the fusion proteins is essential to ensure the CBM- and ZZ-associated bifunctional activity. In this regard, the structural analysis of CBM3, ZZ-CBM3 and ZZ-CBM64 suggests that the purified proteins could be properly folded in solution.

Reversible anchoring of antibodies to cellulose paper *via* ZZ-CBM fusions

The ability of both ZZ-CBM3 and ZZ-CBM64 fusion proteins to attach antibodies to paper was evaluated by exposing paper strips spotted with small amounts (0.2 pmol) of the fusion proteins to a solution of fluorescein-labeled IgG. After washing, the paper strips were analyzed by fluorescence microscopy to look for fluorescein-related fluorescence as an indicator of FITC-IgG anchoring. The photos on column a. of Figure 3-7A show that bright fluorescence spots are observed in the areas where ZZ-CBMs were applied. This result indicates that the ZZ-CBM fusions were able to bind to cellulose through their CBM3 or CBM64 moiety, and that the double-Z domain portion was accessible for interaction with IgG antibodies labelled with FITC. In contrast, no or very low fluorescence intensity was observed in areas where paper was

spotted with CBM3 alone or buffer. The absence of a fluorescent spot in the area where CBM3 was applied indicates that the anchoring of FITC-IgG to paper observed with ZZ-CBM3 and ZZ-CBM64 was specific and due to interaction with the double-Z domain contained in the ZZ-CBM fusions. This attachment of antibodies to cellulose substrates through a ZZ-CBM fusion has been observed previously by Ofir *et al.*, who were able to prepare CBM-based microarrays for protein detection on cellulose-coated glass slides.[44]

In order to investigate if a reversible anchoring of antibodies onto paper could be achieved, a series of consecutive elution-binding-elution experiments were performed (see photos in columns b.-d. of Figure 3-7A) and changes in the spots fluorescence intensity were quantitatively assessed through image analysis (Figure 3-7B). The paper strips modified with ZZ-CBM:FITC-antibody complexes and the control were exposed to a low pH acetic acid solution – pH 2.8 – for antibody elution (Figure 3-7A, column b.). This same solution was used previously to elute the ZZ-CBM fusions from the IgG column during purification and thus is expected to break the ZZ:antibody interaction. The fluorescence intensity at the ZZ-CBM spots was effectively reduced after this exposure to low pH, indicating that FITC-IgG antibodies were detached from the paper, although not completely. Although this decreased fluorescence might be also explained by the fact that FITC fluorescence is affected by pH decrease, we have performed a second incubation of the functionalized paper with FITC-IgG, which resulted in a recovery of the fluorescence signal at the sites where ZZ-CBM fusions had been spotted (Figure 3-7A, column c.).[139] This result indicates that the CBM3 and CBM64-mediated anchoring of fusions onto cellulose is resistant to low pH exposure, and that the ZZ moiety kept its ability to bind IgG. Once more, paper strips were exposed to a low pH solution, resulting in a decrease of fluorescence signal intensity as before (Figure 3-7A, column d.). No significant fluorescence was observed in the areas where CBM3 or buffer had been applied throughout these IgG elution/binding experiments. In a previous study, Eklund *et al.* also observed that a CBM-based fusion with a staphylococcal protein A remained attached to cellulose paper and kept its ability to capture a protein A-binding affibody after being exposed to a low pH solution.[140]

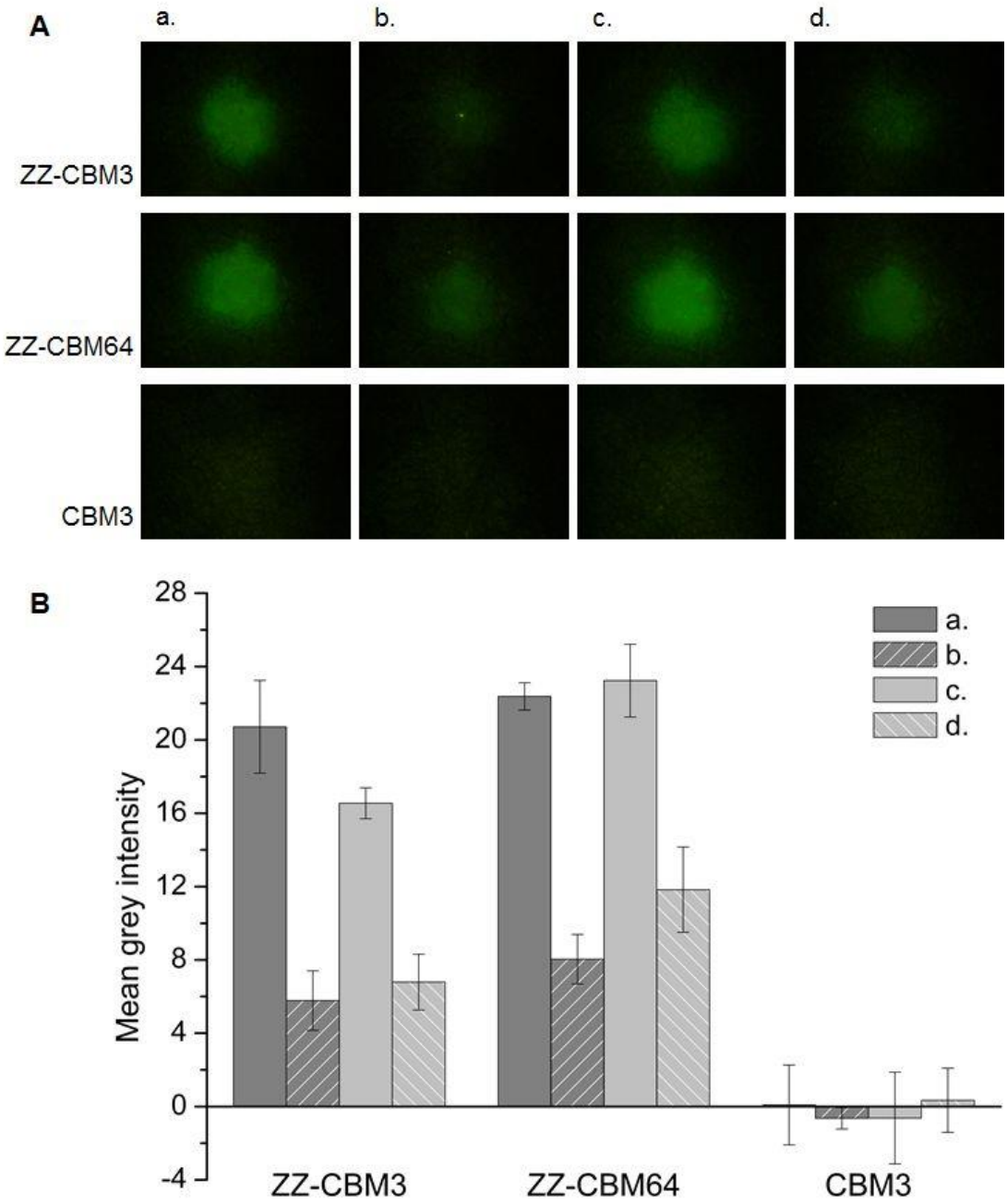

Figure 3-7 Docking of IgG onto cellulose chromatographic paper *via* biochemical coupling using ZZ-CBM fusions. Paper strips were spotted with 40 nl of solutions containing 0.2 pmol of ZZ-CBM3, ZZ-CBM64 and CBM3. After drying, strips were immersed in a solution of 0.01 µM FITC-labeled IgG for 20 min. After washing, the paper strips were inspected by fluorescence microscopy (a.). Paper strips were then incubated in a low pH solution (0.5 M acetic acid, pH 2.8), washed and imaged (b.). Next, the strips were re-immersed into the FITC-IgG solution and washed (c.). Finally, a second low pH elution and washing were performed (d.). CBM3 was used as negative control, whereas TST buffer alone was used as blank. (A) Typical images obtained with an Olympus XC30 camera mounted on a Leica DMLB fluorescence microscope (5x magnification, 1s exposure time). (B) The mean grey intensity of the interior of the spots, for paper modified with ZZ-CBM3, ZZ-CBM64 or CBM3, is shown at each step of the IgG docking assay (a., dark grey bar; b., patterned dark grey bar; c., light grey bar; d., patterned light grey bar). Error bars represent the standard deviation.

These results demonstrate the ability of ZZ-CBM fusions to attach antibodies on paper in a repeated and reversible manner. These properties offer possibilities in changing immobilized antibodies on a cellulose matrix previously functionalized with ZZ-CBM fusions, or in modifying paper through multi-step protocols. Such approach would allow the assembly of a desired multi-molecular complex on paper through bispecific, affinity-driven interactions.

Capture of antigens by antibodies anchored to cellulose paper *via* ZZ-CBM fusions

The ability of antibodies attached to cellulose through ZZ-CBM fusions to capture their target molecules was assessed by exposing a paper strip modified with ZZ-CBM64:anti-biotin IgG complexes to a solution of biotin-AuNPs. The effect of the applied quantity of ZZ-CBM64 fusion on the capture of biotin-AuNPs by the cellulose-immobilized anti-biotin IgG was evaluated by mixing a fixed amount of antibody (5 pmol) with increasing quantities of ZZ-CBM64 fusion (0-10 pmol). After washing, the paper strip was analyzed by observing the appearance of a red color signal on the spotted areas, caused by the accumulation of captured biotin-AuNPs. Figure 3-8A shows intense red color signals in the regions where higher amounts of ZZ-CBM64 were applied. This result indicates that the antibodies retained their ability to bind antigens when attached to paper through the ZZ-CBM64 fusion. The quantitative assessment of the mean color intensity exhibited by each spot further indicates that increased amounts of ZZ-CBM64 in the spots increased the amount of biotin-AuNPs captured by the anti-biotin IgG (Figure 3-8B). Physically adsorbed antibodies, *i.e.* without ZZ-CBM64, were essentially unable to capture biotin-AuNPs, as shown by the absence of color at spots where anti-biotin IgG alone was spotted (Figure 3-8A). Although physical adsorption is the simplest strategy to immobilize antibodies, there is no control of biomolecule orientation, a feature which can affect the recognition of the target. Additionally, since adsorbed antibodies are weakly bound on cellulose paper, they can be displaced by washing.[17,75] In a similar study, Almeida *et al*. also observed a red color signal when biotin-AuNPs were applied directly onto cellulose paper functionalized with a ZZ-CBM3:anti-biotin IgG complex, without a further washing step. Its intensity was significantly lower when the ZZ-CBM3 fusion was absent.[71]

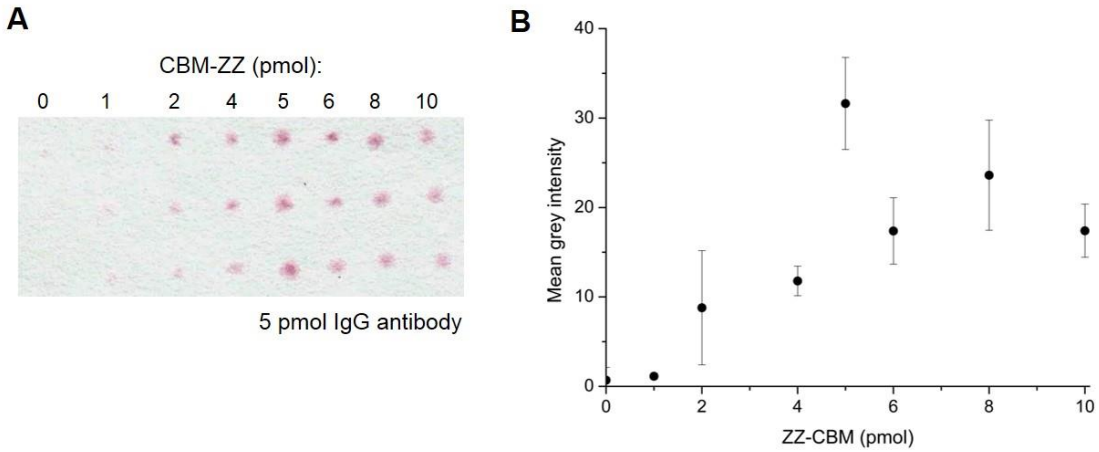

Figure 3-8 Capture of biotin-coated AuNPs by anti-biotin antibodies immobilized on paper via ZZ-CBM64 fusion. A paper strip was spotted with mixtures of 0-10 pmol of ZZ-CBM64 with a fixed amount of anti-biotin IgG (5 pmol), and then immersed into a solution of 12 pM biotin- AuNPs. (A) The capture of biotin-AuNPs by ZZ-CBM:anti-biotin IgG complexes generates red colored spots. (B) The graph shows the mean grey intensity of the spots as a function of increasing ratio of ZZ-CBM (0-10 pmol) to antibody (5 pmol). Error bars represent the standard deviation of the measurements.

This result validates the use of ZZ-CBM fusion as a strategy to immobilize antibodies on cellulose paper with a favorable orientation such that the antigen binding activity is preserved. The superiority of this biochemical coupling strategy over physical adsorption was demonstrated, allowing then the possibility of developing an effective cellulose-based biomolecular recognition system.

3.4 Conclusions

Type A CBMs, such as the CBM3 and CBM64 domains explored in this work, display a planar carbohydrate-binding interface that allows their attachment to the surface of crystalline carbohydrates.[103,105] The binding capacity of family 3 CBM from *C. thermocellum* to cellulose was demonstrated by exposing cellulose microparticles to a CBM3-GFP fusion followed by the visualization of the fluorescence emitted by the CBM-fused GFP.

In pursuing the goal of immobilizing biomolecules onto cellulose paper by taking advantage of the cellulose-binding properties of CBMs, chimeric proteins comprising a staphylococcal double-Z domain fused with CBM3 or CBM64 were designed and successfully produced. Structural characterization of the fusion proteins was performed using CD. Results indicated that both ZZ-CBM3 and ZZ-CBM64 have a similar folding pattern formed by α-helices and β-strands which, most probably, correspond to ZZ domains and CBM proteins, respectively.

Consecutive docking experiments were performed in order to demonstrate the ability of anchoring antibodies to paper through bioconjugation with ZZ-CBM fusions. Fluorescent IgG antibodies were efficiently captured on paper previously functionalized with ZZ-CBM. The fusion proteins remained anchored on paper and retained their IgG-binding properties after repeated washing and incubation at low

pH. These results prove the robustness of using ZZ-CBM fusions for the anchoring of antibodies that can then be used in the recognition of target molecules in cellulose-based platforms. The ability of the biochemically-anchored antibodies to capture target antigens was subsequently evaluated by testing the capture of biotin-coated AuNPs on paper functionalized with ZZ-CBM64:anti-biotin IgG complex. The anti-biotin IgG antibodies remained active after attachment *via* ZZ-CBM64, and an intense red color signal appeared due to the accumulation of captured biotin-AuNPs in the functionalized areas.

Altogether, these results support the functionalization of cellulose using ZZ-CBM fusions for site-directed and oriented immobilization of antibodies. The capability of such bioactive paper to detect AuNP-conjugated antigens offers the possibility of designing more complex, colorimetric biomolecular recognition systems based on a visual readout. Its application in the capture of nucleic acids will be further studied in the next chapters.

3.5 Appendix: Protein secondary structure prediction based on amino acid sequence

PSI (Position Specific Iterative)-blast based secondary structure PREDiction (PSIPRED) is a bioinformatics tool that is used to predict protein secondary structure directly from protein sequences. PSIPRED can correctly predict the fraction of residues in the secondary structure states – helix, strand and coil - with a Q3 accuracy of approximately 80%.[133,141]

The PSIPRED diagrammatic outputs obtained for CBM3, ZZ-CBM3 and ZZ-CBM64 protein sequences are shown in Figure 3-A1. Results indicate that CBM3 contains 37.7% of β-strands and the rest comprising coiled regions. The N-terminal 116 residues of both ZZ-CBM fusions, which correspond to the double Z domain sequence, were predicted to fold mainly into α-helical structures, whereas the rest of the proteins sequences was predicted to be predominantly β-stranded. ZZ-CBM3 is predicted to have 11.9% of α-helices and 27.7% of β-strands. Similarly, ZZ-CBM64 is predicted to contain α-helices (30.5%) and β-strands (12.4%). These estimations are equivalent to the relative proportion of secondary structures calculated for each protein based on the CD measurements (see Table 3-1).

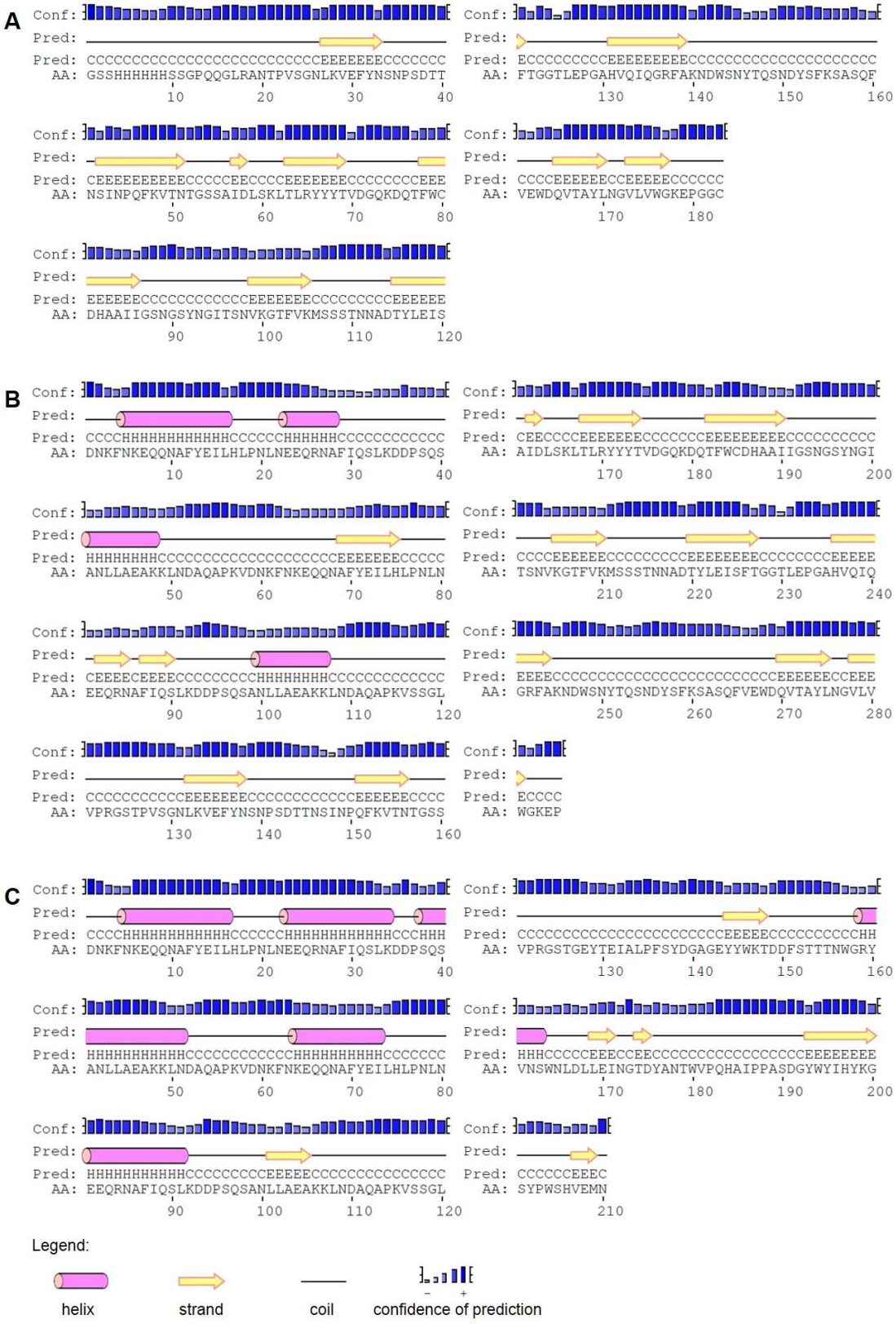

Figure 3-A1 PSIPRED prediction of the secondary structure of (A) CBM3, (B) ZZ-CBM3 and (C) ZZ-CBM64. Alpha helices are marked as pink cylinders or "H", beta strands as yellow arrows or "E", and random coils as black lines or "C". The confidence level of the predicted secondary structure for each residue is provided by the histograms above the cartoon schematics, with higher blue bars indicating a higher confidence prediction.

Chapter 4

Study of intermolecular interactions in the DNA recognition system*

4.1 Introduction

The field of molecular diagnostics uses specific and sensitive techniques to detect DNA or RNA sequences, which may then be associated with a particular disease. The development of DNA sensing systems for an accurate detection and monitoring of infectious diseases, for example, is mainly based on the ability to decode the genetic sequences of pathogens (e.g. bacteria, fungi, viruses, or parasites).[142] Numerous strategies and applications have been developed that are based on the hybridization between a DNA or RNA target and its complementary probe. The targets and probes are often labeled with marker molecules to signal the occurrence of hybridization. For example, a DNA target in a sample can be labeled with biotin during amplification with biotinylated primers so that, after hybridization with the complementary probe, the hybrid can be detected in a subsequent streptavidin-based step. Oligonucleotide probes labeled with fluorescent dyes are also often used for single or multiplexed detection of label-free DNA.[143–146]

In recent years, research efforts have been invested in the development of paper-based devices as alternative tools for bio-sensing. The attractiveness of using cellulose paper as the substrate material is related to its low price, easy disposability, high surface area, and compatibility with bio and chemical applications.[29,32,53] Along with the capacity of transporting fluids by capillarity (*i.e.* without external power sources), paper offers properties with great potential to be used as an effective and affordable platform for bioassays. This is of utmost importance in remote or resource-limited settings, where access to medical laboratory technology can be scarce. For bio-analytical applications, the deposition of suitable bio-recognition agents on paper surface is often required.[17] In this context, carbohydrate-binding modules (CBMs) that exhibit high affinity to cellulose constitute an effective means for the targeted immobilization of biomolecules on paper. CBMs are non-catalytic domains that are involved in the targeting and binding of polysaccharide-degrading enzymes onto their substrates.[89] Genetic engineering approaches have been employed to construct CBM fusion proteins comprising the sequence of the biologically active molecules to be

* The content of this chapter was partially published in the Physical Chemistry Chemical Physics journal. See DOI: 10.1039/C7CP00662D.

attached to cellulose, such as proteins, antibodies, or bacteriophages.[44,126,127,140,147]

Similarly to the recognition system explored in this thesis (see Figure 2-1 of Chapter 2), a paper-based system to detect DNA sequences that uses a three-component biomolecular recognition approach based on CBMs was recently reported (Figure 4-1A).[67] The first recognition element is the fusion protein that combines a family 3 CBM derived from the cellulosomal scaffolding protein A from *Clostridium thermocellum* with a double Z domain (ZZ), which is a variant of the B domain of the staphyloccocal protein A (Figure 4-1A). As demonstrated previously through the binding of CBM3-GFP to cellulose microparticles (see Figure 3-3 of Chapter 3), the CBM part of the fusion binds specifically to crystalline cellulose fibrils.[93,103] On its turn, the ZZ domain is able to capture IgG antibodies *via* their Fc region (see Figure 3-7 of Chapter 3).[121] The second recognition element is a mouse monoclonal anti-biotin antibody (isotype IgG2a), which is anchored onto paper *via* the ZZ-CBM fusion while keeping a favorable orientation to capture its target, as demonstrated previously (Figure 3-8 of Chapter 3). This antibody is subsequently used to capture biotinylated oligonucleotides that were pre-hybridized with the third recognition element, a complementary fluorescein-labeled DNA probe, giving rise to a fluorescent signal in the test area of the paper-device (Figure 4-1A).[67]

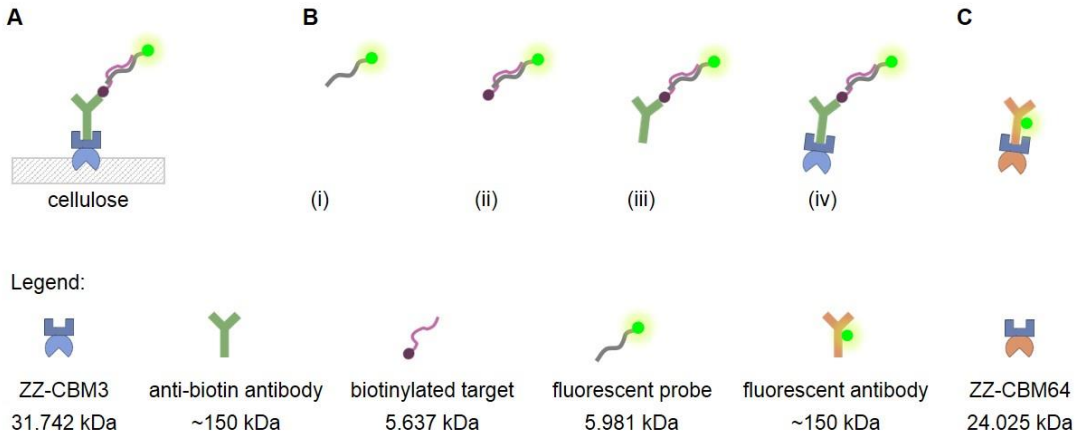

Figure 4-1 Schematic representation of the three-component, DNA biomolecular recognition system studied. (A) On paper, a ZZ-CBM fusion is used to anchor an anti-biotin antibody to cellulose, which then captures hybrids formed by biotin-labeled targets and fluorescent DNA probes. (B) FCS of a fluorescent DNA probe (i) was used to assess the hybridization with the complementary biotin-labeled target (ii), the complexation between the resulting hybrid and an anti-biotin antibody (iii) and the binding of the latter complex to a ZZ-CBM3 fusion (iv). (C) ITC was used to study the capture of fluorescein-labeled IgG antibody by the ZZ-CBM64 fusion. The molecular components are schematically depicted in blue (ZZ-CBM3), green (anti-biotin antibody), grey-green (fluorescent DNA probes), purple (biotinylated target), orange-green (fluorescein-labeled antibody) and orange-blue (ZZ-CBM64).

The development of molecular diagnostic strategies like the one described above can benefit substantially from the availability of basic information regarding the interactions and binding between the different biomolecular components involved. For example, information about the molecular association between DNA hybrids,

antibodies, and/or ZZ-CBM fusions in solution can be obtained from fluorescence correlation spectroscopy (FCS). This technique measures the fluctuations of fluorescence intensity over time from a small number of fluorescent molecules (probe) in the detection volume of an optical microscope (Figure 4-2).[148,149] When the intensity fluctuations are due to Brownian diffusion of fluorescent molecules into and out of the detection volume, a statistical analysis, *e.g.* by means of their time correlation, can yield information about the diffusion of the probed species. Typically, the hydrodynamic radii of free and bound probe are significantly different, thus resulting in a large change of diffusion coefficient, which allows one to follow the binding of the studied molecules by FCS measurements.[150,151] Other processes leading to fluctuations in fluorescence intensity upon binding, *e.g.* emission quenching or enhancement, can also be used to characterize complexation between biomolecules by the FCS technique. Examples include the study of hybridization of oligonucleotides,[152–154] DNA-protein,[155,156] or protein-protein interactions.[157,158]

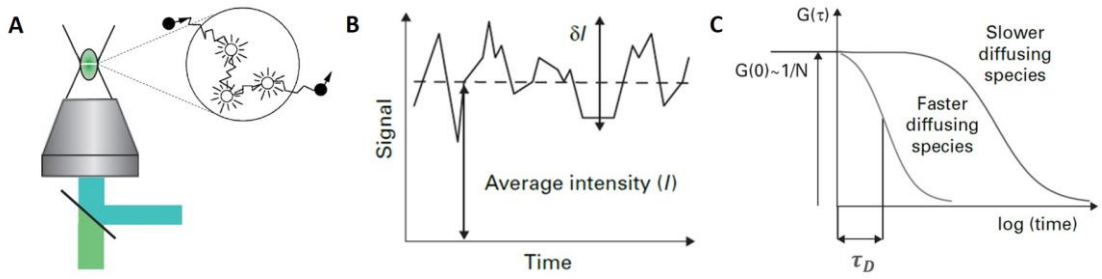

Figure 4-2 Schematic illustration of Fluorescence Correlation Spectroscopy. (A) Fluorescent molecules diffuse in and out of the detection volume. (B) The temporal fluctuation of the fluorescence intensity is detected and recorded, showing fluorescence bursts of average intensity $\langle \boldsymbol{I} \rangle$ and with variance $\boldsymbol{\delta I}$. (C) The autocorrelation analysis characterizes the fluctuations of the fluorescence intensity. Adapted from references [148,159].

Isothermal titration calorimetry (ITC) is another useful technique for studying the formation of biomolecular complexes in solution, *e.g.* for the characterization of protein-protein interactions.[160–162] ITC is used to determine thermodynamic parameters through the measurement of the heat absorbed or released upon a molecular interaction. This technique works by titrating one reactant into a solution containing the other reactant at constant temperature (Figure 4-3). A series of injections are performed and the heat changes in the sample cell are measured with respect to a reference cell, which are expressed as the electrical power required to maintain their temperature difference close to zero. As the molecules in the cell become saturated with the addition of ligand, then less binding occurs and the heat changes decrease until only the heat of dilution is observed. Fitting of the isotherm yields the thermodynamic binding parameters (association constant K_a, stoichiometry n and enthalpy ΔH).[162,163]

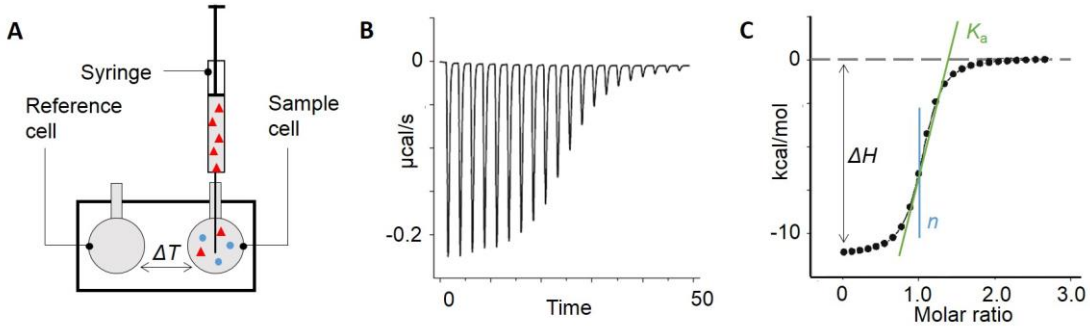

Figure 4-3 Schematic illustration of Isothermal Titration Calorimetry (ITC). (A) The ligand solution (red triangles) is injected repeatedly into the sample cell, triggering the binding reaction with the target molecule (blue circles). The heat of interaction is measured through the changes in the power needed to maintain isothermal conditions between the reference and the sample cells. (B) ITC titration data describing the binding reaction through the differential power signal recorded in the experiment. As the molecule from the sample cell becomes saturated with the ligand, less binding occurs and the heat change decreases. (C) After integration of the area under each peak and normalization per mol of injected ligand, the individual heats are plotted against the molar ratio. The graph illustrates an integrated curve with experimental points (●) and the best fit (–), from which it is possible to estimate the thermodynamic parameters *n*, K_a and ΔH. Adapted from references [161,162].

In the work described in this chapter, FCS was used to study the complexation of oligonucleotides, antibodies, and ZZ-CBM3 fusion in aqueous solutions, which constitutes the basis of the paper test described.[67] Specifically, a 17mer fluorescence-labeled DNA probe (Figure 4-1B-i) was used to assess the hybridization with complementary or non-complementary biotin-labeled DNA of similar size (Figure 4-1B-ii), the complexation between the resulting hybrid and a monoclonal anti-biotin antibody (Figure 4-1B-iii) and the binding of the latter complex to a ZZ-CBM3 fusion (Figure 4-1B-iv). These FCS measurements provided information about the diffusion coefficients of free and complexed species and the fraction of bound species as a function of the concentration of target molecules. The hydrodynamic radii of the set of studied species also afforded estimates of the size of the complexes. In the second part of this chapter, ITC was used to determine the thermodynamic binding parameters of ZZ-CBM fusion with IgG antibody, as a means to complement the FCS data obtained for the ZZ-CBM:antibody complexation. For this purpose, a fluorescently labeled IgG antibody and ZZ-CBM64, a potential alternative to CBM3 with high binding capacity to cellulose, were explored (Figure 4-1C).[105]

4.2 Experimental

Materials

The sequences of oligonucleotides used in this study were as follows: Atto647N -labeled DNA probe (Atto647N-5′ - TTGTGTTTACGCACTTG-3′); complementary DNA target labeled with biotin (biotin-5′ - CAAGTGCGTAAACACAA-3′); non-complementary DNA target labeled with

biotin (biotin-5′ - TCCAGGGAAATGTCACGTCC-3′). The 17mer DNA probe was designed by Deborggraeve *et al.* for the detection of a *Trypanosoma brucei*-specific sequence situated within the 18S rRNA gene.[164] All oligonucleotides were purchased from STABVIDA (Portugal).

Mouse monoclonal anti-biotin (IgG2a) was purchased from Abcam, UK (ab36406) and used in the FCS study. For the ITC analysis, fluorescein isothiocyanate-conjugated rabbit anti-mouse IgG purchased from Sigma-Aldrich (F9137) was used. Atto655-COOH was supplied by Atto-Tec GmbH. All current use chemicals were purchased from Fisher Scientific, except for Tween 20 (VWR), RBS 50 (Fluka), Phosphate Buffered Saline (PBS - pH 7.4, 0.01 M Phosphate buffer, 0.027 M KCl and 0.137 M NaCl for 200 mL) tablets, and ampicillin (Sigma-Aldrich). Ultrapure water was obtained with a Milli-Q purification system (Merck-Millipore).

Microscope cover glasses of Ø 22 mm were supplied by Menzel-Gläser (Gerhard Menzel GmbH).

Construction, production, and purification of ZZ-CBM

The FCS experiments were performed with ZZ-CBM3, while the ZZ-CBM64 was tested in the ITC. ZZ-CBM fusions were prepared as described previously (see Chapter 3).[67] Briefly, the fusion proteins were constructed in a pET21a expression vector (Novagen) by inserting the following sequential coding parts (NZYTech, Portugal): two synthetic IgG-binding domains (ZZ) derived from the staphylococcal protein A[121]; a 10 amino acid long spacer (SSGLVPRGST); and the family 3a carbohydrate-binding module from *Clostridium thermocellum* or the family 64 CBM from *Spirochaeta thermophila*.[93,103,105] Each resultant plasmid with the ZZ-CBM sequence was transformed into *Escherichia coli* DE3 strain BL21 (Novagen) and grown in LB culture medium supplemented with ampicillin. Sixteen hours after induction with isopropyl β-D-1-thiogalactopyranoside (IPTG) for protein expression, cells were harvested by centrifugation, and disrupted by sonication. A second centrifugation step was performed to separate the supernatant containing the fusion protein from cell debris. ZZ-CBM was then purified by affinity chromatography on an IgG Sepharose 6 Fast Flow column (GE Healthcare) that was previously equilibrated with Tris-Saline-Tween buffer (pH 7.6, 50 mM Tris, 150 mM NaCl, and 0.05 % v/v Tween 20); the protein was eluted in 0.5 M acetic acid, pH 2.8, and immediately neutralized with 3.2 M Tris buffer, pH 11. The ZZ-CBM purity was assessed by an SDS-PAGE gel, and the total protein was quantified by the bicinchoninic acid method (Pierce BCA Protein Assay Kit, Thermo Scientific). The purified ZZ-CBM was stored at -20 ºC until further use.

Sample preparation

Separate aqueous solutions in PBS for each target concentration were freshly prepared for FCS measurements from working stock solutions at room temperature. After a single incubation step of 20 minutes minimum, the samples were then measured by

deposition of small drops (2.5 μL) over glass coverslips. Coverslips were extensively cleaned prior to use by sonication in RBS 50 detergent (5% v/v) and absolute ethanol. The coverslips were rinsed with ultrapure water between steps and at the end. After drying, the coverslips were exposed to UV/Ozone (PSD-UV3 Digital UV Ozone System, Novascan) for 2 hours.

Fluorescence Correlation Spectroscopy

The FCS measurements were performed with a Microtime 200 setup from PicoQuant GmbH (Germany). The setup is equipped with a pulsed diode laser excitation source (PDL 800-b, LDH-635-b, PicoQuant, 639 nm, with a repetition rate of 20 MHz) coupled to an Olympus IX-71 inverted microscope. The laser beam was focused ~10 μm deep into the sample solution by a 60x water immersion objective with a numerical aperture of 1.2 (UPLSAPO 60XW, Olympus). Fluorescence was collected by the same objective and passed through a dichroic beam-splitter (650DRLP, Omega) to clean up the back-scattered light from laser excitation. The detected light is further selected by using a 695 AF55 filter (Omega) with a transmission window between 668 and 723 nm. The collected light is then focused by a detection tube lens to a 30 μm pinhole. The re-collimated beam is divided by means of a 50/50 nonpolarizing beam splitter cube, and is detected by two single-photon avalanche diode detectors (SPCM-AQR-13, Perkin Elmer). Time-traces of fluorescence intensity from the two detectors were cross-correlated to avoid after-pulsing artifacts. The output signal was computer processed by a TimeHarp 200 TCSPC card (PicoQuant).

All measurements were made at room temperature (~25 ºC), in at least three different coverslips for each sample solution, with acquisition times of 180 seconds and an excitation power of ~15-20 kW cm^{-2}. The correlation curves were obtained at least twice for each sample drop by performing consecutive measurements. The focal area and the detection volume were calibrated, at the beginning of each set of measurements in every new coverslip, by using Atto655-COOH with an assumed diffusion coefficient, *D*, of 425 $\mu m^2\ s^{-1}$ in water at 25 ºC.[165,166]

FCS data analysis

Individual correlation curves were calculated using the SymPhoTime software (PicoQuant). The correlation curves were initially fitted with a pure diffusion model for a single species, which is given by:

$$G_D(\tau) = \frac{1}{N}\left(1 + \frac{\tau}{\tau_D}\right)^{-1}\left(1 + \frac{\tau}{\kappa^2\tau_D}\right)^{-1/2} \quad (4\text{-}1)$$

where $G_D(\tau)$ is the autocorrelation function, τ_D is the diffusion time of molecules across the focal volume, κ is the geometric factor describing its shape ($\kappa = z_0/\omega_0$, in which z_0 is the axial and ω_0 is the radial dimension of a 3D Gaussian shape assumed for the confocal volume), and *N* is the average number of fluorescent molecules in the focal point.

The diffusion coefficient, D, is related to τ_D, by:

$$D = \frac{\omega_0^2}{4\tau_D} \tag{4-2}$$

The experimental diffusion coefficients were used to estimate the hydrodynamic radius, R_h, of the fluorescently labeled species through the Stokes-Einstein relation:

$$D = \frac{kT}{6\pi\eta R_h} \tag{4-3}$$

where k is the Boltzmann constant, T is the temperature, and η is the viscosity (~1 cP for water at room temperature). Equation 4-3 assumes that the diffusing species is homogeneous and approximately spherical, which is a reasonable approximation for the complexes with the anti-biotin antibody and/or ZZ-CBM. In this case, the diffusion coefficient can be empirically related to the molecular weight by:

$$D = A \times M_W^{-1/3} \tag{4-4}$$

in which A is a constant and has a value of 2.74 x 10^{-5} cm^2 s^{-1} $Da^{1/3}$.[167]

In the case of short DNA strands, their uniform cross-sectional structure is typically represented as a cylindrical rod. Hydrodynamic properties of rod-like objects are more correctly expressed by the following modification of equation 4-3:[168]

$$D = \frac{1}{3}\frac{kT(lnp+C_t)}{\pi\eta L} \tag{4-5}$$

where L is the total contour length of the molecule, p is the aspect ratio ($p = L/d$, in which the diameter d is approximately 1.1 or 2 nm for single or double-stranded DNA, respectively) and C_t refers to the so-called end-effect term. The length L equals the product of the number of monomers and their size, $L = Mb$ (the monomer size b is typically 0.43 nm for ssDNA and 0.34 nm for dsDNA).[168,169] The value of C_t can be determined through the following equation:[168]

$$C_t = 0.312 + \frac{0.565}{p} - \frac{0.100}{p^2} \tag{4-6}$$

Determination of association constants by FCS

Correlation curves obtained for the hybridization study, in which only the diffusion coefficient of the fluorescent probe changes, but not its brightness, were fitted with a two-component model with distinct diffusion times for "free" and "bound" (complexed) fluorescent probe:[170]

$$G(\tau) = \frac{N_f Q_f^2 (1+\frac{\tau}{\tau_f})^{-1}(1+\frac{\tau}{\kappa\cdot\tau_f})^{-1/2} + N_b Q_b^2 (1+\frac{\tau}{\tau_b})^{-1}(1+\frac{\tau}{\kappa\cdot\tau_b})^{-1/2}}{(N_f Q_f + N_b Q_b)^2} \tag{4-7}$$

in which N_f and N_b are the average numbers of free and bound species in the confocal volume, respectively; Q_f and Q_b correspond to the brightness of each species; τ_f and τ_b are the respective diffusion times. The average total number of fluorescent species in the detection volume N equals the sum of free and bound molecules, $N = N_f + N_b$.

Within each set of target-molecule concentrations, the correlation curves were globally fitted by using fixed values for Q_f, Q_b, τ_f and τ_b, which were determined without (free) or in the presence of the highest concentration of target-molecule (bound). The relative values of Q_f, and Q_b were estimated from the ratio between the average fluorescence intensity (photon count) and the total number of fluorescent molecules N (derived from the autocorrelation function) for the two limit situations described above. The confocal volume and geometry factor κ are determined from the calibration measurements and are fixed in the global fitting. The parameters N_f and N_b were allowed to be individually fitted during the minimization of the sum of squared residuals.

The fraction of each bound species, χ_B, for each target molecule concentration was then obtained from the fitted values of N_f and N_b:

$$\chi_B = \frac{N_b}{N_f + N_b} \tag{4-8}$$

Assuming a 1:1 bimolecular interaction for the complex formation between the guest and the host species, then χ_B can be related to the apparent association constant, K_a, through the following equation:

$$K_a = \frac{\chi_B}{(1-\chi_B)([Host]-\chi_B[Guest])} \tag{4-9}$$

The set of experimental values of χ_B measured for the several concentrations of target molecule can be used to determine the apparent K_a from the solution of equation 4-9,

$$\chi_B = \frac{(1/K_a + [Host] + [Guest])}{2\times[Guest]} - \left[\left(\frac{1/K_a + [Host] + [Guest]}{2\times[Guest]}\right)^2 - \frac{[Host]}{[Guest]}\right]^{1/2} \tag{4-10}$$

In the case of complexation between DNA hybrids and anti-biotin IgG, both the diffusion coefficient and the molecular brightness change upon complexation. The dynamics of the complexation reaction then show up as an additional relaxation in the correlation curves. Assuming that fast exchange occurs, *i.e.* the relaxation rate of the reaction is much faster than the typical diffusion times of the fluorescent probe and the complex, then the full correlation function can be expressed as the product of the individual correlation functions for the reaction and the diffusion processes:[171]

$$G(\tau) = G_R(\tau) \times G_D(\tau) \tag{4-11}$$

with the correlation function for reaction $G_R(\tau)$ given by:

$$G_R(\tau) = (1 + A_R e^{-\tau/\tau_R}) \quad (4\text{-}12)$$

where τ_R corresponds to the relaxation time and A_R is the amplitude of the reaction term.

Isothermal Titration Calorimetry[†]

Calorimetric measurements were performed using a Microcal VP-ITC calorimeter (Northampton, MA, USA) at 25 ºC. Before the experimental assay, ZZ-CBM64 and FITC-labeled IgG antibody were dialyzed against Milli Q water via a 12-14 kDa cutoff membrane (Orange Scientific, Braine-l'Alleud, Belgium) at 4 ºC overnight to remove salts and buffer components. The concentration was determined spectrophotometrically using the molar extinction coefficient at 280 nm (ε_{280}) of 210,000 M^{-1} cm^{-1} for IgG and the ε_{280} of 50,880 M^{-1} cm^{-1} computed with the ExPASy ProtParam tool for ZZ-CBM64.[129,172] The antibody concentration was calculated using a correction factor (CF = 0.30) to compensate for absorption of FITC at 280 nm.[173] Both antibody and ZZ-CBM samples were diluted in 10x PBS buffer to a final concentration of 1x PBS (PBS - pH 7.4, 0.01 M Phosphate buffer, 0.027 M KCl and 0.137 M NaCl) and degassed prior to use. The reaction cell contained ZZ-CBM at 5 µM, while the syringe contained the antibody at 62 µM. PBS buffer was used in the reference cell. Titration was performed by a first injection of 2 µl followed by 27 subsequent injections of 10 µl aliquots of antibody at 220-s intervals into the ITC sample cell (volume 1.4467 ml) containing the ZZ-CBM fusion protein. The reference power and stirring speed were set at 15 µcal/s and 307 rpm, respectively. The heat of dilution was determined by taking the average of the last three injections of the thermogram, after the ZZ-CBM was saturated with IgG antibody, and subtracted to experimental data before data analysis. The corrected thermodynamic data was analyzed by nonlinear regression using a single binding model (MicroCal Origin 7.0 software). The fitted data yield the association constant (K_a), stoichiometry (number of binding sites in ZZ-CBM, n) and the binding enthalpy change (ΔH). The Gibbs free energy change, ΔG, and the entropy change, ΔS, were calculated through the following relation:[160,163]

$$\boldsymbol{\Delta G = -RTlnK_a = \Delta H - T\Delta S} \quad (4\text{-}13)$$

where R is the gas constant and T corresponds to the absolute temperature at which the titration was carried out.

[†] ITC experiments were performed at the Centre for Interdisciplinary Research in Animal Health (CIISA), Faculty of Veterinary Medicine, in collaboration with Pedro Bule, Dr. Virgínia Pires and Prof. Carlos Fontes.

4.3 Results and discussion

Hybridization of Atto647N-labeled probe and biotinylated targets

The hybridization between the DNA probe and its biotinylated target, which is the primary biomolecular recognition step in the sensor system, was investigated first in this study (Figure 4-1B-ii). The probe was labeled with the fluorophore Atto647N and FCS measurements were performed at a fixed concentration of 1 nM in PBS buffer. This concentration was maintained constant in subsequent assays with the other components of the system. In order to follow the binding of the DNA probe (5981 Da) to the complementary biotin-labeled DNA sequence (5637 Da), the target concentration in solution was gradually increased from 1 to 1000 nM. Control experiments were performed using a non-complementary biotin-DNA sequence. Normalized correlation functions of the Atto647N-labeled DNA probe alone and in the presence of various concentrations of biotin-labeled target are shown in Figure 4-4A. The correlation curves gradually shifted to longer times with the increment of the complementary target DNA concentration. This reflects the presence of a slower diffusing species in solution, *i.e.* the hybrid that results from the binding of the probe with its complementary target. The diffusion coefficient decreased from about 142 ± 4 $\mu m^2\ s^{-1}$ for the free DNA probe to around 98 ± 5 $\mu m^2\ s^{-1}$ for the hybrids obtained with 1000 nM of complementary DNA target (inset Figure 4-4A). On the basis of equation 4-5, the estimated *D* values are around 137 and 118 $\mu m^2\ s^{-1}$ for free and bound DNA probe, respectively. These estimated values are close to the experimental ones, although a better agreement is found for free DNA than for the DNA·DNA complex. Nevertheless, the expected decrease between free and bound DNA is verified both in theory and experimentally. These experimental values of *D* for free and hybridized DNA probe are consistent with the values reported in the literature for similarly sized oligos. For example, Stellwagen and Stellwagen reported diffusion coefficients of 152 $\mu m^2\ s^{-1}$ and 107 $\mu m^2\ s^{-1}$ for 20 bp single and double stranded oligos measured by capillary electrophoresis.[174]

The observed hybridization was sequence-specific as confirmed by the fact that the diffusion time was not altered (*i.e.* no curve shift occurred) when the probe was exposed to a non-complementary DNA target at a maximum concentration of 1000 nM tested (Figure 4-4A). Subsequent binding studies with anti-biotin antibody and ZZ-CBM were performed with a 200 nM target, a concentration that assures a condition close to complete binding of the DNA probe (Figure 4-4B).

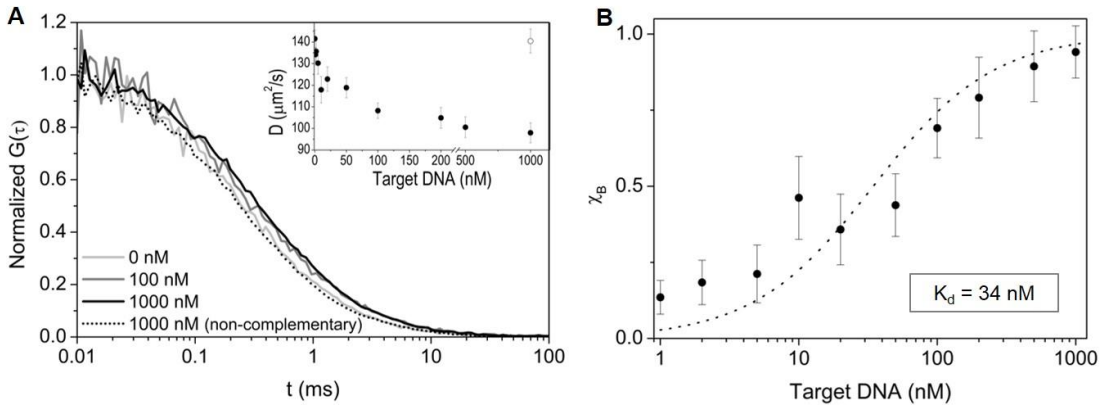

Figure 4-4 Hybridization of the Atto647N-labeled DNA probe with biotinylated target DNA sequences. (A) Normalized FCS autocorrelation curves for Atto647N-DNA probe in aqueous solution, free (light gray) and in the presence of selected concentrations of complementary (100 nM, dark gray; 1000 nM, black) or non-complementary (1000 nM, dotted line) biotin-DNA target. The inset shows the diffusion coefficients as a function of complementary (closed circles) and non-complementary (open circle) target concentration. (B) Bound molar fraction (χ_B) of the DNA probe (1 nM) at several complementary target DNA concentrations (1-1000 nM) in PBS aqueous solution. The dotted line represents the best fit to a 1:1 binding model.

As the single-stranded DNA probe (ssDNA) interacts with its complementary ssDNA target, dsDNA is formed and two fluorescent species coexist in solution: free and bound DNA probes. Surprisingly, it is always possible to fit the correlation curves with a model for a single diffusing species. However, when the two diffusing species (free and bound DNA probes) coexist, the contribution of fluorescence intensity fluctuations from both of them results in diffusion times, or coefficients, that are intermediate between the limit situations of completely free or bound DNA probe (see the inset in Figure 4-4A). Studies reported in the literature suggest that a mixing rule for the intermediate diffusion time, or coefficient, can be used to estimate the molar fraction of each component (see Figure 4-A1 of the section 4.5 "Appendix: Fitting models for the determination of association constants by FCS" - Appendix).[175] As an alternative approach, a two-component model of free and hybridized DNA probes, each with its own diffusion coefficient, is used here to perform a global fit of the experimental correlation curves (see Figure 4-A2 of the Appendix). In this way, it was possible to determine the fraction of hybridized DNA probe for each complementary target concentration. Small changes in the diffusion times were observed upon binding of the fluorescent species with their target molecules, therefore high correlation among the fit parameters can be expected and this could be the reason for some uncertainty in the values of the molar fraction of the bound species, which could affect the fits to the binding model. Figure 4-4B shows that the fraction of hybridized DNA probe (χ_B) increases with the concentration of the target until complete binding is achieved. A dissociation constant K_d value of 34 nM for the hybridization between the DNA probe and its complementary biotin-labeled DNA target was estimated from this plot by using equation 4-10. This K_d value corresponds to an association constant of 2.9×10^7 M^{-1}, which is comparable to the binding constants of DNA oligonucleotide hybridization reported previously.[176,177] For example, Vijayanathan *et al.*[176] used a molecular beacon strategy to determine the K_a values within the range of

4.0-5.7 x 10^7 M^{-1} for DNA·DNA hybrid formation in the presence of different salts. Yu *et al.*[177] studied DNA hybridization with an immobilized DNA oligonucleotide probe using a surface plasmon diffraction sensor, and obtained K_a values of 4.17 to 4.98 x 10^8 M^{-1} and of 1.92 to 2.18 x 10^7 M^{-1} for fully complementary and one base mismatch 15mer-DNA targets, respectively.

Binding of biotinylated DNA·DNA hybrids and anti-biotin IgG antibody

The paper-based DNA detection system described before (Figure 4-1A) relies on the capture of DNA hybrids with an anti-biotin IgG antibody *via* the biotin moiety in the target strand.[67] The interaction between the biotinylated DNA hybrids and the anti-biotin IgG antibody (~150 kDa) was thus studied in solution by mixing a fixed amount of DNA hybrids with increasing antibody concentrations (0-3000 nM) (Figure 4-1B-iii). Specifically, FCS was used to monitor the change in diffusion time that results from the binding of the fluorescently labeled hybrid to the considerably larger anti-biotin antibody. Non-complementary biotinylated DNA was used as a negative control of the complex formation of DNA probe with biotinylated target DNA and anti-biotin IgG. Figure 4-5A shows normalized correlation curves of the DNA·DNA complex in the presence of increasing concentrations of anti-biotin IgG. The FCS curves shifted to longer times when mixing antibody with DNA hybrids, thereby suggesting the formation of a DNA·DNA:antibody complex through the binding of anti-biotin IgG to the biotinylated target DNA hybridized with the fluorescent DNA probe. As shown in the inset, the diffusion coefficient gradually decreased from about 107 ± 6 μm^2 s^{-1} for DNA·DNA hybrids alone to nearly 46 ± 2 μm^2 s^{-1} for supramolecular complexes formed with increasing amounts of antibody up to 2000 nM. From this concentration onwards, the diffusion coefficient remained constant. On the basis of equation 4-4 and of the expected size of a DNA·DNA:antibody complex (*i.e.* around 12 kDa + 150 kDa), the diffusion coefficient is estimated to be ~50 μm^2 s^{-1}. This result is very close to the value obtained experimentally. When a non-complementary sequence was used as the target DNA at binding saturation conditions, the diffusion coefficient value was similar to the one obtained for the free DNA probe in solution (see Figure 4-6). This confirms that the fluorescent DNA probe is not a part of the supramolecular complex, as before, due to the lack of complementarity with the biotinylated target, which nevertheless is likely to have been captured by the anti-biotin IgG.

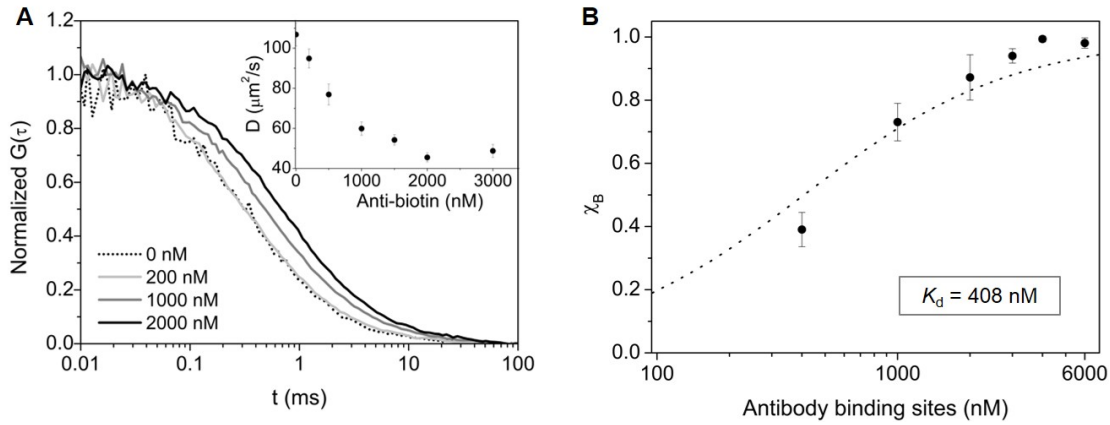

Figure 4-5 Complexation of biotinylated DNA·DNA hybrids with anti-biotin monoclonal IgG antibody. (A) Normalized FCS autocorrelation functions for mixtures of 1 nM Atto647N-DNA and 200 nM biotin-DNA alone (dotted line) and in the presence of increasing concentrations of anti-biotin IgG antibody (200-2000 nM, solid lines). The inset shows the diffusion coefficients as a function of antibody concentration. (B) Bound molar fraction (χ_B) of the DNA·DNA hybrids at various antibody binding site concentrations (0-6000 nM) in PBS, assuming two equivalent and independent binding sites per IgG molecule. The dotted line represents the best fit curve for a 1:1 non-cooperative binding model to the data.

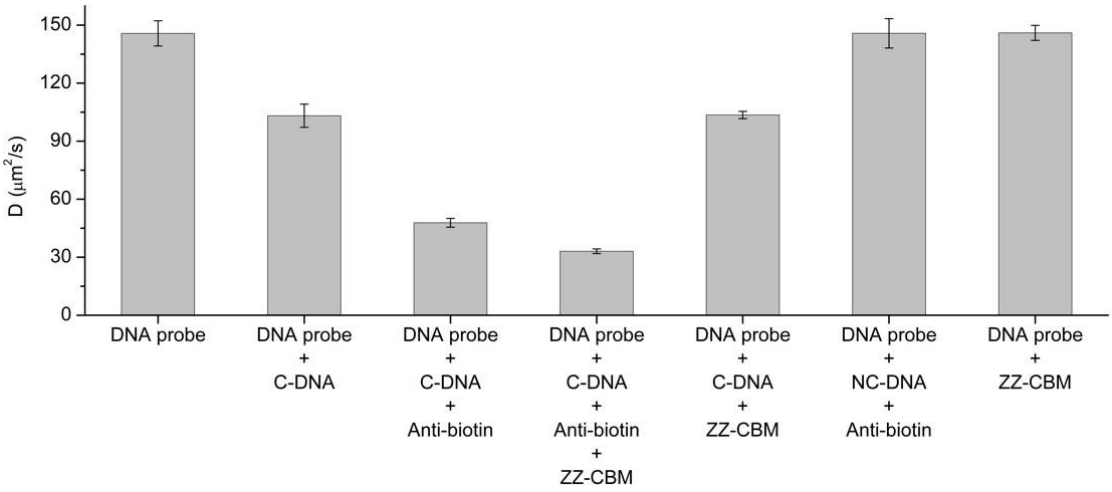

Figure 4-6 Diffusion coefficients obtained from FCS measurements in PBS aqueous solution for controls containing DNA probe (1 nM) alone or in the presence of: complementary target DNA (C-DNA, 200 nM); non-complementary target DNA (NC-DNA, 200 nM); anti-biotin IgG antibody (2000 nM); ZZ-CBM (2000 nM).

The fluorescent DNA·DNA hybrid suffered a nearly 65% loss of fluorescence intensity upon binding to the antibody (see Figure 4-A3 in the Appendix). It is known that interactions between the antibody binding site and the fluorophore moiety may cause quenching.[178,179] FCS data were globally fitted by a two-component model considering the diffusion coefficients indicated earlier for the DNA·DNA hybrid and the DNA·DNA:antibody complex, and their relative molecular brightness (Q_b/Q_f) of 35%. The complex fractions χ_B were calculated and expressed relative to the total concentration of antibody binding sites (Figure 4-5B). Assuming that each IgG molecule contains two equivalent and non-interacting binding sites, and that each binding site accommodates a single ligand, a 1:1 binding model was employed to

evaluate the association constant of the anti-biotin IgG to the biotinylated DNA·DNA hybrid.[178] From this analysis an approximate value of K_d ~ 408 nM was found for the equilibrium dissociation constant, which corresponds to a K_a value of ~2.5 x 10^6 M^{-1}. However, the best fit with a 1:1 binding model still shows deviations from the experimental data. As the antibody can eventually bind bivalently to the biotinylated DNA hybrids, the possibility of cooperativity in the binding process was considered in the analysis of such supramolecular systems. The quantitative assessment of the cooperativity factor can be done through the Hill coefficient (see Figure 4-A5 of the Appendix).[180,181] This value of K_d is within the same order of magnitude as values reported in the literature for the interaction of biotin conjugates with anti-biotin antibodies. For instance, K_d values between 250-500 nM were determined from FCS measurements of the binding of anti-biotin antibody to biotin conjugated quantum dots in solution.[182] However, a two order of magnitude difference was found for the dissociation constant of fluorescein-labeled biotin/anti-biotin antibody complexes in solution (K_d = 1.7 nM), as determined by single-point fluorescence anisotropy measurements.[183] Intermediate values of 24 nM and 62-70 nM were obtained from fluorescence measurements when one of the species was immobilized on a surface.[184,185] Considering the range of binding constant values that have been reported for biotin/anti-biotin antibody interactions, the apparent K_d obtained in the present study suggests that recognition and capture of biotinylated DNA·DNA hybrids by anti-biotin IgG is significant, despite the fact that the biotin label is directly attached to a hybridized oligonucleotide without a spacer. This result validates the use of anti-biotin IgG to detect biotinylated DNA hybrids in the molecular diagnostic system.

Binding of ZZ-CBM fusions to DNA·DNA:antibody complexes

The binding of the DNA·DNA:antibody complex to the ZZ-CBM fusion was studied starting from a situation where the ternary complex is already formed by increasing the concentration of the fusion protein up to 4000 nM (Figure 4-1B-iv). Figure 4-7 shows normalized FCS curves of the DNA·DNA:antibody complex alone or mixed with increasing amounts of ZZ-CBM. The binding of the ZZ-CBM to the anti-biotin antibody attached to the DNA·DNA hybrids is indicated by the shift of the curves toward longer times, which reflects the formation of slower diffusing complexes. The diffusion coefficient decreased to 35 ± 2 μm^2 s^{-1} at a maximum concentration of ZZ-CBM, as shown in the inset of Figure 4-7. As the ZZ-CBM fusion protein is a much smaller molecule (~31.874 kDa) when compared to the anti-biotin IgG antibody (~150 kDa), this accentuated decrease in the diffusion coefficient value was not expected for a 1:1 binding of the small ZZ-CBM fusion to the DNA·DNA:antibody complex. Assuming a spherical shape for complexes and using equation 4-4 with the experimental value of D at ZZ-CBM 4000 nM, the estimated M_w is approximately 460 ± 80 kDa. This value is much higher than the M_w expected for a supramolecular complex comprising the DNA·DNA hybrid of size ~12 kDa, an anti-biotin IgG and the ZZ-CBM fusion, *i.e.* around 194 kDa. This result suggests that aggregation occurs

when the fusion protein is present in the solution, or that more than one IgG molecule binds to ZZ-CBM. Further tests would be required to assess the binding ratio between ZZ-CBM and IgG antibodies and confirm or not the latter case. For this purpose, an ITC experiment was performed using ZZ-CBM and IgG antibody, whose results are shown in the following subsection. Nevertheless, FCS results are supported by an investigation of the IgG-binding capacity of recombinant receptors based on staphylococcal protein A by Ljungquist *et al.*[186], which has indicated that the double Z-domain receptor (ZZ-Cys) can bind to two IgG molecules. Furthermore, Madan *et al.*[187] fused elastin-like-protein (ELP) to Z domains for the purification and recovery of antibodies, and concluded that ELP-ZZ presented a higher binding affinity to IgG than ELP-Z. It was shown very recently that the ZZ-domain (ZZ-Cys) can bind to two IgG molecules forming complexes of 314 kDa, when used as an affinity ligand for antibody purification.[188] This M_W value is close to the one estimated for the experimental *D* value obtained for the four-component mixture, which supports our hypothesis that the ZZ-CBM binds to more than one IgG, most likely in a 1:2 ratio.

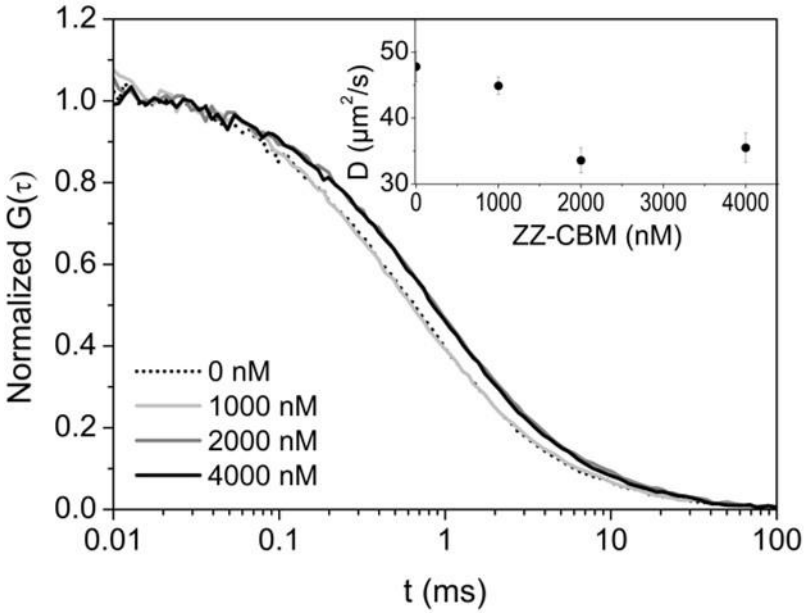

Figure 4-7 Interaction between DNA·DNA:antibody complex with ZZ-CBM fusion protein. Normalized autocorrelation curves for [Atto647N-DNA + biotin-DNA + anti-biotin] free (dotted line), and in the presence of increasing concentrations of ZZ-CBM protein (1000-4000 nM, solid lines). The inset represents the diffusion coefficients as a function of ZZ-CBM concentration.

With regards to controls for specific binding interactions, mixtures were employed without antibody and/or without biotin-labeled complementary target DNA (see Figure 4-6). In the absence of anti-biotin IgG, the resulting diffusion coefficient value was comparable to the one obtained for DNA·DNA hybrids, indicating that ZZ-CBM did not interact with any of the labeled oligonucleotides. When both biotinylated target DNA and anti-biotin antibody were absent, binding between the fluorescence-labeled oligonucleotide and the fusion protein did not occur and the probe remained free in solution, resulting in a diffusion coefficient equivalent to the one obtained for free Atto647N-labeled DNA.

Together with the previous observations regarding the functionality of the DNA recognition system on paper,[67] these results support the usage of ZZ-mediated anchorage of IgG antibodies to paper as the ZZ-CBM binding does not interfere with biotin recognition by the IgG Fab segments.

Interaction mechanism between ZZ-CBM fusion and IgG antibody

The isothermal titration calorimetry (ITC) technique was used to obtain detailed information on the thermodynamic binding parameters associated with the binding ability of IgG to ZZ-CBM fusions. An IgG antibody was titrated into the reaction cell containing a solution of ZZ-CBM. The fusion protein was competent for IgG binding as shown by the titration experiment (Figure 4-8). Upon analysis of the ITC data using a single binding model, results showed that the ZZ-CBM fusion has significant affinity to the IgG antibody with a K_a value of 2.45 x 10^7 M^{-1}, which corresponds to a dissociation constant, K_d, of 41 nM. This value is within the range of previously reported K_d values for the binding of ZZ-based fusions to IgG antibody. For example, a K_d value of 68 nM for the binding of ZZ-ELP (elastin-like protein) fusion to fluorescein-labeled human IgG was obtained by affinity precipitation.[187] However, a one order of magnitude difference was found for the K_a value of ZZ-AP fusion (alkaline phosphatase) binding to immobilized IgG antibody (K_a = 1.46×10^8 M^{-1}) using a surface plasmon resonance system.[189]

The interaction of ZZ-CBM with IgG antibody occurs spontaneously, with a negative free energy change, ΔG, of -10.1 kcal mol^{-1}. ITC data further indicates that the binding is exothermic and enthalpy driven (ΔH = -33.1 kcal mol^{-1}), with an unfavourable entropic contribution ($T\Delta S$ = -23.02 kcal mol^{-1}). In a previous study by ITC, Lund *et al*. found that the interaction between the staphylococcal protein A and IgG antibodies is driven in the same manner.[190]

The stoichiometry, *n*, was determined to be 1.53, suggesting that both potential binding sites (one per Z domain) might be functional in binding to IgG antibody. This result supports the hypothesis that the binding ratio between IgG and ZZ-CBM molecules is larger than 1:1 suggested by FCS, which was based on the large increment in the diffusion time measured when the DNA·DNA:antibody complexes were exposed to the fusion protein. However, the number of IgG binding sites in the CBM-ZZ fusion determined, n = 1.53, is not an integer. This can be explained by an eventual inaccuracy in the determination of the concentration of the two biomolecules, or by assuming that some of the ZZ-CBM binding sites are partially inactive. This result can also be explained by the fact that the fluorescein molecules bound to the antibody could have interfered in the recognition of the Fc fragment by the Z molecules. Moreover, the antibodies present in the tested solution could have been heterogeneously labeled, *i.e.* with various fluorophore:protein ratios. As such, further ITC tests are required, namely with non-labeled IgG antibody.

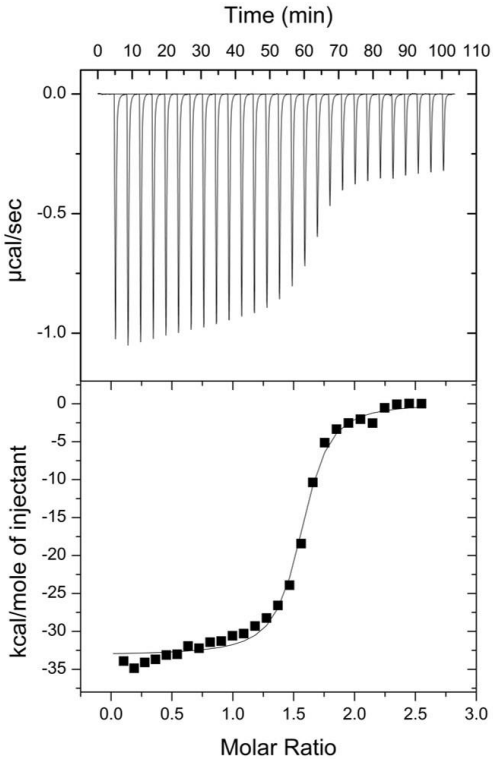

Figure 4-8 Interaction of a ZZ-CBM fusion with an IgG antibody as investigated by isothermal titration calorimetry. The upper panel (thermogram) shows exothermic heat releases upon injection of 10 µl aliquots of IgG antibody into the ZZ-CBM solution. The lower panel shows the integrated and heat of dilution corrected data (binding isotherm). Fitting procedure was performed using a one-site binding model. The assay was performed at 25 ºC in PBS buffer. K_a = 2.45 x 10^7 M^{-1}; n = 1.53 sites; ΔH = -33.10 kcal mol^{-1}; TΔS = -23.02 kcal mol^{-1}; ΔG = -10.1 kcal mol^{-1}.

4.4 Conclusions

The complexation of a 17 nt DNA probe with a complementary biotinylated target, an anti-biotin IgG antibody, and a ZZ-CBM fusion protein in solution was studied by FCS. Specifically, the technique was used to measure changes in the diffusion time of the Atto647N-labeled DNA probe brought about by the addition of increasing amounts of the different molecular components (Figure 4-9). Estimates of the dissociation constant of the DNA probe with its complementary target DNA (K_d ~34 nM) were in agreement with the values reported for short sequences and the technique was able to discriminate complementary from non-complementary targets. Additionally, the accentuated increase in the experimental diffusion time with the addition of antibody suggests that complexation with the biotinylated DNA·DNA hybrids occurred. The apparent dissociation constant of K_d ~408 nM obtained is comparable to values reported in other studies of biotin/anti-biotin interactions, despite the fact that the biotin tag is directly attached to a hybridized oligonucleotide without a spacer. The increment in the diffusion time measured when the DNA·DNA:antibody complexes were exposed to a ZZ-CBM fusion protein suggested that the binding occurs at a stoichiometric ratio of DNA/antibody complex to fusion larger than 1:1. Further studies are required to better characterize the binding

interactions between ZZ-CBM and IgG molecules, for instance, through the use of a fluorescently-labeled ZZ-CBM.

ITC was employed to further characterize the binding interaction between a ZZ-CBM fusion and an IgG antibody. The result suggests a spontaneous, exothermic and enthalpy driven binding reaction between the fusion protein and the antibody. The binding constant was estimated to be 2.45 x 10^7 M^{-1} (K_d ~41 nM), which is in agreement with values reported in the literature for the capture of IgG antibody by ZZ molecules fused with other molecules. The stoichiometry, *n*, was determined to be 1.53, which suggests that both ZZ-CBM binding could bind to IgG molecules. As the antibody was fluorescently labeled, further ITC experiments with non-labeled IgG are advised.

In conclusion, significant information about the intermolecular interactions occurring in a DNA detection system based on the capture of labeled DNA hybrids by an antibody that is conjugated to ZZ-CBM was acquired. Unlike the previous empirical approach used in the development of this DNA recognition strategy,[67] the current study allowed the acquisition of quantitative information regarding the binding/dissociation constants of the complexation of the different components. The results support the functionality of this DNA detection system in solution, and the information obtained can be employed in the design of other molecular diagnostic systems in order to achieve more efficient tests for DNA detection.

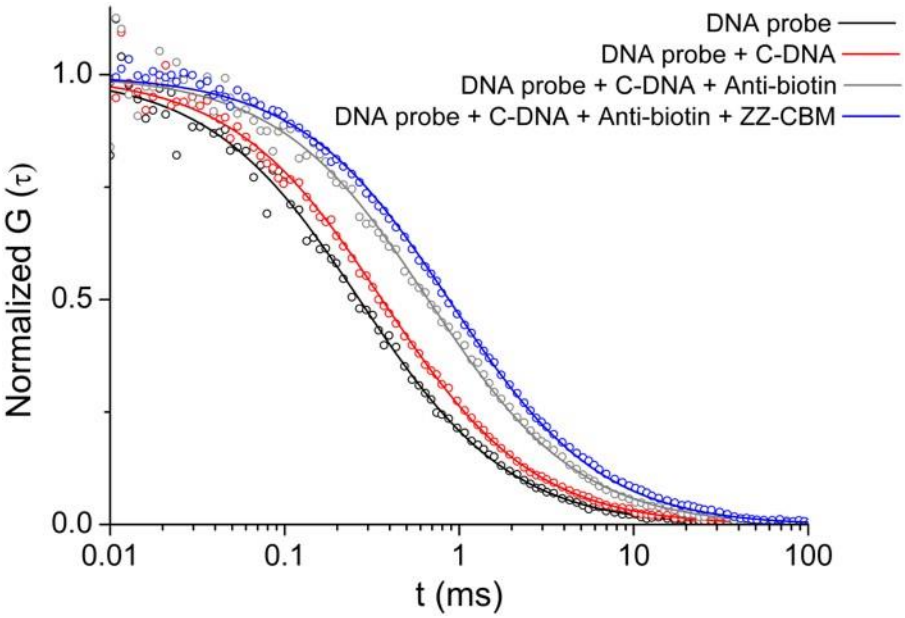

Figure 4-9 Normalized experimental (open circles) or fit (solid lines) FCS correlation curves of the DNA probe alone (black, 1 nM) and in the presence of target molecules at the maximum tested concentration: complementary target DNA (C-DNA, 1000 nM); anti-biotin IgG antibody (3000 nM); ZZ-CBM (4000 nM).

4.5 Appendix: Fitting models for the determination of association constants by FCS

Determination of association constants using average diffusion times

Considering a fast exchange in the host-guest binding reaction during the transit time of the molecule in the confocal volume, Al-Soufi *et al.*[175] proposed that only an averaged diffusion time is obtained. This yielded mean diffusion time depends on the molar fractions of free (χ_F) and bound fluorescent species (χ_B), and is given by:

$$\bar{\tau}_D = \frac{\omega_0^2}{4\bar{D}} \tag{4-A1}$$

in which the average diffusion coefficient, $\bar{D}$, is the weighted sum of individual diffusion coefficients of free (D_F) and bound (D_B) species: $\bar{D} = \chi_B D_B + \chi_F D_F$.

The bound molar fraction χ_B can then be obtained from the corresponding average diffusion coefficient:

$$\chi_B = \frac{(\bar{D} - D_F)}{(D_B - D_F)} \tag{4-A2}$$

The bound molar fractions χ_B from a concentration series can be used to determine the apparent association constant value, K_a, by fitting equation 4-10, while assuming a 1:1 interaction model between guest and host species. Alternatively, the average diffusion coefficient $\bar{D}$ can be used to determine the apparent association constant value K_a by fitting the variation of average diffusion coefficient in a concentration series:

$$\bar{D} = D_F + (D_B - D_F)\chi_B \tag{4-A3}$$

in which χ_B is defined by equation 4-10.

In the case of the mixtures of DNA probe with increasing concentrations of complementary biotin-labeled DNA sequence, as shown in the inset of Figure 4-4A, an average (intermediate) diffusion time is obtained for each target DNA concentration from the fits of the correlation curves. Figure 4-A1A shows the values of bound molar fraction χ_B obtained through equation 4-A2. As expected, the molar fraction of hybridized DNA probe increases with the increment of target DNA until the DNA probe is completely bound. These values were adjusted using equation 4-10, and a K_d value of 20 nM was obtained. On its turn, Figure 4-A1B shows the values of average diffusion coefficient $\bar{D}$ obtained through equation 4-A3. Similarly to the analysis presented, the fitted average diffusion coefficient decreases with the increment of target DNA, from ~136 μm^2/s for the free DNA probe to about 99 μm^2/s in the hybridized form (D_B). An apparent K_d value of 30 nM was obtained. These results are equivalent to the binding constant obtained for this molecular interaction through the two-component model global fit (see Figure 4-4B).

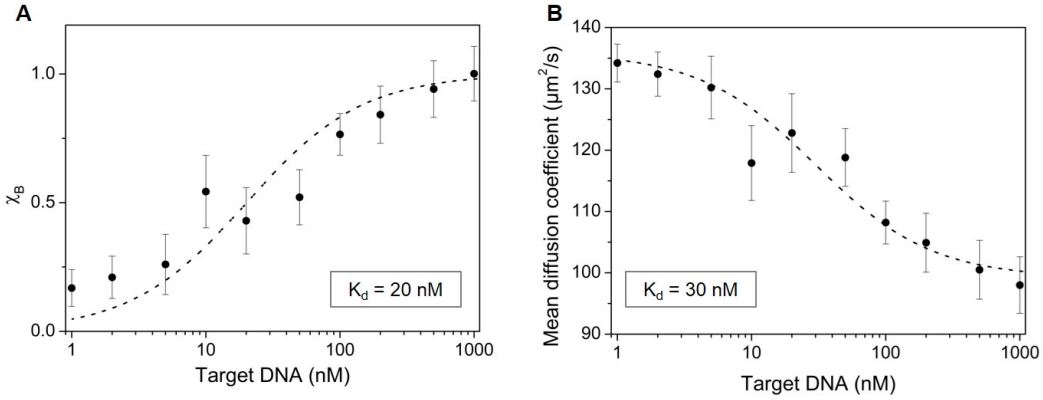

Figure 4-A1 (A) Bound molar fraction (χ_B) of the Atto647N-labeled DNA probe (1 nM) at several complementary biotin-labeled target DNA concentrations (1-1000 nM) in PBS aqueous solution. (B) Average diffusion coefficient obtained for Atto647N-labeled DNA probe (1 nM) mixed with 0-1000 nM of complementary biotinylated target DNA The dotted lines represent the best fit to a 1:1 binding model, as described in the text.

Determination of association constants by two-component model global fit

A number of FCS experimental values were selected to exemplify the determination of association constant, K_a, by two-component model global fit (Figure 4-A2). The fraction of bound species, χ_B, for each target molecule concentration was plotted over the best global fit used to determine the apparent K_a of the complex formed by the DNA probe and its complementary biotin-labeled DNA target (see Figure 4-4B).

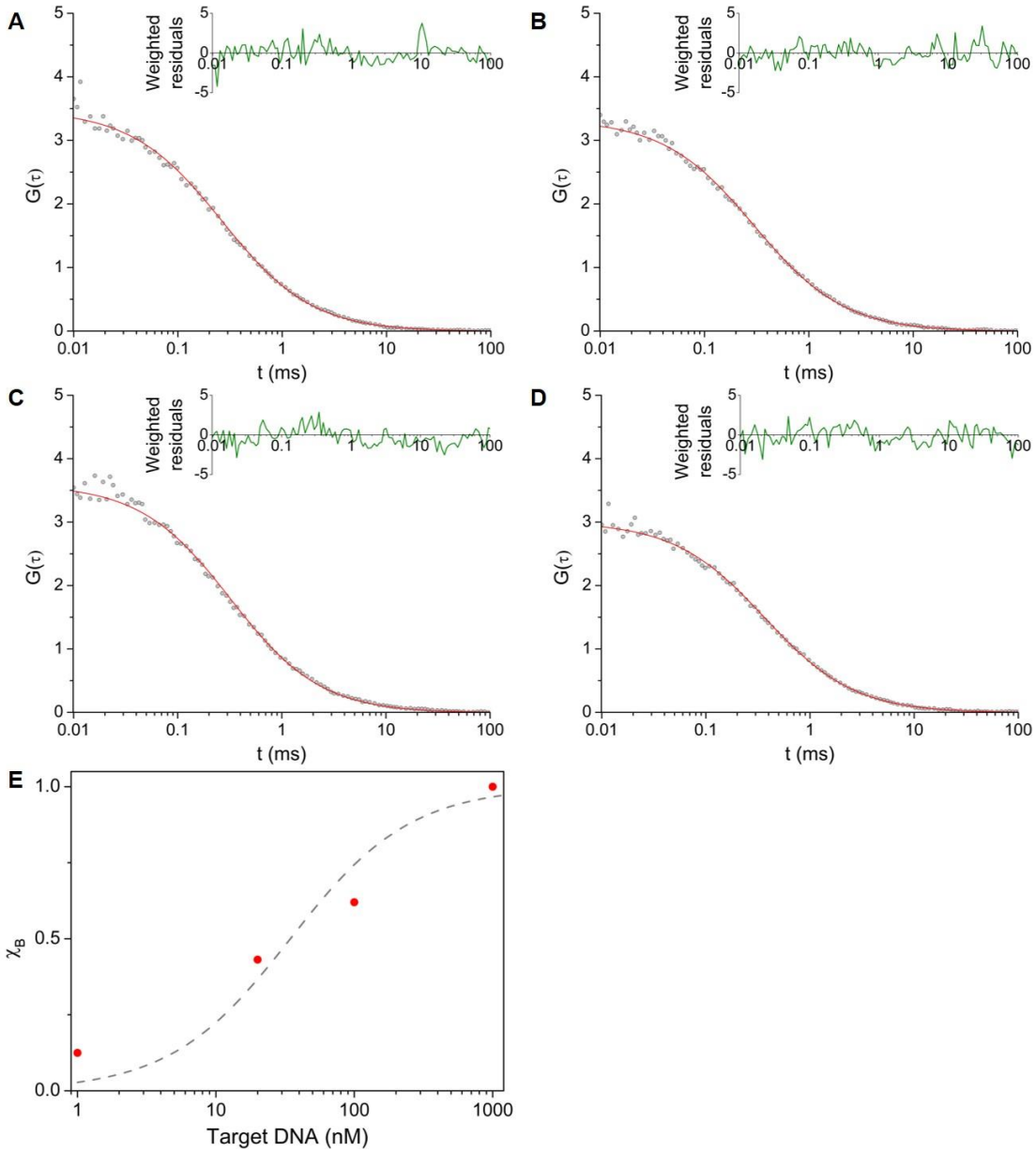

Figure 4-A2 Determination of association constant, K_a, by two-component model global fit. A-D: Typical autocorrelation curves for Atto647N-DNA probe (1 nM) in aqueous solution in the presence of (A) 1 nM, (B) 20 nM, (C) 100 nM or (D) 1000 nM of complementary biotin-DNA target. The insets indicate the respective weighted residuals in function of time (ms), after autocorrelation curves were globally fitted by using fixed values for Q_f, Q_b, τ_f and τ_b (equation 4-7). The average number of free and bound species in the confocal volume were fitted, minimizing the sum of squared residuals. (E) Bound molar fraction (χ_B) of the DNA probe at the selected target DNA concentrations were obtained from the fitted values (equation 4-8), and plotted over the best global fit to a 1:1 biomolecular interaction model (equation 4-10, dashed line).

In the case of the complexation of the biotinylated DNA hybrids with the anti-biotin IgG, the fluorescence intensity decreased about 65% upon binding to the antibody, as illustrated in Figure 4-A3A. Therefore, FCS data were globally fitted by a two-component model considering also the relative brightness, Q_b/Q_f, of ~35% for the DNA·DNA:antibody complex.

Considering this difference in the brightness of the fluorescent DNA·DNA hybrids free or bound to the antibody, it is expected that the correlation curves contain an additional slope denoting a "reaction term" with a relaxation rate of the reaction much faster than the typical diffusion times of guest and complex.[175] The correlation function $G_R(\tau)$ of the chemical equilibrium reaction is described by equation 4-11. The amplitude of the reaction term A_R is given by equation 4-A4, and it can be estimated from the relative brightness of the complex, Q_b/Q_f, and the equilibrium constant of the binding process, K_a:

$$\boldsymbol{A_R} = \frac{\boldsymbol{K}_a[\boldsymbol{Host}](\mathbf{1}-\boldsymbol{Q}_b/\boldsymbol{Q}_f)^2}{(\mathbf{1}+\boldsymbol{Q}_b/\boldsymbol{Q}_f\times\boldsymbol{K}_a[\boldsymbol{Host}])^2} \tag{4-A4}$$

The relaxation time of the reaction term, τ_R, is defined through the following equation:

$$\boldsymbol{\tau_R} = (\boldsymbol{k}_+[\boldsymbol{Host}] + \boldsymbol{k}_-)^{-1} \tag{4-A5}$$

in which the association rate constant k_+ and the dissociation rate constant k_- are related to the equilibrium (association) constant by $K_a = k_+/k_-$. Equation 4-A5 was used to estimate the relaxation time, τ_R, in the case of a binding reaction of guest to the host that is diffusion-limited. For this purpose, it was assumed that the bimolecular rate constant k_+ can be estimated from the Smoluchowski equation:

$$\boldsymbol{k}_+ = \mathbf{4}\boldsymbol{\pi}\boldsymbol{N_A}\boldsymbol{R}(\boldsymbol{D_{Guest}} + \boldsymbol{D_{Host}}) \tag{4-A6}$$

where N_A is Avogadro's number and R is the collision radius, which is generally assumed to be the sum of the molecular radii of each molecule.

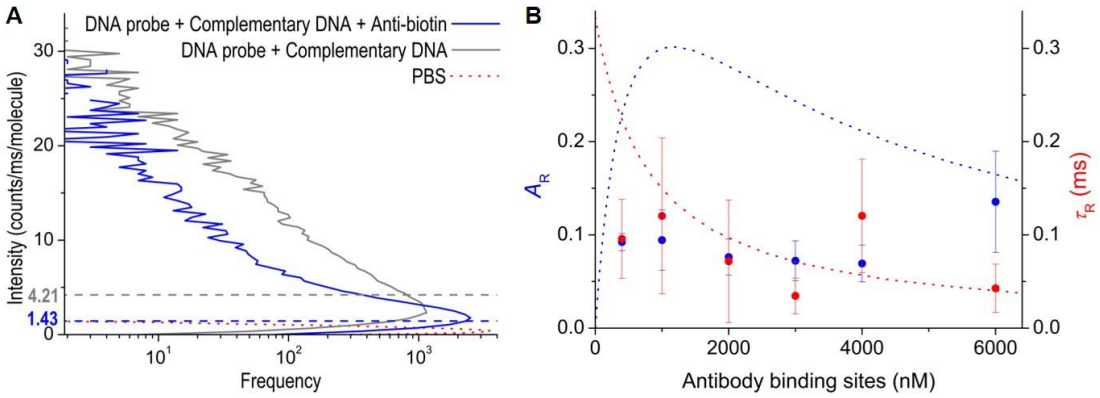

Figure 4-A3 Complexation of biotinylated DNA·DNA hybrids with anti-biotin monoclonal IgG antibody. (A) Typical counts frequency of mixtures of 1 nM Atto647N-DNA and 200 nM biotin-DNA alone (gray) or in the presence of anti-biotin IgG at maximum concentration (3000 nM, blue). Their average fluorescence intensity is represented by the respective colored dashed line. The red dotted line indicates the background noise level measured in buffer solution. (B) Amplitude of the reaction term (A_R, blue) and the relaxation time (τ_R, red) as a function of the antibody binding sites concentration. The respective colored dotted lines represent the simulated variation of A_R and τ_R with increasing antibody binding sites concentration following equations 4-A4 and 4-A5.

It was found that the fitted reaction times, τ_R, are comparable to the estimated values from equations 4-A5 and 4-A6, that is, assuming that the binding reaction is a diffusion-limited process (Figure 4-A3B). However, the relaxation time τ_R is expected to decrease with increasing host (antibody) concentration, but experimental data do not exhibit any tendency. The amplitude of the reaction term A_R obtained from experimental FCS data also does not follow the expected variation with increasing amounts of antibody. These results could be explained by the high uncertainty of the FCS data below 0.01 ms together with the time resolution of the equipment that could not allow the acquisition of data at short time range for an accurate description of the reaction term in the correlation curve (see Figure 4-A4). Nevertheless, the difference in the fitted curves considering or not the correlation function $G_R(\tau)$ is noticeable and renders a lower residuals dispersion. Therefore, the reaction term was considered in the analysis of the binding of the DNA·DNA hybrids to the antibody, as well as in further analysis of the complexation with the ZZ-CBM fusion.

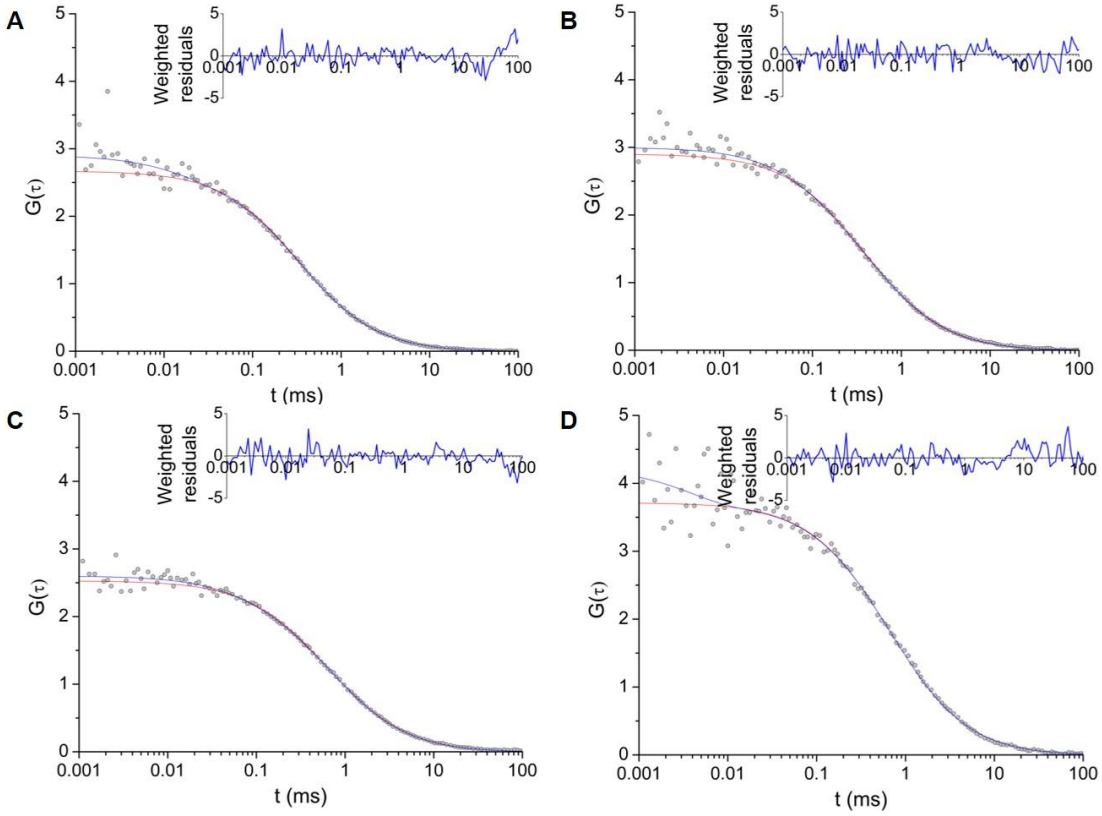

Figure 4-A4 Determination of association constant, K_a, by two-component model global fit considering a change of brightness upon complex formation. A-D: Typical autocorrelation curves for mixtures of 1 nM Atto647N-DNA and 200 nM biotin-DNA in the presence of (A) 200 nM, (B) 500 nM, (C) 1500 nM or (D) 3000 nM of anti-biotin IgG. FCS data were globally fitted considering Q_b=0.35 and either only the diffusion model (red line, equation 4-7) or with an equilibrium reaction term (blue line, equation 4-11). The insets indicate the respective weighted residuals in function of time (ms), after autocorrelation curves were globally fitted considering a reaction term.

Cooperativity in the binding process between DNA·DNA and anti-biotin IgG

One important factor in the analysis of data in supramolecular systems is the cooperativity in a binding process, which can be assessed from Hill equation:

$$\chi_B = \frac{[Host]^{n_H}}{{K_{0.5}}^{n_H} + [Host]^{n_H}} \quad \text{(4-A7)}$$

where $K_{0.5}$ is the host molecule concentration at which half of the guest molecules are bound, and n_H is the Hill coefficient, which describes the cooperativity of host binding.[181] In the binding process of biotinylated DNA hybrids to IgG antibody, n_H will reflect the extent of cooperativity among the two IgG binding sites to capture biotin. An n_H of 1 describes a system where the binding sites are truly identical and independent of each other (non-cooperative binding). Positively ($n_H > 1$) or negatively cooperative binding ($n_H < 1$) refer to situations where the binding of biotinylated DNA·DNA to an IgG binding site enhances or weakens the binding of additional DNA hybrids to the remaining binding site, respectively.

Figure 4-A5 shows the bound molar fraction (χ_B) of the DNA hybrids as a function of the antibody binding sites concentration with two fitted binding curves, which were obtained using equation 4-A7 with either a fixed or floating value for n_H. The data is better fit with an n_H value of 1.6, suggesting positive cooperative binding between the biotinylated DNA hybrids and the anti-biotin antibody. Antibodies can bind bivalently to haptens and, therefore, their overall affinity depends upon both the first and second dissociation constants related to the eventual sequential binding to haptens.[183,191] However, previous studies reported non-cooperative behavior between biotin and anti-biotin, either in bulk solution or in surface-based binding.[183,184,192] The $K_{0.5}$ values obtained with $n_H = 1.0$ and $n_H = 1.6$ are of the same order of magnitude – 408 ± 77 nM and 533 ± 19 nM, respectively; but the degree of uncertainty is higher when a two-site, non-cooperative binding model is considered. Therefore, despite the absence of experimental support, positive cooperative binding should not be disregarded.

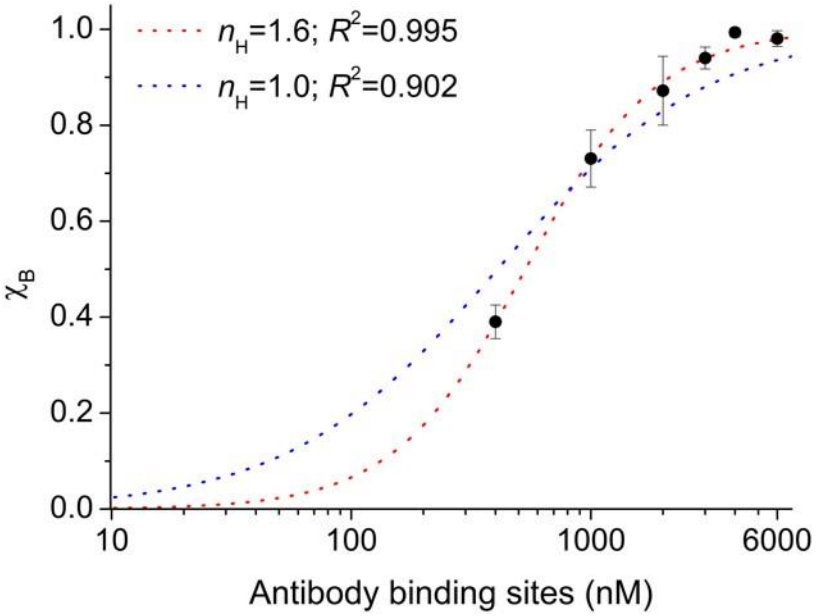

Figure 4-A5 Assessment of the cooperativity in the complexation of biotinylated DNA·DNA hybrids with anti-biotin monoclonal IgG antibody. Closed circles represent the experimental data related to the bound molar fraction (χ_B) of the DNA·DNA hybrids (1 nM Atto647N-DNA and 200 nM biotin-DNA) at various antibody binding sites concentrations (0-6000 nM) in PBS. The blue and red dotted lines represent the best fit curve obtained with a fixed (n_H=1.0) or floating Hill coefficient, respectively. The resultant $K_{0.5}$ values with n_H=1.0 and n_H=1.6 are 408 ± 77 nM and 533 ± 19 nM, respectively.

Chapter 5

Functionalization of gold nanoparticles for DNA detection

5.1 Introduction

Bioactive paper that is capable of detecting biomolecules is required to perform two essential functions: biorecognition and reporting.[17] In chapter 3 it was demonstrated that cellulose can be functionalized with ZZ-CBM fusions for a site-directed immobilization of antibodies. Furthermore, in chapter 4 it was shown that these biorecognition agents, ZZ-CBM·antibodies complexes, are able to recognize and capture labeled DNA hybrids in solution. The development of a robust and convenient reporting system, through which the user is informed about the capture of the target by the biorecognition agents anchored on cellulose, is then the subsequent step.

The previously developed paper-based system for DNA detection, which used CBMs for the attachment of antibodies to cellulose, employed a fluorescently labeled oligonucleotide as probe.[67] Although this fluorescence-based reporting strategy provided an effective means to generate a signal upon capture event, it requires instrumentation for signal readout. Additionally, background fluorescence of some paper materials is often present due to the addition of optical brightening agents in papermaking to achieve a high standard of whiteness.[193] Since white paper provides strong contrast with colored reagents, a colorimetric reporting is a convenient strategy since results can be visually assessed by the naked eye, therefore reducing the dependence on instrumentation. These advantages have motivated researchers to develop colorimetric paper-based assays for the detection of various analytes, such as proteins, glucose, pathogens and heavy metals.[29,70,194,195]

Gold nanoparticles (AuNPs) are popular colorimetric reporters due to their optical properties and bioconjugation possibilities. AuNPs can be dispensed in high density onto reaction zones because of their relatively small size, resulting in an intense colorimetric response that can be visually interpreted.[51] Individual spherical AuNPs with a diameter range between 5-50 nm exhibit an intense red color with an absorption band centered at ~520 nm, and extinction coefficients that are more than three orders of magnitude greater than those of conventional organic chromophores.[117] The deep red color of dispersed AuNPs is caused by the localized surface plasmon resonance, which results from coherent oscillations of the metal's electrons excited by an incident electromagnetic wave, in this case light. When the

optical frequency matches the surface plasmon resonance frequency, a strong absorption or scattering of light occurs, which results in the observed color.[196] The surface plasmon absorption properties of AuNPs can be changed by inter-particle interactions. The assembly or aggregation of AuNPs in solution results in the plasmon coupling between AuNPs, leading to a red-shift, or even a splitting, of the surface plasmon resonance band that induces color changes from red to purple/blue.[197] Colorimetric biodetection strategies based on AuNPs have been developed either by exploring the color changes dependence on the inter-particle spacing, or by using AuNPs just as colored reporters.[198–200]

One of the most frequently applied methods for the synthesis of AuNPs is the citrate reduction of Au(III) to Au(0) in water, with sodium citrate acting as both reducing agent and stabilizer.[201] Through this method, the AuNPs size can be controlled by changing the gold-to-citrate ratio.[202] The surface of AuNPs can then be functionalized with appropriate biomolecules, *e.g.* DNA molecules for nucleic acid detection, by replacing the citrating capping ligands. For example, negatively charged single-stranded DNA (ssDNA) molecules can be attached to negatively charged AuNPs via thiol-gold bonds, namely by a salt-aging method in which salt is incrementally added to the solution containing AuNPs and DNA to screen charge repulsion and allow for the formation of DNA-AuNPs conjugates.[198,203]

This chapter describes the preparation of DNA-conjugated gold nanoparticles (DNA-AuNPs) to be used as colorimetric probes for the recognition of biotin-labeled DNA target, as planned for the cellulose-based DNA detection system (see Figure 2-1 of Chapter 2). The first section is focused on the synthesis of AuNPs by the citrate reduction method and their surface modification with thiolated ssDNA, as well as their structural characterization in terms of size distribution, shape and optical properties. The colloidal stability of nanoparticles is then assessed through salt-induced aggregation experiments. Finally, DNA-AuNPs are tested for their ability to discriminate complementary from non-complementary biotin-labeled DNA, as well as for the subsequent capture of DNA-AuNPs and target biotin-labeled DNA hybrids by anti-biotin antibody, either by measuring the electrophoretic mobility of complexes in agarose gels or by characterizing aggregation profiles in solution.

5.2 Experimental

Oligonucleotides

The sequences of single stranded oligonucleotides used is this study are described in Table 5-1. The target DNA sequences contain a 5’ modification with biotin. The thiol-modified DNA probes include a spacer composed of ten adenines at the 5’ end of the sequences. The same 17-mer DNA probe sequence used in the previous chapter, which was designed by Deborggraeve *et al.* for the detection of a *Trypanosoma brucei*-specific sequence situated within the 18S rRNA gene, will be explored in more

detail in this chapter to describe the functionalization of AuNPs with DNA.[164] For multiplex testing, two other DNA probe sequences were designed for subspecies discrimination among *T.b. gambiense* and *T.b. rhodesiense*, targeting either the *T.b. gambiense* surface glycoprotein (TgsGP, GenBank accession number AJ277951) or the serum resistance-associated (SRA) gene (GenBank accession number Z37159), respectively.[204] These probe sequences were manually designed with reference to the TgsGP and SRA gene sequences and location between the previously designed primer sets for the subspecies-specific amplification.[205,206] Self-dimers, hairpin formation, GC content, and other properties were checked by the OligoAnalyzer 3.1 online tool, and probe sequences were compared using the LALIGN program.[207,208] The resultant TbgDNA and TbrDNA probe sequences contain six nucleotides in a row that are identical (5'-AAGGTA-3'). All oligonucleotides were purchased from STABVIDA (Portugal).

Table 5-1 Sequences and modifications of the DNA probes for *Trypanosoma brucei* (*T.b.*), *Trypanosoma brucei gambiense* (*T.b.g.*) and *Trypanosoma brucei rhodesiense* (*T.b.r*), and their complementary and non-complementary target sequences. The poly-A spacers are highlighted in bold.

Oligonucleotide	DNA sequence (5'-3')
TbDNA: *T.b.* DNA probe	Thiol-**AAAAAAAAAA**TTGTGTTTACGCACTTG
C-TbDNA: *T.b.* complementary target	Biotin-CAAGTGCGTAAACACAA
NC-TbDNA: *T.b.* non-complementary target	Biotin-TCCAGGGAAATGTCACGTCC
TbgDNA: *T.b.g.* DNA probe	Thiol-**AAAAAAAAAA**TATCTAGGAAGGTACGA
C-TbgDNA: *T.b.g.* complementary target	Biotin-TCGTACCTTCCTAGATA
TbrDNA: *T.b.r.*-DNA probe	Thiol-**AAAAAAAAAA**TCACAAGGTAAGACAGA
C-TbrDNA: *T.b.r.* complementary target	Biotin-TCTGTCTTACCTTGTGA

Synthesis of gold nanoparticles

Gold nanoparticles were prepared by the citrate reduction method of $HAuCl_4$, first described by Turkevich *et al.* and Frens.[201,202] In preparation for the synthesis of AuNPs, all glass materials were immersed overnight in a freshly prepared solution of hydrochloric acid and nitric acid in a molar ratio of 1:3 (*aqua regia*), followed by extensive rinsing with deionized and Milli Q water. In the dark, 250 ml of 1 mM Gold(III) chloride trihydrate ($HAuCl_4 \cdot 3H_2O$, Sigma-Aldrich) was brought to boil while in reflux and stirring in a 500 ml round-bottom flask. Twenty five milliliters of 38.8 mM trisodium citrate (Sigma-Aldrich) were quickly added and the mixture was refluxed for 20 minutes, leading to a change in color from pale yellow to deep wine red. Afterwards, the colloidal solution was left at room temperature to cool down while keeping the continuous stirring. The colloidal solution was stored in the dark at room temperature until required. AuNPs concentration was determined by the Lambert-Beer law assuming a molar extinction coefficient for the plasmon resonance band maximum at 526 nm of 2.33×10^8 M^{-1} cm^{-1}, since the molar extinction coefficient depends on the particle size.[209] The absorbance was measured in a Nanodrop spectrophotometer (NanoVue Plus, General Electrics).

Functionalization of gold nanoparticles with thiolated oligonucleotides[‡]

The conjugation of gold nanoparticles with DNA probes was done by an adaptation of the method described by Hurst *et al.*.[203] DNA was prepared by suspending dehydrated thiol-modified oligonucleotides in 50 µl of 1M dithiothreitol (DTT) and incubated at room temperature for one hour, followed by the addition of 450 µl of Milli Q water and incubation for one more hour at room temperature. Afterwards, extraction was performed three times with ethyl acetate at a 1:2 ratio (v/v) by centrifuging the mixture for 5 minutes at 21,380 g and discarding the organic, upper phase. The remaining DNA containing aqueous phase was then purified using a NAP-5 column with Sephadex G-25 according to manufacturer's instructions and using 10 mM phosphate buffer, pH 8, as eluent. The final concentration of purified thiol-DNA was determined by the Lambert-Beer law and using the extinction coefficient at 260 nm provided by the manufacturer.

DNA-functionalized gold nanoparticles (DNA-AuNPs) were prepared by mixing the purified thiolated oligonucleotides with the colloidal solution of AuNPs in a theoretical molar ratio of 1:200 (AuNP:DNA). In addition, the concentrations of phosphate buffer and sodium dodecyl sulfate (SDS) were brought to 10 mM and 0.01 % (w/v) SDS, respectively. After 10 s in an ultrasound bath, the mixture was incubated in the dark for 30 minutes at room temperature. The NaCl concentration was sequentially increased to 50, 100, 200 and 300 mM using a solution of 10 mM phosphate buffer, pH 8, 1.5 M NaCl and 0.01% (w/v) SDS. Between each NaCl increment, the vial was submersed in an ultrasound bath for 10 seconds and allowed to incubate in the dark for 30 minutes at room temperature. The salting process was followed by a 10-s sonication using an ultrasound bath and the solution was allowed to rest for $\geq$ 16 hours in the dark at room temperature. Then, the solution was centrifuged at 21,380 g for 30 min to separate the AuNPs from the unreacted reagents, followed by supernatant removal. The pellet of gold nanoparticles was washed twice with 10 mM phosphate buffer (pH 8) and then once with 10 mM phosphate buffer (pH 8), 100 mM NaCl. Finally, particles were suspended in 10 mM phosphate buffer (pH 8), 100 mM NaCl and their concentration was determined and adjusted by the Lambert-Beer law assuming a molar absorptivity of 2.33×10^8 M^{-1} cm^{-1} at 526 nm.[209] The resulting DNA-functionalized gold nanoparticles were stored in the dark at 4 ºC until required.

Transmission Electron Microscopy (TEM)

The physical size and structural morphology of the synthesized AuNPs and DNA-modified AuNPs were analyzed by TEM. For TEM analysis, 10 µl of nanoparticles solution were applied on copper grids coated with formvar and carbon film, and air-

[‡] Initial training on synthesis and functionalization of gold nanoparticles with thiolated DNA was provided by Prof. Pedro Baptista's research group at the Department of Life Sciences, Faculty of Sciences and Technology (FCT NOVA), with the main collaboration of Dr. Fábio Carlos and Dr. Bruno Veigas.

dried at RT. Images were acquired using a Hitachi H-8100 electron microscope operating at 200 kV, and further analyzed using the straight line tool of ImageJ software to manually determine nanoparticle size (diameter) distribution and shape, as defined by the length-to-width ratio.

Dynamic Light Scattering (DLS)

The hydrodynamic diameter, D_h, of AuNPs and DNA-AuNPs was determined by DLS. This technique detects the scattered light intensity fluctuations of nanoparticles undergoing Brownian motion, calculates their diffusion coefficient and relates it back to their hydrodynamic size by applying the Stokes-Einstein equation and considering particles with a spherical shape.[210] DLS measurements were carried out at 25 ºC using a Zetasizer Nano ZS analyzer (Malvern, UK) equipped with a 633 nm laser. Experiments were performed at 173º scattering angle, with water set as dispersant, and the measurement time was 120 s. Triplicate 1-ml samples of AuNPs or DNA-AuNPs (2.5 nM in phosphate buffer 10 mM, pH 8) were measured in polystyrene cuvettes. Each replicate was analyzed with three runs, each one consisting of 20 consecutive measurements (10 s each).

UV-Visible spectroscopy and salt stability assays

UV-visible spectroscopy was performed to measure the absorbance spectrum of gold nanoparticles in the wavelength range 400 to 700 nm. This technique was also performed to test the stability of functionalized gold nanoparticles upon increasing ionic strength. For this purpose, and to determine the minimal electrolyte concentration needed to induce nanoparticle aggregation, 5 µl of 15 nM DNA-AuNPs were mixed with 20 mM phosphate buffer, pH 8. The solutions were then incubated for 5 minutes at 95 ºC and 5 minutes at 25 ºC in a thermal cycler (Biometra – T Gradient). 5 µl of $MgCl_2$ were then added to the desired final concentration in solution, and the mixtures were allowed to incubate at room temperature in the dark for 30 minutes. Finally, the 400-700 nm absorbance spectrum was measured using a microplate spectrophotometer (SpectraMax Plus 384 Microplate Reader). Images of dispersed or aggregated AuNPs in solution were captured with an Olympus E-PM1 camera

Gel electrophoresis

Gold nanoparticles, their surface modification and ability to form complexes with other biomolecules were also analyzed by gel electrophoresis. Gels were prepared with 1% (w/v) agarose (Fisher Scientific, Waltham, MA) in 0.5x TBE buffer (40 mM Tris-HCl, pH 8.3, 45 mM boric acid, 1 mM EDTA). Sample solutions of 10 µl total volume were prepared and incubated at RT for 30 minutes. The AuNP-containing samples were then mixed with 2 µl of glycerol/water (1:1, v/v), loaded into the wells and run for 4 hours at 50 V. The bands of plain and DNA-conjugated AuNPs were directly visible by the red color of the gold nanoparticles. Images were acquired with a GS-800™ Calibrated Densitometer from Bio-Rad (Hercules, CA, USA). The

migration pattern of each sample was evaluated by measuring the position of each band referring to the start position provided by the wells where the samples had been loaded. The migration distance was measured for each lane by using the plot profile tool of ImageJ software, after setting the scale with a known distance.

Colorimetric hybridization assays in solution

The specific hybridization assays with biotinylated target sequences were performed in solutions with a final total volume of 30 µl with 2.5 nM DNA-AuNPs probes (TbgDNA or TbrDNA) and 10 pmol of biotin-labeled DNA targets in phosphate buffer 10 mM, pH 8. After 5 min of denaturation at 95 ºC followed by 5 min at RT, $MgCl_2$ was added to the mixtures to a final concentration of 30 mM. After a 30 min incubation at RT in the dark, for color development, the absorbance spectra (400-700 nm) were measured in a microplate reader (SpectraMax Plus 384 Microplate Reader).

5.3 Results and discussion

Gold nanoparticles were synthesized by reduction and simultaneous stabilization of tetrachloroaurate with trisodium citrate in an aqueous solution, leading to a colloidal solution of AuNPs with weakly adsorbed citrate anions onto the particles' surface.[201,202] The particles were then conjugated with thiol-modified oligonucleotides to be further used as colorimetric probes for DNA target recognition.[203] The optical and physical properties of AuNPs depend on their size, morphology, agglomeration state and surface modification.[211] Therefore, different techniques were used to characterize the synthesized AuNPs and their functionalization with DNA. Gold nanoparticles conjugated with the TbDNA sequence (Table 5-1) will be used as a reference for the structural characterization of AuNPs-based probes functionalized with 27-nt-long oligonucleotides modified with a thiol group at the 5' and including a 10-adenine spacer.

Size and morphology of uncoated and DNA-coated gold nanoparticles

The size of AuNPs depends on the concentration ratio of sodium citrate to $HAuCl_4$ used in the reduction reaction, wherein a stoichiometric ratio larger than 1.5 is required for the complete conversion of $HAuCl_4$ to AuNPs.[212] In this work, the molar ratio of citrate and $HAuCl_4$ used was of 3.88.

The size and shape of the synthesized AuNPs and TbDNA-modified AuNPs were firstly assessed by TEM, which allows the direct imaging of nanomaterials. The diameter of each particle pictured in all TEM images was measured using the ImageJ software and an average diameter size was determined and displayed in histograms of size distribution. Figure 5-1A shows a TEM image of a suspension of the synthesized AuNPs. The citrate-capped AuNPs presented an average diameter of 14.0 ± 1.2 nm,

as determined by analyzing 158 individual particles from multiple TEM images, and a close to perfect spherical shape with an average asymmetry factor (*i.e.* length-to-width ratio) of 1.04 ± 0.10. The obtained particle size is close to previously reported sizes using the same citrate-to-$HAuCl_4$ molar ratio.[213,214]

Similarly to the results obtained for plain AuNPs, TEM images of TbDNA-functionalized AuNPs revealed round-shaped structures with an average size of 13.9 ± 1.2 nm (n=75 particles) and a comparable low asymmetry with an average length-to-width ratio of 1.05 ± 0.08 (see Figure 5-1B). As TEM analyzes AuNPs in the dry state, *i.e.* only the inorganic core of AuNPs without their solvation shell is imaged, the size similarity between the synthesized AuNPs and the same particles conjugated with DNA was expected.[215]

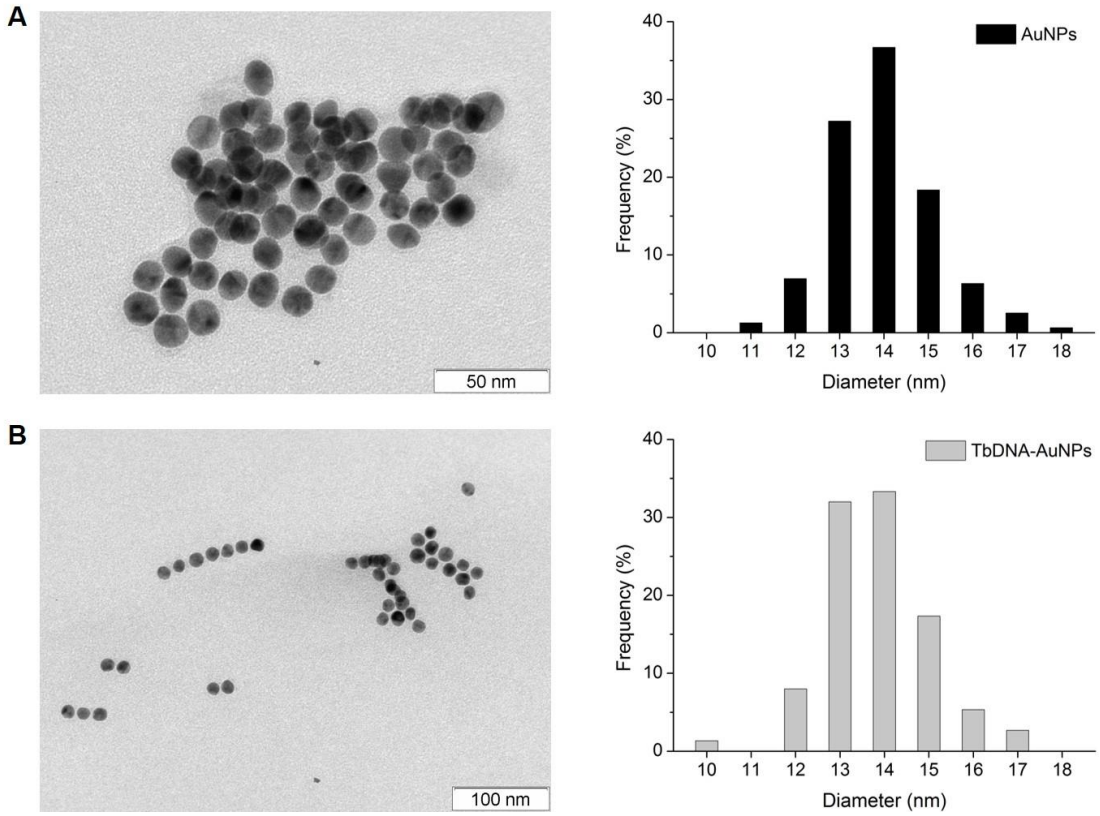

Figure 5-1 Size and morphology of bare and DNA-modified AuNPs assessed by TEM. (A) Characterization of synthesized AuNPs. Left: Typical TEM image acquired for plain AuNPs (scale bar = 50 nm). Right: AuNPs size frequency count histograms as derived by statistical analysis of TEM micrographs, with an average diameter of 14.0 ± 1.2 nm. (B) Characterization of the TbDNA-conjugated AuNPs in a nominal 1:200 ratio (AuNP:oligonucleotides). Left: Representative TEM image acquired for DNA-AuNPs (scale bar = 100 nm). Right: Size distribution of DNA-modified AuNPs as measured from TEM images, with an average diameter of 13.9 ± 1.2 nm.

Spectroscopic measurements of both synthesized AuNPs and DNA-conjugated AuNPs in aqueous solution were performed in 10 mM phosphate buffer pH 8 for a qualitative description of DNA-AuNPs assembly sizes.[216] Figure 5-2 shows UV-visible absorbance spectra ranging from 400 to 700 nm of bare and TbDNA-modified AuNPs. The 14 nm citrate-capped AuNPs presented the typical single absorbance

maximum at 519 nm, confirming the stability and monodispersity of the synthesized nanoparticles.[217] As the optical properties of spherical AuNPs are dependent on their size and wavelength, it is possible to estimate the particle size (diameter, *d*, in nm) by using the method proposed by Haiss *et al.*:[218]

$$\boldsymbol{d = e^{(3\frac{A_{SPR}}{A_{450}} - 2.2)}} \quad (5\text{-}1)$$

where A_{SPR} and A_{450} are the absorbance at the surface plasmon resonance peak (here, 1.0 at 519 nm based on the normalized spectrum) and 450 nm (absorbance = 0.628), respectively. The factors 3 and 2.2 in the correlation above are empirical parameters that were fitted by the authors from their experimental results. Using this relation and the A_{SPR} and A_{450} data (Figure 5-2), a diameter of ~13.2 nm is estimated for the synthesized AuNPs, which is close to the size determined from TEM images.

It has been reported that the absorbance peak of AuNPs shifts to longer wavelengths as the diameter increases.[219,220] A red-shift of the surface plasmon resonance also occurs upon modification of AuNPs surface with thiol groups. The covalent gold-thiol bonds reduce the density of free electrons in the AuNPs surface, which causes a decrease of the metal surface plasmon resonance.[221] Here, the immobilization of thiolated TbDNA oligonucleotides on the surface of the AuNPs resulted in a slight red shift to 523 nm, which confirms that the stability of AuNPs was retained with the salt-aging method used for DNA modification.

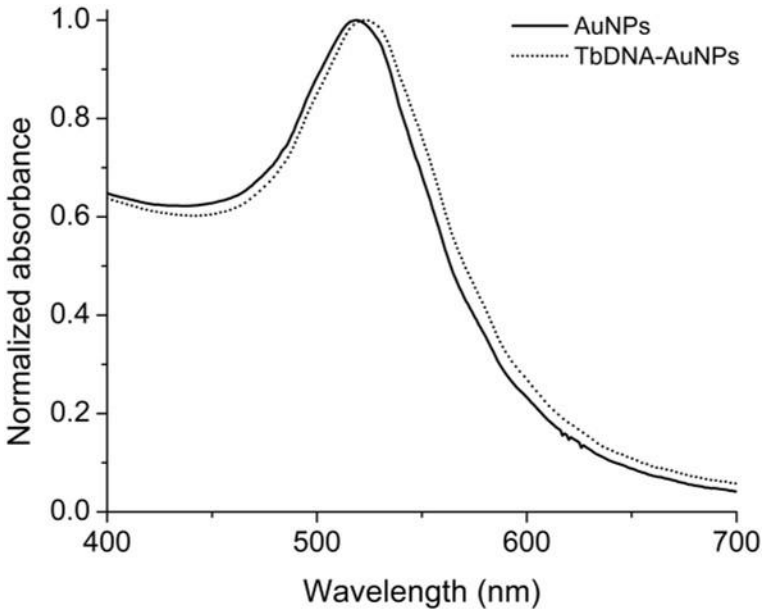

Figure 5-2 UV-Vis absorption spectra of citrate-capped AuNPs (solid line) and AuNPs conjugated with 27 nt-long DNA in a 1:200 nominal ratio (dotted line). The absorbance was normalized to Abs (λ_{max}) = 1.

The hydrodynamic size of nanoparticles was analyzed by DLS in order to characterize AuNPs' surface modification with thiolated DNA. Figure 5-3 shows a clear difference

in the average hydrodynamic diameter, D_h, between AuNPs and TbDNA-AuNPs. The uncoated AuNPs presented an average D_h of 22.6 ± 0.4 nm with a moderate polydispersity index of 0.35. As expected, this value is higher than the size determined from TEM images because DLS estimates the overall hydrodynamic diameter that includes the particle core with the surface coating and solvent layer.[222] The average D_h of AuNPs obtained here is in agreement with the relation between diameters of citrate-capped AuNPs as measured by DLS and TEM that was found by Hinterwirth *et al.*.[215] The authors characterized citrate-capped AuNPs with distinct sizes by DLS and TEM, and thus determined the linear correlation relationship $AuNPs\_DLS\ (nm) = 0.9968 \times AuNPs\_TEM\ (nm) + 8.8371.$

After the addition of thiolated TbDNA oligonucleotide to the AuNPs solution and the salting process, the average D_h increased to 29.1 ± 0.4 nm, with a moderate size distribution (polydispersity index = 0.18). This means that TbDNA was bound to the surface of AuNPs through the covalent bond between gold and sulfur resulting in a higher hydrodynamic diameter.[223]

The conformation and packing of the oligonucleotides at the surface of the AuNPs can influence their accessibility for hybridization.[224] This issue can be addressed through DLS measurements, where average D_h values of AuNPs coated with DNA provide information on the conformational state of the oligonucleotides. After DNA modification with 27-mer TbDNA oligonucleotides, the D_h of the nanoparticles increased 6.5 nm, which is significantly smaller than the estimated D_h at the stretched conformation (~39 nm), yet larger than twice the diameter of single stranded DNA (~1.1 nm).[169] This stretched length of TbDNA oligonucleotide can be estimated from the sum of the ~14 nm diameter of the bare AuNPs, twice the extension of the single stranded DNA (0.43 nm per base), and the thiol group linked by a carbohydrate (C6) at the 5' end (0.92 nm).[169,224,225] The experimentally obtained D_h suggests then that the strands were neither all wrapped around the particles nor fully stretched pointing perpendicular to the surface.

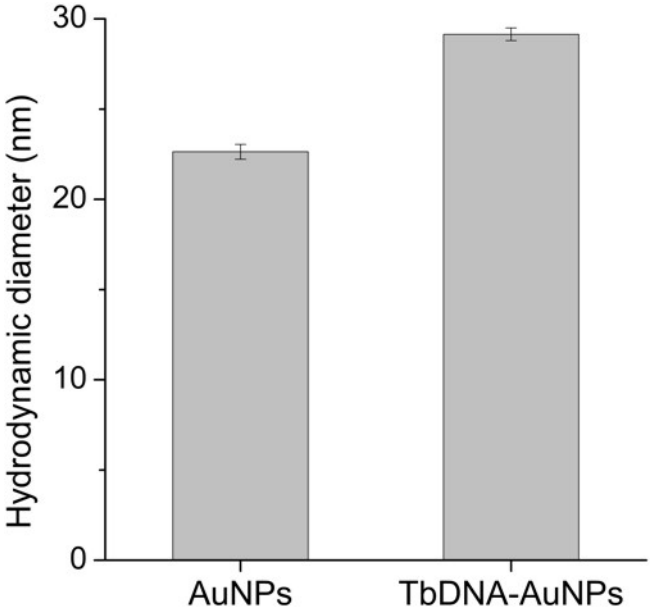

Figure 5-3 Dynamic light scattering (DLS) measurements to determine the average hydrodynamic diameter of AuNPs (22.63 ± 0.41 nm) and DNA-AuNPs (29.14 ± 0.35). Error bars represent standard deviations.

All these data demonstrate that citrate-capped AuNPs were successfully synthesized and modified with DNA to be used as probe.

Stability in solution

The effect of salt concentration in solution on the colloidal stability of AuNPs was investigated using UV-Vis absorption spectroscopy. A salt-induced aggregation test was performed by adding magnesium chloride to aqueous solutions containing nanoparticles, and their absorbance spectrum between 400 nm and 700 nm was measured to evaluate the stability of nanoparticles. If nanoparticles are well-dispersed in solution, as seen previously (Figure 5-2), they will absorb strongly at 520-525 nm and weakly at around 600 nm. After inducing aggregation upon salt addition, the nanoparticles stability can be quantified by taking the ratio between the absorbance at 525 nm (contribution of the fraction of isolated nanoparticles) and the absorbance at 600 nm (contribution of aggregated nanoparticles). Therefore, an A_{525}/A_{600} ratio value lower than 1 is indicative of aggregation, whereas a ratio higher than 1 indicates isolated nanoparticles in solution.

Figure 5-4A shows the absorbance spectra obtained for the synthesized citrate-capped AuNPs without and with $MgCl_2$ (10 mM). With the salt addition, a decrease in the absorbance at 525 nm was observed while the absorbance at 600 nm increased. The changes observed in the spectrum profile, which include a clear surface plasmon resonance shift toward the longer wavelength (λ_{max}~585 nm) and a significant peak broadening, suggest that AuNPs aggregated at this relatively low salt concentration.

The citrate shell surrounding AuNPs is responsible for an overall negatively charged surface and confers a moderate charge stabilization. Increasing the ionic strength of the solution by adding salt decreases the Debye length and, therefore, AuNPs aggregate due to strong van der Waals attraction between AuNPs.[226,227]

A change in the color of the AuNPs solution from red to blue was also observed, as a result of the shortening of the distance between nanoparticles, increased size of AuNPs aggregates, and the consequent changes of resonance absorbance peak (see the insets of Figure 5-4A).[228,229] The extent of AuNPs aggregation was estimated by calculating the A_{525}/A_{600} ratio from the spectra of the AuNP solutions with and without induced aggregation (Figure 5-4B). In agreement with the previous findings, the ratio value obtained is higher than 1 in the absence of $MgCl_2$ and lower than the aggregation threshold upon addition of salt.

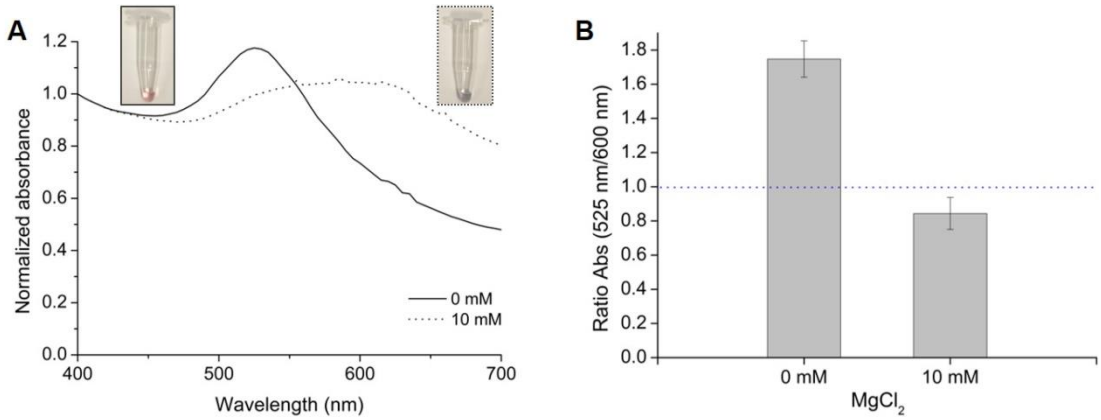

Figure 5-4 Aggregation profile of the synthesized AuNPs. (A) UV-Vis absorption spectra of AuNPs before (solid line) and after the addition of salt (dotted line). The absorbance was normalized to Abs (λ_{400}) = 1. The insets show the change in color that can be visualized by the naked eye. (B) Aggregation measured as the A_{525}/A_{600} ratio. Error bars represent standard deviations of triplicate measurements.

The salt-induced aggregation test performed to evaluate the integrity of the colloidal TbDNA-AuNPs solution after surface modification was based on the addition of increasing amounts of $MgCl_2$ to aqueous solutions containing a fixed concentration of nanoparticles. As shown in Figure 5-5A, the TbDNA-modified AuNPs remained stable between 0 and 120 mM of $MgCl_2$ with absorbance spectra presenting a single peak around 525 nm. With higher amounts of salt, there is a clear shift of the surface plasmon resonance band to longer wavelengths toward approximately 600 nm. The loading of single stranded DNA on the surface of the AuNPs increases the negative charge of the nanoparticles. This improves their stability against aggregation at certain salt concentrations due to an additional increase in electrostatic repulsion.[230] For the quantitative assessment of TbDNA-AuNPs stability upon salt addition, the ratio between the absorbance at 525 nm and absorbance at 600 nm was calculated and plotted against $MgCl_2$ concentration (Figure 5-5B). The ratio value gradually decreases with increasing amounts of salt, but remains higher than 1 (*i.e.* with still some contribution of isolated nanoparticles in solution) at up to 120 mM $MgCl_2$. At higher salt concentrations, the A_{525}/A_{600} ratio is very close to 1 and crosses below the

aggregation threshold value from 180 mM onwards. This result demonstrates the higher stability of DNA-modified AuNPs upon addition of salt, an expected effect as the gold surface is shielded by a layer of conjugated ssDNA that can prevent aggregation until a critical electrolyte concentration is exceeded.

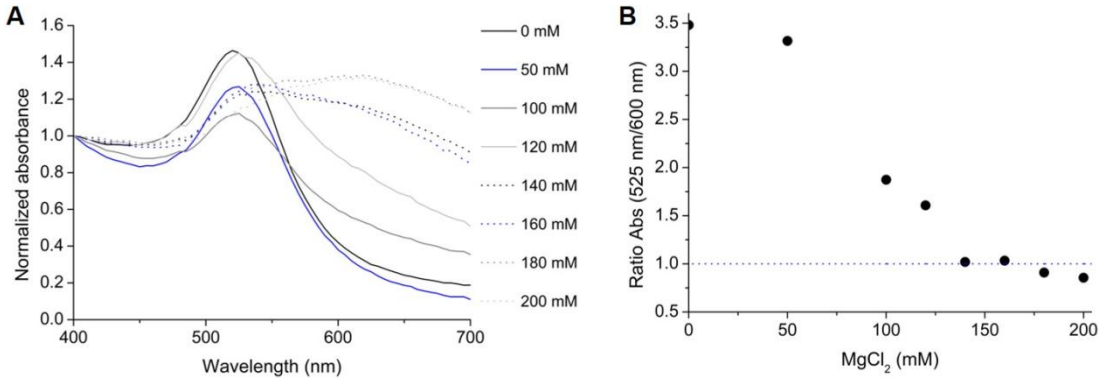

Figure 5-5 Aggregation profile of TbDNA-AuNPs at increasing concentrations of $MgCl_2$. (A) UV-Vis absorption spectra of TbDNA-AuNPs mixed with selected amounts (0-200 mM) of $MgCl_2$. (B) Aggregation measured as the A_{525}/A_{600} ratio across a range of $MgCl_2$ concentrations (0, 50, 100, 120, 140, 160, 180 and 200 mM).

UV-Vis spectroscopy provided a simple method to assess the stability of nanoparticles dispersion in aqueous solution upon addition of salt and assess their surface modification with DNA.

Molecular recognition and complexation

Gold nanoparticles and TbDNA-AuNPs conjugates, as well as their complexes with other components of the DNA recognition system (e.g. biotin-labeled target DNA, anti-biotin IgG), were assayed via agarose gel electrophoresis. Samples were thus prepared that contain AuNPs and different combinations of the different molecular components. The complexes formed within each mixture are expected to migrate differently depending on their relative size and net charge.[231,232] The red color of the colloidal gold was used to visually monitor the progression of the complexes through the gel with the naked eye.

Figure 5-6A shows an image of an agarose gel loaded with bare AuNPs, TbDNA-AuNPs, and mixtures of TbDNA-AuNPs with other biomolecules. Citrate-capped AuNPs (lane 1) were essentially confined to the well and nearby region, showing up as a smeared faint band. This migration pattern suggests that different extents of aggregation occurred and AuNPs could not fully migrate through the gel matrix, even though they are negatively charged on account of the citrate capping.[233,234] On the contrary, the greater stability of AuNPs upon surface modification with DNA, together with the expected increase in the net charge per nanoparticle, allowed a relatively rapid and uniform migration (lane 2). Likewise, complexes containing

TbDNA-AuNPs in the other samples run as sharp bands with distinctive electrophoretic velocities (lanes 3-7).

The addition of biotinylated target DNA and anti-biotin antibody to the TbDNA-modified AuNPs resulted in observable changes in the electrophoretic mobility of the complexes (Figure 5-6B). A gradual retardation of the gel bands occurred when TbDNA-AuNPs were mixed with increasing amounts of complementary target DNA (lanes 3-5), providing a strong indication of the hybridization of the TbDNA sequences attached to the AuNPs surface to the target. The gel bands resulting from the hybridization of TbDNA-AuNPs with different concentrations of complementary DNA are all well-defined and have similar widths, suggesting that the target DNA molecules hybridized evenly with the nanoparticles probes available in solution prior to gel loading. The slower migration of the TbDNA-AuNPs·DNA complex as more targets are included results most likely from an increase in the mass. In the presence of non-complementary DNA (lane 6), the migration pattern was similar to the one obtained for TbDNA-AuNPs alone (lane 2). This indicates that the hybridization observed in lanes 3 to 5 was sequence-specific. The ability of anti-biotin IgG to recognize and bind to the TbDNA-AuNPs·DNA complex was also tested (lane 7). The significant retardation of the band confirms the binding of the antibody to the TbDNA-AuNPs·DNA complex, which resulted in a larger complex with a consequently lower electrophoretic mobility. A reduction in the overall net charge of the complex could also explain this lower mobility. However, given that the isoelectric point of antibodies is in general of the order of 7-8, which is close to the pH of 8.3 of the electrophoresis running buffer, significant changes in the overall charge are not expected.

The migration result observed in lane 7 also indicates that, despite being hybridized with a DNA probe that was attached to AuNPs, the biotin label of the target oligonucleotide was accessible for recognition by the antibody in solution. A control with non-complementary target DNA could have been considered to test non-specific interactions between the antibody and the nanoparticles.

Overall, the differential migration pattern of the complexes observed by electrophoresis analysis confirmed the presence of the expected molecular interactions between the different components of the DNA recognition system, supporting the use of AuNPs coated with DNA probe sequences as a colorimetric reporter.

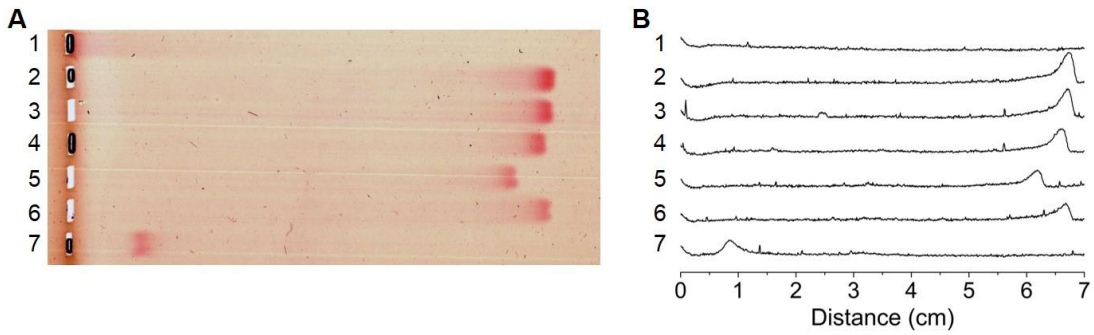

Figure 5-6 Agarose gel electrophoresis analysis of the interactions of TbDNA-modified AuNPs with (non-)complementary target DNA and anti-biotin antibody. (A) Image of the agarose gel with bands that are directly visible by the red color of the AuNPs. Note that tracks 1, 2, 4 and 7 present air bubbles trapped in the wells. (B) Electrophoretic profile plots for all tracks from cathode to anode direction, starting from the sample wells. Lanes ID: 1- AuNPs; 2- TbDNA-AuNPs; 3- TbDNA-AuNPs + C-TbDNA 0.05 pmol; 4- TbDNA-AuNPs + C-TbDNA 0.5 pmol; 5- TbDNA-AuNPs + C-TbDNA 10 pmol; 6- TbDNA-AuNPs + NC-TbDNA 10 pmol; 7- TbDNA-AuNPs + C-TbDNA 10 pmol + anti-biotin IgG.

Sequence-specific target binding

The ability of the TbgDNA-AuNPs and TbrDNA-AuNPs probes to specifically hybridize with their respective complementary DNA sequences was assessed through the non-cross-linking aggregation method developed by Baptista *et al.*.[209,235] This methodology is based on the colloidal stability of DNA-modified AuNPs against salt and on the effect of nanoparticles aggregation on their optical properties. Basically, aggregation of DNA-AuNPs occurs in the absence of a complementary sequence at a critical salt concentration, shifting the absorbance peak to longer wavelengths and turning the solution blue. Upon hybridization with a complementary target, DNA-AuNPs remain dispersed in solution with a red color after salt addition. The color change can be visualized with the naked eye and quantitatively analyzed by UV-Vis spectroscopy.

The minimum amount of $MgCl_2$ required to aggregate each probe was first determined by exposing aqueous solutions with a fixed amount of TbgDNA-AuNPs or TbrDNA-AuNPs to increasing concentrations of salt. Based on the UV-Vis absorbance spectra measured after salt-induced aggregation test, the aggregation statuses were analyzed in terms of the A_{525}/A_{600} ratio and plotted against the concentration of $MgCl_2$ in solution. A ratio value of 1 was considered as threshold to differentiate dispersed (ratio > 1) from aggregated (ratio < 1) nanoparticles. As shown in Figure 5-7A, a minimum of 30 mM $MgCl_2$ caused full aggregation of both probes, so these conditions were selected for testing the specific hybridization of TbgDNA-AuNPs and TbrDNA-AuNPs with their respective target DNA sequences.

The hybridization assay was then performed by incubating each probe with C-TbgDNA or C-TbrDNA sequences, followed by the addition of $MgCl_2$ to a final concentration of 30 mM. Hybridization events were confirmed through the nanoparticles aggregation status, which was visually interpreted through the solution

color and quantitatively analyzed based on the A_{525}/A_{600} ratio. As the ratio value of 1 can be considered as an equilibrium point between dispersed and aggregated nanoparticles, it was used to discriminate complementary (ratio > 1) and non-complementary (< 1) sequences. The data in Figure 5-7B indicates that the TbgDNA-AuNPs and TbrDNA-AuNPs were protected from salt-induced aggregation when mixed with their respective complementary targets, since the solutions remained red after the addition of salt and the resultant ratio A_{525}/A_{600} was higher than 1. This result confirms the formation of TbgDNA-AuNPs·C-TbgDNA and TbrDNA-AuNPs·C-TbrDNA conjugates. The hybridization specificity was further tested by exposing TbgDNA-AuNPs and TbrDNA-AuNPs to C-TbrDNA and C-TbgDNA, respectively. The presence of non-complementary targets did not protect nanoparticles probes from aggregation, since the addition of salt turned the solutions blue and the resultant ratio A_{525}/A_{600} was lower than 1.

Based on this non-cross-linking assay, TbgDNA-AuNPs can differentiate its complementary target sequence C-TbgDNA from C-TbrDNA, and the other way around for TbrDNA-AuNPs.

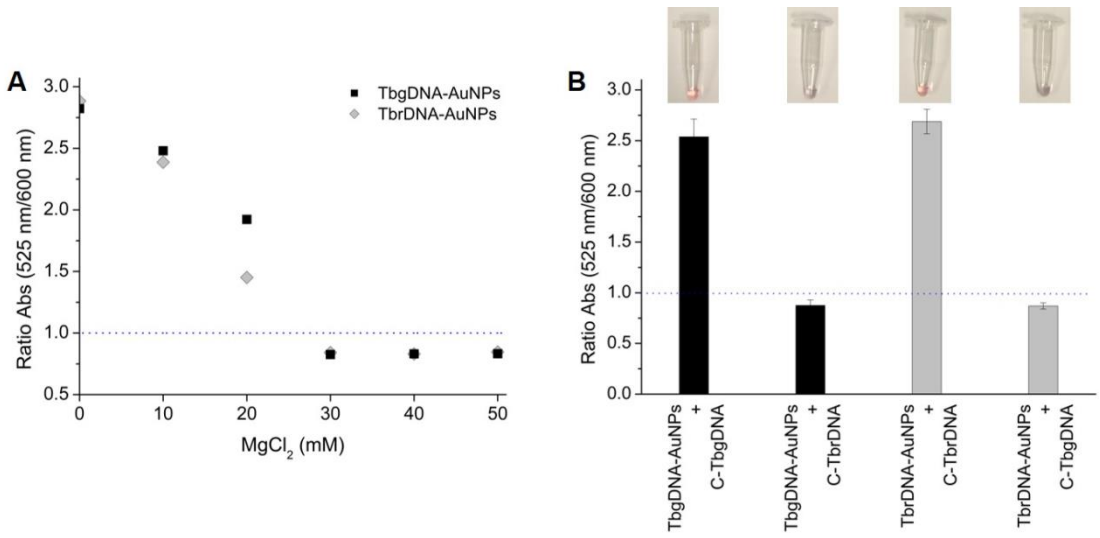

Figure 5-7 Non-cross-linking aggregation method for the differential hybridization of TgbDNA- or TbrDNA-modified AuNPs through the calculation of the ratio of A_{525}/A_{600}. (A) Stability of TbgDNA-AuNPs (black circles) and TbrDNA-AuNPs (gray circles) assessed through their aggregation profiles at increasing concentrations of $MgCl_2$. (B) Hybridization assay (30 µl total volume) between the AuNPs-probes (2.5 nM final concentration) and C-TbgDNA or C-TbrDNA targets (0.33 µM final concentration). Error bars represent the standard deviation of triplicate measurements.

5.4 Conclusions

Gold nanoparticles constitute promising tools for colorimetric bioassays due to their optical properties and predisposition for surface modification.[118] With the intent of

preparing a colorimetric reporter to be incorporated in the cellulose-based DNA recognition system explored in this thesis (see Figure 2-1 of Chapter 2), AuNPs were synthesized using the citrate reduction method. To be used as colorimetric probes for the detection of biotinylated DNA targets, these citrate-capped AuNPs were then conjugated with three different sequences of thiol-modified oligonucleotides of 27-nt length each (TbDNA, TbgDNA and TbrDNA) by the salt-aging method. The synthesized and DNA-functionalized AuNPs were then characterized in terms of their size, structure morphology, optical properties and colloidal stability upon salt addition. The TEM imaging confirmed the synthesis of monodisperse round-shaped AuNPs with an average diameter of ~14 nm. The gold surface modification with thiolated DNA was evaluated by DLS and UV-Vis. An increase in the hydrodynamic diameter and a slight red-shift of the surface plasmon resonance peak was obtained in relation to non-functionalized AuNPs, thus confirming the functionalization of AuNPs surface with TbDNA. Furthermore, the demonstrated colloidal stability of DNA-AuNPs conjugates upon salt addition is compatible with their use as colorimetric probes in molecular recognition tests in which salt-containing solutions are used.

Molecular recognition experiments were carried out to assess the ability of the synthesized DNA-AuNPs to bind to other biomolecules. The electrophoretic migration of TbDNA-AuNPs and complexes prepared thereof by addition of biotinylated target DNA and anti-biotin IgG were analyzed by agarose gel electrophoresis. The electrophoretic mobility of complexes prepared by the specific hybridization of TbDNA-AuNPs with a complementary biotinylated DNA target was lower that the mobility observed for TbDNA-AuNPs alone or in the presence of a non-complementary target. In addition, the accentuated decrease in electrophoretic mobility upon addition of an anti-biotin antibody suggests the formation of complexes of biotinylated DNA·TbDNA-AuNPs conjugates with IgG.

TbgDNA-AuNPs and TbrDNA-AuNPs probes were able to discriminate their respective complementary DNA targets from non-complementary sequences - with TbrDNA as non-complementary target for TbgDNA-AuNPs, and vice versa -, as tested by the non-cross-linking method.

These results confirm the functionality of DNA-AuNPs as probes for the colorimetric detection of DNA targets. Moreover, the capture of DNA-AuNPs hybridized with the biotinylated DNA target through an anti-biotin antibody supports its incorporation in a supramolecular system.

Chapter 6

Colorimetric DNA recognition on cellulose using ZZ-CBM fusions

6.1 Introduction

The development of bioactive paper-based sensors has been aimed at analytical applications in medical diagnostics, food safety and environmental control.[18,22–25] The simplicity of paper devices fabrication, the possibility of cellulose surface modification, as well as the flexibility and versatility of bioactive paper formats, makes paper a convenient platform for bioanalytical tools.[17] Fabrication techniques of paper-based devices can either be based on paper shaping/cutting, on the blocking of pores or on the hydrophobization of paper fibers. Among the current methods, wax-printing has been reported to be a simple, non-toxic and cost-effective approach to manufacture paper devices at laboratory-scale.[51] This method is based on the printing of wax patterns on paper and the subsequent paper heating to melt the wax and create hydrophobic barriers that define hydrophilic zones (channels, reaction wells).[63,64]

Given the suitability of cellulose paper as substrate for analytical devices, various formats of paper-based platforms for nucleic acid detection have been developed. For example: cut paper strips modified with covalently attached ssDNA oligonucleotides for the capture of target DNA through capillarity after soaking the paper strips into the liquid sample; origami-based paper analytical devices (*o*PAD) prepared by wax printing and paper folding into aligned layers, thus creating three-dimensional hydrophobic barriers that define hydrophilic channels and reagents reservoirs for DNA probe and quencher deposition; DNA quantification in wax patterned channels comprising a circular sample loading zone with deposited DNA intercalating dye and a linear test zone, in which dsDNA acts as an eluting agent and is quantified through the migration distance of the dye upon sample loading; among others.[24,73,81]

A convenient paper-based analytical device cannot depend on access to equipment, for example, for output signal reading.[236,237] In this context, colorimetry has been reported to be the most suitable detection technique to integrate with paper sensors, not only because it can allow direct detection by naked-eye but also because it is compatible with relatively affordable reporting systems based on digital image analysis, including mobile device's camera and scanners.[237,238]

In the previous chapters of this thesis, critical components for the development of "reader-free" bioactive paper sensors for nucleic acid detection have been addressed: efficient immobilization of biorecognition agents (antibodies) on cellulose matrices via biochemical coupling using CBMs; colorimetric reporting using DNA-coated gold nanoparticles. This chapter describes the development of bioactive cellulose (paper or microparticles) for the colorimetric nucleic acid detection using the biomolecular recognition approach based on the ZZ-CBM fusions presented in Chapters 3 and 4. The first and second parts of the chapter focus on the implementation of this colorimetric DNA recognition system on wax-printed paper reaction wells and microfluidic channels, respectively (see Figure 6-1A and B). In both paper platforms, the efficiency of the capture of biotinylated DNA by anti-biotin IgG immobilized on paper via ZZ-CBM is compared with a physical adsorption strategy where antibodies are simply spotted and air-dried on paper. In addition, the colored signal intensity obtained with the proposed ZZ-CBM based recognition system at various concentrations of AuNP-labeled DNA is assessed, as well as its ability to discriminate complementary from non-complementary DNA sequences. Finally, an alternative approach using cellulose microparticles functionalized with anti-biotin:ZZ-CBM complexes is tested for the specific capture of labeled complementary DNA in solution (Figure 6-1C).

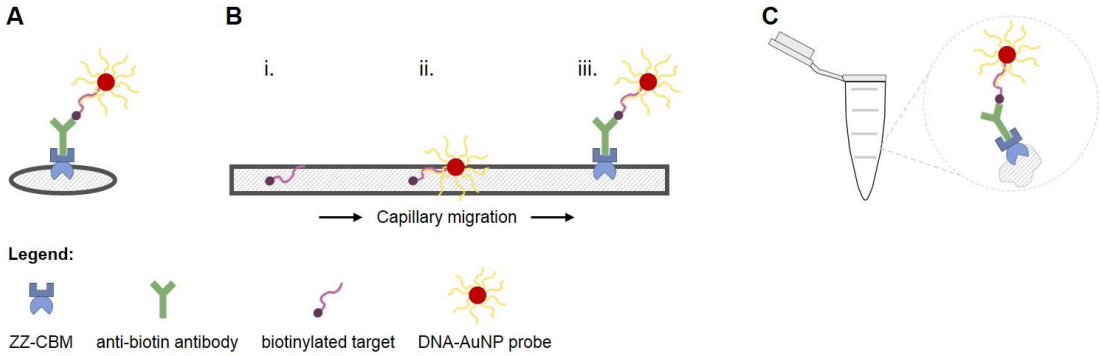

Figure 6-1 Schematic representation of the cellulose-based assays designed for the colorimetric detection of biotin-labeled DNA, after hybridization with DNA-AuNPs probes and subsequent capture by an anti-biotin antibody anchored onto cellulose *via* ZZ-CBM fusions. (A) Paper-based spot test: reaction wells are wax-patterned on paper and a red colored spot is visualized after the capture of target DNA:DNA-AuNPs hybrids by antibody:ZZ-CBM conjugates. (B) Paper-based lateral flow assay using wax printed channels: (i) a sample containing the target DNA is loaded on the paper channel; (ii) during migration by capillarity through the hybridization zone, the solution takes up impregnated DNA-AuNPs probes, which hybridize with the biotinylated target DNA strands; (iii) these hybrids are subsequently captured in the detection zone by an anti-biotin IgG attached through ZZ-CBM fusions resulting in a red colored spot. (C) DNA detection assay in solution using cellulose microparticles, which turn red after the capture of target DNA:DNA-AuNPs hybrids by the IgG:ZZ-CBM conjugates.

6.2 Experimental

Materials

All oligonucleotides used in this study (Table 6-1) were obtained from STABVIDA (Portugal). The 17-nt long target DNA sequences C-TbDNA, C-TbgDNA and C-TbrDNA are biotinylated at the 5' end and are complementary to the probe sequences designed for the detection of *Trypanosoma brucei* species (TbDNA), *T. b. gambiense* (TbgDNA) and *T. b. rhodesiense* (TbrDNA) subspecies, respectively. The biotin-labeled oligonucleotides NC-TbDNA, C-TbrDNA and C-TbgDNA were tested as non-complementary sequences for TbDNA, TbgDNA and TbrDNA probe sequences, respectively. All probe sequences contain a 5' modification with a thiol and a 10-adenine spacer. For details on the sequences design, see section 5.2 "Experimental" of the previous chapter.

Table 6-1 Sequences and modifications of the 17 nt DNA targets from *Trypanosoma brucei* (*T.b.*), *Trypanosoma brucei gambiense* (*T.b.g.*) and *Trypanosoma brucei rhodesiense* (*T.b.r*), and of their respective 27 nt probes. Each DNA probe contains a 10-adenine spacer (highlighted in bold). Both TbgDNA and TbrDNA probe sequences, as well as the respective complementary target sequences, contain six nucleotides in a row that are identical (highlighted in underline). These sequences share ~53% identity as obtained from LALIGN analysis (https://embnet.vital-it.ch/software/LALIGN_form.html).[208]

Oligonucleotide	DNA sequence (5'-3')
TbDNA: *T.b.* DNA probe	Thiol-**AAAAAAAAAA**TTGTGTTTACGCACTTG
C-TbDNA: *T.b.* complementary target	Biotin-CAAGTGCGTAAACACAA
NC-TbDNA: *T.b.* non-complementary target	Biotin-TCCAGGGAAATGTCACGTCC
TbgDNA: *T.b.g.* DNA probe	Thiol-**AAAAAAAAAA**TATCTAGG<u>AAGGTA</u>CGA
C-TbgDNA: *T.b.g.* complementary target	Biotin-TCG<u>TACCTT</u>CCTAGATA
TbrDNA: *T.b.r.*-DNA probe	Thiol-**AAAAAAAAAA**TCAC<u>AAGGTA</u>AGACAGA
C-TbrDNA: *T.b.r.* complementary target	Biotin-TCTGTCT<u>TACCTT</u>GTGA

Whatman grade 1 chromatography paper (25 × 25 cm) was purchased from VWR (catalog number: 3001-878). According to the manufacturer's specifications, it is composed of >98% cellulose, has a linear flow rate of water of 130 mm/30 min, a thickness of 180 µm and a basis weight of 87 g/m^2. This paper substrate has demonstrated to provide a better analytical performance in comparison to other grades of Whatman filter or chromatography paper, with higher color intensity and uniformity.[36] Sigmacell cellulose type 20 microparticles (S3504) was obtained from Sigma-Aldrich (St. Louis, Missouri). Both cellulose chromatography paper and microparticles were used without any previous treatment in all assays.

Mouse monoclonal anti-biotin (IgG2a) was obtained from Abcam, UK (ab36406). All chemicals were purchased from Fisher Scientific, except for Tween 20 (VWR), ampicillin, gold(III) chloride trihydrate and trisodium citrate and DTT (Sigma-Aldrich). Ultrapure water used for buffer preparation was obtained with a Milli-Q

purification system (Merck-Millipore).

Tris-saline Tween 20 buffer (TST; 50 mM Tris buffer, pH 7.6, 150 mM NaCl, 0.05% Tween 20) was used as a reaction buffer in the DNA detection assays on wax-printed paper wells and on cellulose microparticles in solution. TST buffer and its modified version without salt (TT; 50 mM Tris buffer, pH 7.6, 0.05% Tween 20) were used as reaction/washing buffers in the wax-printed microchannel assays for the detection of TbDNA probe target sequences and for the discrimination of the TbgDNA/TbrDNA targets, respectively.

Construction, production and purification of ZZ-CBM fusions

Both ZZ-CBM3 and ZZ-CBM64 fusion proteins were prepared as described previously (see section 3.2 "Experimental" of Chapter 3).[67] Briefly, *E. coli* cells, transformed with the plasmid containing the genes encoding ZZ and CBM3 or CBM64 proteins, were grown and induced with IPTG for protein expression. After the incubation at 37 ºC for 16 hours and harvesting, cells were disrupted by sonication for protein extraction. The fusion proteins were isolated by affinity chromatography on an IgG Sepharose column, and then analysed by SDS-PAGE. The purified ZZ-CBM3 and ZZ-CBM64 fusions were quantified by BCA protein assay and stored at -20 ºC until required.

Synthesis and conjugation of DNA-coated gold nanoparticles

Gold nanoparticles with an average diameter of ~14 nm were synthesized by the citrate reduction method of $HAuCl_4$, first described by Turkevich *et al.* and Frens, as explained previously (see section 5.2 "Experimental" of Chapter 5).[201,202] DNA-coated gold nanoparticles were prepared in a 1:200 (AuNP:DNA) theoretical molar ratio following an adaptation of the method described by Hurst *et al.*.[203] Briefly, nanoparticles were salt-aged to 300 mM NaCl in the presence of the thiol-modified oligonucleotides (TbDNA, TbgDNA or TbrDNA). After a 16-hour incubation in the dark, DNA-AuNPs were washed, resuspended in 10 mM phosphate buffer (pH 8), 100 mM NaCl and stored in the dark at 4 ºC until further use.

Patterning paper by wax printing

Patterns of hydrophobic barriers – circumferences with a nominal diameter of 5 mm or microchannels as represented in Figure 6-2 – were designed as black or yellow lines of 400 µm nominal thickness on a white background using AutoCAD drawing software. The patterns were printed on paper using a Xerox ColorQube 8570 color printer set for enhanced resolution printing. The printed wax was then melted by contacting the back of the paper with a hot plate (magnetic stirrer/heat plate MR Hei-Standard, EKT Hei-Con) for 2 minutes at 150°C. The wax-printed paper is ready to be used after cooling at room temperature.

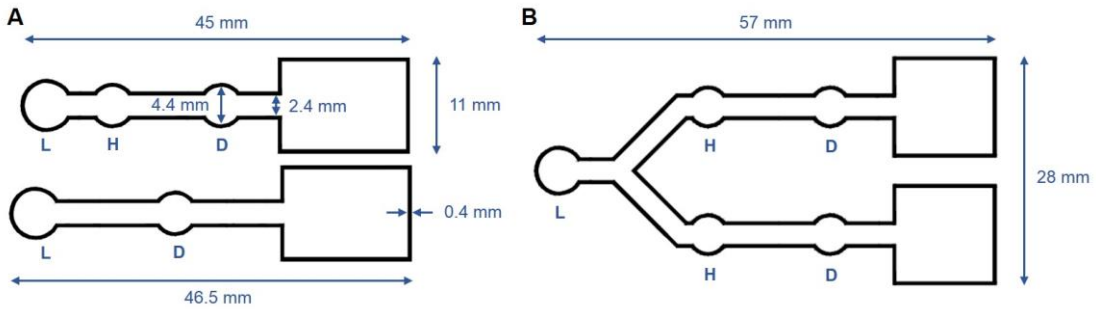

Figure 6-2 Schematic illustration of the general structure of (A) single and (B) two-arm wax patterned channels. The designs essentially comprise circular areas for sample loading (L), hybridization (H) and detection (D), one or two linear channels and a rectangular reservoir on the right side. Nominal dimensions indicated by the drawing software are depicted in blue.

Spot assays in wax-printed circular areas on paper

Wax-printed circular paper wells were used to capture DNA hybrids by antibodies attached to paper through ZZ-CBM fusions. The efficiency of the fusion-mediated capture was compared with the efficiency obtained when antibodies were immobilized by physical adsorption. For paper functionalization by biochemical coupling with CBM-ZZ:anti-biotin IgG conjugates, mixtures of 2 pmol of fusion protein (0.4 µL of 5 µM ZZ-CBM3) and 5 pmol of antibody (0.75 µL of 6.67 µM anti-biotin IgG) were prepared in TST buffer up to a final volume of 2 µL and incubated at RT for 20 min. In parallel, an equal volume solution containing 5 pmol of antibody only in TST buffer was prepared for the physical adsorption strategy. Each solution containing anti-biotin IgG or antibody:ZZ-CBM3 conjugates is then pipetted onto the center of the paper reaction well, 0.5 µL at a time, for four times, with air-drying at RT between applications. Five-microliter DNA solutions - 2.5 µL of 30 nM DNA-AuNPs, 1 µL of biotin-labeled target DNA (0-10 pmol of complementary target or 10 pmol of non-complementary target) and 1.5 µL of TST buffer – pre-incubated for 20 min at RT were then applied to the functionalized paper reaction wells. Paper wells were allowed to dry on air at RT for 35-40 minutes, while hanging horizontally in the air, and then imaged for color intensity analysis (see the subsection entitled “Signal analysis of the wax-printed paper tests” for details).

DNA recognition by capillary transport in wax-printed paper channels

Paper channels with a single reaction zone (Figure 6-2A, bottom) were used to assess the ability of anti-biotin antibodies anchored on paper *via* ZZ-CBM to capture DNA hybrids during migration by capillarity through the channel’s detection zone, and to compare the efficacy of the capture with antibodies attached to paper by plain physical adsorption. Wax-printed paper microchannels were prepared by pipetting onto each detection zone a 2-µL solution containing 5 pmol of antibody (0.75 µL of 6.67 µM anti-biotin IgG), alone or mixed with 2 pmol of fusion protein (0.4 µL of 5 µM ZZ-CBM3). The mixtures were prepared in TST buffer to a total volume of 2 µL

and incubated at RT for 20 minutes prior to application on paper in a series of four, 0.5-µL fractions. The test solutions containing biotinylated target DNA (1 µL of 10 µM C-TbDNA) and probe (2.5 µL of 30 nM TbDNA-AuNPs) were prepared in TST buffer (1.5 µL), and then incubated at RT for 20 minutes. Each test solution was applied in the sample loading zone (see Figure 6-2A) with the paper channel hanging horizontally in the air (see Figure 6-A1 of the section 6.5 "Appendix: Colorimetric detection of labeled DNA hybridized with DNA-coated gold nanoparticles on wax-printed paper" - Appendix). After solution migration along the channel, 15 µL of TST buffer was added to the sample loading zone three times with 5 minutes interval to ensure complete migration of the DNA sample through the detection zone and wash-off excess of non-captured probe into the reservoir area. Once air-dried at RT, the upper part of the paper channels was imaged for detection signal analysis (see the subsection "Signal analysis of the wax-printed paper tests").

Paper channels with two reaction zones (Figure 6-2A, top) were explored to test i) the hybridization of loaded target DNA with DNA-AuNPs, previously deposited in the hybridization zone, during capillary transport, and ii) the subsequent capture of DNA hybrids in the detection zone by antibodies immobilized through the ZZ-CBM3 fusion. In preparation for the hybridization and capture assay, 2.5 µL of 30 nM TbDNA-AuNPs were pipetted onto the hybridization zone 5×0.5 µL volumes with air drying in-between applications, and the detection zone was functionalized with anti-biotin IgG:ZZ-CBM3 conjugates as explained above. Test solutions of 15 µL total volume containing biotinylated target DNA (0-10 pmol of C-TbDNA or 10 pmol of NC-TbDNA) diluted in TST buffer were applied into the sample loading zone, followed by the addition of 3×15 µL TST buffer into the paper channel. After drying, the paper channels were scanned for signal intensity measurements (see the next subsection for further details).

Two-arm paper channels (Figure 6-2B) were used to compare the efficacy of the capture of C-TbDNA:TbDNA-AuNPs hybrids by anti-biotin immobilized *via* ZZ-CBM3 or ZZ-CBM64 fusions and to test the specific hybridization and capture of C-TbgDNA and C-TbrDNA sequences.

The preparation of functionalized paper channels for the hybridization and capture of DNA hybrids by antibody:ZZ-CBM3 or antibody:ZZ-CBM64 conjugates followed a protocol similar to the one used for the preparation of single channels with two reaction zones: the two hybridization zones were prepared by spotting 5×0.5 µL of TbDNA-AuNPs and each detection zone was functionalized either with anti-biotin IgG:ZZ-CBM3 or IgG:ZZ-CBM64 conjugates (mixtures of 5 pmol of antibody and 2 pmol of fusion protein in TST buffer). After applying a 15-µL solution of 10 pmol C-TbDNA in TST buffer, 30 µL of TST buffer were loaded into the paper channels every 5 minutes for a total of three applications. After drying, paper channels were digitalized for detection signal measurements, as explained in the next subsection.

For the functionalization of paper channels for the discrimination of C-TbgDNA and C-TbrDNA, 2-µL mixtures of 5 pmol of antibody (0.75 µL of 6.67 µM anti-biotin IgG) and 2 pmol of fusion protein (0.4 µL of 5 µM ZZ-CBM3) were prepared in a salt-free version of TST buffer (TT; 50 mM Tris buffer, pH 7.6, 0.05% Tween 20), and then incubated 20 minutes at RT for proteins conjugation. Antibody:ZZ-CBM3 conjugates were then applied on the detection zone in a series of 4×0.5 µL applications. The paper channels were then rinsed five times with 30 µL of the TT buffer to remove the salt contained in the conjugates mixture from the detection zone. After air-drying at RT, 5×0.5 µL of TbgDNA-AuNPs or TbrDNA-AuNPs were applied into the respective hybridization zones. Test solutions containing 10 pmol of C-TbgDNA or C-TbrDNA alone (1 µL of 10 µM solutions), or a mixture of 10 pmol of C-TbgDNA and 10 pmol of C-TbrDNA, were prepared in TT buffer to a final volume of 15 µL. After loading each test solution into the sample loading zone, 3×30 µL TT buffer were applied into the channels with 5 minutes intervals. Paper channels were finally imaged after drying at RT for detection signal analysis (see the next subsection for details).

Signal analysis of the wax-printed paper tests

Test results were recorded by scanning the tested paper devices (circles or microchannels) with an HP Scanjet 4400c scanner, with settings set to a medium level of distinctness and a dpi of 600.

The average grey intensity of the circular test areas was measured using the freeware ImageJ as described by Jokerst et al..[70] First, JPEG images were converted to 8-bit and inverted. The colored regions generated by the gold nanoparticles within each circular test area were then individually selected by using the "Circle Tool" macro with a fixed size. The grey intensity of this area, which is proportional to the color intensity of each spot, was then measured using the "Measure" tool. The background was removed by subtracting the mean grey intensity of the non-functionalized paper wells or channels' detection areas exposed to DNA-AuNPs only. Color intensity profiles were generated using the "Plot Profile" and "Surface Plot" commands in ImageJ after drawing a line crossing the center of a DNA detection area and selecting the whole reaction well, respectively (grayscale pixel intensity range from 0 to 255 arbitrary units on an 8-bit scale).

The Red Green Blue (RGB) analysis of paper wells was performed using the ImageJ software. First, RGB type images in JPEG format were converted to multi-channel stacks by using the "Make composite" tool. The center of the paper wells was then individually selected by using the "Circle Tool" macro with a fixed size and the average intensity of each of the red and blue color channels was measured. Finally, the red-to-blue ratio was calculated for each sample.

UV-visible spectroscopy was performed to measure the absorbance spectrum of paper reaction wells in the 400-700 nm region. In preparation for the absorbance

measurements, the outside perimeter of wax-printed circles was cut out and each paper well was placed face-up in each well of a 96 well plate. The absorbance was measured using a SpectraMax Plus 384 Microplate Reader.

Detection of DNA in solution through functionalized cellulose microparticles

The ability of anti-biotin IgG:ZZ-CBM3 conjugates immobilized on suspended cellulose microparticles to capture biotinylated target DNA:DNA-AuNPs hybrids was tested. In preparation for the assay, suspensions of 20 mg/ml cellulose microparticles were prepared by mixing 20 mg of cellulose powder (Sigmacell cellulose type 20) in 1 ml of TST buffer, and then 50 µL of the mixture were pipetted into Eppendorf tubes after vortexing. This step was repeated as necessary to allow preparation of the required number of 50-µL suspensions to be tested. For cellulose functionalization, a 2-µl solution containing anti-biotin antibody:ZZ-CBM3 conjugates (0.75 µL of 6.67 µM anti-biotin IgG, 0.4 µL of 5 µM ZZ-CBM3, 0.85 µl of TST buffer), which was pre-incubated 20 minutes at RT for protein conjugation, was added to each 50-µl cellulose suspension and incubated at RT for 20 minutes. Five µL DNA sample solutions pre-incubated 20 minutes at RT - 2.5 µL of 30 nM DNA-AuNPs, 1 µL of biotin-labeled target DNA (0-10 pmol) and 1.5 µl of TST buffer – were added to the functionalized cellulose microparticles, followed by an incubation of 20 minutes at RT for the capture of complementary DNA hybrids by the immobilized IgG:ZZ-CBM3 conjugates. Images of cellulose microparticles were captured with an Olympus E-PM1 camera after cellulose microparticles settled to the bottom of the tubes by gravity and after centrifugation for 15 minutes at 10,000 g.

Signal analysis of the tests in suspended cellulose microparticles

The relative amount of non-captured probes was assessed by analysing the absorbance of supernatants (30-µL) obtained after gravity settling of the cellulose microparticles at 525 nm (*i.e.*, the typical absorbance peak of DNA-AuNPs). The absorbance spectra (400-700 nm) of supernatants was measured in a microplate reader (SpectraMax Plus 384 Microplate Reader) and corrected by subtracting the spectra of a supernatant obtained when cellulose microparticles were mixed with TST buffer alone. For every set of results the sum of the individual absorbance values at 525 nm of each entire set of concentrations range (0-10 pmol of target DNA) was taken as 100%. The total amount of non-captured probes at each target DNA concentration was then calculated as a partial percentage of the total absorbance.

Scanning Electron Microscopy

Observations of paper reaction wells and cellulose microparticles were performed by scanning electron microscopy (SEM) using a FEG-SEM JEOL model JSM7001F equipment. Selected samples for SEM analysis were as follows: unmodified or modified (with anti-biotin IgG or anti-biotin IgG:ZZ-CBM3) circular paper wells exposed to TbDNA-AuNPs alone or mixed with (non-)complementary biotinylated

target DNA; unmodified or functionalized (with anti-biotin IgG:ZZ-CBM3) cellulose microparticles exposed to TbDNA-AuNPs alone or mixed with C-TbDNA, respectively. Paper samples were directly mounted on a double-coated carbon tape. In preparation for SEM analysis, cellulose microparticles were left to sediment under gravity for about 5 minutes, followed by supernatant removal and addition of 40 µL of TST buffer. This procedure was repeated five times. The washed cellulose microparticles were then placed over aluminum foil and air-dried. Prior to surface analysis, all paper and cellulose microparticles samples were coated with an Au/Pd layer of ~20 nm thickness using a Polaron E5100 coating system (Quorum Technologies).

6.3 Results and Discussion

Cellulose matrices functionalized with anti-biotin IgG antibody anchored on microfibriles through ZZ-CBM fusions were tested for the capture of biotin-labeled DNA in three different formats: wax-printed paper wells (circles, Figure 6-1A); single and branched-paper channels defined by wax printing (Figure 6-1B); cellulose microparticles in a liquid suspension (Figure 6-1C). Gold nanoparticles conjugated with DNA were tested as a reporter probe to generate colored readout signals distinguishable by the naked eye. The biochemical coupling of antibodies to cellulose via ZZ-CBM conjugation was compared with physical adsorption, the most simple and straightforward approach for paper modification through the direct application of reagents to the paper surface.[17] Gold nanoparticles coated with the TbDNA probe sequence were used to test and characterize the detection of target DNA with the three bioactive paper formats, whereas the TbgDNA and TbrDNA probe sequences were used to test the multiplex target capture (Table 6-1).

Colorimetric assays in paper wells

The capture of DNA hybrids by antibodies attached to paper through ZZ-CBM fusions was first tested using circular reaction wells defined on paper by wax printing and pre-modified with anti-biotin IgG:ZZ-CBM complexes (Figure 6-1A). The DNA capture assay involved the hybridization of biotinylated target DNA with DNA-AuNPs probe off-paper and then the application of 5 µL this mixture onto the pre-functionalized paper circles. No washing steps were included and the test was complete after evaporation, a process that takes about 35-40 min. Figure 6-3 shows that the capture of C-TbDNA:TbDNA-AuNPs hybrids by anti-biotin IgG:ZZ-CBM3 conjugates generates a red colored spot in the center of the reaction well. The efficacy of this capture was compared with the capture of hybrids by physically adsorbed antibodies. As expected from the results obtained in chapter 3 regarding the on-paper capture of biotin-AuNPs (refer to Figure 3-8), red colored spots were basically non-

visible when antibodies were physically attached to the paper. A similar readout was obtained in control wells lacking anti-biotin IgG (Figure 6-3A). This indicates that physically adsorbed antibodies are unable to report the capture of biotinylated TbDNA hybridized with TbDNA-AuNPs. The random orientation of IgG when physically adsorbed on paper and its possible displacement to the inner border of the wax printed circle during evaporation of the applied test solution could both explain the failure in capturing and/or reporting the labelled DNA hybrids.[17,75]

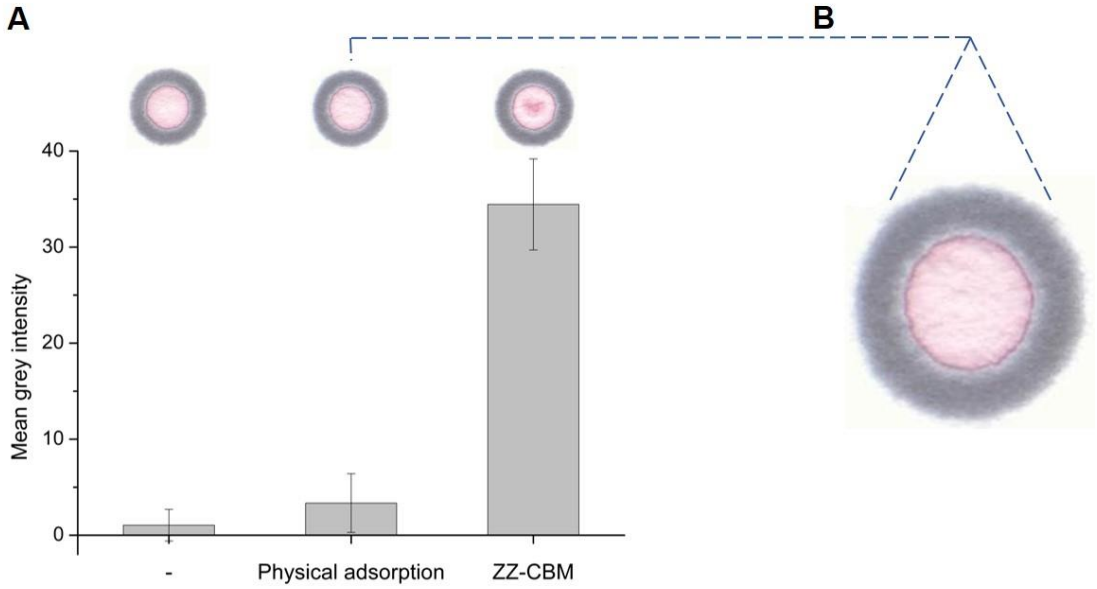

Figure 6-3 Capture of biotinylated C-TbDNA (10 pmol) hybridized with TbDNA-AuNPs (75 fmol) on paper-based reaction wells (5 mm nominal diameter) by anti-biotin IgG, which was either immobilized on paper by physical adsorption or biochemical coupling with ZZ-CBM3. The graph shows the mean grey intensity in each spot plotted against the immobilization method of antibody onto paper (± standard deviation of *n*=3 measurements). Plain, non-functionalized paper was used as a control spot assay (-).

Cross-sectional and surface analyses of the color intensity distribution within the wells gave distinct profiles based on the functionalization method used (Figure 6-4). The two grey intensity maxima in each plot profile at ~1-mm and ~6-mm correspond to the wax barrier that delimits the reaction wells. An inner, narrow peak is present in all profiles at the ~2 mm and ~5-mm marks, next to each wax-related wide peak, as a result of the accumulation of color close to the wax barriers. This migration and accumulation of AuNPs at the inner edges of the wax barriers produced a thin red ring in all three paper wells, as illustrated in Figure 6-3A (see magnified well view in Figure 6-3B). This so-called "coffee ring" phenomenon is observed when a liquid droplet with suspended particles dries on a solid surface and leaves a ring-like structure of deposited particles along the droplet perimeter, similarly to ring stains from dried drops of coffee. During the drying process, particles are transported outward from the center of the droplet by capillary flow, induced by the liquid evaporation at a pinned contact line. After evaporation, suspended particles remain accumulated at the drop edge.[239,240] Following this reasoning, non-hybridized TbDNA-AuNPs and/or non-captured DNA hybrids could have flown by induced

capillarity to the inner edge of the wax barriers during evaporation of the applied test solution.

As expected from the images and analysis shown in Figure 6-3, the grey intensity at the center of the control and antibody-functionalized wells is reduced (Figure 6-4A and B). On the contrary, the plot profile obtained from the paper functionalized with antibody:ZZ-CBM3 conjugates reveals a grey intensity maxima at the center of the reaction well that corresponds to the colored signal from the captured gold nanoparticles (Figure 6-4C).

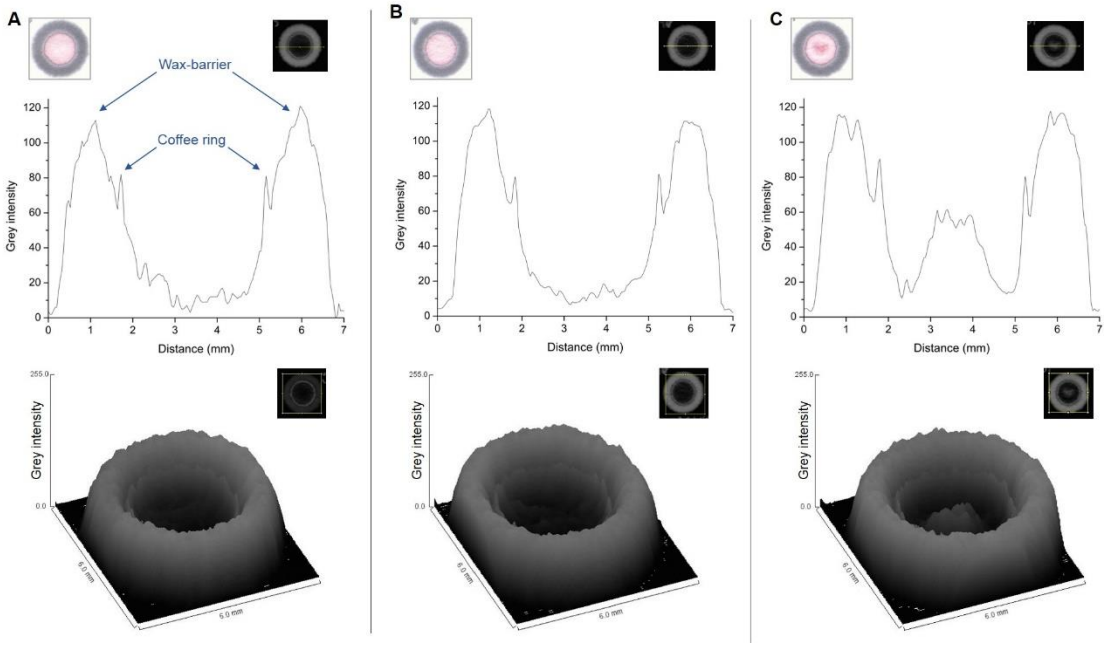

Figure 6-4 Plot profile (upper graphs) and surface plot (lower graphs) analysis of the paper wells used to detect C-TbDNA hybridized with TbDNA-AuNPs: (A) non-functionalized paper; (B) paper containing physically adsorbed anti-biotin IgG; (C) paper functionalized with antibodies through the ZZ-CBM3 fusion protein.

Next, paper wells functionalized with anti-biotin IgG *via* ZZ-CBM3 fusion were tested for their ability to capture various amounts of biotinylated DNA and to discriminate between complementary and non-complementary target DNA (Figure 6-5). In order to assess the lowest amount of target DNA that can be optically detected in this paper-based system, test solutions containing C-TbDNA amounts in a range between 0 and 10 pmol were incubated with a fixed amount of TbDNA-AuNPs probe (75 fmol) and then applied over the respective paper reaction wells. As shown in Figure 6-5A, the color intensity gradually increased with the increment of complementary target DNA in the test solutions. The lowest amount of DNA that can be visualized with the naked eye is of ~0.05 pmol. Colored spots obtained with DNA quantities below this amount were not detected either visually or through image analysis. The specificity of the capture of biotinylated target DNA was assessed through the use of a non-complementary sequence, NC-TbDNA, at the maximum tested concentration. Figure 6-5B shows that a high-intensity red colored spot was visible when 10 pmol of C-TbDNA was applied, whereas the same amount of NC-

TbDNA was not optically detectable. The colored spot associated with the capture of target DNA starts emerging just a few minutes after dispensing the test solution on the paper reaction well, as illustrated in Figure 6-5C.

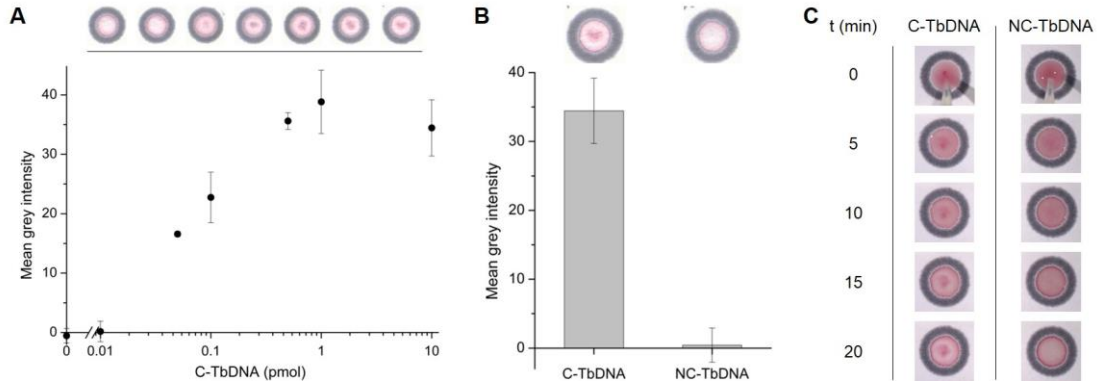

Figure 6-5 Detection of labeled DNA targets hybridized with TbDNA-AuNPs (75 fmol) on paper-based spots, which were functionalized with antibody:ZZ-CBM3 complexes. (A) Determination of the lowest detectable amount of target DNA using samples containing increasing amounts of biotin-labeled complementary TbDNA (C-TbDNA) (0.01-10 pmol). (B) Capture of 10 pmol of targets complementary (C-TbDNA) or non-complementary (NC-TbDNA) to the TbDNA-AuNPs probe. (C) Sequential static frames from a video showing the capture of complementary (C-TbDNA, 10 pmol) or non-complementary (NC-TbDNA, 10 pmol) targets mixed with TbDNA-AuNPs probe. Note that a 5-µl test solution applied into a paper spot takes about 35-40 min to air dry completely. However, heat accelerated evaporation occurred through the use of nearby light lamps when capturing the video.

To further characterize the DNA capture on the bio-functionalized paper wells and investigate the origin of the differences in color intensity after exposing paper wells to test solutions containing TbDNA-AunPs, the paper wells were analyzed by SEM. Following the application of solutions containing TbDNA-AuNPs alone or mixed with biotinylated DNA, SEM images were obtained from the center of all selected reaction wells. Despite the absence of visible red colored spots in some of the paper reaction wells, all samples reveal the presence of gold nanoparticles on the surface of the cellulose fibers (Figure 6-6). However, the patterns of AuNP dispersion vary according to the method of functionalization of paper and the target DNA tested.

The application of TbDNA-AuNPs directly on plain, non-functionalized paper, results in an extensive agglomeration of AuNPs over the paper matrix (observable as white clusters in Figure 6-6A). Clustering of AuNPs is also observed in paper wells functionalized with adsorbed anti-biotin IgG only and exposed to C-TbDNA:TbDNA-AuNPs hybrids (Figure 6-6B). This similarity of the distribution pattern of AuNPs (Figure 6-6A and B), resultant from the application of DNA hybrids either onto non-funtionalized control wells or paper wells functionalized with physically adsorbed antibodies, is consistent with the similar color intensity obtained previously (Figure 6-3). On the contrary, paper modified with anti-biotin:ZZ-CBM3 conjugates and exposed to DNA hybrids presents a pattern of well dispersed and individualized AuNPs (Figure 6-6C). This suggests that the biochemical coupling is responsible for a uniform distribution of antibodies, and hence of captured AuNP-labeled hybrids. The effective capture of hybrids by anti-biotin:ZZ-CBM3 conjugates, which is

macroscopically reported by the appearance of a red spot (Figure 6-3), thus corresponds to a homogeneous distribution of AuNPs at the microscopic scale.

When applied into the modified paper wells, biotinylated C-TbDNA:TbDNA-AuNPs hybrids are immediately captured by the cellulose-immobilized anti-biotin IgG:ZZ-CBM3 complexes, which are homogenously distributed over the cellulose fibers. The inter-AuNP distance is maintained during liquid evaporation, originating the red colored spot that is caused by the localized surface plasmon resonance of AuNPs.[196] SEM images of paper functionalized with IgG:ZZ-CBM3 conjugates and tested for the capture of non-complementary biotinylated DNA reveal the presence of agglomerated AuNPs (Figure 6-6D). While in this case the biotin-labeled NC-TbDNA target was most likely captured by the anti-biotin IgG immobilized through the fusion protein, the TbDNA-AuNPs probe remains separate from the supramolecular complex since no hybridization occurs due to the lack of complementarity between the two DNA sequences.

The distribution pattern of AuNPs over the cellulose fibers appears to be related to the exhibition or not of a red colored spot at the center of the reaction well. In the case of the agglomerated patterns, the shortening of the inter-particle distance most likely shifts the resonance absorbance peak towards higher wavelengths (see Figure 5-4). This results in a change of the color imparted by the AuNPs from the red towards the blue.[228,229] As a result, no red spot is visible in situations where AuNP clustering is observed (Figure 6-6A, B and D).

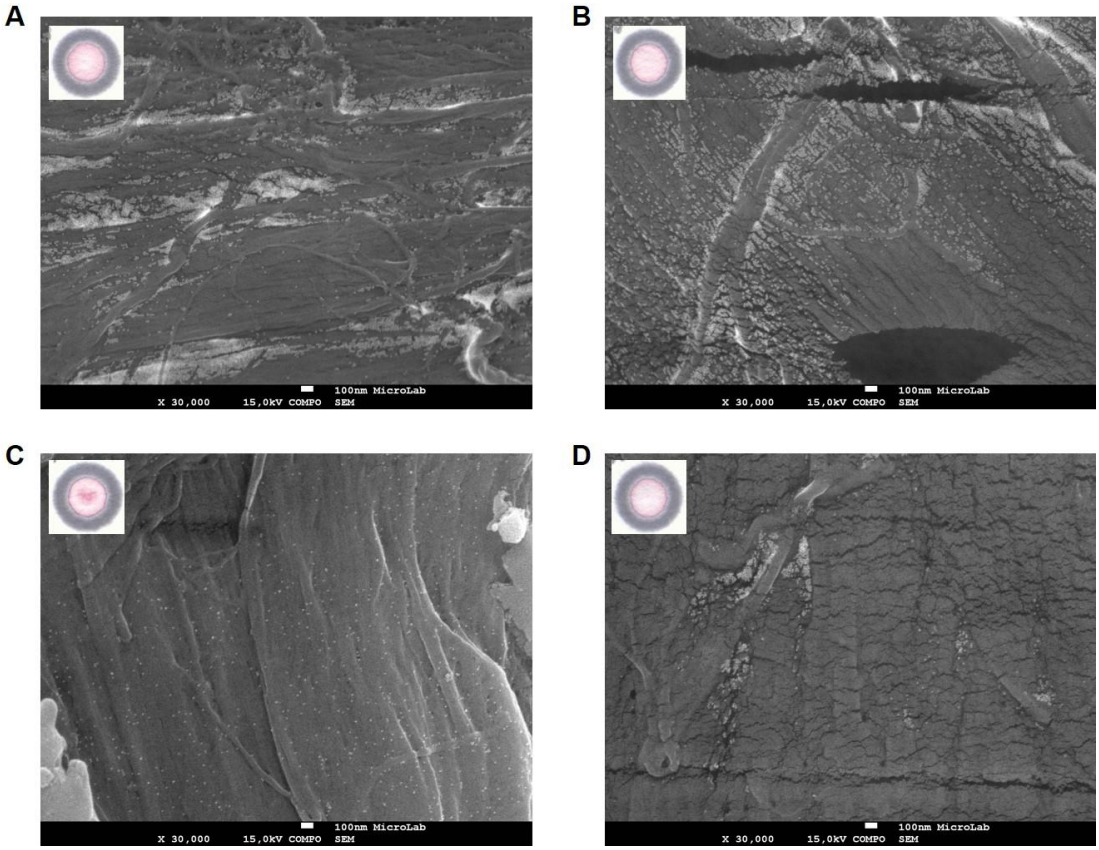

Figure 6-6 SEM analysis of the distribution of TbDNA-AuNPs probes (75 fmol) on wax-printed paper wells. (A) TbDNA-AuNPs applied on plain, non-functionalized paper. (B) Biotinylated C-TbDNA:TbDNA-AuNPs hybrids (10 pmol:75 fmol) applied on paper functionalized with physically adsorbed anti-biotin IgG or (C) antibody:ZZ-CBM3 complexes. (D) Mixture of non-complementary biotinylated TbDNA (NC-TbDNA) and TbDNA-AuNPs applied on paper functionalized with antibodies *via* ZZ-CBM3. The insets in each SEM photo show images of the corresponding paper wells. White scale bars = 100 nm.

The dispersion pattern of AuNPs on the tested paper wells and its relation to the exhibition of a red spot were further assessed through an RGB analysis of the optical spectrum of paper samples. The rationale behind this test is equivalent to that of the absorption spectrum analysis of AuNPs in suspension, which was performed to assess their aggregation status (see Chapter 5). Since the inter-particle distance affects the optical spectrum of AuNPs through surface plasmon coupling, *i.e.* individualized/dispersed AuNPs exhibit a red color whereas their agglomerates displays a color change from red to purple/blue, it is then possible to assess their relative aggregation status based on the measurement of the intensity of each color (red or blue) in the center of the paper well.[197] Figure 6-7A shows the ratio of average intensity of the red and blue channels obtained for the same type of tested paper wells selected for SEM analysis, including the control composed of TbDNA-AuNPs applied on plain paper wells. The red-to-blue ratio obtained for paper wells functionalized with IgG:ZZ-CBM3 conjugates and tested for the capture of C-TbDNA:TbDNA-AuNPs hybrids tends to be higher than the ratio obtained for the other samples (Figure 6-7A). Although the contribution of aggregated nanoparticles on paper (blue

color) does not exceed the contribution of the dispersed ones (red) in none of the samples, since the ratio value is always higher than 1, the increase of the blue color intensity is noticeable. The absorption spectra of the central zone of the wells confirms these results, with a lowering and broadening of the absorbance peak at 525 nm in the absence of IgG:ZZ-CBM3 conjugates and of complementary target DNA (Figure 6-7B).

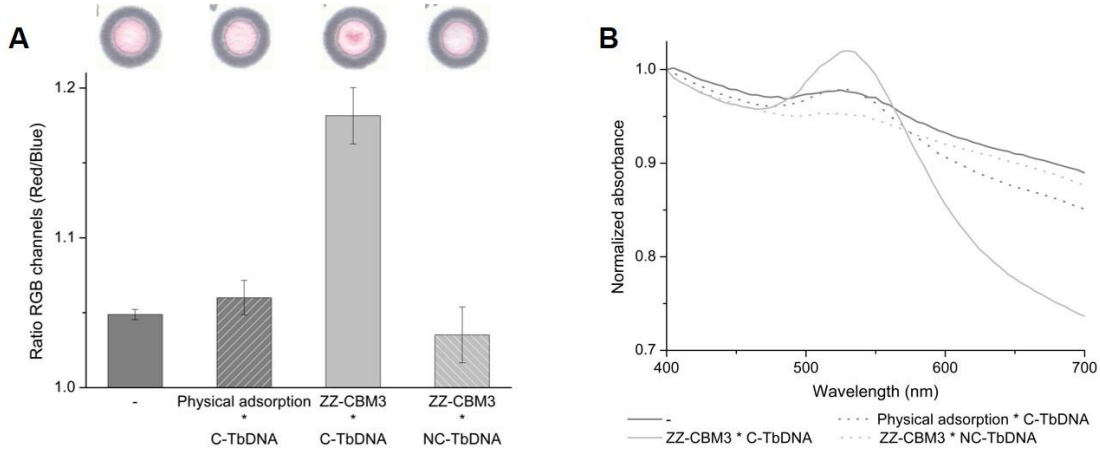

Figure 6-7 Aggregation profile of TbDNA-AuNPs on paper, alone or mixed with biotinylated target DNA, assessed by a color intensity analysis of the tested paper wells. (A) The graph shows the ratio of TbDNA-AuNPs aggregation as measured by image RGB analysis using ImageJ (ratio of average intensity of the red and blue channels). Error bars represent standard deviations of three measurements. (B) UV-Vis absorbance spectra in the 400-700 nm range.

These results from the RGB analysis and absorption spectra (Figure 6-7B) support the observations from SEM analysis and are in agreement with other findings reported in the literature, as detailed next. Veigas *et al.* have shown previously, by applying the non-cross linking aggregation method on a wax-printed microplate paper for complementary DNA detection, the same relationship found here between the aggregation status of DNA-AuNPs on paper wells and the resultant color through image RGB analysis, with an increasing contribution of the blue channel color intensity with nanoparticle aggregation.[46] It was recently reported by Almeida *et al.* that biotin-coated AuNPs aggregate when applied directly on plain paper, in contrast with biotin-AuNPs that remain dispersed on paper modified with anti-biotin:ZZ-CBM conjugates.[71] The authors hypothesized that AuNPs applied over unmodified paper accompany the liquid that is left behind during the evaporation process and segregate into smaller liquid spots over the paper, resulting in agglomerates of nanoparticles. Additionally, the increase in the concentration of the reaction buffer components (TST buffer) during liquid evaporation could also contribute to the aggregation of AuNPs.[71] The latter hypothesis was tested by depositing suspensions of DNA-coated AuNPs diluted in each of the TST buffer components (50 mM Tris buffer, pH 7.6; 150 mM NaCl; 0.05% Tween 20) into paper wells and analyzing them by SEM (see Figure 6-A2 of the Appendix). It was found that Tween 20 contributes to the aggregation of TbDNA-AuNPs on paper. In fact, surfactant-induced depletion interaction between AuNPs in solution has been demonstrated previously.[241] In the presence of a free polymer or surfactant above a critical concentration, depletion

interactions between colloidal particles occur when the inter-particle distance is of the order of the size of the smaller-sized polymer/surfactant molecules. The exclusion of these smaller molecules from the inter-particle space results in a local concentration gradient, with a low concentration of polymer/surfactant between nanoparticles and a higher concentration surrounding the nanoparticles, which will produce osmotic pressure. The solvent then tends to move from the inter-particle space to the outer area where there is a higher concentration of polymer/surfactant, creating an entropic depletion attraction between the nanoparticles, *i.e.* depletion flocculation.[241] In the DNA detection system described in this thesis, the increase in the concentration of Tween 20 during evaporation of the applied test solution promotes AuNPs aggregation. This changes the color properties of the system, with an increased contribution of the blue color, due to the inter-particle plasmon coupling.

The DNA detection system based on the modification of wax-printed paper wells with ZZ-CBM3 complexes was then tested for the discriminatory detection of C-TbgDNA and C-TbrDNA, two target sequences that share ~53% identity. In order to assess the specific capture of fully complementary DNA, each probe (TbgDNA-AuNPs and TbrDNA-AuNPs) was incubated with each one of the target sequences. Each mixture was then pipetted into the modified paper wells and tested for the capture of DNA hybrids by the immobilized anti-biotin IgG via the fusion protein. Figure 6-8 shows the results obtained for all tested conditions: TbgDNA-AuNPs mixed with C-TbgDNA or C-TbrDNA, and TbrDNA-AuNPs mixed with C-TbrDNA or C-TbgDNA. As expected, a positive capture red spot was obtained at the center of the paper wells when each probe was mixed with the corresponding 100% complementary target DNA. Although with less intensity, red colored spots were also obtained when the probes were mixed with non-fully complementary targets. This non-specific detection is due to the row of six identical nucleotides shared by both probes/targets (see Table 6-1), which allows partial DNA hybridization and consequent capture by the immobilized antibodies. In this context, reaction conditions for the specific detection of DNA between these two sequences were assessed (see Figure 6-A3 of the Appendix). It was found that the wax-printed paper wells format is not suitable for the discrimination between each of the two non-fully complementary DNA targets and the corresponding match, due to the stabilizing effect of salt present in the anti-biotin IgG storage buffer over the duplex state of the pairs C-TbgDNA:TbrDNA-AuNPs and C-TbrDNA:TbgDNA-AuNPs.[242,243]

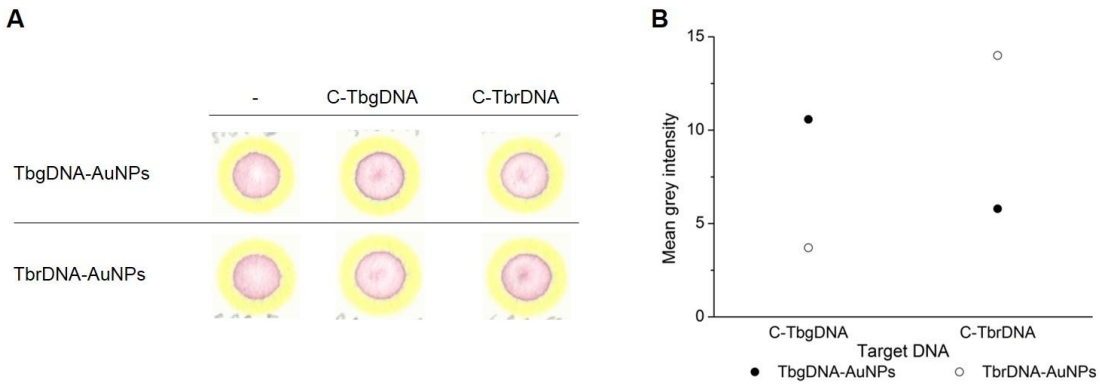

Figure 6-8 Discriminatory detection of biotinylated DNA targets on antibody:ZZ-CBM functionalized paper wells. (A) Paper well assays tested for the discriminatory detection of complementary TbgDNA or TbrDNA targets using TbgDNA-AuNPs or TbrDNA-AuNPs probes, respectively, and vice versa. The control solution (-) is composed of the respective DNA-AuNPs probe applied into plain, non-functionalized paper. (B) The graph shows the mean grey intensity in each reaction/detection area after subtracting blank value, which was obtained after applying the respective DNA-AuNPs probes on plain, non-functionalized paper (-).

The results presented in this sub-section demonstrate the ability of cellulose paper functionalized with anti-biotin:ZZ-CBM3 conjugates, when used in wax-printed paper wells format, to capture biotinylated DNA hybridized with DNA-AuNPs probe and generate a red colored signal that can be visualized with the naked eye. However, the system was not able to discriminate between two partially complementary DNA sequences.

Single and multiplex paper-based lateral flow tests

The DNA recognition system was then tested on paper channels defined by solid wax hydrophobic barriers in order to implement assays of the lateral flow type. The paper platform comprises hydrophilic channels, reaction zones and fluid reservoirs (see Figure 6-2). The idea is that an aqueous solution containing the target DNA is loaded onto one end of a dry paper channel, migrates along the channel by capillarity and is exposed to binding sites in the defined reaction zones.

The recognition and capture of labeled DNA by immobilized antibodies during capillary migration was first tested using biotinylated C-TbDNA hybridized with TbDNA-AuNPs probe prior to sample loading on the paper channels. The efficiency of the capture of these hybrids by antibodies attached on paper by biochemical coupling using the ZZ-CBM3 fusion or immobilized by physical adsorption was then tested and compared. As shown in Figure 6-9A, an intense red colored spot was obtained in channels modified with IgG:ZZ-CBM3 conjugates, whereas the detection zone of paper channels modified with physically adsorbed anti-biotin IgG presents a circular red signal with a fading color inside, resembling a coffee ring spot. Consistent with those observations, an analysis of the signal intensity alongside the paper channel revealed distinct profiles based on the method used to attach antibodies to

paper (Figure 6-9B). In both cases, plot profiles present two grey intensity maxima that correspond to the wax barriers that delimit the sample loading zone (maximum on the left) and the fluid reservoir (maximum on the right). A high-intensity narrow peak is obtained at the detection zone where antibody:ZZ-CBM3 conjugates were applied, which indicates the accumulation of AuNPs as a result of the capture of DNA hybrids. In contrast, the plot profile obtained for the wax-printed paper channel modified with antibody only reveals a low-intensity signal delimited by two mid-intense peaks at the detection zone. These results suggest that antibodies pipetted directly onto paper tended to accumulate along the droplets perimeter and were partially leached from the detection zone with the exposure to the sample liquid.

The intensity of the red-colored spot in the detection zone resultant from the capture of hybrids by antibody:ZZ-CBM3 conjugates or antibody alone was compared (Figure 6-9C). Similarly to the results obtained with paper wells, the color intensity of the signal was higher in detection zones modified with antibody:ZZ-CBM3 conjugates. Once again, this observation supports the advantage of the bioconjugation method to attach antibodies onto paper. Moreover, the ability of Whatman grade 1 CHR paper to transport test solution reagents through the channel and the resultant color intensity of the capture signal support the suitability of this substrate to fabricate bioactive paper. This paper substrate has been reported previously to yield a better analytical performance in comparison to other thicker substrates, in terms of solutions transfer and color intensity and uniform distribution of the analyte detection signal.[36]

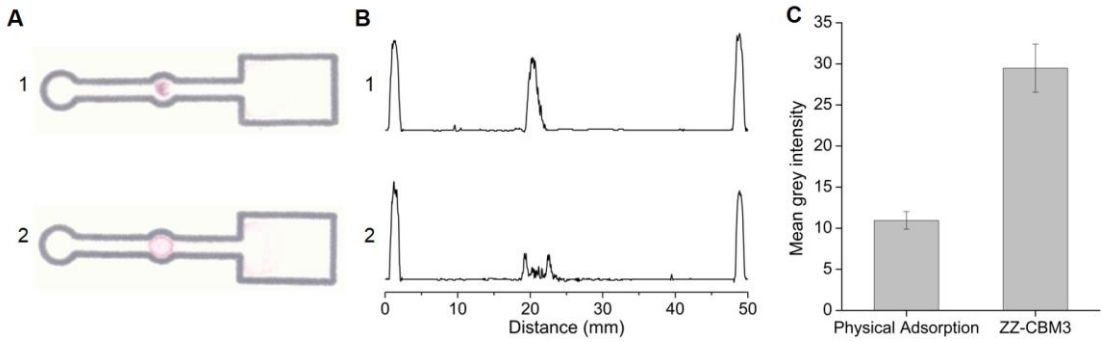

Figure 6-9 Capture of biotinylated C-TbDNA (10 pmol) hybridized with TbDNA-AuNPs (75 fmol) on wax-printed paper channels by cellulose-attached anti-biotin IgG on the detection zone. Antibodies were immobilized either through ZZ-CBM3 fusion (1, top) or by physical adsorption (2, bottom). (A) Paper channels exhibiting red colored capture signals in the detection zones. (B) Longitudinal plot profile analysis of the paper channels showing typical capture signals obtained in the detection zones according to the paper modification method. (C) Mean grey intensity measured in detection zones plotted against the immobilization method. Error bars represent standard deviations from three measurements.

An advantage of the lateral flow format is the ability to expose a sample consecutively to a series of reagents or binding sites along the paper channel. From this angle, paper channels with two reaction zones (Figure 6-2A, top channel) were used to test the ability of biotinylated oligonucleotides in a loaded sample to hybridize on paper with DNA-AuNPs probes pre-impregnated in a hybridization zone, and then

be recognized by immobilized anti-biotin IgG during capillary migration through the porous paper substrate.

Figure 6-10A shows the presence or absence of a positive capture signal in the detection zone of paper channels tested with solutions containing or missing complementary target DNA, respectively. After loading the test solution containing 10 pmol of C-TbDNA into the channel, the complementary DNA strands migrated through the hybridization zone by capillarity and interacted with the pre-impregnated TbDNA-AuNPs probes (75 fmol). The resultant DNA hybrids were subsequently captured through the biotin label by anti-biotin antibody:ZZ-CBM3 conjugates immobilized in the detection zone and originated a red colored spot from the accumulation of AuNPs. In the absence of target DNA, TbDNA-AuNPs probes alone migrate through the detection zone without being recognized by the immobilized antibody and thus producing no capture signal. The lack of red color in the detection zone in the absence of target DNA also indicates that non-specific interactions between TbDNA-AuNPs probe and cellulose-immobilized anti-biotin IgG *via* ZZ-CBM3 are negligible.

The longitudinal and cross-sectional analysis of the paper channels and the respective detection zones reveal different grey intensity profiles according to the tested solutions applied into each channel. In both cases, the low-intensity peaks at around 11 mm distance suggest that the impregnated AuNPs were not completely eluted from the hybridization zone after exposure to the test solution. In the presence of C-TbDNA, the increment of grey intensity resultant from the accumulation of AuNPs in the detection zone originates a narrow peak at ~22 mm distance, which corresponds to the red capture signal (Figure 6-10B). In the paper channel tested with the control solution, *i.e.* without target DNA, a grey intensity peak was obtained at 34 mm distance that corresponds to the accumulation of AuNPs in the migration front after consecutive applications of buffer post sample loading. The cross-sectional analysis of the detection zones confirms the accumulation of color in the presence of target DNA. Contrary to the observations from the analysis of paper wells in Figure 6-4, no coffee ring effect is detected in the DNA capture zone either in the presence or absence of target DNA. While in paper wells AuNPs were likely to be transported outward from the center to the inner edges of the wax circles, here non-captured TbDNA-AuNPs were pushed to the reservoir compartment on the right by the washing buffer (Figure 6-10A2).

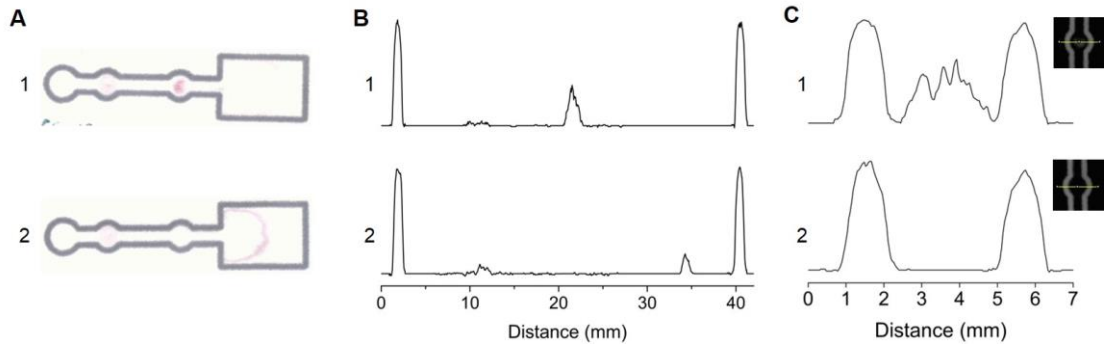

Figure 6-10 Hybridization of biotinylated C-TbDNA with impregnated TbDNA-AuNPs in the hybridization zone, and subsequent capture of DNA hybrids in a detection zone functionalized with anti-biotin IgG:ZZ-CBM3 conjugates. Paper channels were tested with 10 pmol (1, top) or 0 pmol of C-TbDNA (2, bottom). (A) Images of paper channels exhibiting typical red colored capture signals in the detection zones. (B) Longitudinal plot profile analysis of the paper channels. (C) Cross-sectional plot profiles of the detection zones.

The time course of the paper channel hybridization/capture tests is illustrated by the sequence of still frames taken from a video and shown in Figure 6-11. When a sample containing biotinylated C-TbDNA is loaded (top), AuNPs are retained in the detection zone as soon as the solution flows through that area, as a consequence of the recognition and capture of hybridized biotinylated complementary DNA by anti-biotin antibody. Although antibody:ZZ-CBM3 conjugates were pipetted into the center of the detection zone, and therefore tend to distribute as a circular spot, the formation of the red-colored detection signal starts with a quarter-moon shape. This observation suggests that the retention of AuNPs in the detection zone follows the progressive contact of DNA hybrids in the wicked fluid with the immobilized antibodies. In the absence of biotin-labeled complementary DNA, non-hybridized TbDNA-AuNPs flow through the detection zone without being captured and migrate towards the fluid reservoir, pushed by the solution buffer (Figure 6-11, bottom).

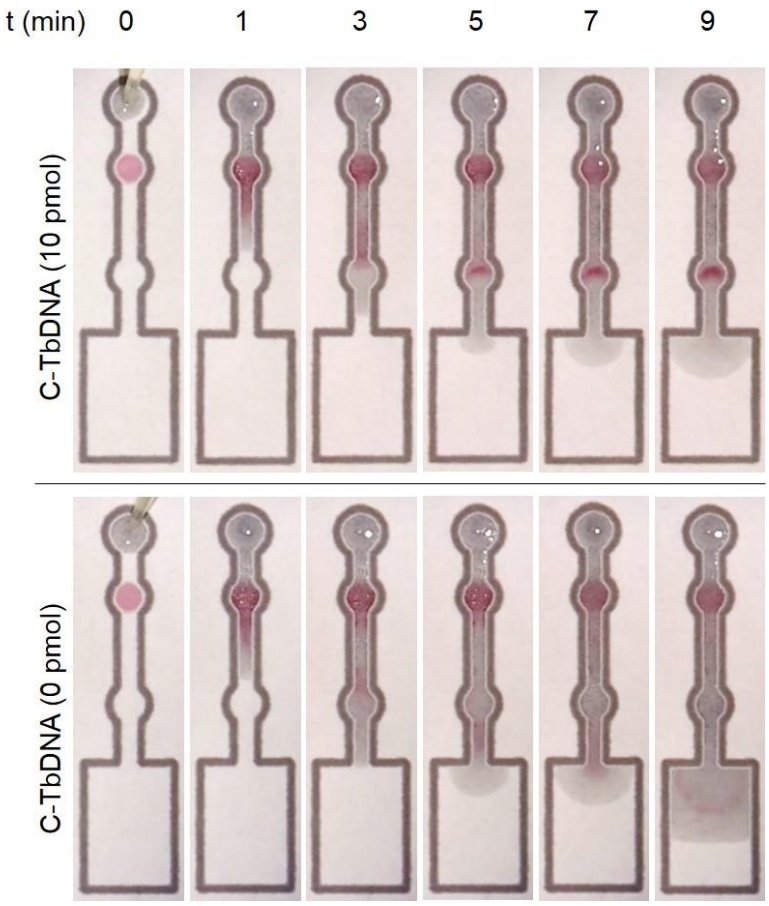

Figure 6-11 Sequential static frames from a video showing the hybridization of a complementary C-TbDNA target (C-TbDNA, 10 pmol) with impregnated TbDNA-AuNPs probes in the hybridization zone, and subsequent capture of DNA hybrids in the detection zone with immobilized anti-biotin IgG:ZZ-CBM3 conjugates. The paper channel in the bottom was tested with a blank (no target) solution.

Next, a set of wax-printed paper channels were prepared with two reaction zones: a hybridization zone impregnated with TbDNA-AuNP probe (75 fmol) and a DNA detection zone modified with anti-biotin IgG:ZZ-CBM3 conjugates. These channels were tested for their ability to capture different amounts of target DNA and to discriminate between complementary and non-complementary targets (Figure 6-12). Test solutions containing 0 to 10 pmol of C-TbDNA were loaded into different paper channels and run with buffer as usual. Figure 6-12A shows that the intensity of the capture signal in the detection zone gradually increased with the increment of complementary targets applied into the channels. The red colored spot was hardly detected when the test solution contained 0.01 pmol of target DNA. In a previous study, paper channels modified with anti-biotin IgG:ZZ-CBM3 and impregnated with fluorescein-labeled DNA probe yielded a detection signal down to 1 pmol.[67] Here, the use of AuNPs as colorimetric reporting agents seems to reduce the interference of fluorescent background noise related to the fluorescent properties of paper materials.[193]

The capture of biotinylated target DNA was sequence-specific as demonstrated by the absence of a red colored spot in the detection zone when a NC-TbDNA was applied at

the maximum tested amount of 10 pmol (see Figure 6-12B). In this case, and while the biotin-labeled NC-TbDNA oligonucleotides was likely captured by the anti-biotin IgG in the detection zone, the inability of TbDNA-AuNPs to hybridize with the non-complementary strands resulted in no accumulation of AuNPs in the detection zone.

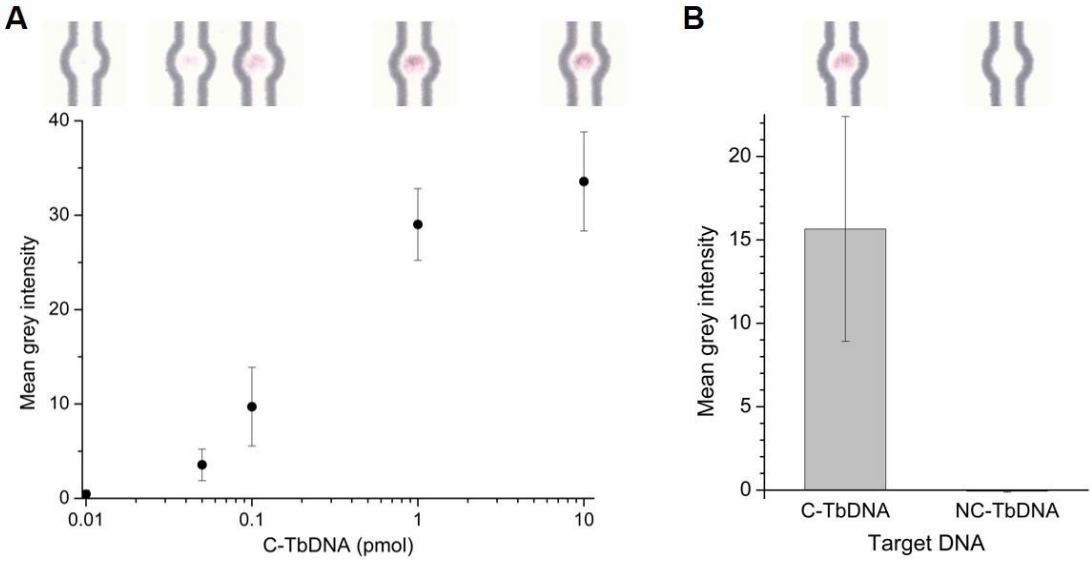

Figure 6-12 Detection of biotinylated DNA targets on wax-printed paper channels with impregnated TbDNA-AuNPs in the hybridization zone and anti-biotin IgG:ZZ-CBM3 complexes immobilized in the detection zones. (A) Mean grey intensity analysis of the detection zones in paper channels tested for the hybridization and capture of increasing amounts of complementary target (C-TbDNA, 0-10 pmol). (B) Average intensity of the capture signal obtained for complementary (C-TbDNA, 10 pmol) or non-complementary (NC-TbDNA, 10 pmol) biotinylated targets. Error bars represent standard deviations obtained from three measurements.

Wax-printed paper devices can be designed with two or more hydrophilic channels so that a sample can be split into multiple parts and directed to different reaction zones on the paper surface. By taking advantage of this feature, two-arm paper channels with one inlet were used to compare the ability of anti-biotin IgG attached to cellulose either *via* ZZ-CBM3 or ZZ-CBM64 to recognize and capture biotinylated DNA hybrids. For this purpose, a solution containing 10 pmol of C-TbDNA was applied into the loading area. During capillary migration, the solution split into the two separate channels and was subsequently directed to the hybridization zones impregnated with TbDNA-AuNPs (75 fmol per each) and to the detection zones modified with antibody:ZZ-CBM3 or antibody:ZZ-CBM64 conjugates. As shown by the presence of red colored spots in the two detection zones (Figure 6-13), both conjugates were effective in the recognition and capture of biotinylated DNA hybrids. While similar capture signals were obtained in both cases, the variation of the signal intensity is noticeable. This inconsistency between replicates can be a consequence of the lack of controlled capillary flow conditions during the interaction between DNA hybrids and antibody:ZZ-CBM complexes.

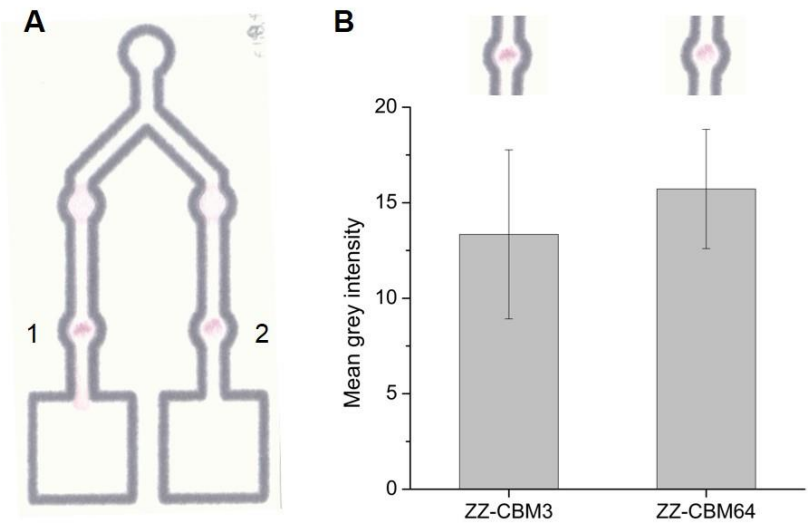

Figure 6-13 Capture of biotin-labeled DNA hybrids during capillary flow by anti-biotin IgG immobilized onto paper through ZZ-CBM3 or ZZ-CBM64 fusions. (A) Hybridization and capture of 10 pmol of C-TbDNA in two-armed paper channels with TbDNA-AuNPs impregnated in the hybridization zones and antibody:ZZ-CBM3 (1) or antibody:ZZ-CBM64 (2) conjugates attached to paper in the detection zone. (B) The graph shows the mean grey intensity of the capture signals obtained in the detection zones 1 (antibody:ZZ-CBM3) and 2 (antibody:ZZ-CBM64).

Lateral flow can be used to remove unbound components, which may interfere with the DNA detection assay, from a region of the paper channel. In this context, and following the functionalization of the detection zones with anti-biotin IgG:ZZ-CBM3 complexes, a salt-free washing buffer was loaded into the paper channel to wash-off the salt from the antibody storage buffer. This washing step was introduced to minimize the interference of salt in multiplex assays used to discriminate between two DNA targets with partially identical sequences. As shown previously, the removal of salt from the paper surface minimizes its influence in the hybridization between the non-fully complementary pairs C-TbgDNA:TbrDNA-AuNPs and C-TbrDNA:TbgDNA-AuNPs, which otherwise gives rise to a non-specific capture signal (see Figure 6-A3 from the Appendix).

Figure 6-14A shows images of Y-shaped paper channels with a single inlet, which were tested for the discriminatory capture of C-TbgDNA and C-TbrDNA. The corresponding TbgDNA-AuNPs and TbrDNA-AuNPs probes were impregnated in separate hybridization zones. A single positive signal, *i.e.* one red colored spot, was obtained when loading samples containing only one of the target sequences, *i.e.* either C-TbgDNA or C-TbrDNA. As expected, the capture signal appeared in the detection zone of the channel pre-impregnated with the corresponding complementary DNA-AuNPs probe. In this case, although the DNA target migrated through the two channel branches and was exposed to the two probes, only the fully complementary target hybridized with the respective probe and was subsequently captured in the detection zone. As shown in the graph pictured in Figure 6-14B, the color intensity of the detection signal is virtually zero for the branch of the channel containing the non-

complementary probe. Contrary to the positive signals obtained in the paper spot assays for the capture of non-fully complementary pairs C-TbgDNA:TbrDNA-AuNPs or C-TbrDNA:TbgDNA-AuNPs (see Figure 6-8), the discriminatory detection of C-TbgDNA and C-TbrDNA was effective in the paper channel format, as long as a pre-washing step is used to remove salt from the detection zone (accumulated after paper functionalization) and minimize the stabilization of non-fully complementary DNA hybrids. When a solution containing the two DNA target sequences was loaded into the paper channel, a double positive signal with one red colored spot in each branch was detected. This outcome results from the hybridization of each target sequence with the complementary probe in the respective branch of the channel, followed by the subsequent capture of the DNA hybrids by the immobilized antibody through the biotin tag.

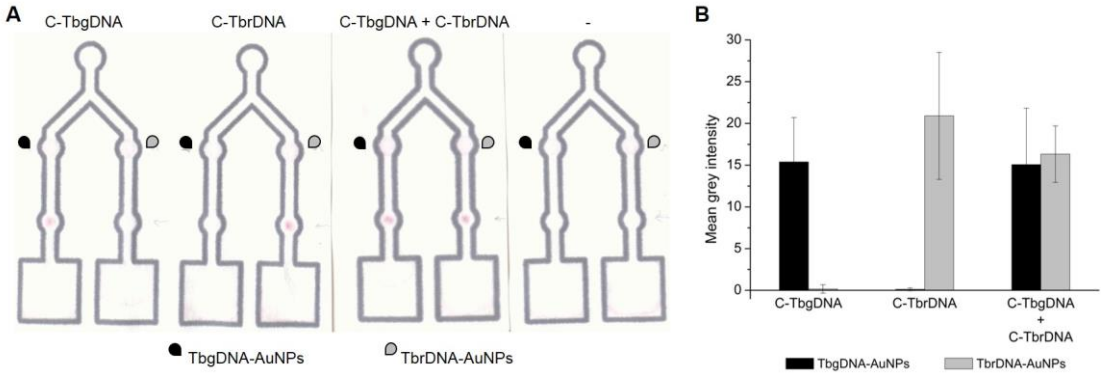

Figure 6-14 Discriminatory detection of C-TbgDNA and C-TbrDNA targets by using two-armed paper channels with separate hybridization zones impregnated with either TbgDNA-AuNPs or TbrDNA-AuNPs probes. (A) From left to right, paper channels tested with solutions containing 10 pmol of C-TbgDNA, C-TbrDNA or both targets. Paper channels with impregnated DNA-AuNPs probes in the respective hybridization zones, but with non-modified detection zones, were used as blanks after being tested with reaction buffer only (paper channel on the right). (B) Mean grey intensity analysis of the capture signals obtained in the detection zones (± standard deviation of *n*=3 measurements).

The sequence of video frames in Figure 6-15 shows images of Y-shaped paper channels that were tested for the detection of C-TbgDNA and C-TbrDNA. The sample solution migrates along the cellulose matrix by capillary transport and then splits into the two branches of the Y-shaped paper test towards the hybridization areas.

The frame at time t=0 shows that the DNA-AuNPs impregnated in the hybridization zones of the two-branches exhibit a blue color when dried on paper. This contrasts with the red color obtained when DNA-AuNPs were impregnated in the single-channel paper tests described earlier (see Figure 6-11). The difference in the color of the hybridization zones prior to sample loading can be explained as follows. Since the channels used for multiplex testing were rinsed with TT buffer (Tris, Tween 20) to remove salt from the detection zone and hence minimize hybridization events between non-fully complementary DNA sequences, the paper surface became covered

with Tween 20. As a result, AuNPs deposited afterwards could agglomerate due to depletion interactions induced by the surfactant on the paper surface (see Figure 6-A2 of the Appendix). During migration of the sample solution through the hybridization zone, the concentration of surfactant on the surface decreases and the agglomeration state of AuNPs is reversed. Hybridization between the DNA targets and DNA-AuNPs then occurs during capillary migration when solution takes up the impregnated probes. The AuNPs become retained and form two red colored spots as soon as the test solution flows through the detection zones (Figure 6-15), which suggests a rapid capture of biotinylated DNA hybrids by the immobilized IgG.

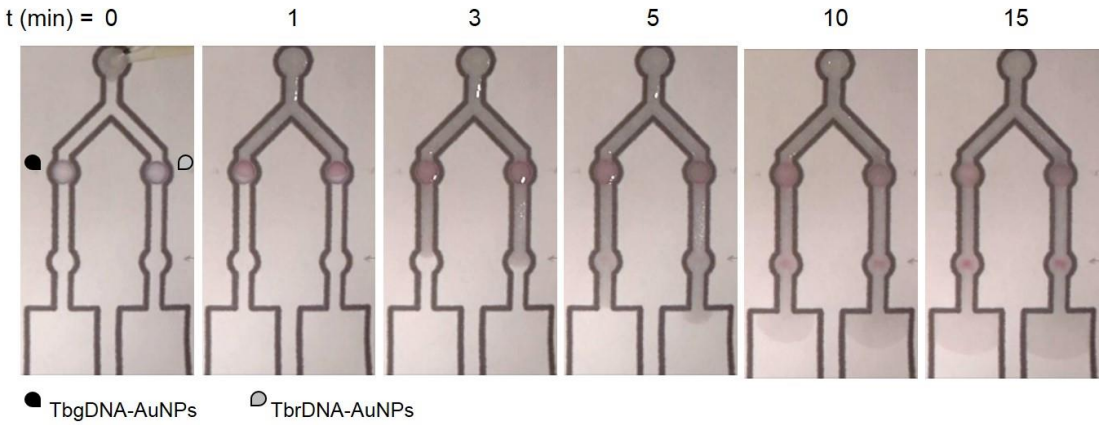

Figure 6-15 Sequential video frames of the hybridization and subsequent capture of biotinylated DNA targets in a wax-printed, two-armed paper channel impregnated with TbgDNA-AuNPs and TbrDNA-AuNPs in separate hybridization zones. Both detection zones were modified with anti-biotin IgG:ZZ-CBM3 complexes. The test solution contains 10 pmol of each biotin-labeled target sequences, C-TbgDNA and C-TbrDNA.

Altogether, these results demonstrate the hybridization of biotinylated DNA targets with cellulose-impregnated DNA-AuNPs probe during capillary wicking, followed by the specific capture of DNA hybrids in the detection zones functionalized with anti-biotin IgG attached to paper *via* ZZ-CBM fusions. The multiplex format allowed the colorimetric discrimination between partially identical C-TbgDNA and C-TbrDNA sequences.

Colorimetric assay in solution with cellulose microparticles[§]

The feasibility of implementing the DNA recognition system on suspended cellulose microparticles was studied next. The exploration of alternative cellulose platforms intends to overcome some of the current limitations of paper-based devices, which relate to the material properties of paper and the fabrication techniques available.

[§] The content of this section was published in the Biotechnology Journal. See DOI: 10.1002/biot.201800590.

Specifically: i) sample delivery to reaction zones can be affected by sample retention within paper-based microfluidic channels or sample evaporation during transport, and ii) wax barriers can become ineffective in retaining liquids with surfactants or organic solvents.[53,64]

The detection of labelled complementary DNA in solution was tested using 20 µm Sigmacell cellulose microparticles pre-functionalized with anti-biotin antibody:ZZ-CBM3 conjugates. Each suspension of modified cellulose microparticles was exposed to pre-incubated test solutions composed of a fixed amount of TbDNA-AuNPs probe and various concentrations of complementary or non-complementary biotin-labeled target - C-TbDNA or NC-TbDNA, respectively. As shown in Figure 6-16, the cellulose microparticles tend to sediment on the bottom of the tube under the influence of gravity. In the absence of complementary target DNA, the supernatant continues to exhibit a red color after the incubation due to the colloidal AuNPs present in solution, whereas the cellulose microparticles remain white (see Figure 6-16A). The initial red color of the solution visibly fades after incubating with increasing amounts of biotinylated C-TbDNA:TbDNA-AuNPs hybrids (Figure 6-16A). This is accompanied at the same time by a reddening of the sedimented cellulose microparticles. These results suggest that the AuNPs became anchored on the surface of the modified cellulose microparticles through the DNA:DNA:IgG:ZZ-CBM3 complex. In the presence of non-complementary target DNA, AuNPs remained dispersed in solution and the cellulose microparticles maintained their white color (see tube marked NC in Figure 6-16A). The lack of complementarity with the biotinylated target, which is likely to have been captured by the immobilized anti-biotin IgG, prevented the attachment of TbDNA-AuNPs on the surface of the cellulose microparticles.

Additional observations can be made after centrifuging the tubes (Figure 6-16B). When target was absent, AuNPs accumulated and formed a red pellet in the bottom of the tube upon centrifugation, which contrasts with the white color of the cellulose microparticles (see the right-hand side tube in Figure 6-16B). This indicates that in the absence of hybridization events, either due to the lack of complementary target DNA or in the presence of a non-complementary DNA target, TbDNA-AuNPs are not captured by the immobilized anti-biotin IgG:ZZ-CBM3 conjugates and are forced to settle upon centrifugation. The size of the pellet of AuNPs decreases with the increment of the amount of complementary DNA in the test solution since increasing amounts of C-TbDNA:TbDNA-AuNPs hybrids are captured by the immobilized IgG:ZZ-CBM3 conjugates on the cellulose surface, reddening the microparticles. At higher amounts of complementary target DNA (1 and 10 pmol of C-TbDNA), the absence of a red pellet in the bottom indicates that the majority of the TbDNA-AuNPs were captured.

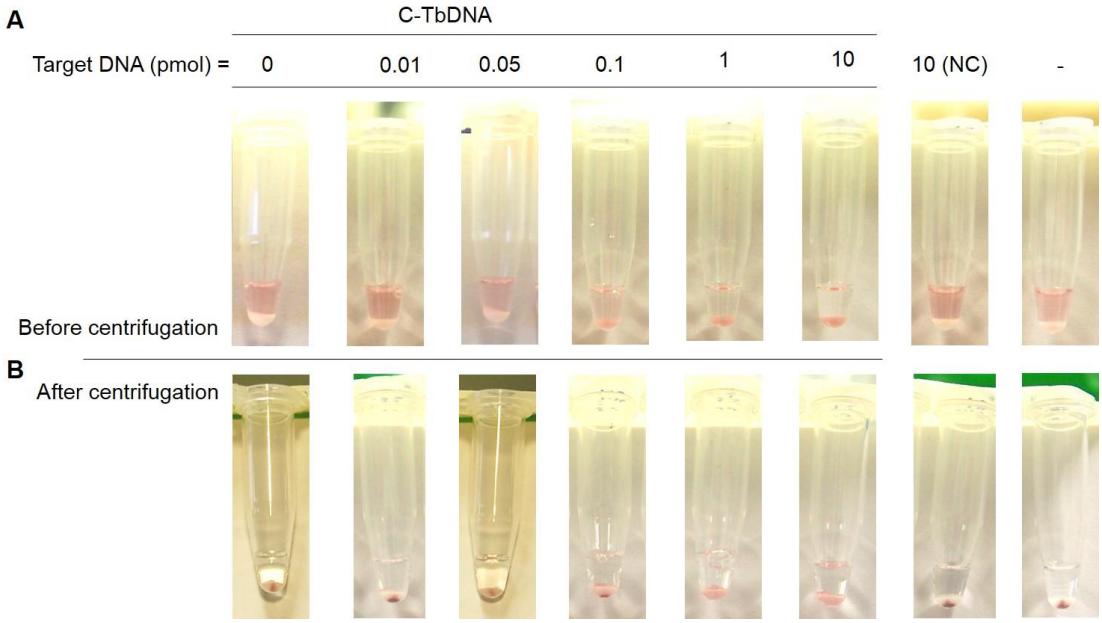

Figure 6-16 Capture of biotinylated DNA targets hybridized with TbDNA-AuNPs (75 fmol) by immobilized anti-biotin IgG:ZZ-CBM3 conjugates on cellulose microparticles. Functionalized cellulose microparticles were tested for the capture of increasing amounts of complementary target (C-TbDNA, 0-10 pmol) and non-complementary target (NC-TbDNA, 10 pmol). As control, non-functionalized cellulose microparticles were incubated with TbDNA-AuNPs probe only (-). Images are shown of microparticles in solution (A) before and (B) after centrifugation.

The capture of DNA hybrids by modified cellulose microparticles was indirectly monitored by measuring the absorption spectrum of the suspensions recovered after incubation and without centrifugation. As shown in Figure 6-17A, the typical single absorbance peak at around 520-525 nm, which is characteristic for ~14-nm AuNPs coated with DNA (see Chapter 5), was obtained in test solutions containing no or low complementary target DNA. This is attributed to the presence of non-captured, dispersed AuNPs in the supernatant. As expected, a decrease in peak intensity is observed when increasing the amount of complementary target DNA because of the capture of C-TbDNA:TbDNA-AuNPs hybrids onto the surface of the modified cellulose microparticles. For the evaluation of the capture of biotinylated C-TbDNA:TbDNA-AuNPs hybrids by the immobilized anti-biotin IgG:ZZ-CBM3 conjugates onto the surface of the cellulose microparticles, the absorbance at 525 nm was plotted against the amount of target DNA present in the test solution (Figure 6-17B). As expected, the absorbance gradually decreased with increasing amounts of complementary target DNA. The capture of target DNA was sequence-specific as confirmed by the high absorbance of the supernatant with the maximum amount of non-complementary target NC-TbDNA, which indicates that the DNA-coated AuNP probes remained dispersed in solution after incubation with the modified cellulose microparticles.

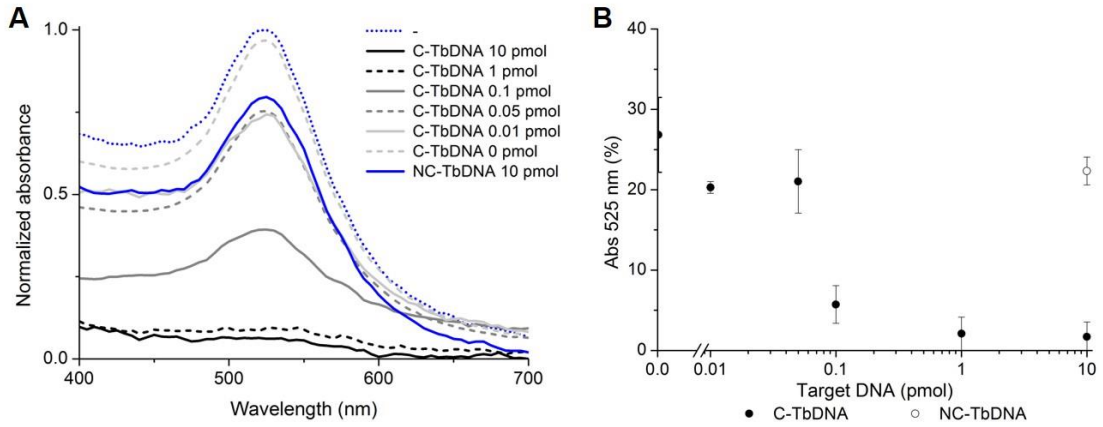

Figure 6-17 Spectrophotometric analysis of the supernatants from solutions containing gravity-settled cellulose microparticles (no centrifugation), functionalized with anti-biotin IgG:ZZ-CBM3 conjugates and tested for the capture of biotinylated DNA targets mixed with DNA-AuNPs probes. Non-functionalized cellulose microparticles were incubated with TbDNA-AuNPs probe only as control (-). (A) UV-Vis absorbance spectra in the 400-700 nm range. (B) Relative absorbance intensity, expressed as the individual percentage from the total absorbance at 525 nm, plotted against target DNA concentration. Error bars were obtained from the standard deviations of three measurements.

The DNA capture system based on functionalized cellulose microparticles in suspension was further characterized by scanning electron microscopy. Following the incubation of modified cellulose microparticles with biotinylated target-probe DNA hybrids, SEM images of the surface of the microparticles were obtained (Figure 6-18A-C). Functionalized cellulose microparticles exposed to C-TbDNA:TbDNA-AuNPs exhibit a rough surface with white dots that suggests a homogeneous distribution of AuNPs similar to the one observed in paper (Figure 6-6C). On the contrary, the control sample composed of plain, non-functionalized cellulose microparticles which were previously exposed to the TbDNA-AuNPs probe only, reveal a smooth surface that suggests the absence of AuNPs anchored on the cellulose surface (Figure 6-18D).

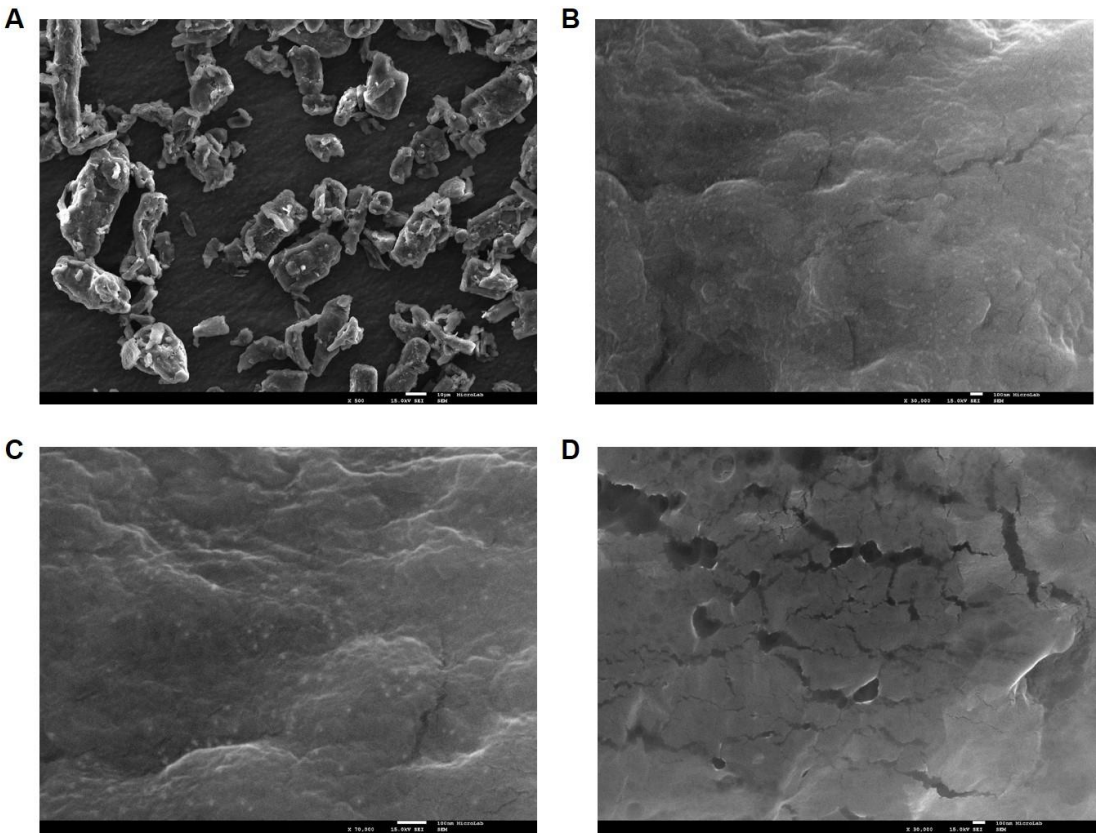

Figure 6-18 Micrographs of cellulose microparticles mixed with test solutions and washed prior to SEM analysis. Microparticles modified with anti-biotin IgG:ZZ-CBM3 conjugates and tested for the capture of 10 pmol of C-TbDNA hybridized with TbDNA-AuNPs probe (75 fmol) at (A) 500x, (B) 10,000x and (C) 70,000x magnification. (D) Non-functionalized microparticles exposed to TbDNA-AuNPs (30,000x).

The specificity of the cellulose microparticles-based assay for nucleic acid detection was further assessed by using the probes TbgDNA-AuNPs and TbrDNA-AuNPs, each one tested for the discrimination of the respective complementary DNA target from non-fully complementary sequences – with TbrDNA as non-complementary target for TbgDNA-AuNPs, and vice-versa. As shown in Figure 6-19A, the capture of complementary DNA hybrids C-TbgDNA:TbgDNA-AuNPs or C-TbrDNA:TbrDNA-AuNPs was visually confirmed through the exhibition of the red color by the cellulose microparticles as a result of the anchoring of gold nanoparticles in the surface of the cellulose microparticles through the DNA:DNA:IgG:ZZ-CBM3 complex. On the contrary, the DNA-AuNPs probes remained dispersed in solution in the presence of a non-fully complementary target, and formed a red colored pellet at the bottom of the reaction tube after centrifugation. The inability of TbgDNA-AuNPs or TbrDNA-AuNPs to hybridize with a non-fully complementary target in solution, which was already demonstrated previously in chapter 5 by using the non-cross-linking aggregation method (see Figure 5-7), prevented the anchoring of gold nanoparticles onto the surface of cellulose microparticles. When the suspensions recovered after incubation and without centrifugation were spectrophotometrically evaluated, significant differences in absorbance at 525 nm were observed. The data in Figure 6-19B indicates a low absorbance when the DNA-AuNPs probes were incubated with

100% complementary DNA targets, which supports the attachment of gold nanoparticles onto the surface of the sedimented cellulose microparticles through the recognition of the biotinylated hybrids C-TbgDNA:TbgDNA-AuNPs or C-TbrDNA:TbrDNA-AuNPs by the cellulose immobilized anti-biotin antibody. The high absorbance of the suspensions tested with non-fully complementary targets, *i.e.* C-TbgDNA and TbrDNA-AuNPs or C-TbrDNA and TbgDNA-AuNPs, supports that the capture of target DNA in solution is sequence-specific. Although the targets C-TbgDNA and C-TbrDNA share ~53% nucleotide identity with the probes TbrDNA-AuNPs and TbgDNA-AuNPs, respectively, results suggest that hybridization did not occur and gold nanoparticles remained dispersed in solution. Hence, suspensions remained red and with a high absorbance at 525 nm.

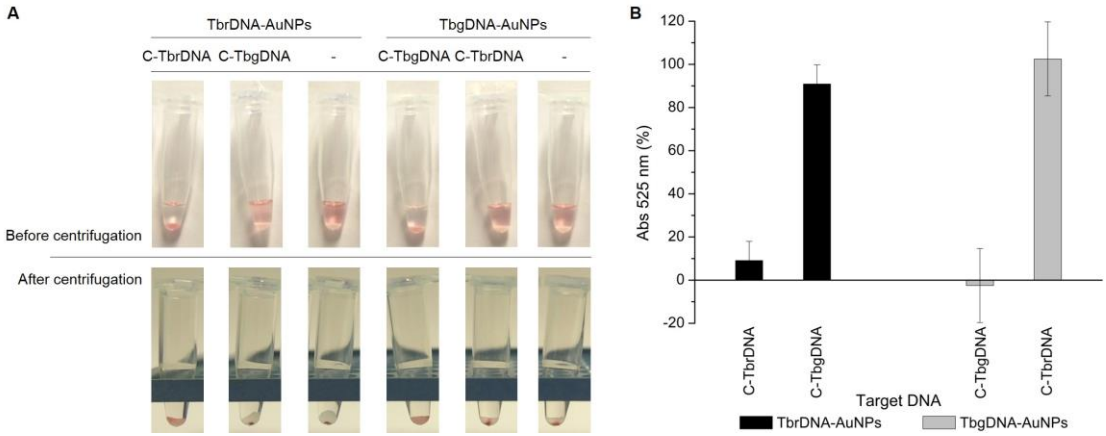

Figure 6-19 Cellulose microparticles tested for the discriminatory capture of C-TbgDNA and C-TbrDNA using the respective TbgDNA-AuNPs and TbrDNA-AuNPs probes, and vice versa. (A) Tested microparticles in solution before (top) and after centrifugation (bottom). (B) Relative absorbance intensity at 525 nm of supernatants from solutions containing sedimented microparticles, without prior centrifugation.

These results confirm the efficacy of DNA hybrids capture in solution by antibodies attached to cellulose microparticles surface through ZZ-CBM fusion. Direct and indirect analysis of DNA capture in solution, either by visualizing the reddening of microparticles or solution, respectively, support the ability of this assay format to discriminate partially identical C-Tbg-DNA and C-TbrDNA sequences.

Alternative strategies for detecting DNA on cellulose paper have been reported previously. Araújo *et al.* activated cellulose surface for covalent attachment of DNA probe and subsequent hybridization of fluorescent Cy3-labeled target DNA.[81] This methodology exempts the intermediation of antibodies for target DNA capture. However, such chemical coupling strategy for paper functionalization requires the use of organic compounds (e.g., DMSO, DMF, ethanolamine) which could compromise wax barriers if reaction zones were wax-printed on paper. In addition, fluorescent detection poses a challenge for "reader-free" testing. Veigas *et al.* reported a cellulose paper-based platform for DNA detection which relied on the optical properties of gold

nanoparticles depending on the interparticle distance.[46] The colorimetric DNA detection assay integrates the non-cross-linking aggregation method with wax printed paper wells impregnated with salt that is capable of inducing AuNPs aggregation. This strategy gives a straightforward, colorimetric visual readouts of the presence of the target DNA. However, this strategy is limited in regards to the format of the paper platform since, for example, salt would likely to be washed-off in lateral-flow testing formats.

6.4 Conclusions

Paper-supported assays constitute a promising approach for the development of simple and affordable analytical devices.[17] By making use of ZZ-CBM fusion proteins with high affinity to cellulose (CBM3 or CBM64) and IgG antibodies (ZZ), three different types of cellulose-based assays were developed: wax-printed paper wells, wax-printed paper channels, cellulose microparticles in solution.[103,105,121] All three assays were tested for the capture of biotinylated target DNA by anti-biotin IgG attached to the cellulose surface. Gold nanoparticles conjugated with DNA were used as probes for colorimetric reporting based on the generation of a red colored signal in the event of target DNA capture. The AuNPs provided an intense color contrast with the paper white background.

Wax-printed paper wells with immobilized antibodies via ZZ-CBM fusions were successfully tested for the capture of complementary target DNA pre-hybridized with the probe. Results from tests performed with complementary and non-complementary DNA targets – C-TbDNA and NC-TbDNA, respectively – support the capability of this assay format to specifically capture biotinylated-DNA without washing steps down to ~0.05 pmol, which could be assessed with the naked eye. Using SEM analysis, it was possible to assess the distribution of gold nanoparticles over the paper spotting platform. SEM images revealed that the red colored spot, generated upon the application of test solution containing complementary target DNA, is accompanied by the homogeneous distribution of AuNPs on the paper surface. On the other hand, the absence of a capture signal relates to differential aggregation events that result in plasmon coupling effects, which occur depending on the extent of the paper functionalization or the content of the applied test solution: direct application of antibodies on cellulose, the absence of C-TbDNA, the presence of NC-TbDNA. This methodology of detecting biotinylated DNA hybrids in paper wells was, however, unable to discriminate DNA oligonucleotides with partially identical sequences.

Paper channels defined with hydrophobic wax were tested for the hybridization and subsequent capture of DNA by capillary flow, either in a single or in a multiplex format. Similarly to the results observed in paper wells, antibodies immobilized via ZZ-CBM were more effective in the capture of biotinylated DNA hybrids than physically adsorbed antibodies. Wax-printed paper channels, impregnated with probe in the hybridization zone and modified with antibodies via ZZ-CBM in the detection

zone, reported the capture of target DNA down to ~0.01 pmol. Similar red colored spots were obtained upon capture of DNA by antibodies conjugated with either ZZ-CBM3 or ZZ-CBM64, thus proving the efficacy of the immobilization of antibodies with either fusion protein. Single and two-armed paper channels combined with washing steps proved to be effective in the sequence-specific detection of DNA, having been able to discriminate complementary from non-complementary target sequences and DNA targets with ~53% nucleotide identity, respectively.

Finally, cellulose microparticles modified with anti-biotin:ZZ-CBM were also able to capture biotinylated DNA hybrids, acquiring a red color that is proportional to the quantity of target DNA present in solution. The capture of target DNA was indirectly assessed through spectrophotometric analysis of the suspensions after incubation of modified microparticles with test solutions, i.e. the solution lost or retained the original red color in the presence or absence of complementary target DNA, respectively. This methodology proved to be effective in the discrimination of complementary from non-complementary target DNA, as well as from partially complementary targets.

In conclusion, the biomolecular recognition approach developed for the colorimetric detection of DNA on cellulose was effective and demonstrated to be versatile in regards to the format of cellulose platforms for the DNA capture. The results support the functionality of the supramolecular system either on paper matrices or in solution by using cellulose microparticles. Furthermore, AuNPs can be readily modified with different probe DNA sequences. As such, diverse bioactive paper applications can be envisaged in which the detection method provides simplicity by generating an immediate visual readout, and the cellulose substrate confers advantages in terms of affordability and safe disposability.[32,51]

6.5 Appendix: Colorimetric detection of labeled DNA hybridized with DNA-coated gold nanoparticles on wax-printed paper

Setup of paper devices for sample testing

Both paper channels and wells were horizontally placed over support structures in a way that would prevent gravity forces from impelling sample flow through the channels. As exemplified in sections A-C of Figure 6-A1, paper devices were left hanging in the air without the inner side wax-printed patterns touching directly on other surfaces. Another means of handling wax-patterned paper devices includes the printing of wax in a lower grayscale inside the channels or wells in order to create hemichannels/wells.[74] Alternatively, and without changing the original drawings of channels and wells, adhesive film can be used to cover the back of the paper strip.[72] Despite its simplicity, this strategy implies a hybrid system to fabricate paper devices

based on wax-printing and sealing with tape.

In preparation for the measurement of absorbance spectra of the center of the paper wells, each already-tested well was cut out by following the wax-printed pattern and placed on a 96-well plate in order to be measured by a microplate reader (Figure 6-A1D).

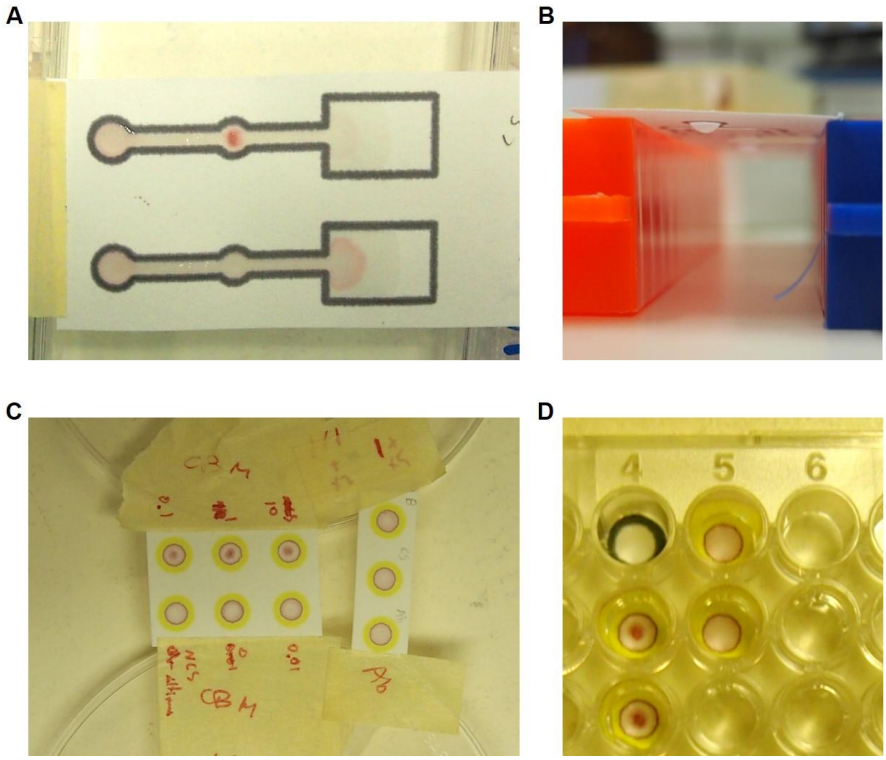

Figure 6-A1 Arrangement of paper devices for sample testing. (A) Top and (B) lateral views of paper channels during sample testing, which were placed over and between microplates or microtubes racks, respectively. (C) Top view of paper wells which were placed over and between two Petri dishes, and fixed with paper tape. (D) After sample testing, the paper wells were individually cut out and placed on a 96-well plate for absorbance measurement in a microplate reader.

Effect of Tween 20 on the distribution of gold nanoparticles on paper

The contrasting distribution profiles of AuNPs on paper, which occurs in the DNA detection system described here (Figure 6-6), emerge during the evaporation of the test solution, possibly as a consequence of the increase in the concentration of the reaction buffer components. In order to investigate this phenomenon, the effect of the TST buffer components on the distribution of AuNPs on paper was studied by SEM. In preparation for this assay, 5-µL suspensions containing 2.5 µL of TbDNA-AuNPs (30 nM) and 1 µL of ultrapure water were diluted in 1.5 µL of TST buffer or in one of its components: 50 mM Tris buffer, pH 7.6; 150 mM NaCl; 0.05% Tween 20. Each red colored test solution was then pipetted into a wax-printed paper well (5 mm nominal diameter, 400 µm nominal barrier width), air-dried and then analyzed by SEM. Figure 6-A2 shows that AuNPs appear aggregated at the center of the paper

wells when mixed with TST buffer or with Tween 20 only, whereas nanoparticles are homogeneously distributed on paper fibers in the presence of Tris or NaCl. These results indicate that nanoparticle aggregation is induced by the increased concentration of the Tween 20 surfactant during evaporation of the test solution.

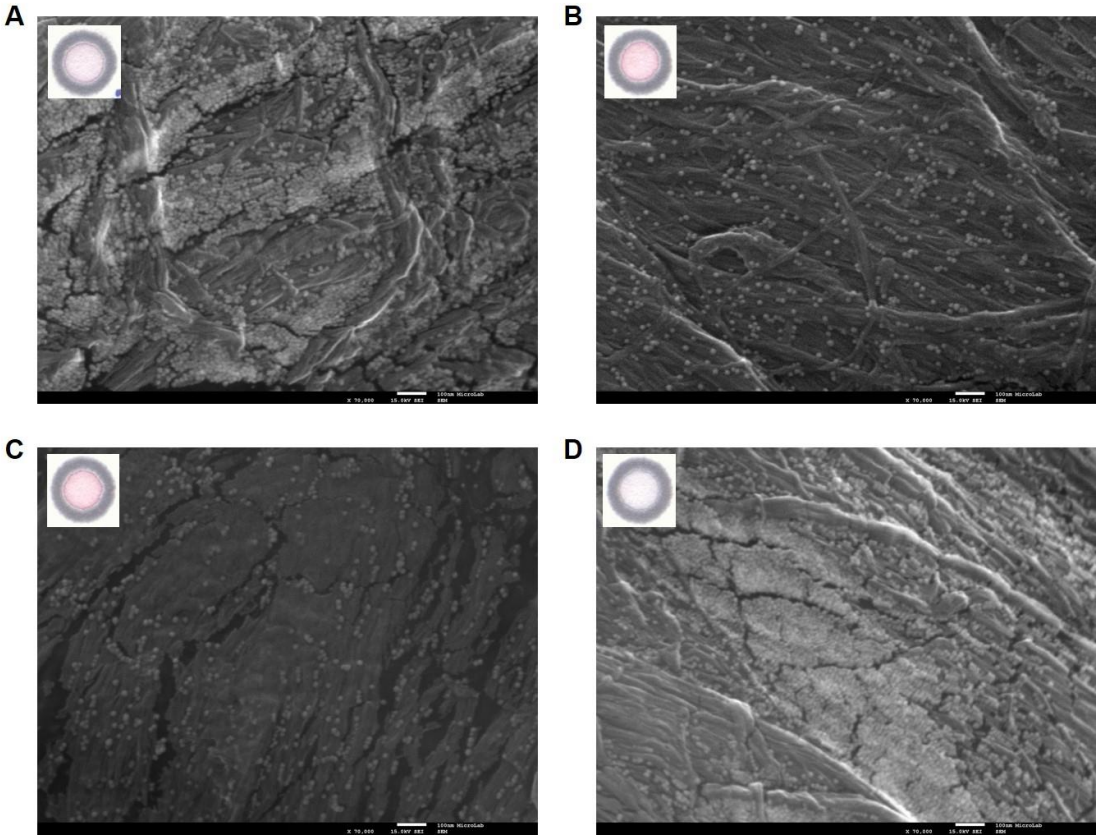

Figure 6-A2 Effect of the TST reaction buffer components on the distribution of TbDNA-AuNPs on paper wells, as assessed by SEM analysis: (A) TST buffer; (B) 50 mM Tris buffer, pH 7.6; (C) 150 mM NaCl; (D) 0.05% Tween 20. Scale bars represent 100 nm.

Discriminatory detection of TbgDNA and TbrDNA target sequences on wax-printed wells/channels

The inability of the DNA detection system based on paper wells functionalized with IgG:ZZ-CBM3 conjugates to discriminate the C-TbgDNA and C-TbrDNA targets (~53% identity) was addressed by testing the effect of salt content in the TST reaction buffer. The effect of sodium ions in the stabilization of DNA-DNA duplexes is generally attributed to the screening of electrostatic repulsions between the negatively charged DNA backbones, which favor their separation.[242,244] Given that these two target sequences are partially complementary to each other's probe (see Table 6-1), destabilization of duplexes formation between C-TbgDNA and TbrDNA-AuNPs, and vice versa, was promoted at low ionic strength by preparing a modified version of the reaction buffer without NaCl (TT; 50 mM Tris buffer, pH 7.6, 0.05% Tween 20).

In preparation for the colorimetric well assay, 2-µL solutions of ZZ-CBM3 (2 pmol;

0.4 µL of 5 µM) and anti-biotin IgG (5 pmol; 0.75 µL of 6.67 µM) were prepared in TT buffer and incubated at RT for 20 min. Anti-biotin IgG:ZZ-CBM3 conjugates were then applied onto the center of paper wells, 0.5 µL at a time, and air-dried at RT between applications. Five-microliter test solutions containing 10 pmol of C-TbgDNA or C-TbrDNA alone (1 µL of 10 µM) mixed with each one of the respective probes (2.5 µL of 30 nM TbgDNA-AuNPs or TbrDNA-AuNPs) were prepared in TT buffer. After a 20-min incubation step at RT, test solutions were applied on the modified paper wells and let to dry at RT for 35-40 min. As shown in Figure 6-A3A, a red colored spot was obtained when each probe was mixed with any of the two DNA targets, although with less intensity for the non-fully complementary target (see graph on the right). Despite the absence of salt in the reaction buffer, non-specific hybridization occurred between C-TbgDNA and TbrDNA-AuNPs, and vice versa, giving rise to a positive signal due to the capture of the partially hybridized DNA duplexes by the immobilized antibody.

The stabilization of DNA hybrids could have been promoted by the components of the air-dried mixture of anti-biotin:ZZ-CBM3 complexes on the modified paper. According to the manufacturer's information, the anti-biotin IgG storage buffer contains high salt content (0.5 M sodium chloride, together with 0.01 M PBS, pH7.4, and 15 mM sodium azide) and, as a result, the test solution could have taken up the impregnated NaCl from the storage buffer. The effect of NaCl from the antibody storage buffer was tested by using paper channels, which allow salt to be removed from the reaction (detection) zone through washing steps. The immobilization of anti-biotin IgG on the detection zone of paper channels followed a protocol similar to the one used for the preparation of paper reaction wells: mixtures of 5 pmol of antibody and 2 pmol of ZZ-CBM3 in TT buffer were pipetted in a series of 4×0.5 µL applications and air-dried at RT. The paper channels were then rinsed with 15 µL of TT buffer every 2.5 minutes for three times to wash-off the impregnated salt from the detection zone. After applying the same test solution used in the paper wells, 15 µL of TT buffer were loaded into the paper channels every 5 minutes for three times to ensure complete migration of the DNA mixtures through the detection area and wash-off excess of non-captured probe to the reservoir zone. Figure 6-A3B shows that the positive capture signal was obtained only when each DNA-AuNPs probe was mixed with the corresponding 100% complementary biotinylated target. No red colored spot was visible in the detection zone when functionalized paper channels were tested for the capture of C-TbgDNA:TbrDNA-AuNPs or C-TbrDNA:TbgDNA-AuNps duplexes, resulting in a signal intensity equivalent to the one obtained for non-modified detection zones tested with DNA-AuNPs only (see graph on the right). The absence of salt in the reaction buffer combined with the removal of salt from the detection zone through washing steps resulted in a poor screening of electrostatic repulsions between the probes and the non-fully complementary DNA targets, which allow the discrimination between C-TbgDNA and C-TbrDNA sequences by using their respective complementary probes.

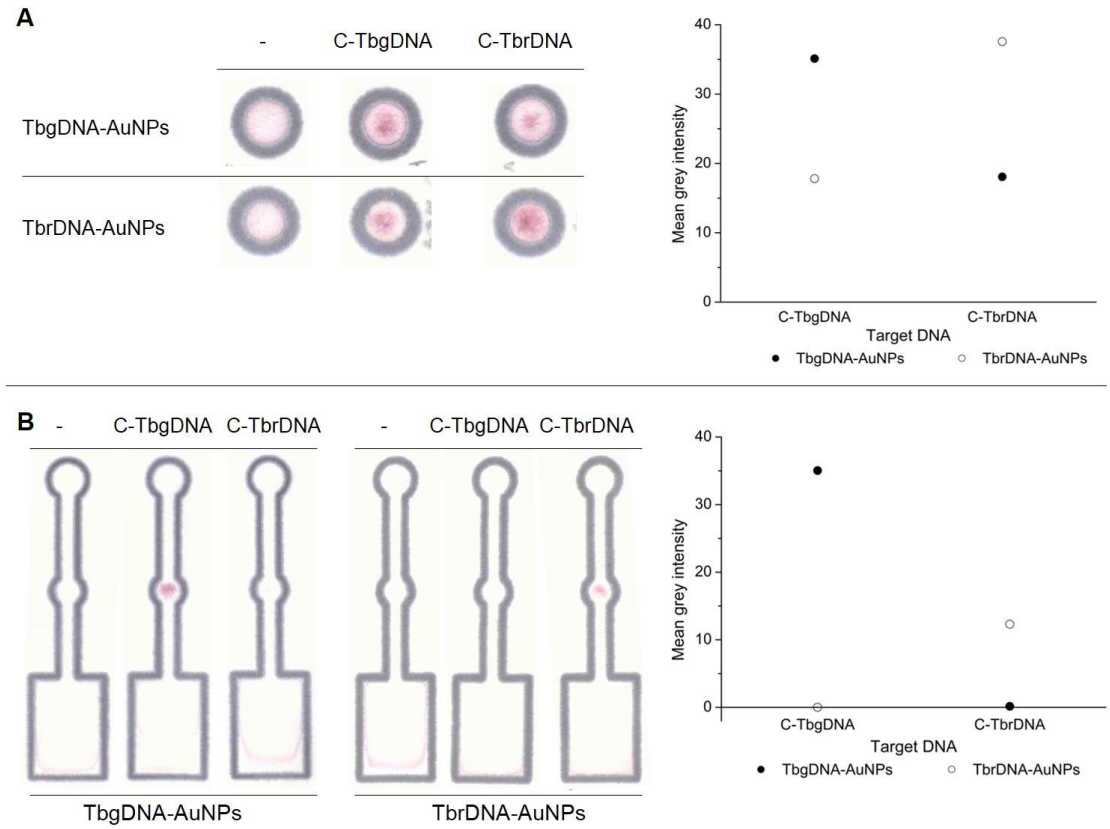

Figure 6-A3 Discriminatory detection of complementary TbgDNA and TbrDNA targets on antibody:ZZ-CBM functionalized paper using TST or its salt-free version as reaction buffer. (A) Paper well tests and (B) paper channel assays for the detection of C-TbgDNA or C-TbrDNA using TbgDNA-AuNPs or TbrDNA-AuNPs probes, respectively, and vice versa. Graphs show the mean grey intensity in each reaction/detection area after subtracting blank value, which was obtained after applying the respective DNA-AuNPs probes on plain, non-functionalized paper (-).

Chapter 7

Final remarks

The experimental work described in this thesis focuses on the development of a three-component biomolecular recognition system combined with cellulose-based platforms for the colorimetric detection of nucleic acids. This recognition approach is based on a fusion protein that combines a carbohydrate-binding module with high affinity to cellulose (family 3 CBM derived from the cellulosomal scaffolding protein A from *Clostridium thermocellum* or family 64 CBM from *Spirochaeta thermophila*) with a double Z (ZZ) domain, a synthetic derivative of the staphylococcal protein A that has high affinity to the Fc fragment of IgG antibodies.[93,105,121] The second recognition element is an anti-biotin IgG antibody, which is attached onto cellulose through the ZZ-CBM fusion. This antibody is subsequently used to capture biotin-labeled oligonucelotides that are pre-hybridized with the third recognition element, a probe composed of gold nanoparticles conjugated with complementary DNA, giving rise to a red colored signal in the cellulose matrix. Experimental results were presented in four chapters, which were arranged according to the specific objectives set for this work.

The first objective consisted in the preparation of fusion proteins comprising ZZ domains bound to a CBM (CBM3 or CBM64), and the assessment of their ability to attach antibodies on cellulose. As this work explores the combined use of the carbohydrate-binding module and its cellulose substrate, the binding capacity of CBM to cellulose was tested first. In **Chapter 3**, the ability of CBM to anchor GFP onto cellulose substrates was demonstrated through the exposure of cellulose microparticles to a CBM-GFP fusion in solution followed by the visualization of fluorescence emitted by the bound fluorescent fusion. Fusion proteins comprising a CBM (CBM3 or CBM64) bound to ZZ domains were then produced and purified in order to be used in the mediation of the attachment of antibodies onto cellulose. The structural characterization of ZZ-CBM3 and ZZ-CBM64 fusion proteins by circular dichroism indicated similar folding patterns formed by α-helices and β-strands, which correspond to the expected structure of ZZ domains and CBM proteins, respectively.[89,105,137] The ability of ZZ-CBM fusions to anchor antibodies on paper was demonstrated by the attachment of fluorescein-labeled IgG which generated fluorescent spots. Anti-biotin IgG immobilized onto cellulose via ZZ-CBM was able to recognize and capture gold nanoparticles coated with biotin, producing red colored spots on paper. These results support the use of ZZ-CBM fusions as a strategy to anchor antibodies on cellulose with preserved antibody target binding activity.

The study of the intermolecular interactions involved in the biomolecular recognition system developed in this work is described in **Chapter 4** and constituted the second objective of this thesis. FCS measurements were performed to assess changes in the diffusion time of an Atto647N-labeled DNA probe upon exposure to increasing concentrations of complementary biotinylated target DNA, anti-biotin IgG antibody and ZZ-CBM fusion protein in solution.[245] The increase in the experimental diffusion time upon addition of each molecular component supports the occurrence of complexation events between the different elements. Estimates of the dissociation constants of K_d ~34 nM and K_d ~408 nM were obtained for the hybridization of the fluorescent DNA probe with its complementary biotin-labeled DNA target and for the binding of biotinylated DNA:DNA hybrids with anti-biotin IgG antibody, respectively. The interaction of ZZ-CBM with IgG antibody was further studied by ITC. A dissociation constant of K_d ~41 nM and a stoichiometry, *n*, of 1.53 were estimated, which suggests a significant affinity between IgG antibody and ZZ-CBM fusion with a binding ratio larger than 1:1.

With the goal of using a colorimetric reporter for target DNA capture events by the IgG antibodies immobilized on cellulose via ZZ-CBM fusions, AuNPs were conjugated with distinct DNA probe sequences. **Chapter 5** described the preparation of DNA-AuNPs probes, as well as functional assays for the specific hybridization with 17-mer biotinylated target sequences and subsequent capture by anti-biotin IgG. Spherical-shaped AuNPs with an average diameter of ~14 nm were synthesized by the citrate reduction method of $HAuCl_4$ and functionalized with thiolated DNA oligonucleotides.[201,202] AuNPs were conjugated with DNA sequences specific for *T. brucei* (TbDNA), *T.b. gambiense* (TbgDNA) and *T.b. rhodesiense* (TbrDNA), the last two with ~53% nucleotide identity. The TbDNA-AuNPs probe was able to specifically hybridize with the biotin-labeled DNA target and subsequently bind to anti-biotin IgG as verified by the differential electrophoretic mobility in gel. The ability of TbgDNA-AuNPs and TbrDNA-AuNPs probes to discriminate their respective complementary targets in solution was demonstrated using the non-cross-linking method.[209,235] Binding events in both molecular recognition assays with DNA-AuNPs probes were assessed based on the optical properties of AuNPs, either by visualizing the progression of red bands through an agarose gel or by monitoring the color change of test solutions upon aggregation of nanoparticles, suggesting their suitability as colorimetric reporters.

In pursuing the fourth objective of implementing a recognition system in cellulose-based platforms for the colorimetric detection of DNA hybrids, cellulose matrices were functionalized with anti-biotin IgG:ZZ-CBM conjugates and tested for the capture of biotin-DNA:DNA-AuNPs hybrids. As described in **Chapter 6**, bioactive cellulose was developed in three formats: wax-printed paper wells for the detection of pre-hybridized DNA hybrids; wax-printed paper channels for the hybridization of biotinylated DNA with DNA-AuNPs, previously impregnated on paper, and subsequent capture by anti-biotin IgG:ZZ-CBM conjugates during capillary flow;

suspended cellulose microparticles for the detection of pre-hybridized, biotinylated DNA hybrids in solution. Anti-biotin IgG antibodies attached to cellulose via ZZ-CBM were able to capture biotin-labeled DNA hybridized with DNA-AuNPs probe, generating a red capture signal visible with the naked eye and with an intensity that increases with the increasing amount of complementary target DNA tested. Antibodies attached to paper either via ZZ-CBM3 or ZZ-CBM64 were effective in the capture of labeled DNA hybrids. In comparison to anti-biotin IgG antibodies applied directly on dry paper, antibodies immobilized on paper via ZZ-CBM fusions displayed a more intense colored signal upon the capture of DNA hybrids. While the capture of DNA hybrids on functionalized cellulose was sequence-specific, paper wells were unable to discriminate oligonucleotides sequences with partial complementarity due to the lack of washing steps. The versatility of this three-component biomolecular recognition system was demonstrated through the specific capture of labeled DNA oligonucleotides either in single or multiplex assays, the latter being carried out in two-armed paper channels with a single sample loading zone, and by testing the target capture in wet or dry cellulose matrices.

Overall, the objectives set for this thesis were achieved. This work provides an experimental proof of concept of the use of cellulose matrices functionalized with antibody:ZZ-CBM conjugates for the colorimetric detection of labeled nucleic acids with DNA-coated AuNPs. As the detection of specific DNA sequences offers a convenient means of identifying a biological source, this work contributes to the development of cost effective and "reader-free" molecular diagnostic tests for the screening of infectious diseases in low tech settings. In addition, the study of the molecular interactions involved in this biomolecular recognition strategy provided information that can be used for the rational design of molecular diagnostic systems.

Further validation of this biomolecular recognition system with DNA extracted from biological samples is essential, including with different clinical isolates to assess specificity. For high levels of sensitivity and specificity testing, nucleic acid amplification is usually required. Isothermal nucleic acid amplification methods, such as loop-mediated isothermal amplification (LAMP), are a promising amplification approach since they do not require the use of expensive equipment to carry out the thermocycling reactions.[246] In fact, LAMP has been adapted previously to paper microfluidic devices.[247,248] Signal amplification strategies could also be envisioned for highly sensitive testing, and be adapted to cellulose paper-based devices as reported previously.[249] Other applications could be explored by making use of gold nanoparticles coupled to cellulose matrices functionalized with ZZ-CBM fusions, namely immunoassays for the colorimetric detection of specific antibodies/antigens.

References

1. Burgess, D. C. H., Wasserman, J. & Dahl, C. A. Global health diagnostics. *Nature* **S1**, 1–2 (2006).
2. Akobeng, A. K. Understanding diagnostic tests 1: sensitivity, specificity and predictive values. *Acta Paediatr.* **96**, 338–41 (2007).
3. Lang, T. & Secic, M. *How to report statistics in medicine: annotated guidelines for authors, editors, and reviewers*. (American College of Physicians, 2006).
4. Burd, E. M. Validation of laboratory-developed molecular assays for infectious diseases. *Clin. Microbiol. Rev.* **23**, 550–76 (2010).
5. Chiu, R. W. K., Lo, Y. M. D. & Wittwer, C. T. Molecular diagnostics: a revolution in progress. *Clin. Chem.* **61**, 1–3 (2015).
6. Debnath, M., Prasad, G. & Bisen, P. *Molecular diagnostics: promises and possibilities*. (Springer, 2010).
7. Seo, J. H., Lee, J. W. & Cho, D. The market trend analysis and prospects of cancer molecular diagnostics kits. *Biomater. Res.* **22**, 1–8 (2018).
8. Kamble, A. & Bawkar, S. *Molecular Diagnostics Market Report*. (Allied Market Research, 2017).
9. Drain, P. K. *et al.* Diagnostic point-of-care tests in resource-limited settings. *Lancet Infect. Dis.* **14**, 239–249 (2014).
10. Wang, S. *et al.* Advances in addressing technical challenges of point-of-care diagnostics in resource-limited settings. *Expert Rev. Mol. Diagn.* **16**, 449–459 (2016).
11. Mabey, D., Peeling, R. W., Ustianowski, A. & Perkins, M. D. Diagnostics for the developing world. *Nat. Rev. Microbiol.* **2**, 231–40 (2004).
12. FIND. Available at: https://www.finddx.org/. (Accessed: 10th November 2019)
13. Global Grand Challenges. Available at: https://gcgh.grandchallenges.org/. (Accessed: 9th November 2019)
14. Bill & Melinda Gates Foundation. Available at: https://www.gatesfoundation.org/. (Accessed: 9th November 2019)
15. Diagnostics For All, Inc. Available at: http://dfa.org/. (Accessed: 9th November 2019)
16. Urdea, M. *et al.* Requirements for high impact diagnostics in the developing world. *Nature* **S1**, 73–79 (2006).
17. Pelton, R. Bioactive paper provides a low-cost platform for diagnostics. *Trends Anal. Chem.* **28**, 925–942 (2009).
18. López-Marzo, A. M. & Merkoçi, A. Paper-based sensors and assays: a success of the engineering design and the convergence of knowledge areas. *Lab Chip* **16**, 3150–3176 (2016).
19. Nogueira, F., Vaz, J., Mouro, C., Piskin, E. & Gouveia, I. Covalent modification of cellulosic-based textiles: a new strategy to obtain antimicrobial properties. *Biotechnol. Bioprocess Eng.* **19**, 526–533 (2014).
20. Miao, J. *et al.* Lysostaphin-functionalized cellulose fibers with antistaphylococcal activity for wound healing applications. *Biomaterials* **32**, 9557–9567 (2011).
21. Barbiroli, A. *et al.* Antimicrobial activity of lysozyme and lactoferrin incorporated in cellulose-based food packaging. *Food Control* **26**, 387–392 (2012).
22. Kavruk, M., Özalp, V. C. & Öktem, H. A. Portable bioactive paper-based sensor for quantification of pesticides. *J. Anal. Methods Chem.* **2013**, 932946 (2013).
23. Arciuli, M., Palazzo, G., Gallone, A. & Mallardi, A. Bioactive paper platform for colorimetric phenols detection. *Sensors Actuators B Chem.* **186**, 557–562 (2013).
24. Wang, A. G. *et al.* Paper-based DNA reader for visualized quantification of soil-transmitted helminth infections. *ACS Sensors* **3**, 205–210 (2018).

25. Magro, L. *et al.* Paper-based RNA detection and multiplexed analysis for Ebola virus diagnostics. *Sci. Rep.* **7**, 1347 (2017).
26. Martinez, A. W., Phillips, S. T., Whitesides, G. M. & Carrilho, E. Diagnostics for the developing world: microfluidic paper-based analytical devices. *Anal. Chem.* **82**, 3–10 (2010).
27. Sher, M., Zhuang, R., Demirci, U. & Asghar, W. Paper-based analytical devices for clinical diagnosis: recent advances in the fabrication techniques and sensing mechanisms. *Expert Rev. Mol. Diagn.* **17**, 351–366 (2017).
28. Free, A. H., Adams, E. C., Kercher, M. Lou, Free, H. M. & Cook, M. H. Simple specific test for urine glucose. *Clin. Chem.* **3**, 163–168 (1957).
29. Martinez, A. W., Phillips, S. T., Butte, M. J. & Whitesides, G. M. Patterned paper as a platform for inexpensive, low-volume, portable bioassays. *Angew Chem Int Ed* **46**, 1318–20 (2007).
30. Migliozzi, D. & Guibentif, T. Assessing the potential deployment of biosensors for point-of-care diagnostics in developing countries: technological, economic and regulatory Aspects. *Biosensors* **8**, 1–10 (2018).
31. Roman, M. Model cellulosic surfaces: history and recent advances. in *Model Cellulosic Surfaces* 3–53 (ACS Symposium Series, 2009).
32. Credou, J. & Berthelot, T. Cellulose: from biocompatible to bioactive material. *J. Mater. Chem. B* **2**, 4767–4788 (2014).
33. Moon, R. J., Martini, A., Nairn, J., Simonsen, J. & Youngblood, J. Cellulose nanomaterials review: structure, properties and nanocomposites. *Chem. Soc. Rev.* **40**, 3941–3994 (2011).
34. Heinze, T. Cellulose: structure and properties. in *Cellulose chemistry and properties: fibers, nanocelluloses and advanced materials* 1–52 (Advances in Polymer Science, 2016).
35. Klemm, D., Heublein, B., Fink, H. & Bohn, A. Cellulose: fascinating biopolymer and sustainable raw material. *Angew Chem Int Ed Engl* **44**, 3358–3393 (2005).
36. Evans, E., Gabriel, E., Coltro, W. & Garcia, C. Rational selection of substrates to improve color intensity and uniformity on microfluidic paper-based analytical devices. *Analyst* **139**, 2127–2132 (2014).
37. Martin, J. *Concise encyclopedia of the structure of materials*. (Elsevier Ltd, 2007).
38. Prazeres, D. M. & Rosa, A. M. M. Microscopic structure of chromatographic paper (100X). (2015). doi:10.6084/m9.figshare.1608695.v3
39. Prazeres, D. M. & Rosa, A. M. M. Microscopic structure of chromatographic paper (300X). (2015). doi:10.6084/m9.figshare.1608697.v3
40. Prazeres, D. M. & Rosa, A. M. M. Microscopic structure of chromatographic paper (700X). (2015). doi:10.6084/m9.figshare.1608696.v2
41. Prazeres, D. M. & Rosa, A. M. M. Microscopic structure of chromatographic paper (1,500X). (2015). doi:10.6084/m9.figshare.1608698.v2
42. Hong, J., Ye, X. & Zhang, Y.-H. P. Quantitative determination of cellulose accessibility to cellulase based on adsorption of a nonhydrolytic fusion protein containing CBM and GFP with its applications. *Lagmuir* **23**, 12535–12540 (2007).
43. Carrilho, E., Phillips, S. T., Vella, S. J., Martinez, A. W. & Whitesides, G. M. Paper Microzone Plates. *Anal. Chem.* **81**, 5990–5998 (2009).
44. Ofir, K. *et al.* Versatile protein microarray based on carbohydrate-binding modules. *Proteomics* **5**, 1806–14 (2005).
45. Schaude, C., Meindl, C., Fröhlich, E., Attard, J. & Mohr, G. J. Developing a sensor layer for the optical detection of amines during food spoilage. *Talanta* **170**, 481–487 (2017).
46. Veigas, B. *et al.* Gold on paper–paper platform for Au-nanoprobe TB detection. *Lab Chip* **12**, 4802–4808 (2012).
47. Bahadır, E. B. & Sezgintürk, M. K. Lateral flow assays: principles, designs and labels. *Trends Anal. Chem.* **82**, 286–306 (2016).
48. Butler, S. A., Khanlian, S. A. & Cole, L. A. Detection of early pregnancy forms of

human chorionic gonadotropin by home pregnancy test devices. *Clin. Chem.* **47**, 2131–2136 (2001).
49. Carrell, C. *et al.* Beyond the lateral flow assay: a review of paper-based microfluidics. *Microelectron. Eng.* **206**, 45–54 (2019).
50. Cate, D. M., Adkins, J. A., Mettakoonpitak, J. & Henry, C. S. Recent developments in paper-based microfluidic devices. *Anal. Chem.* **87**, 19–41 (2015).
51. Yetisen, A. K., Akram, M. S. & Lowe, C. R. Paper-based microfluidic point-of-care diagnostic devices. *Lab Chip* **13**, 2210–2251 (2013).
52. Xia, Y., Si, J. & Li, Z. Fabrication techniques for microfluidic paper-based analytical devices and their applications for biological testing: a review. *Biosens. Bioelectron.* **77**, 774–789 (2016).
53. Li, X., Ballerini, D. R. & Shen, W. A perspective on paper-based microfluidics: current status and future trends. *Biomicrofluidics* **6**, 11301–1130113 (2012).
54. Bruzewicz, D. A., Reches, M. & Whitesides, G. M. Low-cost printing of poly(dimethylsiloxane) barriers to define microchannels in paper. *Anal. Chem.* **80**, 3387–92 (2008).
55. Li, X., Tian, J., Nguyen, T. & Shen, W. Paper-based microfluidic devices by plasma treatment. *Anal Chem* **80**, 9131–9134 (2008).
56. Olkkonen, J., Lehtinen, K. & Erho, T. Flexographically printed fluidic structures in paper. **82**, 10246–10250 (2010).
57. Chitnis, G., Ding, Z., Chang, C.-L., Savran, C. A. & Ziaie, B. Laser-treated hydrophobic paper: an inexpensive microfluidic platform. *Lab Chip* **11**, 1161–5 (2011).
58. Fenton, E. M., Mascarenas, M. R., López, G. P. & Sibbett, S. S. Multiplex lateral-flow test strips fabricated by two-dimensional shaping. *ACS Appl. Mater. Interfaces* **1**, 124–9 (2009).
59. Oliveira, R. A. G. De, Camargo, F., Pesquero, N. C. & Faria, R. C. A simple method to produce 2D and 3D microfluidic paper-based analytical devices for clinical analysis. *Anal. Chim. Acta* **957**, 40–46 (2017).
60. Li, X., Tian, J., Garnier, G. & Shen, W. Fabrication of paper-based microfluidic sensors by printing. *Colloids Surfaces B Biointerfaces* **76**, 564–570 (2010).
61. Abe, K., Suzuki, K. & Citterio, D. Inkjet-printed microfluidic multianalyte chemical sensing paper. *Anal. Chem.* **80**, 6928–34 (2008).
62. Dungchai, W., Chailapakul, O. & Henry, C. S. A low-cost, simple, and rapid fabrication method for paper-based microfluidics using wax screen-printing. *Analyst* **136**, 77–82 (2011).
63. Lu, Y., Shi, W., Jiang, L., Qin, J. & Lin, B. Rapid prototyping of paper-based microfluidics with wax for low-cost, portable bioassay. *Electrophoresis* **30**, 1497–500 (2009).
64. Carrilho, E., Martinez, A. W. & Whitesides, G. M. Understanding wax printing: a simple micropatterning process for paper-based microfluidics. *Anal. Chem.* **81**, 7091–5 (2009).
65. Garcia, P. de T., Cardoso, T., Garcia, C., Carrilho, E. & Coltro, W. A handheld stamping process to fabricate microfluidic paper-based analytical devices with chemically modified surface for clinical assays. *RSC Adv.* **4**, 37637–37644 (2014).
66. Gallibu, C., Gallibu, C., Avoundjian, A. & Gomez, F. A. Easily fabricated microfluidic devices using permanent marker inks for enzyme assays. *Micromachines* **7**, E6 (2016).
67. Rosa, A. M. M. *et al.* Capture and detection of DNA hybrids on paper via the anchoring of antibodies with fusions of carbohydrate binding modules and ZZ-domains. *Anal. Chem.* **86**, 4340–4347 (2014).
68. Jang, I. & Song, S. Facile and precise flow control for a paper-based microfluidic device through varying paper permeability. *Lab Chip* **15**, 3405–3412 (2015).
69. Washburn, E. W. The dynamics of capillary flow. *Phys. Rev.* **17**, 273–283 (1921).
70. Jokerst, J. C. *et al.* Development of a paper-based analytical device for the

colorimetric detection of selected foodborne pathogens. *Anal. Chem.* **84**, 2900–2907 (2012).
71. Almeida, A., Rosa, A. M. M., Azevedo, A. M. & Prazeres, D. M. F. A biomolecular recognition approach for the functionalization of cellulose with gold nanoparticles. *J. Mol. Recognit.* **30**, e2634 (2017).
72. Ruivo, S., Azevedo, A. M. & Prazeres, D. M. F. Colorimetric detection of D-dimer in a paper-based immunodetection device. **538**, 5–12 (2017).
73. Scida, K., Li, B., Ellington, A. D. & Crooks, R. M. DNA detection using origami paper analytical devices. *Anal. Chem.* **85**, 9713–9720 (2013).
74. Renault, C., Koehne, J., Ricco, A. J. & Crooks, R. M. Three-dimensional wax patterning of paper fluidic devices. *Langmuir* **30**, 7030–7036 (2014).
75. Kong, F. & Hu, Y. F. Biomolecule immobilization techniques for bioactive paper fabrication. *Anal. Bioanal. Chem.* **403**, 7–13 (2012).
76. Welch, N. G., Scoble, J. A., Muir, B. W. & Pigram, P. J. Orientation and characterization of immobilized antibodies for improved immunoassays (Review). *Biointerphases* **12**, 02D301 1-13 (2017).
77. Huang, Z., Gengenbach, T., Tian, J., Shen, W. & Garnier, G. Effect of Bovine Serum Albumin treatment on the aging and activity of antibodies in paper diagnostics. *Front. Chem.* **6**, 161 (2018).
78. Costa, M. N. *et al.* A low cost, safe, disposable, rapid and self-sustainable paper-based platform for diagnostic testing: lab-on-paper. *Nanotechnology* **25**, 094006 (2014).
79. Su, S., Ali, M. M., Filipe, C. D. M., Li, Y. & Pelton, R. Microgel-based inks for paper-supported biosensing applications. *Biomacromolecules* **9**, 935–41 (2008).
80. Evans, E., Gabriel, E., Benavidez, T., Coltro, W. & Garcia, C. Modification of microfluidic paper-based devices with silica nanoparticles. *Analyst* **139**, 5560–5567 (2014).
81. Araújo, A. C., Sonda, Y., Lundeberg, J., Ståhl, P. L. & Brumer, H. Activated paper surfaces for the rapid hybridization of DNA through capillary transport. *Anal. Chem.* **84**, 3311–3317 (2012).
82. Böhm, A., Trosien, S., Avrutina, O., Kolmar, H. & Biesalski, M. Covalent attachment of enzymes to paper fibers for paper-based analytical devices. *Front. Chem.* **6**, 214 (2018).
83. Orelma, H., Johansson, L., Filpponen, I., Rojas, O. J. & Laine, J. Generic method for attaching biomolecules via avidin-biotin complexes immobilized on films of regenerated and nano fibrillar cellulose. *Biomacromolecules* **13**, 2802–2810 (2012).
84. Oliveira, C., Carvalho, V., Domingues, L. & Gama, F. M. Recombinant CBM-fusion technology - applications overview. *Biotechnol. Adv.* **33**, 358–369 (2015).
85. Andrade, F. K., Moreira, S. M. G., Domingues, L. & Gama, F. M. P. Improving the affinity of fibroblasts for bacterial cellulose using carbohydrate-binding modules fused to RGD. *J. Biomed. Mater. Res. Part A* **92**, 9–17 (2010).
86. Hussack, G. *et al.* Purification of plant-derived antibodies through direct immobilization of affinity ligands on cellulose. *J. Agric. Food Chem.* **58**, 3451–3459 (2010).
87. Walker, J. A. *et al.* Multifunctional cellulase catalysis targeted by fusion to different carbohydrate-binding modules. *Biotechnol. Biofuels* **8**, 1–20 (2015).
88. Singh, S., Hinkley, T., Nugen, S. R. & Talbert, J. N. Colorimetric detection of *Escherichia coli* using engineered bacteriophage and an affinity reporter system. *Anal. Bioanal. Chem.* **411**, 7273–7279 (2019).
89. Boraston, A. B., Bolam, D. N., Gilbert, H. J. & Davies, G. J. Carbohydrate-binding modules: fine-tuning polysaccharide recognition. *Biochem. J.* **382**, 769–781 (2004).
90. Shoseyov, O., Shani, Z. & Levy, I. Carbohydrate binding modules: biochemical properties and novel applications. *Microbiol. Mol. Biol. Rev.* **70**, 283–295 (2006).
91. Lombard, V., Ramulu, H. G., Drula, E., Coutinho, P. M. & Henrissat, B. The carbohydrate-active enzymes database (CAZy) in 2013. *Nucleic Acids Res.* **42**, 490–495 (2014).

92. CAZY - Carbohydrate- Active enZYmes, Carbohydrate-binding module family classification. Available at: http://www.cazy.org/Carbohydrate-Binding-Modules.html. (Accessed: 10th November 2019)
93. Tormo, J. *et al.* Crystal structure of a bacterial family-III cellulose-binding domain: a general mechanism for attachment to cellulose. *EMBO J.* **15**, 5739–51 (1996).
94. Schwarz, W. H. The cellulosome and cellulose degradation by anaerobic bacteria. *Appl. Microbiol. Biotechnol.* **56**, 634–649 (2001).
95. Fontes, C. M. G. A. & Gilbert, H. J. Cellulosomes: highly efficient nanomachines designed to deconstruct plant cell wall complex carbohydrates. *Annu. Rev. Biochem.* **79**, 655–681 (2010).
96. Lamed, R., Setter, E. & Bayer, E. a. Characterization of a cellulose-binding, cellulase-containing complex in *Clostridium thermocellum*. *J. Bacteriol.* **156**, 828–36 (1983).
97. Gerngross, U. T., Romaniec, M. P., Kobayashi, T., Huskisson, N. S. & Demain, a L. Sequencing of a *Clostridium thermocellum* gene (cipA) encoding the cellulosomal SL-protein reveals an unusual degree of internal homology. *Mol. Microbiol.* **8**, 325–34 (1993).
98. Bayer, E. a, Chanzy, H., Lamed, R. & Shoham, Y. Cellulose, cellulases and cellulosomes. *Curr. Opin. Struct. Biol.* **8**, 548–57 (1998).
99. Brás, J. L. A. *et al.* Diverse specificity of cellulosome attachment to the bacterial cell surface. *Sci. Rep.* **6**, 38292 (2016).
100. Hong, W. *et al.* The contribution of cellulosomal scaffoldins to cellulose hydrolysis by *Clostridium thermocellum* analyzed by using thermotargetrons. *Biotechnol. Biofuels* **7**, 80 (2014).
101. Bule, P., Pires, V. M., Fontes, C. M. & Alves, V. D. Cellulosome assembly: paradigms are meant to be broken! *Curr. Opin. Struct. Biol.* **49**, 154–161 (2018).
102. Morag, E. *et al.* Expression, purification, and characterization of the cellulose-binding domain of the scaffoldin subunit from the cellulosome of *Clostridium thermocellum*. *Appl. Environ. Microbiol.* **61**, 1980–6 (1995).
103. Yaniv, O. *et al.* Structure of a family 3a carbohydrate-binding module from the cellulosomal scaffoldin CipA of *Clostridium thermocellum* with flanking linkers: Implications for cellulosome structure. *Acta Crystallogr. Sect. F Struct. Biol. Cryst. Commun.* **69**, 733–737 (2013).
104. Lehtiö, J. *et al.* The binding specificity and affinity determinants of family 1 and family 3 cellulose binding modules. *Proc. Natl. Acad. Sci. U. S. A.* **100**, 484–9 (2003).
105. Pires, V. M. R. *et al.* Stability and ligand promiscuity of type A carbohydrate-binding modules are illustrated by the structure of *Spirochaeta thermophila St*CBM64C. *J. Biol. Chem.* **292**, 4847–4860 (2017).
106. DeLano, W. The PyMOL molecular graphics system. (2002).
107. Singh, A. *et al.* Paper-based sensors: emerging themes and applications. *Sensors* **18**, 1–22 (2018).
108. Yu, J., Wang, S., Ge, L. & Ge, S. A novel chemiluminescence paper microfluidic biosensor based on enzymatic reaction for uric acid determination. *Biosens. Bioelectron.* **26**, 3284–3289 (2011).
109. Lo, S. *et al.* A simple imaging device for fluorescence-relevant applications. *Micromachines* **9**, 1–10 (2018).
110. Ali, M. M. *et al.* A printed multicomponent paper sensor for bacterial detection. *Sci. Rep.* **7**, 1–10 (2017).
111. Wang, C. *et al.* A paper-based "pop-up" electrochemical device for analysis of beta-hydroxybutyrate. *Anal. Chem.* **88**, 6326–6333 (2016).
112. Zhao, W., Ali, M. M., Aguirre, S. D., Brook, M. A. & Li, Y. Paper-based bioassays using gold nanoparticle colorimetric probes. *Anal. Chem.* **80**, 8431–8437 (2008).
113. Yen, C. *et al.* Multicolored silver nanoparticles for multiplexed disease diagnostics: distinguishing dengue, Yellow Fever, and Ebola viruses. *Lab Chip* **15**, 1638–1641 (2015).
114. Tsai, T. *et al.* Diagnosis of tuberculosis using colorimetric gold nanoparticles on a

paper-based analytical device. *ACS Sensors* **2**, 1345–1354 (2017).
115. Cordeiro, M., Ferreira Carlos, F., Pedrosa, P., Lopez, A. & Baptista, P. Gold nanoparticles for diagnostics: advances towards points of care. *Diagnostics* **6**, 43 (2016).
116. Link, S. & El-Sayed, M. A. Size and temperature dependence of the plasmon absorption of colloidal gold nanoparticles. *J. Phys. Chem. B* **103**, 4212–4217 (1999).
117. Liu, J. & Lu, Y. Accelerated color change of gold nanoparticles assembled by DNAzymes for simple and fast colorimetric Pb^{2+} detection. *J. Am. Chem. Soc.* **126**, 12298–12305 (2004).
118. Yeh, Y.-C., Creran, B. & Rotello, V. M. Gold nanoparticles: preparation, properties, and applications in bionanotechnology. *Nanoscale* **4**, 1871–1880 (2012).
119. Huang, X. & El-Sayed, M. A. Gold nanoparticles: optical properties and implementations in cancer diagnosis and photothermal therapy. *J. Adv. Res.* **1**, 13–28 (2010).
120. Baptista, P. V. Gold nanoprobe-based non-cross-linking hybridization for molecular diagnostics: an update. *Expert Rev. Mol. Diagn.* **18**, 767–773 (2018).
121. Nilsson, B. *et al.* A synthetic IgG-binding domain based on staphylococcal protein A. *Protein Eng.* **1**, 107–113 (1987).
122. WHO. Control and surveillance of human African trypanosomiasis. *World Health Organ. Tech. Rep. Ser.* **984**, 1–237 (2013).
123. Bonnet, J., Boudot, C. & Courtioux, B. Overview of the diagnostic methods used in the field for Human African Trypanosomiasis: what could change in the next years? *Biomed Res. Int.* **2015**, 1–10 (2015).
124. Büscher, P. & Deborggraeve, S. How can molecular diagnostics contribute to the elimination of human African trypanosomiasis? *Expert Rev. Mol. Diagn.* **15**, 607–615 (2015).
125. McCartney, L., Gilbert, H. J., Bolam, D. N., Boraston, A. B. & Knox, J. P. Glycoside hydrolase carbohydrate-binding modules as molecular probes for the analysis of plant cell wall polymers. *Anal. Biochem.* **326**, 49–54 (2004).
126. Hussack, G. *et al.* Multivalent anchoring and oriented display of single-domain antibodies on cellulose. *Sensors* **9**, 5351–67 (2009).
127. Cao, Y., Zhang, Q., Wang, C., Zhu, Y. & Bai, G. Preparation of novel immunomagnetic cellulose microspheres via cellulose binding domain-protein A linkage and its use for the isolation of interferon α-2b. *J. Chromatogr. A* **1149**, 228–35 (2007).
128. Jendeberg, L. *et al.* Kinetic analysis of the interaction between protein A domain variants and human Fc using plasmon resonance detection. *J. Mol. Recognit.* **8**, 270–278 (1995).
129. Gasteiger, E. *et al.* Protein identification and analysis tools on the ExPASy Server. in *The Proteomics Protocols Handbook* (ed. Walker, J. M.) 571–607 (Humana Press, 2005). doi:10.1385/1-59259-890-0:571
130. Atkins, P. & de Paula, J. *Physical chemistry*. (W. H. Freeman, 2006).
131. Greenfield, N. J. Using circular dichroism spectra to estimate protein secondary structure. *Nat. Protoc.* **1**, 2876–2890 (2006).
132. Micsonai, A. *et al.* Accurate secondary structure prediction and fold recognition for circular dichroism spectroscopy. *Proc. Natl. Acad. Sci. U. S. A.* **112**, E3095–E3103 (2015).
133. McGuffin, L. J., Bryson, K. & Jones, D. T. The PSIPRED protein structure prediction server. *Bioinformatics* **16**, 404–405 (2000).
134. Schneider, C. A., Rasband, W. S. & Eliceiri, K. W. NIH Image to ImageJ: 25 years of image analysis. *Nat. Methods* **9**, 671–675 (2012).
135. Hochuli, E., Bannwarth, W., Döbeli, H., Gentz, R. & Stüber, D. Genetic approach to facilitate purification of recombinant proteins with a novel metal chelate adsorbent. *Nat. Biotechnol.* **6**, 1321–1325 (1988).
136. Greenfield, N. & Fasman, G. D. Computed circular dichroism spectra for the

evaluation of protein conformation. *Biochemistry* **8**, 4108–4116 (1969).
137. Zheng, D., Aramini, J. M. & Montelione, G. T. Validation of helical tilt angles in the solution NMR structure of the Z domain of Staphylococcal protein A by combined analysis of residual dipolar coupling and NOE data. *Protein Sci.* **13**, 549–554 (2004).
138. The PyMOL Molecular Graphics System, Version 1.3 Schrödinger, LLC.
139. Ritter, S. C., Milanick, M. A. & Meissner, K. E. Encapsulation of FITC to monitor extracellular pH: a step towards the development of red blood cells as circulating blood analyte biosensors. *Biomed. Opt. Express* **2**, 2012–2021 (2011).
140. Eklund, M., Sandström, K., Teeri, T. T. & Nygren, P. A. Site-specific and reversible anchoring of active proteins onto cellulose using a cellulosome-like complex. *J. Biotechnol.* **109**, 291–300 (2004).
141. Yan, R., Song, J., Cai, W. & Zhang, Z. A short review on protein secondary structure prediction methods. in *Pattern Recognition in Computational Molecular Biology: Techniques and Approaches* (eds. Elloumi, M., Iliopoulos, C. S., Wang, J. T. L. & Zomaya, A. Y.) 99–113 (JohnWiley & Sons, Inc., 2016). doi:10.1002/9781119078845.ch6
142. Dutse, S. W. & Yusof, N. A. Microfluidics-based lab-on-chip systems in DNA-based biosensing: an overview. *Sensors* **11**, 5754–5768 (2011).
143. Sassolas, A., Leca-bouvier, D. & Blum, J. DNA biosensors and microarrays. *Chem. Rev.* **108**, 109–139 (2008).
144. Yeh, C. H., Chang, Y. H., Chang, T. C., Lin, H. P. & Lin, Y. C. Electro-microchip DNA-biosensor for bacteria detection. *Analyst* **135**, 2717–22 (2010).
145. Muangsuwan, W. *et al.* Development of an immunoFET biosensor for the detection of biotinylated PCR product. *Heliyon* **2**, e00188 (2016).
146. Hu, R. *et al.* Multicolor fluorescent biosensor for multiplexed detection of DNA. *Anal. Chem.* **86**, 5009–5016 (2014).
147. Minikh, O., Tolba, M., Brovko, L. Y. & Griffiths, M. W. Bacteriophage-based biosorbents coupled with bioluminescent ATP assay for rapid concentration and detection of *Escherichia coli*. *J. Microbiol. Methods* **82**, 177–183 (2010).
148. Breusegem, S. Y., Levi, M. & Barry, N. P. Fluorescence correlation spectroscopy and fluorescence lifetime imaging microscopy. *Nephron - Exp. Nephrol.* **103**, e41–e49 (2006).
149. Lakowicz, J. R. *Principles of fluorescence spectroscopy*. (Springer, 2006).
150. Elson, E. T. & Magde, D. Fluorescence correlation spectroscopy. I. Conceptual basis and theory. *Biopolymers* **13**, 1 (1974).
151. Elson, E. L. Fluorescence correlation spectroscopy: past, present, future. *Biophys. J.* **101**, 2855–2870 (2011).
152. Kinjo, M. & Rigler, R. Ultrasensitive hybridization analysis using fluorescence correlation spectroscopy. *Nucleic Acids Res.* **23**, 1795–1799 (1995).
153. Dong, C., Zhang, P., Bi, R. & Ren, J. Characterization of solution-phase DNA hybridization by fluorescence correlation spectroscopy: rapid genotyping of C677T from methylenetetrahydrofolate reductase gene. *Talanta* **71**, 1192–1197 (2007).
154. Werner, A., Skakun, V. V., Meyer, C. & Hahn, U. RNA dimerization monitored by fluorescence correlation spectroscopy. *Eur. Biophys. J.* **40**, 907–921 (2011).
155. Kobayashi, T., Okamoto, N., Sawasaki, T. & Endo, Y. Detection of protein-DNA interactions in crude cellular extracts by fluorescence correlation spectroscopy. *Anal. Biochem.* **332**, 58–66 (2004).
156. Octobre, G., Lemercier, C., Khochbin, S., Robert-Nicoud, M. & Souchier, C. Monitoring the interaction between DNA and a transcription factor (MEF2A) using fluorescence correlation spectroscopy. *Comptes Rendus - Biol.* **328**, 1033–1040 (2005).
157. Grünwald, D., Cardoso, M. C., Leonhardt, H. & Buschmann, V. Diffusion and binding properties investigated by fluorescence correlation spectroscopy (FCS). *Curr. Pharm. Biotechnol.* **6**, 381–6 (2005).
158. Tanaka, S. & Takakuwa, Y. Intracellular interactions between protein 4.1 and

glycophorin C on transport vesicles, as determined by fluorescence correlation spectroscopy. *FEBS Lett.* **586**, 668–674 (2012).
159. Valeur, B. *Molecular fluorescence: principles and applications*. **8**, (Wiley-VCH Verlag GmbH, 2001).
160. Wiseman, T., Williston, S., Brandts, J. F. & Lin, L.-N. Rapid measurement of binding constants and heats of binding using a new titration calorimeter. *Anal. Biochem.* **179**, 131–137 (1989).
161. Pierce, M. M., Raman, C. S. & Nall, B. T. Isothermal titration calorimetry of protein-protein interactions. *Methods* **221**, 213–221 (1999).
162. Velazquez-Campoy, A., Leavitt, S. A. & Freire, E. Characterization of protein–protein interactions by isothermal titration calorimetry. in *Methods in Molecular Biology, vol. 261: Protein-Protein Interactions: Methods and Protocols* (ed. Fu, H.) 35–54 (Humana Press, 2004).
163. Jelesarov, I. & Bosshard, H. R. Isothermal titration calorimetry and differential scanning calorimetry as complementary tools to investigate the energetics of biomolecular recognition. *J. Mol. Recognit.* **12**, 3–18 (1999).
164. Deborggraeve, S. *et al.* Molecular dipstick test for diagnosis of sleeping sickness. *J. Clin. Microbiol.* **44**, 2884–2889 (2006).
165. Dertinger, T. *et al.* Two-focus fluorescence correlation spectroscopy: a new tool for accurate and absolute diffusion measurements. *ChemPhysChem* **8**, 433–443 (2007).
166. Müller, C. B. *et al.* Precise measurement of diffusion by multi-color dual-focus fluorescence correlation spectroscopy. *Eur. Lett.* **83**, 46001 (2008).
167. Polson, A. Some aspects of diffusion in solution and a definition of a colloidal particle. *J. Phys. Chem.* **54**, 649–652 (1950).
168. Ortega, a. & García de la Torre, J. Hydrodynamic properties of rodlike and disklike particles in dilute solution. *J. Chem. Phys.* **119**, 9914–9919 (2003).
169. Meagher, R. J. *et al.* End-labeled free-solution electrophoresis of DNA. *Electrophoresis* **26**, 331–350 (2005).
170. Garcia-Fernandez, E., Paulo, P. M. R. & Costa, S. M. B. Evaluation of electrostatic binding of PAMAM dendrimers and charged phthalocyanines by fluorescence correlation spectroscopy. *Phys. Chem. Chem. Phys.* **17**, 4319–4327 (2015).
171. Widengren, J. & Mets, Ü. Conceptual basis of fluorescence correlation spectroscopy and related techniques as tools in bioscience. in *Single Molecule Detection in Solution: Methods and Applications* (eds. Zander, C., Enderlein, J. & Keller, R. A.) 69–120 (John Wiley & Sons, Ltd, 2002).
172. Johnstone, A. P. & Thorpe, R. *Immunochemistry in practice*. (Blackwell Scientific Publications, 1982).
173. ThermoScientific. *Calculate dye:protein (F/P) molar ratios. Thermo Scientific TECH TIP #31* (2011).
174. Stellwagen, E. & Stellwagen, N. C. Determining the electrophoretic mobility and translational diffusion coefficients of DNA molecules in free solution. *Electrophoresis* **23**, 2794–2803 (2002).
175. Al-Soufi, W. *et al.* Fluorescence correlation spectroscopy, a tool to investigate supramolecular dynamics: inclusion complexes of pyronines with cyclodextrin. *J. Am. Chem. Soc.* **127**, 8775–8784 (2005).
176. Vijayanathan, V., Thomas, T., Sigal, L. H. & Thomas, T. J. Direct measurement of the association constant of HER2/*neu* antisense oligonucleotide to its target RNA sequence using a molecular beacon. *Antisense Nucleic Acid Drug Dev.* **12**, 225–33 (2002).
177. Yu, F., Yao, D. & Knoll, W. Oligonucleotide hybridization studied by a surface plasmon diffraction sensor (SPDS). *Nucleic Acids Res.* **32**, e75 (2004).
178. Tetin, S. Y. & Hazlett, T. L. Optical spectroscopy in studies of antibody-hapten interactions. *Methods* **20**, 341–361 (2000).
179. Hazlett, T. L., Ruan, Q. & Tetin, S. Y. Application of fluorescence correlation spectroscopy to hapten-antibody binding. in *Methods in molecular biology (Clifton,*

N.J.) **305**, 415–38 (2005).
180. Thordarson, P. Determining association constants from titration experiments in supramolecular chemistry. *Chem. Soc. Rev.* **40**, 1305–1323 (2011).
181. Gesztelyi, R. *et al.* The Hill equation and the origin of quantitative pharmacology. *Arch. Hist. Exact Sci.* **66**, 427–438 (2012).
182. Temirov, J., Bradbury, A. R. M. & Werner, J. H. Surface-immobilized antibody-antigen binding studies by single molecule fluorescence imaging. *Proc. SPIE* **6092**, 60920O-60920O1-10 (2006).
183. Jung, H. *et al.* Impact of hapten presentation on antibody binding at lipid membrane interfaces. *Biophys. J.* **94**, 3094–3103 (2008).
184. Jung, H., Robison, A. D. & Cremer, P. S. Detecting protein-ligand binding on supported bilayers by local pH modulation. *J. Am. Chem. Soc.* **131**, 1006–1014 (2009).
185. Temirov, J. P., Bradbury, A. R. M. & Werner, J. H. Measuring an antibody affinity distribution molecule by molecule. *Anal. Chem.* **80**, 8642–8648 (2008).
186. Ljungquist, C., Jansson, B., Moks, T. & Uhlen, M. Thiol-directed immobilization of recombinant IgG-binding receptors. *Eur. J. Biochem.* **186**, 557–561 (1989).
187. Madan, B., Chaudhary, G., Cramer, S. M. & Chen, W. ELP-z and ELP-zz capturing scaffolds for the purification of immunoglobulins by affinity precipitation. *J. Biotechnol.* **163**, 10–16 (2013).
188. Bao, R.-M., Yang, H.-M., Yu, C.-M. & Tang, J.-B. Oriented covalent immobilization of engineered ZZ-Cys onto maleimide-Sepharose: an affinity platform for IgG purification. *Chromatographia* **79**, 1271–1276 (2016).
189. Tang, J.-B. *et al.* Comparative characterization of recombinant ZZ protein-alkaline phosphatase and its application in enzyme immunoassays. *Appl. Microbiol. Biotechnol.* **97**, 153–158 (2013).
190. Lund, L. N. *et al.* Exploring variation in binding of Protein A and Protein G to immunoglobulin type G by isothermal titration calorimetry. *J. Mol. Recognit.* **24**, 945–952 (2011).
191. Yang, T., Baryshnikova, O. K., Mao, H., Holden, M. A. & Cremer, P. S. Investigations of bivalent antibody binding on fluid-supported phospholipid membranes: the effect of hapten density. *J. Am. Chem. Soc.* **125**, 4779–4784 (2003).
192. Nguyen, T. T., Sly, K. L. & Conboy, J. C. Comparison of the energetics of avidin, streptavidin, neutrAvidin, and anti-biotin antibody binding to biotinylated lipid bilayer examined by second-harmonic generation. *Anal. Chem.* **84**, 201–208 (2012).
193. Shadkami, F., Helleur, R. & Sithole, B. B. The analysis of optical brightening agents in paper samples using liquid chromatography with high-resolution mass spectrometry. *J. Wood Chem. Technol.* **31**, 42–57 (2011).
194. Vella, S. J. *et al.* Measuring markers of liver function using a micropatterned paper device designed for blood from a fingerstick. *Anal. Chem.* **84**, 2883–2891 (2012).
195. Li, M. *et al.* "Periodic-table-style" paper device for monitoring heavy metals in water. *Anal. Chem.* **87**, 2555–2559 (2015).
196. Link, S. & El-Sayed, M. A. Optical properties and ultrafast dynamics of metallic nanocrystals. *Annu. Rev. Phys. Chem.* **54**, 331–366 (2003).
197. Jain, P. K., Huang, W. & El-Sayed, M. A. On the universal scaling behavior of the distance decay of plasmon coupling in metal nanoparticle pairs: a plasmon ruler equation. *Nano Lett.* **7**, 2080–2088 (2007).
198. Mirkin, C. A., Letsinger, R. L., Mucic, R. C. & Storhoff, J. J. A DNA-based method for rationally assembling nanoparticles into macroscopic materials. *Nature* **382**, 607–609 (1996).
199. Jauset-Rubio, M. *et al.* Ultrasensitive , rapid and inexpensive detection of DNA using paper based lateral flow assay. *Sci. Rep.* **6**, 1–10 (2016).
200. Doria, G. *et al.* Noble metal nanoparticles for biosensing applications. *Sensors* **12**, 1657–1687 (2012).
201. Turkevich, J., Stevenson, P. C. & Hillier, J. A study of the nucleation and growth processes in the synthesis of colloidal gold. *Discuss. Faraday Soc.* **11**, 55–75 (1951).

202. Frens, G. Controlled nucleation for the regulation of the particle size in monodisperse gold suspensions. *Nature* **241**, 20–22 (1973).
203. Hurst, S. J., Lytton-Jean, A. K. R. & Mirkin, C. A. Maximizing DNA loading on a range of gold nanoparticle sizes. *Anal. Chem.* **78**, 8313–8318 (2008).
204. Matovu, E., Kuepfer, I., Boobo, A., Kibona, S. & Burri, C. Comparative detection of trypanosomal DNA by loop-mediated isothermal amplification and PCR from flinders technology associates cards spotted with patient blood. *J. Clin. Microbiol.* **48**, 2087–2090 (2010).
205. Radwanska, M. *et al.* The serum resistance-associated gene as a diagnostic tool for the detection of *Trypanosoma brucei rhodesiense*. *Am. J. Trop. Med. Hyg.* **67**, 684–690 (2002).
206. Radwanska, M. *et al.* Novel primer sequences for polymerase chain reaction-based detection of *Trypanosoma brucei gambiense*. *Am. J. Trop. Med. Hyg.* **67**, 289–295 (2002).
207. Owczarzy, R. *et al.* IDT SciTools : a suite for analysis and design of nucleic acid oligomers. *Nucleic Acids Res.* **36**, W163–W169 (2008).
208. Huang, X. & Miller, W. A time-efficient, linear-space local similarity algorithm. *Adv. Appl. Math.* **12**, 337–357 (1991).
209. Baptista, P., Doria, G., Henriques, D., Pereira, E. & Franco, R. Colorimetric detection of eukaryotic gene expression with DNA-derivatized gold nanoparticles. *J. Biotechnol.* **119**, 111–117 (2005).
210. Pecora, R. Dynamic light scattering measurement of nanometer particles in liquids. *J. Nanoparticle Res.* **2**, 123–131 (2000).
211. Shah, M., Badwaik, V. D. & Dakshinamurthy, R. Biological applications of gold nanoparticles. *J. Nanosci. Nanotechnol.* **14**, 344–362 (2014).
212. Kumar, S., Gandhi, K. S. & Kumar, R. Modeling of formation of gold nanoparticles by citrate method. *Ind. Eng. Chem. Res.* **46**, 3128–3136 (2007).
213. Grabar, K. C., Freeman, R. G., Hommer, M. B. & Natan, M. J. Preparation and characterization of Au colloid monolayers. *Anal. Chem.* **67**, 735–743 (1995).
214. Yu, C.-J. & Tseng, W.-L. Colorimetric detection of mercury(II) in a high-salinity solution using gold nanoparticles capped with 3-mercaptopropionate acid and adenosine monophosphate. *Langmuir* **24**, 12717–12722 (2008).
215. Hinterwirth, H. *et al.* Comparative method evaluation for size and size-distribution analysis of gold nanoparticles. *J. Sep. Sci.* **36**, 2952–2961 (2013).
216. Witten, K. G., Bretschneider, J. C., Eckert, T., Richtering, W. & Simon, U. Assembly of DNA-functionalized gold nanoparticles studied by UV/Vis-spectroscopy and dynamic light scattering. *Phys. Chem. Chem. Phys.* **10**, 1870–1875 (2008).
217. Wang, X. *et al.* Chiral surface of nanoparticles determines the orientation of adsorbed transferrin and its interaction with receptors. *ACS Nano* **11**, 4606–4616 (2017).
218. Haiss, W., Thanh, N. T. K., Aveyard, J. & Fernig, D. G. Determination of size and concentration of gold nanoparticles from UV - vis spectra. *Anal. Chem.* **79**, 4215–4221 (2007).
219. He, Y. Q., Liu, S. P., Kong, L. & Liu, Z. F. A study on the sizes and concentrations of gold nanoparticles by spectra of absorption, resonance Rayleigh scattering and resonance non-linear scattering. *Spectrochim. Acta, Part A Mol. Biomol. Spectrosc.* **61**, 2861–2866 (2005).
220. Wang, A. *et al.* Gold nanoparticles: synthesis, stability test, and application for the rice growth. *J. Nanomater.* **2014**, 1–6 (2014).
221. Zijlstra, P., Paulo, P. M. R., Yu, K., Xu, Q. H. & Orrit, M. Chemical interface damping in single gold nanorods and its near elimination by tip-specific functionalization. *Angew. Chemie - Int. Ed.* **51**, 8352–8355 (2012).
222. Shortell, M. P., Fernando, J. F. S., Jaatinen, E. A. & Waclawik, E. R. Accurate measurement of the molecular thickness of thin organic shells on small inorganic cores using dynamic light scattering. *Langmuir* **30**, 470–476 (2014).
223. Li, F., Zhang, H., Dever, B., Li, X.-F. & Le, X. C. Thermal stability of DNA

functionalized gold nanoparticles. *Bioconjug. Chem.* **24**, 1790–1797 (2013).
224. Parak, W. J. *et al.* Conformation of oligonucleotides attached to gold nanocrystals probed by gel electrophoresis. *Nano Lett.* **3**, 33–36 (2003).
225. Wang, W., Ding, X., He, M., Wang, J. & Lou, X. Kinetic adsorption profile and conformation evolution at the DNA- gold nanoparticle interface probed by dynamic light scattering. *Anal. Chem.* **86**, 10186–10192 (2014).
226. Bishop, K. J. M., Wilmer, C. E., Soh, S. & Grzybowski, B. A. Nanoscale forces and their uses in self-assembly. *Small* **5**, 1600–1630 (2009).
227. Liu, B. & Liu, J. Methods for preparing DNA-functionalized gold nanoparticles, a key reagent of bioanalytical chemistry. *Anal. Methods* **9**, 2633–2643 (2017).
228. Kreibig, U. & Genzel, L. Optical absorption of small metallic particles. *Surf. Sci.* **156**, 678–700 (1985).
229. Jiang, Z., Pan, H. & Yuan, W. Change color effect and spectral properties of gold nanoparticle-cationic surfactants system. *Chem. Res. Chinese Univ.* **20**, 523–528 (2004).
230. Li, H. & Rothberg, L. Colorimetric detection of DNA sequences based on electrostatic interactions with unmodified gold nanoparticles. *Proc. Natl. Acad. Sci. U. S. A.* **101**, 14036–14039 (2004).
231. Pellegrino, T., Sperling, R. A., Alivisatos, A. P. & Parak, W. J. Gel electrophoresis of gold-DNA nanoconjugates. *J. Biomed. Biotechnol.* **2007**, 1–9 (2007).
232. Kim, R., Yokota, H. & Kim, S.-H. Electrophoresis of proteins and protein-protein complexes in a native agarose gel. *Anal. Biochem.* **282**, 147–149 (2000).
233. Chen, Y., Liu, H., Ye, T., Kim, J. & Mao, C. DNA-directed assembly of single-wall carbon nanotubes. *J. Am. Chem. Soc.* **129**, 8696–8697 (2007).
234. Voliani, V., Luin, S., Ricci, F. & Beltram, F. Single-step bifunctional coating for selectively conjugable nanoparticles. *Nanoscale* **2**, 2783–2789 (2010).
235. Baptista, P. V, Koziol-Montewka, M., Paluch-Oles, J., Doria, G. & Franco, R. Gold-nanoparticle-probe-based assay for rapid and direct detection of *Mycobacterium tuberculosis* DNA in clinical samples. *Clin. Chem.* **52**, 1433–1434 (2006).
236. Peeling, R., Holmes, K., Mabey, D. & Ronald, A. Rapid tests for sexually transmitted infections (STIs): the way forward. *Sex Transm Infect* **82**, v1-6 (2006).
237. Morbioli, G. G., Mazzu-Nascimento, T., Stockton, A. M. & Carrilho, E. Technical aspects and challenges of colorimetric detection with microfluidic paper-based analytical devices (μPADs) - A review. *Anal. Chim. Acta* **970**, 1–22 (2017).
238. Martinez, A. W. *et al.* Simple telemedicine for developing regions : camera phones and paper-based microfluidic devices for real-time , off-site diagnosis. *Anal. Chem.* **80**, 3699–3707 (2008).
239. Yunker, P. J., Still, T., Lohr, M. A. & Yodh, A. G. Suppression of the coffee-ring effect by shape-dependent capillary interactions. *Nature* **476**, 308–311 (2011).
240. Shen, X., Ho, C.-M. & Wong, T.-S. Minimal size of coffee ring structure. *J. Phys. Chem. B* **114**, 5269–5274 (2010).
241. Park, K., Koerner, H. & Vaia, R. A. Depletion-induced shape and size selection of gold nanoparticles. *Nano Lett.* **10**, 1433–1439 (2010).
242. Schildkraut, C. & Lifson, S. Dependence of the melting temperature of DNA on salt concentration. *Biopolymers* **3**, 195–208 (1965).
243. Owczarzy, R. *et al.* Effects of sodium ions on DNA duplex oligomers: improved predictions of melting temperatures. *Biochemistry* **43**, 3537–3554 (2004).
244. Qiao, W., Chiang, H., Xie, H. & Levicky, R. Surface vs. solution hybridization: effects of salt, temperature, and probe type. *Chem. Commun.* **51**, 17245–17248 (2015).
245. Rosa, A. M. M., Prazeres, D. M. & Paulo, P. M. R. Fluorescence correlation spectroscopy study of the complexation of DNA hybrids, IgG antibody, and a chimeric protein of IgG-binding ZZ domains fused with a carbohydrate binding module. *Phys. Chem. Chem. Phys.* **19**, 16606–16614 (2017).
246. Notomi, T. *et al.* Loop-mediated isothermal amplification of DNA. *Nucleic Acids Res.* **28**, E63 (2000).

247. Connelly, J. T., Rolland, J. P. & Whitesides, G. M. ‘Paper machine’ for molecular diagnostics. *Anal. Chem.* **87**, 7595–7601 (2015).
248. Rodriguez, N. M., Wong, W. S., Liu, L., Dewar, R. & Klapperich, C. M. A fully integrated paperfluidic molecular diagnostic chip for the extraction, amplification, and detection of nucleic acids from clinical samples. *Lab Chip* **16**, 753–763 (2016).
249. Huang, J.-Y. *et al.* Signal amplified gold nanoparticles for cancer diagnosis on paper-based analytical devices. *ACS Sensors* **3**, 174–182 (2018).